Understanding microbially-mediated pyrrhotite dissolution in the Duluth Complex, northern MN

A DISSERTATION SUBMITTED
TO THE FACULTY OF THE GRADUATE SCHOOL
OF THE UNIVERSITY OF MINNESOTA
BY

Kathryn Kiku Hobart

IN PARTIAL FULFILLMENT OF THE
REQUIREMENTS FOR THE DEGREE OF
DOCTOR OF PHILOSOPHY

Joshua M. Feinberg and Daniel S. Jones

October 2022

Acknowledgements

The University of Minnesota is built on the ancestral lands of the Wahpekute band that was ceded to the United States by the Treaty of Traverse des Sioux in July of 1851, in an agreement that was not paid in full and whose underlying aim was the dissolution of the Dakota culture. The University has also benefited from Chippewa and Dakota (Mede-wakanton, Wahpekuta, Wahpeton and Sisseton Bands) land ceded by treaty and given to the University of Minnesota via the Morrill Act. Due to its land-grant status, the infrastructure, financial foundations, and faculty, students, and staff at the University of Minnesota all continue to benefit directly from these ceded lands, and I wish to acknowledge this support in my research.

The work presented here would not have been possible without the support of numerous individuals. A huge thank you goes to my friends at the University of Minnesota, whose support over my six years has gotten me through a departmental building move, an apartment fire, a global pandemic, two years of classes, my written and oral exams, numerous conferences, and years of happy hour trivia success.

To the IRM faculty, staff, postdocs, and students – thank you for your tireless support setting up experiments, helping me analyze and interpret data, and for teatimes, barbeques, and the finest day-old pastries.

Special thanks go to the Bailey Lab and its members, past and present – Jake and Bev, this work would not have been possible without your support! Special thanks also go to my direct collaborators, Elizabeth Roepke, Michael Volk, Zhaazhaawaanong Greensky, and Kimberly Hernandez, whose work has directly supported the projects that are presented here, and to the support and assistance of my New Mexico Tech colleagues, Mackenzie Best, Zoë Havlena, Katelyn Green, and Abagail Brown, for their microbiological and bioinformatic support and for welcoming me to New Mexico whenever I visit.

To my advisors, Joshua Feinberg and Daniel Jones: thank you for your endless support in all scientific, educational, and personal endeavors and for teaching me about magnetic minerals *and* about microorganisms and microbial metabolisms. I could not have found better advisors for my PhD and I look forward to working with you both for years to come!

And finally, to my family, for supporting me throughout my PhD and for always encouraging me to do what I love.

Table of Contents

List of Tables

List of Figures

Chapter 1: Introduction

The Duluth Complex, located in northern Minnesota, represents the largest undeveloped copper, nickel, and platinum-group element deposit in the world. The majority of previous work on the environmental impacts of sulfide mineral mining has been conducted on the mineral pyrite (FeS_2), and the microbial communities that drive pyrite oxidation and generate highly acidic, metal-rich effluent. In contrast, the primary gangue (waste) sulfide in Duluth Complex ores is pyrrhotite ($Fe_{1-x}S$, $0 \leq x \leq 0.125$), and the relatively low concentration of sulfide minerals in the rock and the geochemistry of the host silicate minerals mean that waste rock and tailings from these deposits is not expected to generate highly acidic drainage (discussed further in Chapter 2). Studies on abiotic pyrrhotite dissolution are limited, and while dissolution rates in acidic systems are reported as 10 to 100 times higher than pyrite, studies of abiotic pyrrhotite dissolution at more neutral pH frequently present contradictory results. Further, the impact of microorganisms on pyrrhotite dissolution – particularly microorganisms that are endemic to northern Minnesota – is poorly understood.

The goal of my dissertation research, therefore, is to better understand the dissolution of pyrrhotite under "Duluth Complex" conditions. This can be further divided into four chapters that each address a facet of this question. A high-level summary of each of the chapters is presented here, with the goal of highlighting the connections between each individual project.

Chapter 2 examines the complex relationship between heating, mineral structure, and magnetic properties in the mineral pyrrhotite. Pyrrhotite is conventionally separated into the antiferromagnetic hexagonal and ferrimagnetic monoclinic polytypes. Both polytypes undergo temperature-dependent magnetic transitions, with ferrimagnetic, monoclinic pyrrhotite becoming nonmagnetic on cooling through the Besnus transition (-241°C, 32 K), while antiferromagnetic, hexagonal pyrrhotite becomes ferrimagnetic on heating through the λ-transition (217°C, 490 K). However, recent studies have shown that the relationship between pyrrhotite polytype and magnetic properties is more complex, with some forms of pyrrhotite that are ferrimagnetic at room temperature but lack the characteristic low-temperature Besnus transition. This chapter describes the utility of combining temperature-dependent X-ray diffraction experiments with temperature-dependent measurements of magnetic properties. This combination of structural and magnetic characterization techniques provides a clearer picture of mineral transformations that occur in pyrrhotite on heating than either technique can provide alone. This chapter was written for submission to *JGR: Solid Earth*, where it is currently under review. This chapter is connected to the following chapters in two ways. First, two of the pyrrhotite samples characterized in this chapter (Po2 and Po3) were used as substrates for microbial

growth in chapters 3 and 4. Second, many of the magnetic techniques used to characterize pyrrhotite in this study were also used to characterize pyrrhotite and iron oxides after the dissolution experiments described in Chapter 4.

Chapter 3 evaluates the effect of microorganisms on pyrrhotite dissolution in laboratory experiments. These experiments compare the impact of sulfur-oxidizing isolate microorganisms and microbial communities on pyrrhotite dissolution and use pyrrhotite characterized as part of the work presented in Chapter 2. This chapter compares the dissolution of pyrrhotite under abiotic conditions to pyrrhotite in batch reactors inoculated with different isolate strains of *Sulfuriferula*, a strain of *Thiobacillus*, and an enrichment community of microorganisms, under a range of pH conditions from 4.5 to 7.0. Pyrrhotite dissolution and was measured by a novel combination of geochemical and magnetic techniques. The structure and crystallinity of iron oxide precipitates were examined by combining scanning electron microscopy and measurement of magnetic properties. I find that sulfur-oxidizing microorganisms increase the amount of pyrrhotite dissolved over abiotic dissolution at pH conditions ranging from 4.5 to 7, and that *Sulfuriferula* is an important player but not the only important organism implicated in environmental pyrrhotite dissolution.

Chapter 4 compares the microbial communities found on naturally-weathered Duluth Complex outcrops to the microbial communities found on waste rock and tailings, and evaluates potential avenues for management of waste rock and tailings from Duluth Complex mines. One of the goals of Chapter 3 is to evaluate the role of environmentally-relevant microorganisms on pyrrhotite dissolution, and so this chapter provides the basis for evaluating how similar the laboratory experiments are to natural weathering environments. The microbial communities from naturally-weathered outcrops of Duluth Complex rock are compared to the communities present at a reclaimed test pit where ore material was extracted in the mid-1970s, and the communities at both the naturally-weathered and reclaimed sites to the microbial communities found in experimentally-weathered mine waste and tailings. I find that the naturally-weathered and reclaimed sites have more similar microbial community compositions than the waste rock and tailings experiments, highlighting the role of microbial metabolisms other than sulfur oxidizers and interaction between microbial communities. This work also includes a test of bioshrouding, which is a technique for controlling the growth of lithotrophic sulfur- and iron-oxidizing microorganisms by encouraging algal growth on tailings or waste rock. I find that algae had an inhibitory effect on some of the autotrophic sulfur-oxidizing microorganisms, particularly those that increased pyrrhotite dissolution in Chapter 3. This chapter was originally written for submission to *Environmental Microbiology*.

Chapter 5 compares the growth behavior and metabolic capabilities of four different strains of sulfur-oxidizing *Sulfuriferula* spp. used in the laboratory experiments in Chapter 2. Complete genomes of four isolate strains of *Sulfuriferula* are described in this

chapter, with a detailed accounting of genes that code for enzymes involved in carbon, nitrogen, sulfur, and iron cycling. The four *Sulfuriferula* strains described in this chapter each have distinct metabolic capabilities, including different metabolic pathways for sulfur oxidation and putative iron oxidation genes, and so the detailed analysis of their growth behavior and genetic potential presented in this chapter provide a link between the differences in the strains' observed behavior in Chapter 3 as well as differences in the environmental distribution of related organisms described in Chapter 4.

I. Pyrrhotite Crystallography and Magnetic Properties

a. Crystallographic Properties

Pyrrhotite is a non-stoichiometric iron sulfide mineral that occupies the compositional space between FeS and Fe_7S_8. This range in possible chemical composition leads to a diversity of crystallographic and magnetic behaviors. Pyrrhotite crystallizes in the NiAs structure, with hexagonally close-packed S atoms and octahedrally-coordinated Fe^{2+} atoms in alternating layers (Nakazawa & Morimoto, 1971). In the most iron-rich polytype (FeS, troilite), all iron sites are filled. With decreasing iron content, some of the iron sites are left vacant, with overall charge compens*at*ed by increasing the number of Fe^{3+} atoms (Morimoto et al., 1970). The arrangement of these vacancies within the lattice leads to a variety of structural and magnetic properties that depend both on the iron/sulfur ratio of the mineral and on its formation history (e.g., temperature/pressure conditions, cooling rate, chemical environment) (Bertaut, 1953; Morimoto et al., 1970). Figure 1-1 shows the idealized NiAs structure and the structure of troilite.

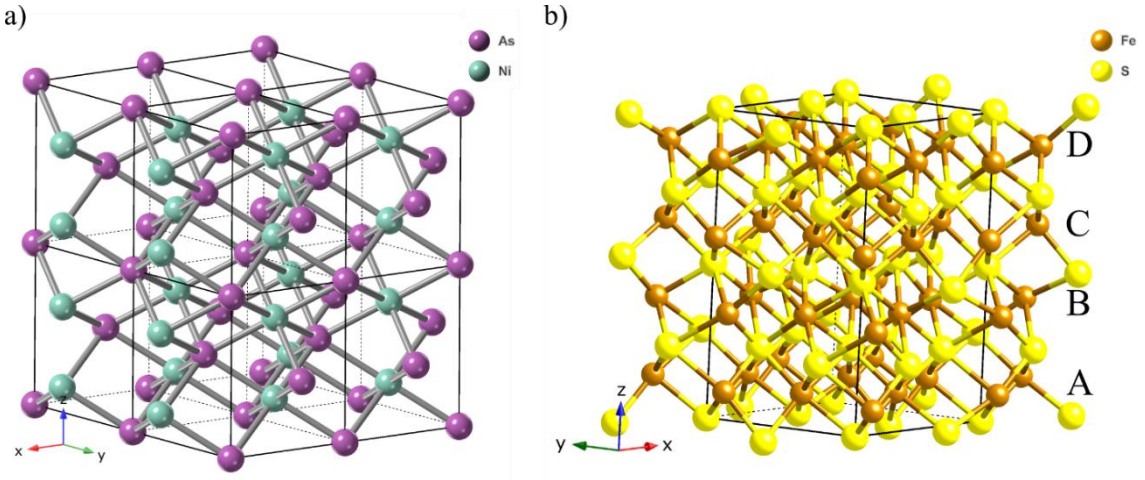

Figure 1-1: Crystal structures of (a) eight unit cells of the idealized NiAs structure and (b) one unit cell of troilite, FeS. Unit cell dimensions are indicated by the solid black line. Structure images generated using CrystalMaker® (CrystalMaker Software Ltd, Oxford, England; www.crystalmaker.com), with crystallographic data from Evans (1970) for troilite.

The periodic repetition of iron vacancy sites in iron-deficient pyrrhotites occur beyond the dimensions of a single NiAs unit cell, and so pyrrhotites are categorized by superstructures. The naming convention for these superstructures refers to the number of repeats of the unit cell in a particular crystallographic direction that are required to fully describe the atom and vacancy positions. Troilite can also be described as 2C pyrrhotite because it requires 2 repeats of the unit cell in the c crystallographic direction to fully describe the arrangement of atoms within the unit cell.

There are 5 major integral "NC" polytypes of pyrrhotite (2C (FeS), 4C (Fe_7S_8), 5C (Fe_9S_{10}), 11C ($Fe_{10}S_{11}$), and 6C ($Fe_{11}S_{12}$)) where N refers to the number of integer multiples along the NiAs *c* axis required to fully describe the arrangement of iron vacancies – for example, 4C pyrrhotite requires 4 repeats of the NiAs unit cell to fully describe the vacancy positions in the iron layers (Morimoto et al., 1970; Nakazawa & Morimoto, 1971). Most of these NC polytypes are hexagonal (the angle between the *a* and *b* axes is ≅120°), with the exception of 4C, which is monoclinic (De Villiers et al., 2009; Koto et al., 1975; Morimoto et al., 1975). The structure of 5C pyrrhotite has also been reported with respect to the orthorhombic crystal system (Elliot, 2010). These polytypes are generally differentiable by powder X-ray diffraction, but there are only small differences in the 2θ position of the major peaks and comprehensive structural identification depends on the low-intensity, high d spacing superstructure peaks.

The relative concentrations of hexagonal and monoclinic pyrrhotite can be estimated by powder X-ray diffraction using a technique developed by Arnold (1966, 1967). Briefly, "hexagonal" pyrrhotite shows one peak, representing the (102) reflection at ~43.5° 2θ (for Cu-kα, ~56° 2θ for Co-kα), while "monoclinic" pyrrhotite shows a doublet peak set, the (202)-($20\bar{2}$) reflections. Arnold's method compares the height of the single (102) peak associated with "hexagonal" pyrrhotite and the second doublet (202) peak associated with "monoclinic" 4C pyrrhotite (see e.g., fig. 3 in Arnold 1966). This tool remains widely used in evaluating natural and synthetic pyrrhotite samples and is still useful for screening samples that contain more than one polytype. Arnold also noted that as the Fe-content decreased in pyrrhotite, the 2θ value for the (102) peak increased (Arnold, 1962). Thus, Arnold argued that the position of the (102) peak can be used as a rough measure of a pyrrhotite's composition. However, this tool should not be used quantitatively, as it only provides an estimate of the bulk composition. The presence of multiple polytypes can be superimposed to produce a single peak, and so the shape of the peak (e.g., width and symmetry of the peak, presence of shoulders or secondary peaks) needs to be considered to determine if multiple polytypes are present. It is also worth noting that the full range of (102) peak positions from iron-rich troilite to the iron-deficient 4C polytype is less than a degree in 2θ space, so careful calibration of the diffractometer is required.

Integral superstructures can be identified with greater accuracy using the low-angle superstructure peaks in the ~16-20° 2θ range (for Co-kα). Li and Franzen (1996) provide some of the first discussion of the utility of examining the low-angle superstructure peaks in addition to the most intense reflections as a method for discerning pyrrhotite polytype(s), although they were described earlier (see e.g., Vaughan et al. (1971), Schwarz and Vaughan (1972)). These are low-intensity diffraction peaks that occur from planes separated by a large d-spacing (and therefore, occur at a low 2θ), and the detailed arrangement of superstructure peaks is characteristic of specific superstructures of pyrrhotite. For example, the calculated powder diffraction pattern for 4C pyrrhotite (Powell et al., 2004) shows four peaks in the 16-24° 2θ window (a pair of peaks at 17.85° and 18.05° 2θ, a peak at 19.55° 2θ, and finally a peak at 22.0° 2θ, with Co-kα), while the calculated powder diffraction pattern for 5C pyrrhotite (Elliot, 2010) shows three peaks in this window (singlet peaks at 17.6°, 18.7°, and 20.3° 2θ, with Co-kα). Despite the low intensity of these peaks, the fact that they do not overlap to the same degree as the most intense "doublet" peaks (at ~56° 2θ) makes them ideal for identifying and quantifying integral (and possibly non-integral) pyrrhotite polytypes in mixed samples. The superstructure peaks for the integral polytypes of pyrrhotite are presented in Figure 1-2(a), and the full diffraction patterns in Figure 1-2(b).

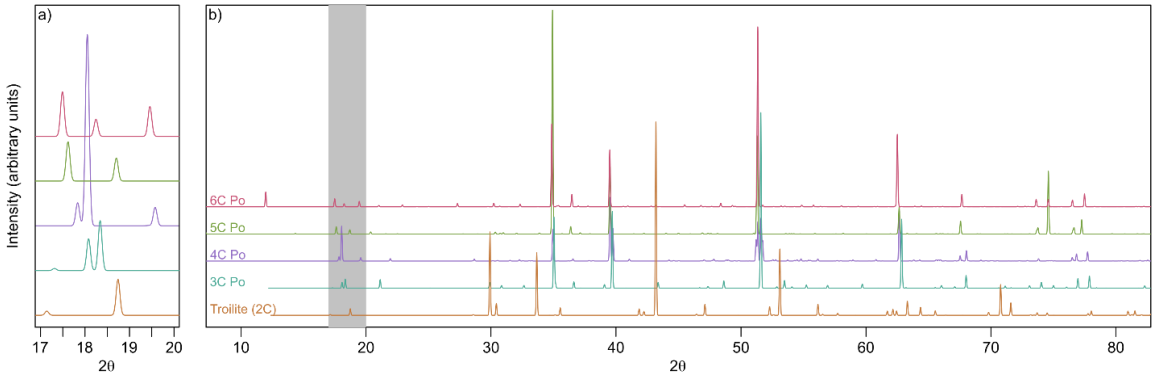

Figure 1-2. (a) Superstructure peaks and (b) full diffraction patterns for troilite (2C pyrrhotite, Bertaut, 1953), 3C pyrrhotite (sometimes 3T, Keller-Besrest et al., 1983), 4C pyrrhotite (Powell et al., 2004), 5C pyrrhotite (Elliot, 2010), and 6C pyrrhotite (De Villiers & Liles, 2010). The grey shaded area in (b) indicates the range of the superstructure peaks in (a).

Non-integral polytypes of pyrrhotite (structures that lack long-range order in iron vacancy arrangements) with a bulk composition between 5C and 6C pyrrhotite are also hexagonal, but are believed to be metastable phases that would exsolve over geologic tine into finely intergrown mixtures of integral pyrrhotite phases, with the specific mixture and arrangement of intergrown phases controlled by the composition and cooling history of the parent phase (Morimoto et al., 1975). However, intergrown mixtures of integral and non-

integral polytypes are frequently found in natural samples, (e.g., Arnold, 1966, 1967; Harries et al., 2011, 2013; Jin et al., 2021) and there is some evidence that the arrangement of vacancies in the structure can vary on the length-scale of a few unit cells (Pósfai & Buseck, 1997). Additional superstructural polytypes (e.g., NA, MC) with varying amounts of vacancy disorder at elevated temperatures are included in pyrrhotite phase diagrams (e.g., Wang and Salveson, 2005; Harries, 2012; Herbert et al., 2015; Haines et al., 2019), but the mechanism(s) that control vacancy ordering and the rate at which ordering occurs remain poorly understood. Further, the stability of integral and non-integral polytypes with changes in temperature (and any dependence of these transformations on heating or cooling rate) is not well constrained. For example, see the two phase diagrams in Figure 1-3, after Harries (2012) (a) and Haines et al. (2019) (b).

b. Magnetic Properties

Pyrrhotite polytypes are broadly divided into two categories based on their room-temperature magnetic properties: ferrimagnetic, monoclinic 4C polytype, and antiferromagnetic, hexagonal NC polytypes. Most pyrrhotite polytypes are antiferromagnetic, with the spins of the iron atoms ferromagnetically coupled such that spins are uniformly aligned within Fe layers (e.g., in Figure 1(b), layers A and C have spins aligned up (↑↑↑↑) and layers B and D have spins aligned down (↓↓↓↓)) but are antiferromagnetically coupled to Fe atoms in adjacent planes. The iron vacancies in the antiferromagnetic pyrrhotite polytypes (e.g., 2C, 5C, 11C, 6C) are arranged such that no unpaired spins exist and the net magnetic moment is zero (e.g., in Figure 1(b), the moment of layer A is symmetrically opposed by the moment of layer B (↑↓↑↓)) (Townsend et al., 1979). The arrangement of iron vacancies in the 4C polytype, however – where in every other layer, one out of every eight Fe sites is vacant – results in unpaired electron spins and consequently is ferrimagnetic (Dekkers, 1988).

Temperature-dependent transitions in magnetic properties are a useful tool for identifying and separating pyrrhotite polytypes, although the mechanistic underpinnings that control these transitions are not in all cases well understood. All forms of pyrrhotite undergo a high-temperature Neél transition at ≈325°C (sometimes called the β-transition, indicated in Figure 1-3 by the blue dashed line), where magnetic ordering is lost above this temperature due to a combination of structural and thermal effects. Below the Neél temperature, magnetic spins are aligned ferrimagnetically within layers and antiferromagnetically coupled between layers, while above the Neél temperature the pyrrhotite behaves as a paramagnet (where spins are randomly oriented unless in the presence of an external magnetic field). However, since antiferromagnetic pyrrhotites lack a net external magnetization, the loss of magnetic ordering when heating through the Neél temperature is most apparent in the ferrimagnetic 4C polytype, where heating through this transition results in a sharp loss in magnetization (Powell et al., 2004). While Koulialias et

al. (2019, 2021) find that vacancy ordering occurs upon quenching through the Neél temperature in 4C pyrrhotite (implying that the ferrimagnetic vacancy arrangement in 4C pyrrhotite persists above the Neél temperature, and quenching a sample through the Neél temperature simply "snaps" the magnetic spins into alignment), the reversibility of this transition has not been established for all heating/cooling rates. The ferrimagnetic 4C polytype also has a characteristic, reversible low-temperature Besnus transition at ≋32 K (-241.15°C), where induced and remanent magnetization decrease on cooling (Besnus & Meyer, 1964; Dekkers, 1989; Volk et al., 2018). While the mechanism(s) driving the Besnus transition remain a topic of active research (Haines et al., 2019; Koulialias, Charilaou, et al., 2018; Koulialias, Schäublin, et al., 2018; Koulialias et al., 2019; Volk et al., 2016, 2018; Wolfers et al., 2011), low-temperature remanence measurements are often used as a tool to detect ferrimagnetic pyrrhotite.

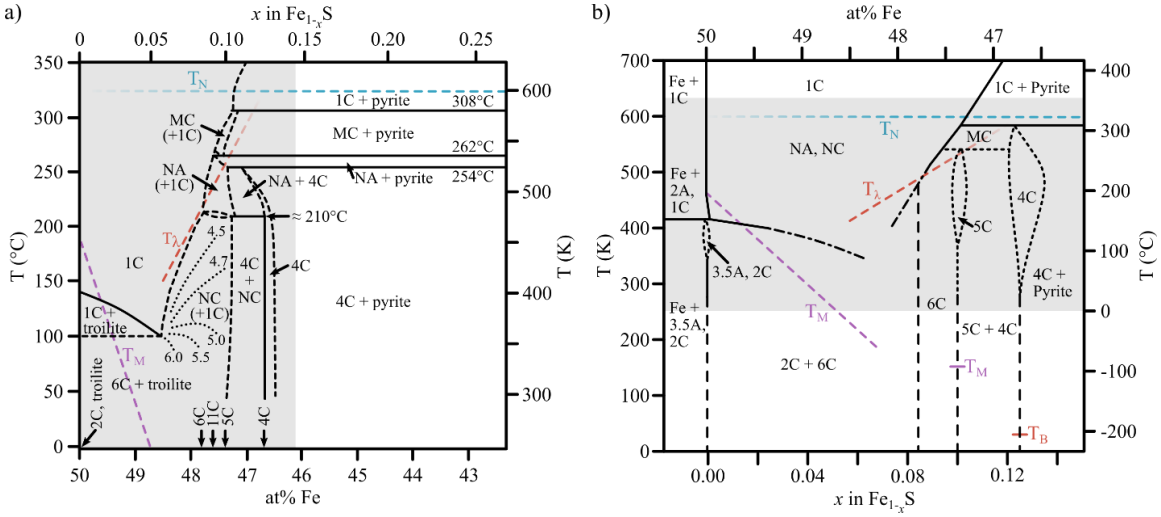

Figure 1-3: Fe-S phase diagram after (a) Harries (2012) and (b) Haines et al. (2019). In both (a) and (b), the high-temperature λ-transition is marked by the red dashed line (T_λ) (Grønvold & Haraldsen, 1952), the Neél temperature is marked by the blue dashed line (T_N) (Dekkers, 1989), and the temperature-composition dependent FeS spin-flop (Morin-type, T_M) transition by the purple dashed line (Horwood et al., 1976). 1C refers to a polytype with completely randomized vacancies. In (a), tentative phase boundaries are indicated by dashed lines and values of N for the NC polytypes are indicated by the dotted lines, after Nakazawa and Morimoto (1971). In (b), the dashed lines represent the "ideal" superstructure-composition pairs for the 6C, 5C, and 4C polytypes extended to the origin, with observed occurrence of these polytypes marked by the dotted lines. The dot-dash lines indicate the poorly constrained phase transition behavior at elevated temperature between the integral, non-integral, and high-temperature superstructures. (b) also includes the 32 K Besnus transition (TB) of 4C pyrrhotite (Volk et al., 2016) and the Morin transition in 5C (Haines et al., 2020). In each phase diagram the temperature and Fe-S space described in the opposite diagram is marked by the grey shaded region.

Antiferromagnetic pyrrhotite polytypes lack the Besnus transition, but undergo a temperature-dependent magnetic transition at ≈220°C (Haraldsen, 1937). The λ-transition (sometimes called the γ-transition, indicated in Figure 1-3 by the red dashed line) is seen as an irreversible increase in magnetic susceptibility on heating, proposed to be due to increasing thermal disorder (Kissin & Scott, 1982) or due to a change in superstructural ordering to a "4C-like" polytype (Hobart et al., 2021 and Chapter 2, this thesis). The precise temperature of the λ-transition varies depending on the pyrrhotite polytype(s) present in the sample (Kontny et al., 2000), the arrangement of the intergrowths, and the prior cooling history of the sample (Koulialias et al., 2021). A general increase in the temperature of the λ-transition with decreasing iron content, from 150°C in 48.5%Fe pyrrhotite and increasing in temperature with decreasing iron content until the ferrimagnetic 4C endmember is reached, is reported by Haraldsen (1937) and Grønvold and Haraldsen (1952). Some researchers have identified the λ-transition as a crystallographic transformation from the NC to 1C polytype, although this identification is debated (Haines et al., 2019; Koulialias et al., 2021). Some studies show that 1C pyrrhotite is paramagnetic and stable only above ~350°C (Koulialias et al., 2019), which would preclude its role in the λ-transition. Magnetic susceptibility then decreases on continued heating at the Neél temperature for pyrrhotite (or at slightly lower temperature, beginning at ≈255°C (Bennett & Graham, 1981)) but unlike in 4C pyrrhotite, this transition is not reversible, with a permanent increase in bulk susceptibility preserved on cooling (Herbert et al., 2015). Some studies find that the temperature of the Neél transition in antiferromagnetic pyrrhotite is affected by the application of a magnetic field during heating (Dorogina et al., 2015). One of the complications in measuring these thermomagnetic properties is that pyrrhotite frequently oxidizes to magnetite and pyrite on heating (even in a non-oxidizing Ar atmosphere), with the alteration behavior of the sample being different even in chemically identical samples of pyrrhotite exposed to the same heating conditions (see e.g., Dekkers (1990)). It can therefore be difficult to separate the irreversible transformation of antiferromagnetic to ferrimagnetic pyrrhotite polytypes from the oxidative transformation of antiferromagnetic pyrrhotite to magnetite and pyrite.

Troilite (2C pyrrhotite, FeS) lacks the λ-transition due to completely antiferromagnetic behavior; since all iron sites are filled there is no vacancy rearrangement on heating (Dorogina et al., 2015). In addition to the Neél temperature, FeS shows the α-transition (indicated in Figure 1-3 by the purple dashed line), a Morin-type spin-flop transition at 172°C (445 K) that decreases in temperature with decreasing iron content to a low of ≈-103°C (170 K) at 48.3% Fe. Above this temperature, magnetic spins are oriented perpendicular to the crystallographic c axis, and rotate to parallel to the c axis below this temperature (Haines et al., 2019; Horwood et al., 1976). The α-transition is not frequently discussed in other antiferromagnetic polytypes, however Haines et al. (2020) report the presence of a Morin transition at ≈155 K in 5C pyrrhotite, resulting in a small but

measurable change in magnetization. While the magnitude of this transition is approximately 100X smaller than that of the Bensus transition, the detectible presence of this transition suggests that other polytypes may also show similar low-temperature magnetic transitions.

Rock magnetic studies frequently interpret the results of thermomagnetic experiments using the conventional framework that all ferrimagnetic pyrrhotite is 4C pyrrhotite. This interpretation is based on the conventional model where the 4C polytype is the only one capable of retaining a spontaneous magnetization at room temperature. However, this interpretation is rarely confirmed by detailed powder diffraction or other structural analyses, and recent work has demonstrated that other pyrrhotite polytypes (and other structurally-similar iron sulfide minerals) are capable of retaining permanent magnetizations (Horng, 2018; Horng et al., 2020; Horng & Roberts, 2018; Li & Franzen, 1996; Roberts et al., 2011). Horng (2018) and Horng and Roberts (2019) reported the presence of a ferrimagnetic "3C" form of pyrrhotite in marine methane seep sediments. The 3C (or 3T) polytype was previously described in synthetic samples with the composition Fe_7S_8 (Fleet, 1971; Keller-Besrest et al., 1983; Nakano et al., 1979), and as a modification of the 4C structure due to Ti substitution for Fe in Fe_7S_8 (Baranov et al., 2014). The natural sample containing 3C pyrrhotite is ferrimagnetic at room temperature and displays a Neél temperature of ≈318°C, but lacks the low-temperature Besnus transition characteristic of 4C pyrrhotite, and is crystallographically distinct (Horng, 2018; Horng & Roberts, 2018).

These magnetic properties are complicated further by the presence of intergrowths on the micron to millimeter scale (Arnold, 1966; Fleet & Macrae, 1969; Harries et al., 2011, 2013; Rao & Rao, 1968), twinned crystals (Bin & Pauthenet, 1963; Wolfers et al., 2011), and nonintegral superstructures that persist at room temperature (Harries et al., 2011; Jin et al., 2021; Pósfai & Buseck, 1997). All of these features could result in locally uncompen*sat*ed magnetic moments, producing a net magnetization even in antiferromagnetic pyrrhotite polytypes. Further, the presence of other ferrimagnetic iron sulfide minerals, such as smythite (Fe_9S_{11}) or greigite (Fe_3S_4), can complicate the deconvolution of magnetic signals from natural samples (Hoffmann et al., 1993; Horng et al., 2020; Roberts et al., 2011).

c. Abiotic Pyrrhotite Dissolution

Pyrrhotite is an acid-soluble sulfide mineral, and so can dissolve by both oxidative and non-oxidative processes. These processes are complicated by the variable stoichiometry and crystal structure of pyrrhotite. It is generally reported that pyrrhotite has oxidation rates of one to two orders of magnitude greater than pyrite under equivalent conditions, although most of the studies that publish kinetic rates do not distinguish between polytypes (or, if they do, only establish whether the pyrrhotite is monoclinic,

hexagonal, or a mixture). A review by Belzile et al. (2004) reports that pyrrhotite dissolves between 20 to 100 times faster than pyrite under acidic conditions (below pH 4) depending on the conditions of the study. Dissolution rate appears to be pH dependent, although studies rarely agree on how pH affects dissolution rate. For example, Nicholson and Scharer (1993) find that at 10°C and 22°C, there is negligible change in pyrrhotite dissolution rate with pH, but at 33°C, there is a dramatic doubling in rate between pH 2 and pH 6, with a rate minimum at pH 4. Conversely, a rate equation generated by Chiriță and Rimstidt (2014) that combined existing literature data and new experiments predict that rate increases with decreasing pH. Interestingly, both Nicholson and Scharer (1993) and Chiriță and Rimstidt (2014) use natural pyrrhotite with a bulk stoichiometry of Fe_9S_{10}, determined using the method of Arnold (1967) in the case of Nicholson and Scharer (1993), and by a combination of electron microprobe analysis and X-ray diffraction in Chiriță and Rimstidt (2014). Bădică and Chiriță (2015) report a dramatic decrease in dissolution rate for synthetic troilite between pH 4 and 5, which they link to a change in oxidation mechanism due to the significant decrease in Fe^{3+} solubility above pH 4. Most other reported rates are at a pH ≅ 2 and focus on temperature and the effect of different oxidants rather than pH (Belzile et al., 2004). Voltametric studies of pyrrhotite oxidation (with a nominal Fe:S ratio corresponding to 4C pyrrhotite) in alkaline solutions (pH 4.6, 9.2, and 13.0) found that the formation of a passivation layer of elemental sulfur and iron oxides strongly inhibited oxidation (Hamilton & Woods, 1981).

Regardless of rate, pyrrhotite can be oxidized abiotically by either ferric iron or oxygen, depending on pH conditions and the aqueous geochemistry of the system by the "polysulfide mechanism" (McGuire & Hamers, 2000; Schippers & Sand, 1999). Under acidic conditions, where aqueous ferric iron can be present at high concentrations, pyrrhotite can be oxidized by ferric iron, either completely to sulfate (1) or partially to elemental sulfur (2):

$$Fe_{1-x}S_{(s)} + (8-2x)Fe^{3+} + 4H_2O \rightarrow (9-3x)Fe^{2+} + SO_4^{2-} + 8H^+ \quad (1)$$

$$Fe_{(1-x)}S_{(s)} + (2-2x)Fe^{3+} \rightarrow (3-3x)Fe^{2+} + S^0_{(s)} \quad (2)$$

Acidity is produced by complete oxidation of pyrrhotite to sulfate, but not during partial oxidation to elemental sulfur. When oxygen is the primary oxidant, the overall oxidation of pyrrhotite to sulfate (3) can release anywhere from no acidity, for the oxidation of FeS, up to 0.25 mol protons for 4C pyrrhotite (x = 0.125) (Nicholson & Scharer, 1993). Due to vacancies in the structure and resultant uncompen*sat*ed charge, iron exists as both Fe^{2+} and Fe^{3+} states in pyrrhotite, although the presence of Fe^{3+} cannot be confirmed by Mössbauer spectroscopy due to rapid electron transfer between states (Levinson & Treves, 1968; Wang & Salveson, 2005).

$$\mathrm{Fe_{(1-x)}S_{(s)}} + \left(2 - \frac{x}{2}\right)\mathrm{O_2} + xH_2O \rightarrow (1-x)Fe^{2+} + SO_4^{2-} + 2xH^+ \quad (3)$$

$$\mathrm{Fe^{2+} + 0.25O_2 + 1.5H_2O \rightarrow Fe(OH)_{3\,(s)} + 2H^+} \quad (4)$$

$$\mathrm{Fe_{(1-x)}S_{(s)}} + \left(\frac{1-x}{2}\right)O_2 + 2(1-x)H^+ \rightarrow (1-x)\mathrm{Fe^{2+}} + \mathrm{S^0_{(s)}} + (1-x)H_2O \quad (5)$$

Acid can also be produced by the oxidation and precipitation of dissolved iron as iron oxyhydroxide minerals (4). However, if pyrrhotite is oxidized incompletely to elemental sulfur by oxygen, acid may be consumed (5), although above pH 4 this will be offset somewhat by the precipitation of iron oxyhydroxides and the balance of acidity generated or consumed depends on the stoichiometry of the pyrrhotite (Nicholson & Scharer, 1993).

Pyrrhotite can also dissolve non-oxidatively (with respect to the sulfur atoms) by proton attack in the polysulfide mechanism, releasing Fe^{2+} and H_2S. The H_2S is then oxidized by Fe^{3+} ions to form the $H_2S^{\bullet+}$ radical (shown as one step in 6), which then dissociates to H^+ and the $HS^{\bullet-}$ radical.

$$\mathrm{FeS_{(s)} + Fe^{3+} + 2H^+ \rightarrow 2Fe^{2+} + H_2S^{\bullet+} \rightarrow 2Fe^{2+} + HS^{\bullet-} + H^+} \quad (6)$$

Two or more $HS^{\bullet-}$ radicals can react to form polysulfides of varying chain lengths, which can then decompose to elemental sulfur (7) or oxidize further by oxygen or Fe^{3+} to thiosulfate, polythionates, or sulfate (8, 9) (Schippers & Sand, 1999).

$$\mathrm{H_2S_9 \rightarrow H_2S + S_{8\,(s)}} \quad (7)$$

$$\mathrm{H_2S_n + {}^3/_2\,O_2 \rightarrow H_2S_2O_3 + \left({}^{(n-2)}/_8\right)S_{8\,(s)}} \quad (8)$$

$$\mathrm{H_2S_n + 6Fe^{2+} + 3H_2O \rightarrow H_2S_2O_3 + \left({}^{(n-2)}/_8\right)S_{8\,(s)} + 6Fe^{2+} + 6H^+} \quad (9)$$

Pyrrhotite dissolution appears to be controlled by both charge transfer (redox) and mass transfer (diffusion) processes at the mineral surface. Many experimental studies report the formation and progressive enrichment of a sulfur-rich layer on the surface of pyrrhotite grains. One study reports the conversion of pyrrhotite surfaces to more S-rich smythite (Fe_9S_{11}) (Taylor, 1971), which is supported by further studies that find metal-deficient sulfides are the initial oxidation products of pyrrhotite oxidation (Buckley & Woods, 1985). Extensive study of pyrrhotite surfaces by X-ray photoelectron spectroscopy (XPS) and Auger electron spectroscopy (AES) as oxidation in air and sulfuric acid progressed found that an initial layer of iron(III)-oxyhydroxides formed on the mineral surface, with a sulfur-enriched layer of the oxidized pyrrhotite immediately below the iron oxyhydroxides increasing in thickness over time (Mycroft et al., 1995; Pratt et al., 1994, 1996). Other studies have noted the formation of elemental sulfur as a component of this

reaction layer, typically between the outer iron-oxide layer and the inner metal-deficient sulfide (Buckley & Woods, 1985; Chandra & Gerson, 2010; Chiriță, 2016; Harries et al., 2013).

Orlova et al. (1988) is the source of the frequently cited assertation that hexagonal pyrrhotite is more reactive than monoclinic (they report activation energies of 46.23 kJ/mol for hexagonal pyrrhotite and 50.21kJ/mol for monoclinic) at pH 1. However, this does not appear to hold true for all pH conditions. One study reports that monoclinic pyrrhotite (Fe_7S_8, determined by the method of Arnold (1967)) dissolved in concentrated sulfuric acid ($pH \ll 1$) has a lower activation energy than that of troilite (FeS) (Bugajski & Gamsjäger, 1982), suggesting that there is a crystallographic control on dissolution. Harries et al. (2013), who used H_2O_2 as the oxidant, find that NC pyrrhotite (N~4.85) oxidizes more quickly than 4C pyrrhotite below pH 2.7, but above that pH the behavior inverts (with 4C pyrrhotite oxidizing more rapidly) and rates drop by two orders of magnitude. Conversely, the rate equation determined by Chiriță and Rimstidt (2014) predicts no statistically significant differences in dissolution rate between troilite, hexagonal pyrrhotite, and monoclinic pyrrhotite, which is supported by the findings of Janzen et al. (2000) who further suggest that dissolution rate is primarily controlled by available surface area rather than crystallographic or chemical differences in pyrrhotite polytype.

II. The Duluth Complex

a. The Midcontinent Rift

The Duluth Complex is part of the larger Mesoproterozoic Midcontinent Rift system, which represents the record of a major tectonic rifting event around 1.1Ga. A large volume of intrusive and extrusive igneous rock was emplaced over a relatively short period (~30 million years) (Woodruff et al., 2020). Surface-exposed outcrops of the Midcontinent Rift are primarily found in the Lake Superior region, although significant aeromagnetic and gravity anomalies extend the rift system through north-central Oklahoma on the western side and into contact with the fold-and-thrust belts of the Grenville orogenies in south-eastern Michigan on the eastern side (Hinze & Chandler, 2020). A third, less-developed branch of the Midcontinent Rift system has been identified where similar-aged mafic/ultramafic sills continue into Canada as the Nipigon Embayment (Franklin et al., 1980), although this identification is still debated (Hinze & Chandler, 2020). There is some evidence that the gravity high found in Ohio and Kentucky is a continuation of the Midcontinent rift system (Drahovzal et al., 1992; Moecher et al., 2018; Stein et al., 2018), although this gravity anomaly could also be linked to crustal thickening from the Grenville orogeny (Dufréchou & Harris, 2013). The Southwestern Laurentia large igneous province in Texas and New Mexico has also been proposed as an extension of the rift system (Adams & Keller, 1994; Bright et al., 2014) although these intrusions are compositionally distinct

from those of the Midcontinent rift system (Kargi & Barnes, 1995). The volume of igneous rock emplaced (conservative estimates suggest 1.5-2 million km^3 of extrusive basalt, with an equivalent volume of intrusive deposits) suggest that a mantle plume was the ultimate source of the magma emplaced during rifting (Cannon, 1992; Hutchinson et al., 1990; Nicholson et al., 1997). This is further supported by combined paleomagnetic pole paths and high-precision U-Pb dates that suggest upwelling from this mantle plume resulted in the rapid movement of Laurentia and ultimately the tectonic collisions associated with the Grenville orogeny (Swanson-Hysell et al., 2019).

The Midcontinent Rift system is characterized by three intervals of magmatic activity, a "post-rift" period of clastic sedimentation and subsidence, and a late deformational event (Woodruff et al., 2020). The ~1112 to ~1105 Ga Plateau Stage is the first stage of magmatic activity, and is characterized by the deposition of a ~10km thick basaltic plateau around the Lake Superior region (Cannon, 1992; Green, 1989), accompanied by intrusions of sills and plutons like the Coldwell Complex in Ontario (Heaman & Machado, 1992) and the Felsic Series and Early Gabbro Series that represent the oldest Duluth Complex rocks (Miller et al., 2002). This stage is not characterized by significant normal faulting and graben development (consistent with an extensional tectonic regime) but rather the formation of a broad sag basin (Allen et al., 1997; Green, 1983) consistent with mantle downwelling (Middleton, 1989). Following a ~5 Ma interval without significant volcanic or intrusive igneous activity, the ~1105 to ~1090 Ma Rift Stage is the second major interval of igneous activity in the rift system (Woodruff et al., 2020). The Rift Stage is characterized by frequent, wide-spread eruptions of basaltic magma that filled the subsiding extensional basin (White, 1960), interspersed with continuous conglomerate and sandstone units (Merk & Jirsa, 1982). Mafic intrusions into the middle and upper crust created the Duluth and Beaver Bay Complexes in northern Minnesota, where layered, thin sheets of magma intruded into the country rock forming the Anorthosite and Layered Series intrusions (Miller et al., 2002). The final interval of igneous deposition is the ~1090 to ~1083 Ma Late-Rift Stage, which is broadly characterized by decreased magmatism and increased sedimentation, along with continued subsidence in the central rift basins. There was localized volcanism around the current western rim of Lake Superior (like the Schroeder-Lutsen basalts in Northern MN and the Lakeshore Traps on the upper peninsula of MI), and this interval also saw the formation of hydrothermal mineral deposits along the north shore of Lake Superior into the Thunder Bay and Mamainse Point areas (Woodruff et al., 2020).

The Post-Rift Stage reflects the time between the end of significant magmatic influence (~1083 Ma) and the onset of compression due to a phase of the Grenville orogeny (~1060 Ma). Significant sedimentation and accumulation of lacustrine, marine, and clastic sedimentary sequences occurred during this interval as the central rift basins continued to subside (Daniels, 1982). Finally, tectonic forces due to the Grenville orogeny led to reverse

faulting, folding, and deformation during the Compressional Stage. The major compressional fault through these rocks, the Keweenaw fault, is dated to 1060 ± 20 Ma (Cannon et al., 1993). Hydrothermal native copper and silver deposits were generated during this stage by burial metamorphism and dehydration of basalts (Bornhorst & Mathur, 2017), which have been dated to 1053 ± 7 Ma (Symons & Kawasaki, 2019).

b. Ore Geology of the Duluth Complex

The Duluth Complex is a set of plutonic to subvolcanic intrusive rocks emplaced into the base of the North Shore Volcanic Group between 1108 and 1098 Ma, and represent the largest intrusive component of the Midcontinent Rift (Miller, 2011). The intrusive igneous rocks are thought to have intruded as multiple thin sheets into the Paleoproterozoic and Archean rocks that now make up the footwall of the Duluth Complex. Four general rock series within the Duluth Complex can be distinguished based on age, dominant lithology, internal structure, and position within the complex, which are reviewed in greater detail in Miller et al. (2002). The sulfide mineral deposits in the Duluth Complex are located in the Layered Series and concentrated along the basal contact of the Duluth Complex with the country rock where magma intruded and incorporated metasedimentary and granitic rocks (Miller et al., 2002). Major sulfide mineral deposits are found in the Partridge River intrusion (Bonnichsen, 1974), which hosts at least four copper-nickel deposits and at least seven potential Fe-Ti deposits (Miller et al., 2002), and the South Kawishiwi intrusion, which hosts at least seven copper-nickel deposits and a potential platinum-group element-copper-nickel deposit (Benko et al., 2015; Gál et al., 2011, 2011; Lee & Ripley, 1995).

The ore mineralization in the Layered Series is categorized as a contact-type Cu-Ni-PGE magmatic sulfide deposit. This type of mineralization occurs where country rock sulfur mixes with mafic melts resulting in the formation and enrichment of immiscible sulfide melts (Zientek, 2012). In the Duluth Complex, the source of the sulfur appears to be from interactions with sulfur-bearing metasedimentary footwall rocks, specifically the carbonaceous shales, siltstones, and sandstones of the Virginia Formation (Andrews & Ripley, 1989; Mainwaring & Naldrett, 1977; Ripley et al., 2007; Thériault et al., 1997, 2000; Tyson & Chang, 1984). Detailed study of $\delta^{34}S$ values and S/Se ratios identify the likely source of sulfur as the "bedded pyrrhotite" unit of the Virginia Fm., a sulfide-rich shale layer (Queffurus & Barnes, 2014). This sulfide-rich metasedimentary layer has been recognized in the footwall of sulfide deposits (Severson, 1994; Thériault et al., 1997; Zanko et al., 1994) and as xenoliths within Duluth Complex rocks (Severson et al., 1996; Williams et al., 2010). The highest sulfide concentrations in the intruded rocks appear to be spatially related to contact with the "banded pyrrhotite" unit of the Virginia Fm. (Hauck et al., 1997). A massive sulfide ore zone in the Babbitt deposit (within the Partridge River intrusion) hosts the highest PGE concentrations reported for the Duluth Complex, and contains 5-

25% Cu, 11ppm Pd, and 8ppm Pt. Total amount of ore in the Duluth Complex is estimated at ~5 billion tons, at about 1% Cu and 0.2% Ni (Eckstrand & Hulbert, 2007).

Throughout these ore deposits the primary sulfide minerals are pyrrhotite, chalcopyrite ($CuFeS_2$), cubanite ($CuFe_2S_3$), and pentlandite ($(Fe,Ni)_9S_8$), and are generally disseminated throughout the host mafic igneous rocks, although some local areas can be more massive. Ore mineralization in the Partridge River intrusion is described as consisting of three distinct styles: Cu-rich, PGE-poor disseminated sulfides, Cu-rich, PGE-rich disseminated sulfides, and semi-massive to massive sulfides (Thériault et al., 2000), while ore mineralization in the South Kawishiwi Intrusion is more consistently restricted to enriched zones (Gál et al., 2011).

III. Microbial Sulfide Mineral Dissolution

Most of the previous work evaluating the role microorganisms play in sulfide mineral dissolution has been conducted on pyrite (FeS_2), which is briefly summarized here. In acidic systems (below pH ~4), microorganisms are thought to accelerate the dissolution of pyrite by oxidizing aqueous Fe^{2+} to Fe^{3+}. Pyrite is not directly acid-soluble and requires oxidation of reduced iron or sulfur, typically by aqueous Fe^{3+} or O_2, for dissolution to proceed. However, because pH affects the solubility of Fe^{3+} in oxygenated systems, pyrite dissolution rate is typically much faster in acidic systems due to increased aqueous Fe^{3+}. The overall reactions for pyrite oxidation by dissolved oxygen (10) and Fe^{3+} (11) are as follows:

$$FeS_{2\,(s)} + {}^{7}/_{2}\,O_{2\,(aq)} + H_2O_{(l)} \rightarrow Fe^{2+}{}_{(aq)} + 2SO_4^{2-}{}_{(aq)} + 2H^{+}{}_{(aq)} \qquad (10)$$

$$FeS_{2\,(s)} + 14Fe^{3+}{}_{(aq)} + 8H_2O_{(aq)} \rightarrow 15Fe^{2+}{}_{(aq)} + 2SO_4^{2-}{}_{(aq)} + 16H^{+}{}_{(aq)} \qquad (11)$$

The production of sulfate from sulfide-mineral-bound reduced sulfur requires the transfer of 8 e^- per sulfur atom, requiring the sequential oxidation of intermediate sulfur compounds at the surface of the mineral (Moses et al., 1987). This is described as the "thiosulfate mechanism," where oxidation of disulfides like pyrite by ferric iron produces ferrous iron (Fe^{2+}) and thiosulfate (12), and the thiosulfate is oxidized (either abiotically or by microorganisms) to sulfate (13) (Edwards et al., 2000; Sand et al., 1995; Schippers, 2004):

$$FeS_{2(s)} + 6\,Fe^{3+}{}_{(aq)} + 3\,H_2O_{(l)} \rightarrow 7\,Fe^{2+}{}_{(aq)} + S_2O_3^{2-}{}_{(aq)} + 6\,H^{+}{}_{(aq)} \qquad (12)$$

$$S_2O_3^{2-}{}_{(aq)} + 8\,Fe^{3+}{}_{(aq)} + 5\,H_2O_{(l)} \rightarrow 8\,Fe^{2+}{}_{(aq)} + 2\,SO_4^{2-}{}_{(aq)} + 10\,H^{+}{}_{(aq)} \qquad (13)$$

Pyrite oxidation by Fe^{3+} is much more rapid than oxidation by O_2, with oxidation by O_2 typically forming intermediate oxidation state sulfur compounds like thiosulfate and polythionates (Moses & Herman, 1991).

Microorganisms appear to indirectly promote oxidation of sulfide minerals in acidic environments by regenerating Fe^{3+} in solution, which oxidizes the mineral surface and releases partially oxidized sulfur compounds to the surrounding environment (as opposed to "directly" transfer electrons to mineral surfaces by enzymes as proposed by Silverman (1967)) In acidic systems, microorganisms such as *Acidithiobacillus ferrooxidans*, which use Fe^{2+} as a source of metabolic energy, generate aqueous Fe^{3+} up to 1,000,000x faster than abiotic Fe^{2+} oxidation (Meruane & Vargas, 2003; Morgan & Lahav, 2007; Vera et al., 2013). This indirect mechanism can be further subdivided into "contact" and "non-contact" mechanisms that describe the position of cells relative to the mineral surface, where the "contact" mechanism is mediated by mineral-surface-attached cells and the "non-contact" mechanism is mediated by planktonic cells (Baker & Banfield, 2003; Rohwerder & Sand, 2003). Mutualistic interactions between iron-oxidizing, sulfur-oxidizing, and heterotrophic organisms have been extensively researched as tools for biomining, where iron-oxidizing organisms are the "oxidant manufacturers" who refresh the supply of Fe^{3+} necessary for sulfide mineral oxidation, sulfur-oxidizing organisms are the "acid generators" who maintain the acidic conditions necessary for microbial Fe^{2+} oxidation and Fe^{3+} solubility, and heterotrophic "janitors" which degrade organic compounds that are potentially toxic to iron- and sulfur-oxidizing microorganisms (Johnson, 2018; Rawlings & Johnson, 2007). Sulfur-oxidizing microorganisms have a variety of enzymatic tools that use different types of reduced or intermediate oxidation sulfur compounds which are discussed further in Chapter 6.

Chapter 2: Combining temperature-dependent magnetic and diffraction data to understand pyrrhotite phase transitions

Pyrrhotites are a class of geologically important nonstoichiometric iron sulfides with the general composition of Fe1-xS ($0 \leq x \leq 0.125$) and are found in a variety of intergrown polytypes, conventionally separated into the antiferromagnetic hexagonal and the ferrimagnetic monoclinic (4C) varieties. Both structures undergo magnetic phase transitions, where antiferromagnetic polytypes display the λ-transition at ~490 K and the 4C polytype shows the Besnus transition at ~30 K. However, recent studies have shown the relationship between pyrrhotite polytypes and their magnetic behavior is more complex and non-monoclinic polytypes (e.g., 3C) are also capable of retaining a spontaneous magnetization at room temperature. These advances raise the level of detail needed to characterize pyrrhotite in rock magnetic and paleomagnetic studies. We demonstrate the utility of combining X-ray diffraction data collected as a function of temperature with low- and high-temperature magnetic measurements to characterize natural samples. We analyze two natural samples that contain mixtures of 4C, 5C, and 6C polytypes and describe how their polytypes and magnetic properties vary as a function of temperature across the λ-transition and how and when pyrite and greigite form during heating. We also report the effect on natural samples of an annealing protocol commonly used to elevate the concentration of the 4C polytype in synthetic samples and found that annealing transforms some antiferromagnetic pyrrhotite into a form whose diffraction pattern most closely resembles the 4C polytype with a room temperature spontaneous magnetization but lacks the characteristic Besnus transition.

This work was originally formatted for submission to the journal *JGR: Solid Earth* and is currently undergoing revisions for resubmission. A previous version of this manuscript is available as Hobart et al. (2021). Co-author Michael Volk conducted the magnetic and HTXRD experiments on Po1. All co-authors assisted with data analysis and interpretation.

I. Introduction

Pyrrhotite, $Fe_{1-x}S$ ($0 \leq x \leq 0.125$), is a structurally and magnetically complex non-stoichiometric iron sulfide. It is the second-most abundant Fe-sulfide mineral in the Earth's crust after pyrite and occurs across a wide range of terrestrial and extraterrestrial settings. Pyrrhotite occurs in magmatic and metamorphic rocks (Dunlop & Özdemir, 2001), claystones and shales (Aubourg & Pozzi, 2010; Horng et al., 2012; Rochette, 1987), limestones (Muttoni, 1995), as secondary authigenic sulfides (Horng, 2018; Horng & Roberts, 2018; Weaver et al., 2002), and even as inclusions in diamonds originating in the deep mantle (Gilder et al., 2011). Pyrrhotite can form via the thermal alteration of pyrite

(Y.-H. Chen et al., 2019; L. Liu et al., 2020; Toulmin & Barton, 1964; Yang et al., 2018). Furthermore, pyrrhotite can be found in several classes of meteorites, including Martian (e.g., Fu et al., 2021; Rochette et al., 2001) and chondritic meteorites (e.g., Watson et al., 1975; Zhang et al., 2008). Pyrrhotite is also an important indicator mineral for economic geology because it is often associated with elevated concentrations of Cu, Ni, and Pt group elements (Severson et al., 2002). Given its widespread occurrence and geophysical importance, it is essential to develop methods that allow researchers to (1) identify which forms of pyrrhotite are present in a natural sample, (2) evaluate whether these represent the sample's original magnetic mineral assemblage, and (3) interpret when and how a recorded magnetization was acquired.

Pyrrhotite occurs in a variety of polytypes defined by composition and crystal structure. Pyrrhotite crystallizes in the NiAs structure, where the atoms form a hexagonal close-packed structure with iron and sulfur atoms layered normal to the c-axis (Nakazawa & Morimoto, 1971). While all sulfur positions in the unit cell are filled, some iron layers contain vacancies (Morimoto et al., 1970). These vacancies can be arranged randomly or can be ordered, the extent to which is dependent on the total Fe content and its heating and cooling history, leading to many possible vacancy superstructures (Bertaut, 1953; Morimoto et al., 1970). Pyrrhotite polytypes can be described by the repeating structural arrangement of such iron vacancies. Most of these polytypes are of "NC" type (e.g., 4C (Fe_7S_8), 5C (Fe_9S_{10}), 11C ($Fe_{10}S_{11}$), and 6C ($Fe_{11}S_{12}$)), where the N refers to the number of integer multiples along the NiAs c-axis (Morimoto et al., 1970; Nakazawa & Morimoto, 1971) required to describe the repeating arrangement of iron vacancies. Most of these NC polytypes are assumed to be hexagonal, with the exception of 4C, which is monoclinic. (De Villiers et al., 2009; Morimoto et al., 1975) 5C pyrrhotite has been reported to be orthorhombic (Elliot, 2010). Characterization of these NC polytypes typically relies on powder diffraction methods to constrain the relative concentration of different vacancy superstructures. Non-integral pyrrhotites (that is, pyrrhotites without long-range order in their iron vacancies) with a bulk composition between 5C and 6C are also hexagonal, but are believed to be metastable, and over geologic time exsolve into finely intergrown mixtures of Fe_7S_8, Fe_9S_{10}, $Fe_{10}S_{11}$, or $Fe_{11}S_{12}$ depending on the composition and cooling history of the parent phase (Morimoto et al., 1975). Nevertheless, these non-integral phases are frequently found in natural samples (e.g. Harries et al., 2011, 2013; Jin et al., 2021). Notably, Pósfai & Buseck (1997) find that intergrown pyrrhotites can vary on the length scale of a few unit cells. Additional polytypes (e.g., NA, MC) with ordered vacancies at elevated temperatures are included in pyrrhotite phase diagrams (e.g., Haines et al., 2019; Harries et al., 2011; Herbert et al., 2015; Wang & Salveson, 2005), but the mechanism that controls vacancy ordering and the rate at which ordering occurs remains poorly constrained.

Conventional thinking about the magnetic properties of pyrrhotite polytypes relies on the existence of two categories: a monoclinic ferrimagnetic form (4C), and a collection

of antiferromagnetic hexagonal forms, corresponding to the structural forms described above. These forms often occur simultaneously in natural samples (Arnold, 1966; Graham, 1969) and are frequently found intergrown from millimeter to sub-micrometer scales (e.g. Harries et al., 2013), with evidence that structural variability occurs even at the unit cell scale (Pósfai & Buseck, 1997). Most pyrrhotite polytypes are antiferromagnetic, where the spins of the iron atoms are ferromagnetically coupled such that spins are aligned uniformly within Fe layers but are antiferromagnetically coupled to Fe atoms in adjacent planes. The iron vacancies in antiferromagnetic pyrrhotite polytypes (e.g., 5C, 6C, and 11C) are arranged so that no unpaired Fe spins exist and the net magnetic moment is zero (Townsend et al., 1979). However, the vacancy structure of monoclinic 4C pyrrhotite contains unpaired spins and consequently is ferrimagnetic (Dekkers, 1988). The 4C ferrimagnetic polytype is especially important for paleo- and planetary magnetism because it can carry a strong remanent magnetization (Besnus & Meyer, 1964; Dekkers, 1988; Feinberg et al., 2015; Rochette et al., 1990; Volk et al., 2016). A diagnostic feature of the 4C polytype is a low-temperature magnetic transition, the "Besnus" transition, at ~32 K, where it loses much of its original room-temperature remanence on cooling (Besnus & Meyer, 1964; Dekkers, 1989; Volk et al., 2018). The mechanisms driving the Besnus transition remain a topic of active research (Haines et al., 2020; Koulialias et al., 2016, 2018; Volk et al., 2016, 2018; Wolfers et al., 2011). Low temperature remanence measurements are often used as a rapid, non-destructive method to detect ferrimagnetic pyrrhotite, rather than more destructive high temperature magnetic measurements. The Neél temperature at ~325°C coincides with a structural transition from 4C to 1C pyrrhotite (that is, pyrrhotite without long-range vacancy ordering) (Powell et al., 2004), thought to occur via diffusion (Herbert et al., 2015).

Antiferromagnetic pyrrhotite polytypes undergo magnetic transitions on heating at the λ-transition (sometimes referred to as the γ-transition) at ~220°C (Haraldsen, 1937). During the λ-transition, iron vacancies become disordered, thereby allowing ferrimagnetic behavior observed as an irreversible magnetic susceptibility increase upon heating (Kissin & Scott, 1982). The precise temperature of the λ-transition varies depending on the pyrrhotite polytype(s) present in a sample (e.g., Kontny et al., 2000) as well as its prior cooling history (e.g., Koulialias et al., 2021). Some researchers have identified the magnetic products of NC pyrrhotite heating as the 1C polytype, although this identification is debated (Haines et al., 2019; Koulialias et al., 2021) and some studies show that 1C pyrrhotite is paramagnetic and stable above ~350°C (e.g., Koulialias et al., 2019). Metastable ferrimagnetic pyrrhotite polytypes can be produced upon quenching from high temperatures or found on sampling heated samples from depth (e.g., (Bennett & Graham, 1981; Kontny et al., 2000; Pósfai et al., 2000; Rochette et al., 1990) although these polytypes have not been unambiguously identified and may lack long-range vacancy ordering. While Koulialias et al. (2019, 2021) find that vacancy ordering occurs upon quenching in 4C pyrrhotite, there is limited evidence that this is a consistent behavior

across all polytypes. More frequently, in rock magnetic studies the ferrimagnetic pyrrhotite produced by the λ-transition is interpreted as the 4C polytype. This interpretation is based on the conventional model where the 4C polytype is the only one capable of retaining a spontaneous magnetization. However, this interpretation is rarely confirmed by detailed powder diffraction analyses and recent work has demonstrated that other pyrrhotite polytypes and closely related iron sulfides are capable of retaining permanent magnetizations (Horng, 2018; Horng & Roberts, 2018; Li & Franzen, 1996). Horng (2018) and Horng and Roberts (2018) reported the presence of a ferrimagnetic "3C" form of pyrrhotite (also referred to as 3T pyrrhotite, Keller-Besrest et al., 1983) in marine methane seep sediments, demonstrating that the conventional assumption that monoclinic 4C is the only ferrimagnetic form of pyrrhotite in natural samples can no longer be made. Defects and lattice mismatches between pyrrhotite intergrowths on the micron to millimeter scale (Harries et al., 2011, 2011; Pósfai & Buseck, 1997) could result in locally uncompen*sat*ed magnetic moments, producing a net magnetization even in antiferromagnetic pyrrhotite polytypes. Further, the presence of other ferrimagnetic iron sulfide minerals, such as smythite (Fe_9S_{11}), can complicate the deconvolution of magnetic signals from natural samples (Hoffmann et al., 1993; Horng et al., 2020).

Notably, the λ-transition is absent in the monoclinic 4C ferrimagnetic form of pyrrhotite, which makes the λ-transition useful in detecting hexagonal polytypes in natural and synthetic samples (Dunlop & Özdemir, 2001). However, irreversible mineral transformations associated with the λ-transition and concomitant magnetic property changes can be problematic for thermal demagnetization and paleointensity experiments in paleomagnetic studies because the creation of new magnetic minerals during heating can be associated with apparent self-reversals, spurious partial thermal remanent magnetizations, and magnetic mineral assemblages that continue to alter with successive heating cycles.

Recently, there has been growing appreciation of the diversity of pyrrhotite polytypes and other iron sulfide minerals that may contribute to sample magnetizations (e.g., Horng, 2018; Horng et al., 2020; Horng & Roberts, 2018). Further, the importance of nonintegral polytypes, or polytypes of pyrrhotite which lack long-range defect ordering (e.g., Jin et al., 2021; Pósfai & Buseck, 1997) and increasing understanding of the complex relationships between polytypes (e.g., Charilaou et al., 2015; Haines et al., 2019; Harries et al., 2011, 2013; Koulialias et al., 2016, 2018, 2019, 2021) complicates this binary description of polytype behavior. Even in samples with the same chemical composition heated under the same conditions, different magnetic behavior can be observed (e.g., Dekkers, 1990). This growing recognition of the presence of many different ferrimagnetic iron sulfides in natural samples requires a more nuanced combination of magnetic and non-magnetic tools to differentiate among pyrrhotite polytypes and other ferrimagnetic iron sulfide minerals. Here we argue that collecting diffraction patterns as a function of temperature (rather than at room temperature before and after heating) across the λ-

transition and coupling them with an array of low and high temperature magnetic measurements provides a clearer understanding of the different polytypes present in a sample and their relative stability with temperature. In this study, we monitor magnetic and structural changes at elevated temperatures spanning the λ-transition and correlate them with high and low temperature magnetic properties in two different natural pyrrhotite samples: a single crystal pyrrhotite sample containing finely intergrown 4C and 5C pyrrhotite polytypes, and a natural massive sulfide dominated by 5C pyrrhotite, with lesser amounts of the 4C and 6C polytypes as well as several other metal sulfides. This study is unique due to the combination of two factors: (1) we report powder diffraction, hysteresis, and low field magnetic susceptibility data all collected as a function of temperature across the λ-transition, and (2) we examine natural pyrrhotite samples. When powder diffraction has been included in previous rock magnetic studies of pyrrhotite, usually only pre- and post-heating powder diffraction patterns are collected.

Few studies combine magnetic measurements as a function of temperature with some form of crystallographic analysis. For example, Dekkers (1988, 1990), Krs et al. (1992, 1993), Kontny et al. (2000), and Herbert et al. (2015) examined the temperature dependence of various magnetic phenomena, but collected X-ray diffraction (XRD) data only at room temperature before and after heating. Powell et al. (2004) examined crystallographic and magnetic changes in a synthetic stoichiometrically pure 4C pyrrhotite (Fe_7S_8) from 11 K to 773 K (500°C) using neutron diffraction. This study is the only one of which we are aware that uses a well-characterized natural pyrrhotite sample and tracks its crystallographic changes with temperature in tandem with changes in atomic-scale magnetic behavior. Studies on mono-phase synthetic pyrrhotite polytypes like Powell et al. (2004), and fine-scale investigation of the superstructures of nonintegral pyrrhotites by techniques like TEM are essential for understanding the mechanistic underpinnings of phase transitions in these (relatively) simple samples. However, the applicability of such studies to the behavior of natural pyrrhotites, which frequently contain intergrown integral and nonintegral polytypes, is unknown. This study is unique in that powder diffraction data are presented as a function of temperature for intergrown natural samples, rather than single phase synthetics, alongside hysteresis and susceptibility measurements collected at equivalent temperatures. We argue that understanding the complex phase transitions of the pyrrhotite system requires a two-pronged approach: careful examination and characterization of synthetic pyrrhotites, and detailed study of the rock-forming natural pyrrhotites.

II. Materials and Methods

a. Mineral Samples

In this study, we examine two natural pyrrhotite samples. One is a single crystal of pyrrhotite (MSM16667) from the Stari Trg Mine, Kosovo (Po1), provided by the Bavarian Mineralogical State Collection, Munich, Germany. The second is a massive mixed sulfide

sample from Galax, Virginia, USA, purchased from Ward Scientific, which was crushed and sieved to a grain size of between 75 and 150 μm (Po2). The composition of these samples was measured using X-ray diffraction (described below) and Po2 was additionally examined by electron microprobe analysis conducted using a JEOL JXA-8530FPLUS Electron Probe Microanalyzer at the University of Minnesota. Both energy and wavelength dispersive spectroscopy measurements were collected (EDS and WDS). WDS measurements were calibrated using well established mineral standards and analyzer crystals.

b. Annealing

The protocol of O'Reilly et al. (2000) was originally designed to increase the proportion of 4C pyrrhotite in synthetic samples and was applied here to explore whether additional monoclinic 4C pyrrhotite could be produced in an intergrown natural pyrrhotite sample in the same manner. Crushed and sieved 75-150 μm pyrrhotite grains were flushed repeatedly with N2 gas, sealed in an evacuated (10^{-2} torr) quartz glass tube and heated for 24 hours at 500 °C and then cooled at 10 °C/min to 250 °C, and were then annealed for an additional 50 hours. The first stage of the annealing treatment brings all of the pyrrhotite phases into the stability field of the 1C phase (e.g., Haines et al., 2019), thereby randomizing any pre-existing vacancy structure in the pyrrhotite. The second stage of the annealing treatment at 250°C allows the pyrrhotite to acquire a lower energy vacancy ordering configuration enriched in both 4C and 6C vacancy structures. The pyrrhotite that resulted from the annealing experiment on Po2 is referred to as Po3.

c. X-Ray Diffraction Heating Experiments

High-temperature powder X-ray diffraction measurements (HTXRD) were performed with a Bruker D8 Advance (Co-Kα, λ = 0.1789 nm) at discrete temperature steps in an N2 atmosphere. The samples were heated stepwise from room temperature (25°C) to 320°C and then cooled back to room temperature. Samples were heated to a particular temperature (e.g., 150°C), a diffraction measurement was collected while the sample was held at that temperature, and then the samples were heated or cooled to the next temperature step (e.g., 200°C). The heating/cooling rate was 12 °C/min with a 5-minute equilibration time after the set temperature was reached. After this equilibration time, HTXRD measurements were collected at each elevated temperature step. The angular step size was 0.02° 2θ with 1-second integration time. Additional X-ray diffraction patterns before and after the high-temperature XRD were collected using a PANalytical X'Pert Pro X-ray diffractometer with a Co source (λ = 0.1789 nm) and X'Celerator detector from 10° to 90° 2θ at 0.017° 2θ steps with 0.5-second integration time. Additional synchrotron XRD patterns were recorded on the 11BM beamline of the Advanced Photon Source at Argonne National Laboratories. Synchrotron patterns were recorded from 0° to 6° 2θ with a wavelength λ11BM = 0.413Å at 0.001° 2θ steps with 0.1-second integration time. Phase

identification was performed with the software package Match! (Putz et al., 2020) using reference patterns identified from the literature, and the American Mineralogist Crystal Structure Database. Reference patterns used are listed in Table 2-1. Diffraction pattern indexing and refinement (Rietveld, 1969) was used to estimate the amounts of various phases in the samples with the FullProf software package (Rodríguez-Carvajal, 1993). Iron-sulfur mass balance calculations are presented in the supplement for this chapter as Table B-1, and heating and cooling paths for these experiments are placed on the phase diagrams of Haines et al. (2019) and Harries (2012) in the supplementary information for this chapter as Figure B-1 and Figure B-2.

Table 2-1: Reference patterns used in Rietveldt refinement of samples.

Phase	**Composition**	**Source**
3C Po	$Fe_{21.05}S_{24}$	Keller-Besrest et al. (1983)
4C Po	Fe_7S_8	Powell et al. (2004)
5C Po	Fe_9S_{10}	Elliot (2010)
6C Po	$Fe_{44}Ni_{4.04}S_{48}$	de Villiers and Liles (2010)
Pyrite	FeS_2	Ramsdell (1925)
Marcasite	FeS_2	Buerger (1931)
Greigite	Fe_3S_4	Skinner et al. (1964)
Magnetite	Fe_3O_4	Bragg (1915)
Sphalerite	ZnS	Skinner (1961)
Chalcopyrite	$CuFeS_2$	Knight et al. (2011)
Galena	PbS	Ramsdell (1925)

d. Magnetic Experiments

All magnetic measurements were conducted at the Institute for Rock Magnetism at the University of Minnesota. High-temperature alternating current (AC) susceptibility was measured with a Geofyzika KLY-2 Kappabridge (300 Am^{-1} field at 920 Hz) with a CS2 furnace at 10°C/min in flowing N_2. Hysteresis loops and backfield measurements (Po1 only) were measured on a Princeton Measurements Corporation vibrating sample magnetometer (VSM) and were collected across a range of discrete temperatures during heating and cooling in a He flow furnace. The heating rate is higher here than in the HTXTD experiments because these instruments do not maintain a completely oxygen-free environment and so there is a risk of oxidation during heating. The sample was mixed with high-temperature Omega cement, which made mass normalization implausible. Thus, magnetization values are normalized to the room temperature value of *sat*uration magnetization ($M_s(T0)$). Low temperature magnetic properties were measured using a Quantum Design Magnetic Property Measurement System (MPMS). The measurements consist of (1) low temperature (10 K) cycling of a 2.5 T room temperature *sat*urating isothermal remanent magnetization (RTSIRM) in zero-field, (2) field cooling (FC) in a 2.5 T magnetic field and subsequent warming of the remanence acquired at 10 K after FC (FC-LTSIRM), and (3) zero-field warming of a 2.5 T SIRM imparted at 10 K (ZFC-LTSIRM),

after cooling in zero-field (ZFC). All MPMS measurements were conducted using a heating/cooling rate of 5 K/min in 5 K steps. Low temperature measurements were performed on samples before (Po1 and Po2) and after HTXRD analysis (Po1H and Po2H), as well as on Po3.

Table 2-2. Estimates of mineral and polytype abundance from XRD indexing using Rietveldt refinement. Percent change from the unheated (Po1, Po2) to the heated (Po1H, Po2H) and the annealed (Po3) samples are listed in italics. Full diffraction patterns for each pyrrhotite (Po1, Po1H, Po2, Po2H, Po3) are presented in the supplement for this chapter as Figure B-3, Figure B-4, Figure B-5, Figure B-6, cand Figure B-7.

	Po1	Po1H		Po2	Po2H		Po3	
	%	%	% change	%	%	% change	%	% change
3C Po		12.1		3.9	4.5	+15.4	3.3	-15.4
4C Po	52.6	59.6	+13.3	4.7	17.3	+268.1	11.4	+142.6
5C Po	46.9	5.5	-88.3	68.3	44.1	-35.4	55.0	-19.5
6C Po				5.4	5.4		10.5	+133.3
Pyrite		2.9		3.0	3.5	+16.7	3.7	+23.3
Marcasite		8.0			3.9		2.6	
Greigite		9.6			4.6		2.7	
Magnetite		2.4			2.7		1.8	
Sphalerite				9.8	10.4	+6.1	5.7	-41.8
Chalcopyrite				1.4	2.7	+92.9	2.6	+85.7
Galena				0.3	1.1	+266.7	0.6	+100.0
Total	99.5	100.1		100.0	100.0		99.9	

III. Results

a. Structural Changes on Heating

Room temperature powder X-ray diffraction patterns before and after the HTXRD experiment for both the Po1 and Po2 samples are compared in Figure 2-1(a). The starting compositions of these samples, determined by Rietveldt (1969) refinement of the X-ray diffraction patterns, are given in Table 2-2. Electron microprobe measurements reveal an average composition for Po2 of $Fe_{7.5}S_8$ (48.45±0.14 at.% Fe, 51.53±0.13 at.% S). Grains of Po2 contain rare intergrowths in backscatter imaging mode at a scale of ~1 μm. Approximately 80% of the grains are pyrrhotite, ~15% of grains are mixed, intergrown sulfides (pyrrhotite, pyrite, chalcopyrite, sphalerite, and galena), and <5% of the grains were non-sulfides.

Superstructure peaks from 17-19° 2θ for Po1 and Po2 and calculated diffraction patterns for 6C, 5C, 4C, and 3C pyrrhotite are shown in Figure 2-1(b). These large d-spacing, small angle peaks are distinctive for each pyrrhotite polytype (e.g., the doublet for 4C Po at 17.8 and 18.1° 2θ) and can be diagnostic if their intensity is sufficient. Similarly, the exact location and number of peaks at ~51° 2θ (Figure 2-1c) is also diagnostic of different pyrrhotite polytypes and is especially helpful for distinguishing the monoclinic 4C pyrrhotite, which has a characteristic doublet, from the single reflection in 5C and 6C

pyrrhotites. The ratio of total peak height to the height of the "shoulder" is often used to rapidly estimate the quantity of monoclinic and hexagonal polytypes (e.g., Graham 1962). XRD patterns for both Po1 (Po1H) and Po2 (Po2H) after the full HTXRD heating cycle are shown in Figure 2-1 (in red). Several new peaks associated with pyrite occur in the posting-heating pattern for Po1 (e.g., at 40.4 and 40.8° 2θ), and superstructure peaks in this post-heating sample have changed to resemble those of 4C pyrrhotite. Finally, evidence of marcasite and pyrite is observed at peaks near 43.5° 2θ (marked by the * in Figure 2-1a) and greigite is evident in the intensification of the peak at 35° 2θ and as small, discrete peaks in the synchrotron data at ~29°, ~42.5° and ~62° 2θ (marked by ♦ in Figure 2-1a).

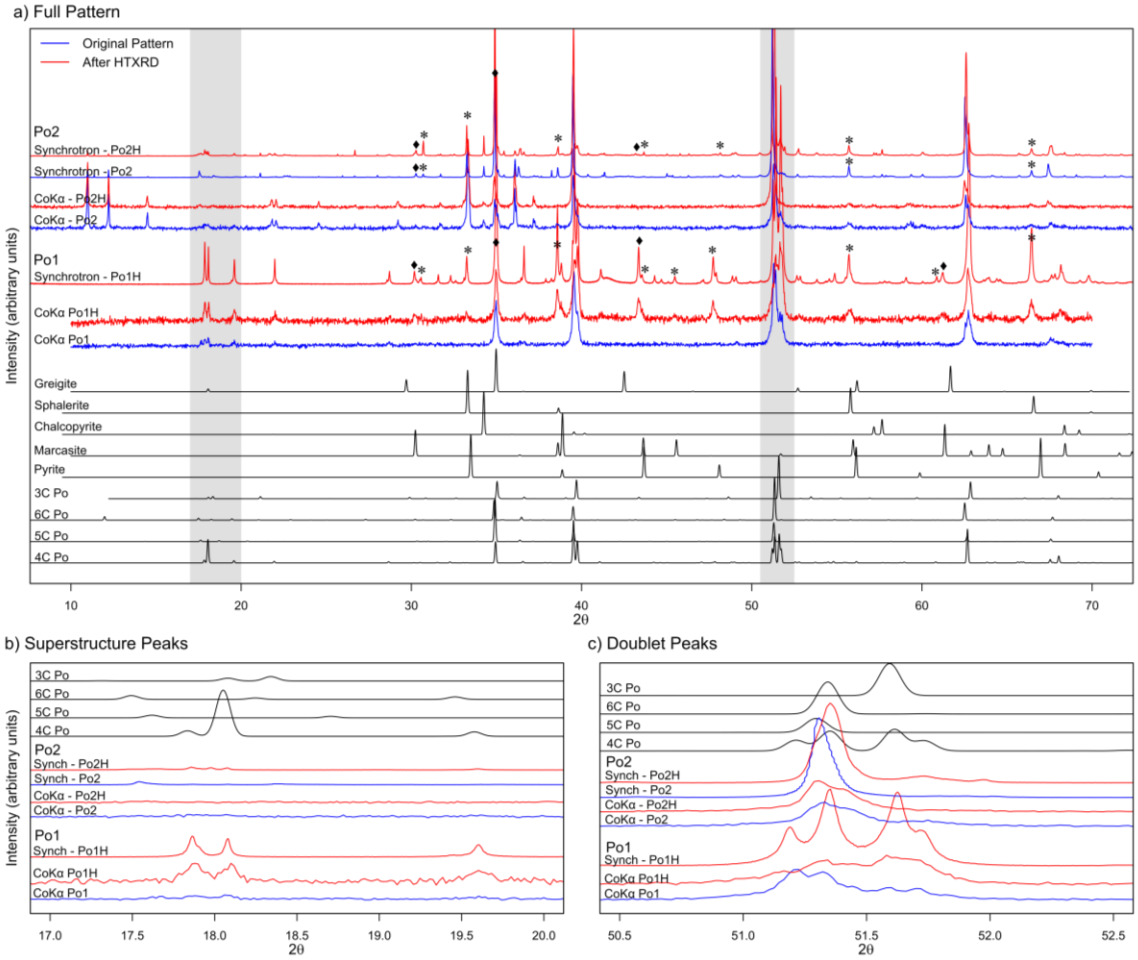

*Figure 2-1. Room-temperature X-Ray diffraction patterns for Po1 and Po2 before and after the heating experiment. (a) Full 2θ range collected for Po1 and Po2 with calculated reference patterns used for refinement. (b) Superstructural peaks that are useful to identify different pyrrhotite polytypes. (c) Doublet peaks commonly used to separate monoclinic and hexagonal pyrrhotite polytypes as in Arnold (1966). The 2θ range of data shown in (b) and (c) are highlighted by the grey bars in (a). Peak intensities for the reference and experimental patterns are normalized to the highest peak (i.e. intensity values are scaled to 1). The intensity of the Co Kα peaks was doubled and the intensity of synchrotron peaks was multiplied by 5 to show the features more accurately. Marcasite and pyrite peaks are marked by * and greigite peaks are marked by ♦ in part (a).*

Analysis of the XRD patterns collected during heating (Figure 2-2) reveals crystallographic changes in both Po1 and Po2 and growth of new polytypes and non-pyrrhotite minerals. In both Po1 and Po2 (Figure 2-2b and c), the 5C low angle superstructure peaks at 17.5° and 18.6° disappear between 200 and 220°C, whereupon the 4C reflections at higher temperatures increase in intensity. This can also be seen in the changes in the high-intensity doublet peaks at about 52° (marked by ★ in Figure 2-2a, b, c), with the increased intensity of the higher 2θ shoulder indicating an increased amount of the monoclinic polytpe (Arnold, 1966). The progressive increase in the separation of the 4C superstructure peaks near 18° 2θ with continued heating reflects the thermal expansion of the unit cell. Evidence of growth of the 4C polytype occurs at different temperatures within different 2θ intervals of the HTXRD patterns which suggests that the λ-transition may occur in progressive steps rather than as an instantaneous transformation, which is consistent with the multistep process described by Haines et al. (2019). Peaks that align with pyrite and marcasite between 40° and 50° 2θ appear at 260°C on warming in Po1, and intensify on cooling (marked by * in Figure 2 a, b, and shown as a heatmap in Figure 2-3a, b).

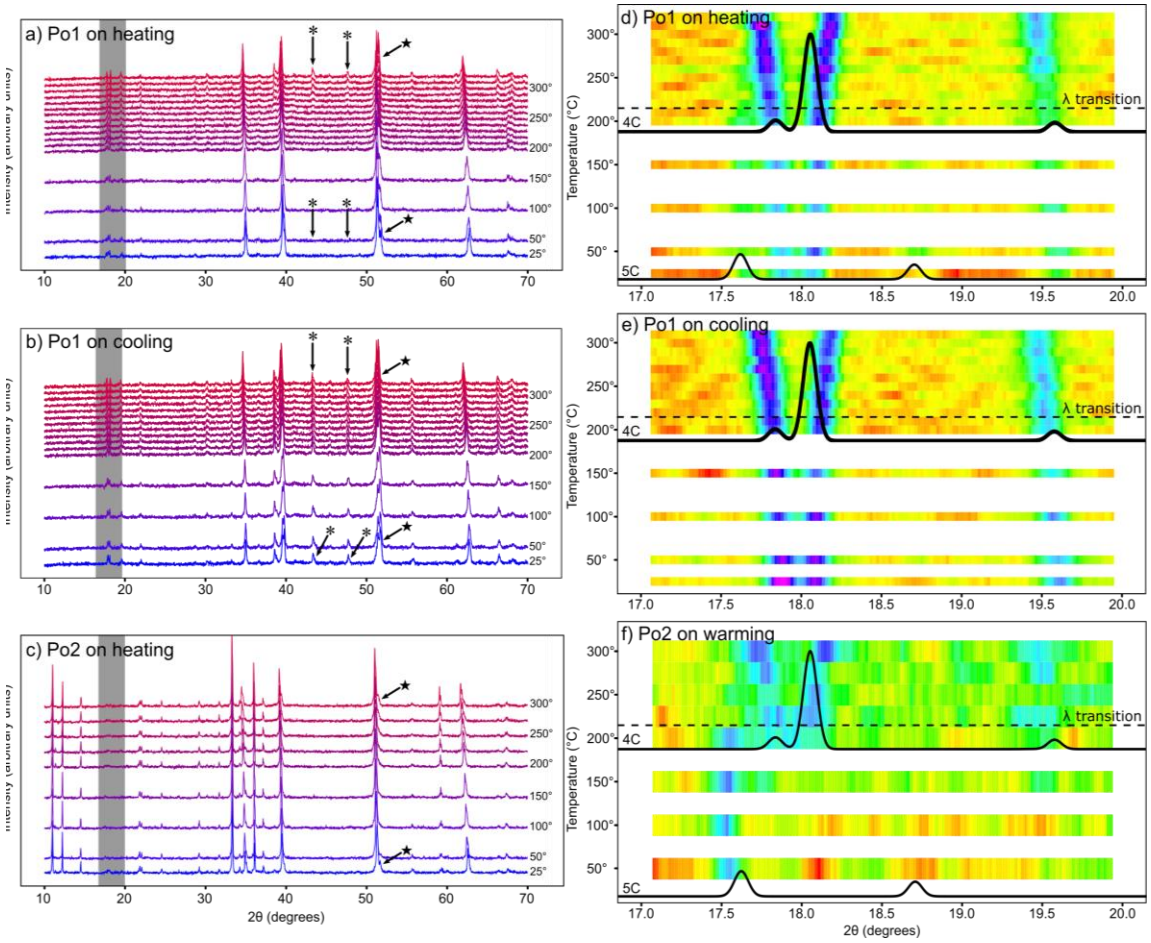

Figure 2-2. XRD with temperature data for Po1 (warming, a and d; cooling b and e) and Po2 (c and f). In a, b, and c the full diffraction patterns are shown, while in d, e, and f changes in

*superstructure peaks are highlighted. The location of d, e, and f is shown in gray in a, b, and c. Higher intensity peaks are indicated by blue-green colors on the heatmap, while low intensity sections of the diffraction pattern are indicated by red-yellow colors. The temperature of the λ-transition (215°C, Schwarz, 1968, 1975) is highlighted in d, e, and f by a black, dashed line. Calculated diffraction patterns for 4C and 5C Po are shown for reference on the superstructural heatmaps. The growth of pyrite in Po1 on heating and cooling is indicated by *, and the changing height of the shoulder on the diagnostic monoclinic/hexagonal peaks at the ~52° 2θ interval is indicated on Po1 and Po2 by ★.*

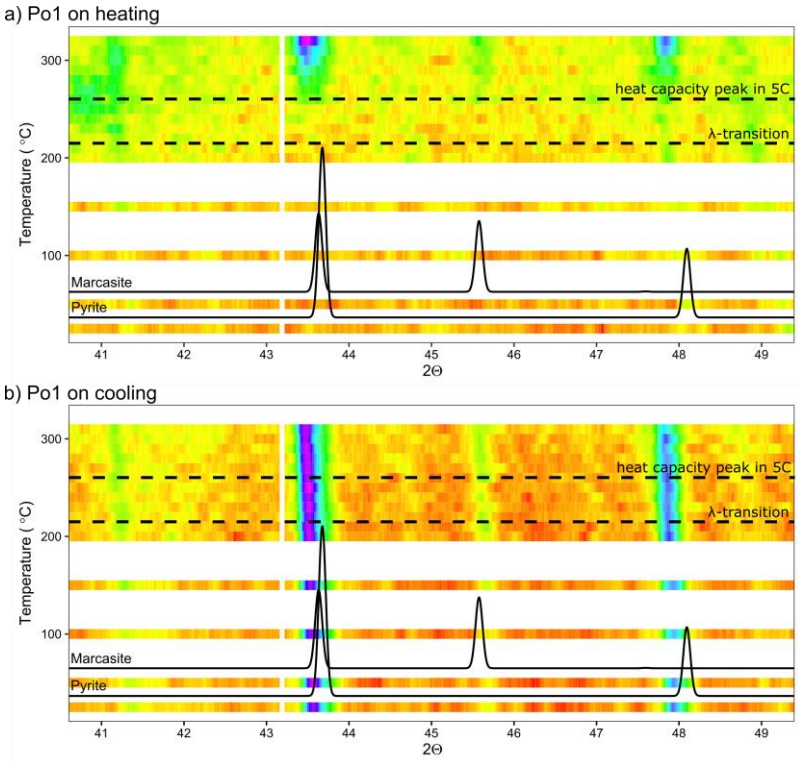

Figure 2-3. Heatmaps of XRD data between 40° and 50° 2θ for Po1 on heating (a) and cooling (b) show pyrite and marcasite growth during the experiment. Pyrite and marcasite first appear at 260°C on heating and the peaks intensify as the sample is cooled back to room temperature. Higher intensity peaks are indicated by blue-green colors on the heatmap, while low intensity sections of the diffraction pattern are indicated by red-yellow colors. The temperature of the λ-transition (215°C, Schwarz, 1968, 1975) and the heat capacity peak for 5C pyrrhotite (261°C, Grønvold et al., 1991) are marked by dotted lines.

The changing composition of Po1 with temperature is illustrated in Figure 2-4(a) and (b). The nearly even initial mix of the 4C and 5C polytypes slowly changes on heating to 200°C, with a decrease in the amount of 4C and 5C polytypes and a compens*at*ing increase in the amount of the 3C polytype, which makes up >20% of the sample by 150°C, despite not being present in the starting sample. Between 200° and 240°C, 4C, 5C, and 3C pyrrhotite each make up approximately 30% of the sample, with a small increase in the observed amount of pyrite, marcasite, greigite, and magnetite. These phase identifications are complicated by the likely presence of non-integral pyrrhotite polytypes, which would

have primary structural peaks (e.g., those at ~51˚ 2θ), but would not have strong or consistent superstructure peaks at low angles, reflecting their short- or long-range disorder when compared to the integral pyrrhotite polytypes. By 250°C, the amount of 4C pyrrhotite appears to rapidly increase at the expense of the 5C polytype, while 3C pyrrhotite remains steady (at the resolution of this method) at about 25% of the total pyrrhotite assemblage. Above 300°C, it becomes increasingly challenging to index the various polytypes, and we avoid over-interpreting the apparent dramatic fluctuations in the amounts of 3C, 4C, and 5C. Throughout heating there is a decrease in the total amount of pyrrhotite from 100% to about 80% pyrrhotite, consistent with the growth of the iron sulfides pyrite, marcasite, and greigite, and the iron oxide magnetite. On cooling (Figure 2-4b), the amount of 3C and 5C pyrrhotite decreases monotonically. After cooling to 25°C, the amount of 5C pyrrhotite has decreased to 5.5% and the amount of 3C pyrrhotite has decreased from its peak of 35.1% at 300°C on warming to 12.1%. 4C pyrrhotite increases over this interval to 59.6% of the total phases identified at 25°C. About a quarter of the sample at the end of the experiment is made up of non-pyrrhotite minerals such as marcasite (8.0%), pyrite (2.9%), greigite (9.6%), and magnetite (2.4%).

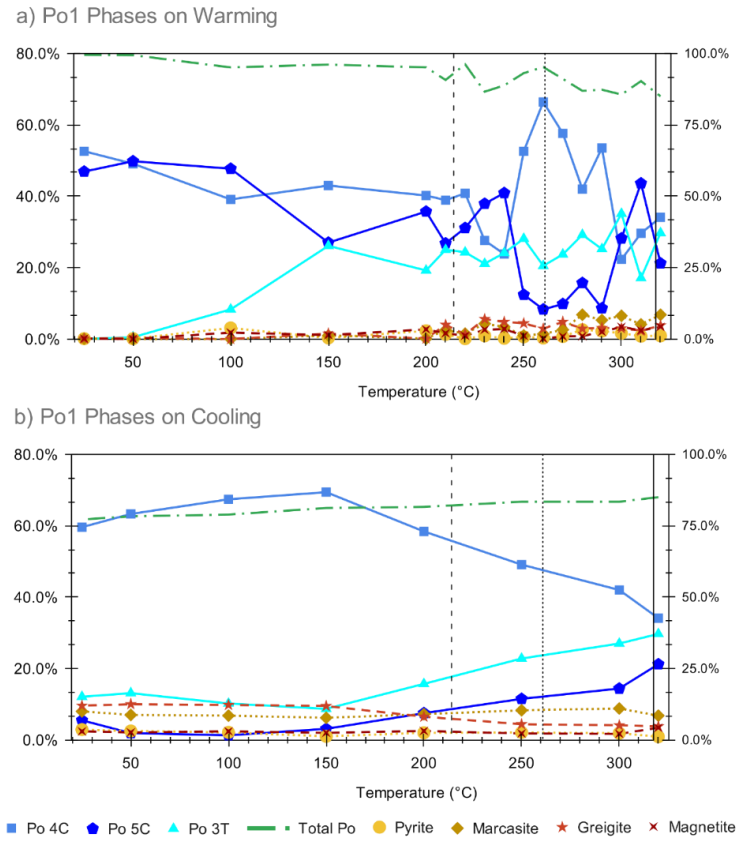

Figure 2-4. Pyrrhotite polytype vs. temperature for Po1 on (a) heating from 25°C to 320°C in a N2 atmosphere, and subsequent cooling (b), showing the transition from a nearly even mixture of 4C and 5C pyrrhotite to a mixture of 4C, 5C, 3C, and pyrite, marcasite, greigite, and magnetite. Total pyrrhotite (green dash-dot line) is plotted on the right-hand axis. The

approximate temperature of the λ-transition (215°C) reported by Dunlop and Özdemir (1997) is marked by the dashed line, the second heat capacity peak in 5C Po (261°C) reported by Grønvold et al. (1991) is marked by the dotted line, and the Néel temperature of 4C pyrrhotite (318°C) reported by Dekkers (1989) and Haraldsen (1937) is marked by the solid line in each plot. Phase quantification and fit quality information for these data are presented in the supplement for this chapter as Table B-2 and Table B-3.

The massive sulfide sample Po2 represents a more complex mineral system, which impacts our ability to utilize Rietveldt (1969) refinement to deconvolve accurate estimates of mineral abundance during heating in this sample. However, changes in the occurrence and position of superstructure peaks in the diffraction data for Po2 (e.g. Figure 2-2c, f) provide strong non-quantitative evidence for pyrrhotite polytype transformations. Despite this increased complexity, similar mineral transformations to those suggested by diffraction pattern indexing in Figure 2-3 for Po1 are observed in the diffraction patterns for Po2 on heating (Figure 2-2). At 200°C the 5C low-angle superstructure peaks at ≈ 17.6° 2θ (Figure 2-2d) begin to transform into the doublets at ≈ 17.9 and 18.1° 2θ that are consistent with the 4C polytype. By 250°C there is a shift in the more intense diagnostic peaks for 4C pyrrhotite at ~51° 2θ. The most intense peak in hexagonal 5C pyrrhotite is at 51.2° 2θ, which is present (although broadened by other pyrrhotite polytypes) in the initial 25°C ((Figure 2-2c), blue, bottom) X-ray pattern. At 300°C ((Figure 2-2c), red, top), this peak has broadened, with a shoulder to higher 2θ indicating the increased presence of what would be interpreted at room-temperature as additional 4C pyrrhotite, which has its most intense peaks as a doublet at 51.41° and 51.67° 2θ (indicated by ★ in Figure 2-2c). These superstructural differences in both the primary and lower-intensity superstructure peaks are maintained during quench cooling of these samples and are shown in the high-resolution synchrotron diffraction data in Figure 2-1. The composition of Po2H after cooling to room temperature is shown in Table 2-1. While the amounts of sphalerite, pyrite, chalcopyrite, and galena determined after the HTXRD experiments remain relatively unchanged (within the margin of error of the analyses) and some marcasite and greigite have grown, the most striking changes occur in the pyrrhotite polytypes. The amount of 5C pyrrhotite decreased, while 4C pyrrhotite increased dramatically from 4.7% in Po2 to 17.3% in Po2H. This matches the visual examination of superstructure peaks in Figure 2-2(f), where at 215°C there is a sharp transition from the "5C-like" superstructure to a more "4C-like" superstructure.

b. Magnetic Changes on Heating

Low field thermomagnetic curves (Figure 2-5a) of Po1 on heating have a constant susceptibility (χ) of ≈ 18μm3/kg to 210°C and at 214°C increases to reach a maximum of 42 μm^3/kg at 244°C. This increase is consistent with the literature temperature for the λ-transition of pyrrhotite (Kissin & Scott, 1982; Li & Franzen, 1996; Townsend et al., 1979) and the changes to a more "4C-like" structure seen in the HTXRD (see e.g., Marusak &

Mulay, 1980). Determining the λ-transition temperature from the maximum of the second derivative yields T_λ = 226°C. The peak is followed by a χ decrease to 290°C and a further decline at the Néel temperature (T_N) of the 4C polytype at 322°C, consistent with the literature value (318°C, Dunlop & Özdemir, 2001). At higher temperatures, χ decreases to a plateau near zero. While the HTXRD experiments indicate the formation of greigite and possibly magnetite during those experiments, no other magnetic phases are detectable in the thermomagnetic curve. This is unsurprising given the Curie temperatures for both phases are near or greater than the peak temperatures reached during the thermomagnetic experiments (380-400°C), where Tc is ~580°C for magnetite and >350°C for griegite (L. Chang et al., 2008; Vandenberghe et al., 1992). Bulk susceptibility increases on cooling at 317°C and sharply increases at 283°C reaching a maximum value of 91.4 μm^3/kg near 240°C. The first magnetization increase can be attributed to the 4C pyrrhotite remaining in the sample, while the latter possibly represents the Néel temperature of a newly formed ferrimagnetic phase (potentially greigite). After the full heating-cooling cycle, the room temperature susceptibility increases by a factor of 3.5 to 64 μm^3/kg.

The bulk susceptibility of Po2 on heating undergoes similar transitions to those described in Po1. χ is initially lower because of the reduced amount of 4C Po and remains nearly constant at ≈0.9 μm^3/kg until 215°C, peaking at 250°C, where there is a factor of 4.6 increase to a maximum of 4.2 μm3/kg that is consistent with crystallographic changes from primarily 5C to a "4C-like" pyrrhotite in the XRD data. The calculated λ-transition temperature for Po2 is 235°C, slightly higher than Po1. χ continues to decrease on warming, with a shoulder between 280 and 300°C suggesting the growth of a new magnetic phase. χ decreases to near 0 μm3/kg at 325°C, again consistent with the literature value for the Néel temperature of 4C Po and remains low but increases slightly on heating to 400°C, indicating the growth of a new ferrimagnetic phase. On cooling, χ of Po2 remains low, with a subtle decrease and inflection point at the Neél temperature of 4C Po, before a rapid increase in χ at 270°C that reaches a peak of about 17.6 μm^3/kg at 230°C and then progressively decreases on continued cooling to room temperature. Po2 undergoes an order of magnitude increase in the final room-temperature χ (a factor of 13.4), indicating growth of a new magnetic phase. Such growth could arise from two mechanisms: pyrrhotite superstructures altering to different, more ferrimagnetic polytypes, or ferrimagnetic iron oxides or sulfides (greigite) produced by oxidation (despite thermal cycling in an Ar atmosphere).

Hysteresis loop and backfield measurements were performed at a range of discrete temperatures during heating and cooling in a He-flow furnace. Changes in hysteresis properties with temperature are shown in Figure 5. Initially, Po1 has a M_s = 7.9x10^{-5} Am^2/kg, a remanence ratio of M_r/M_s = 0.3, a coercivity of B_c = 27 mT, and a coercivity of remanence B_{cr} = 38 mT. After the complete heating cycle, M_r and M_s increased by a factor of 1.5 and 1.7, respectively, with M_s reaching 11.4 x 10^{-5} Am^2/kg. The hysteresis loop narrows after heating and has lower B_c (20 mT) and B_{cr} values (26 mT). M_s(T) decreases

up to 210°C on heating. At this temperature, M_s (Figure 2-5b) increases as the antiferromagnetic to ferrimagnetic transformation of the λ transition occurs. At 225°C M_s reaches a maximum and then decreases monotonically to the Néel temperature of the 4C phase at ≈ 315°C. Similar behavior can be seen in $M_{rs}/M_s(T_0)$ (Figure 2-5b), with a generally decreasing trend and a less pronounced peak at T_λ = 225°C. Coercivity (Figure 2-5c) and B_{cr} (Figure 2-5d) also decrease with increasing temperature. Determination of B_c and B_{cr} was not possible for T > 315°C, which is close to the Néel temperature of the 4C polytype. On cooling, both M_s and remanence increase, with typical $M_s(T)$ behavior (Dunlop & Özdemir, 2001). Similarly, the coercivities increase on cooling but show a discontinuity between 290°C and 280°C.

The magnetization of Po2 increases from 0.52Am^2kg^{-1} to 2.9 Am^2kg^{-1} after heating. The remanence ratio of Po2 decreases on heating, with M_r/M_s dropping from 0.32 at room temperature to a local minimum of 0.23 at 175°C until immediately before the λ-transition, where M_r/M_s increases to 0.30 at 225°C. M_r/M_s again drops at the Néel temperature, reaching a minimum of 0.03 at 325°C. Coercivity decreases dramatically on heating, with a room-temperature value of 42.8 mT decreasing to a minimum of ~5mT at 300°C. These behaviors are consistent with the antiferromagnetic to ferrimagnetic transition of hexagonal pyrrhotite polytypes at the λ-transition. With continued heating to 500°C and subsequent cooling to 350°C, $M_s/M_s(T_0)$ and M_r/M_s ratios show an approximate sixfold increase.

The low temperature magnetic properties for all samples are summarized in Table 3 and are shown in Figure 2-6. The magnitude of the Besnus transition, ΔM_B, is the change in magnetization between 40 K and 10 K. M_s values were determined from the cooling portion of RTSIRM experiments and the change in magnitude over the same interval for the FC and ZFC experiments. The shape of the RTSIRM curves for both Po1 and heated Po1H are nearly identical (Figure 2-6). On cooling, both curves undergo a slight increase in magnetization to 250-200 K, after which the magnetization declines. At ≈ 30 K, the magnetization drops across the Besnus transition (Besnus & Meyer, 1964). While the shape of the Po1H RTSIRM is nearly identical to that of Po1, its magnetization is offset to higher values by a factor of 1.4. The room temperature M_s for Po1 rose after heating from 10.8 Am^2kg^{-1} to 15.3 Am^2kg^{-1}, which indicates the growth of new magnetic minerals, although both values are lower than the Ms of a pure 4C crystal (21 Am^2kg^{-1}) (Néel, 1953; Volk et al., 2016). This relationship also holds for the FC and ZFC experiments, where Po1H retains more remanence at 10 K than the unheated Po1 sample. Both sets of FC and ZFC curves lose remanence during warming through the Besnus transition and then continue to linearly decrease on continued warming to 300 K.

The low temperature magnetic behavior of the more complex mineral assemblage in Po2 is broadly similar to that of Po1. The room-temperature M_s for Po2 is 0.6 Am^2kg^{-1}. Assuming that the 4C polytype is the only mineral capable of retaining a remanence, we can use its *sat*uration magnetization of 21 Am^2kg^{-1} (Néel, 1953; Volk et al., 2018) to

estimate a concentration of ~3%, which is consistent with the estimate from XRD analysis. RTSIRM data for Po2 display a clear Besnus transition at 32 K, indicating the presence of 4C pyrrhotite (Figure 2-6). Both the total magnetization and the magnitude of the Besnus transition is much lower than for Po1, which corroborates the smaller concentration of 4C pyrrhotite found in Po2. After heating, overall magnetization (an increase of 0.5 Am^2kg^{-1} at 10K) and the magnitude of the Besnus transition both increase (e.g., ΔM_B increased from 0.037 Am^2kg^{-1} in Po2 to 0.082 Am^2kg^{-1} in Po2H during RTSIRM warming). Surface oxidation of the sample to hematite between the XRD experiment and the low-temperature magnetic analyses is reflected in the decrease in magnetization of Po2H between 300 and ~270 K. Similar behavior is seen in the field-cooled curves for Po2 and Po2H, with an increase in overall magnetization after the heating experiment as well as the Besnus transition magnitude.

Table 2-3. Low temperature magnetic properties of samples Po1 and Po2 before and after the HTXRD experiments (Po1H and Po2H) and the annealing experiment conducted on Po2 (Po3). M(300 K) is the magnetization at 300K. M(10 K) represents the magnetization at. ΔMB represents the magnitude of the Besnus transition (difference between the magnetization at 10 K and at 40 K).

	Sample	FC-LTSIRM (Am^2kg^{-1})	ZFC-LTSIRM (Am^2kg^{-1})	RTSIRM (cooling) (Am^2kg^{-1})	RTSIRM (warming) (Am^2kg^{-1})
M (300 K)	Po1	2.18	2.13	3.54	2.86
	Po1H	4.57	4.41	5.06	3.51
	Po2	0.19	--	0.23	0.17
	Po2H	0.63	0.62	1.22	0.60
	Po3	0.16	--	0.19	0.15
M (10 K)	Po1	6.76	6.85	2.49	2.49
	Po1H	9.78	8.62	3.15	3.15
	Po2	0.49	--	0.16	0.16
	Po2H	2.59	2.35	0.61	0.61
	Po3	0.35	--	0.16	0.16
ΔM_B	Po1	3.49	3.64	0.51	0.92
	Po1H	4.57	4.41	0.55	0.85
	Po2	0.14	--	0.05	0.04
	Po2H	0.98	0.96	0.06	0.08
	Po3	Not present	--	Not present	Not present

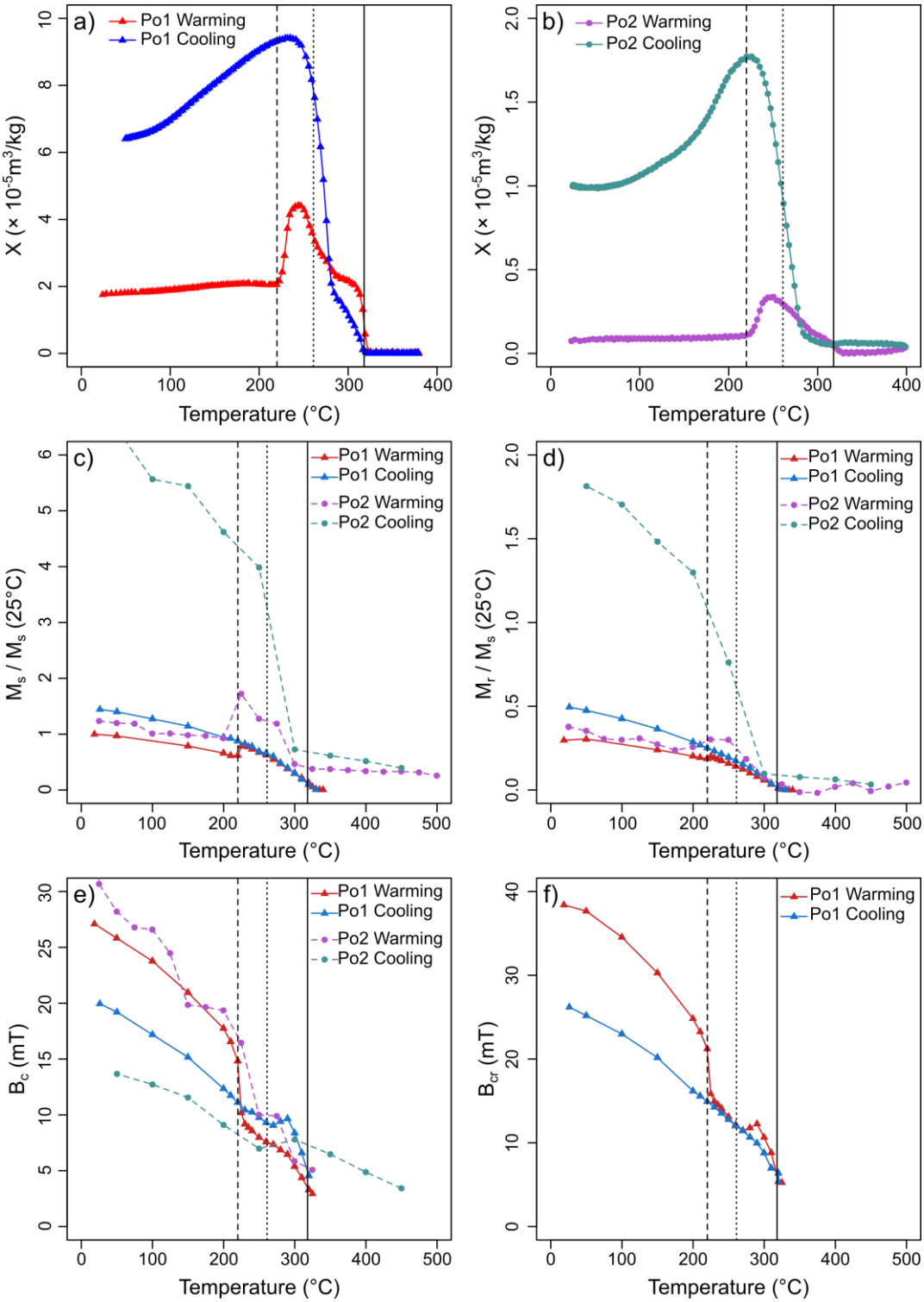

Figure 2-5: Bulk rock magnetic properties for Po1 (triangles, solid lines) and Po2 (circles, dotted lines). (a) and (b) Bulk magnetic susceptibility with temperature data for Po1 and Po2. Hysteresis parameters are shown as a function of temperature in (c) $M_s/M_s(T_0)$, (d) M_r/M_s, (e) B_c, and (f) B_{CR} (Po1 only). The approximate temperature of the λ-transition (215°C) reported by Schwarz, (1968, 1975) is marked by the dashed line, the second heat capacity peak for 5C Po (261°C) reported by

Grønvold et al. (1991) is marked by the dotted line, and the Néel temperature of 4C pyrrhotite (318°C) reported by Dekkers (1989) and Haraldsen (1937)is marked by the solid line in each plot.

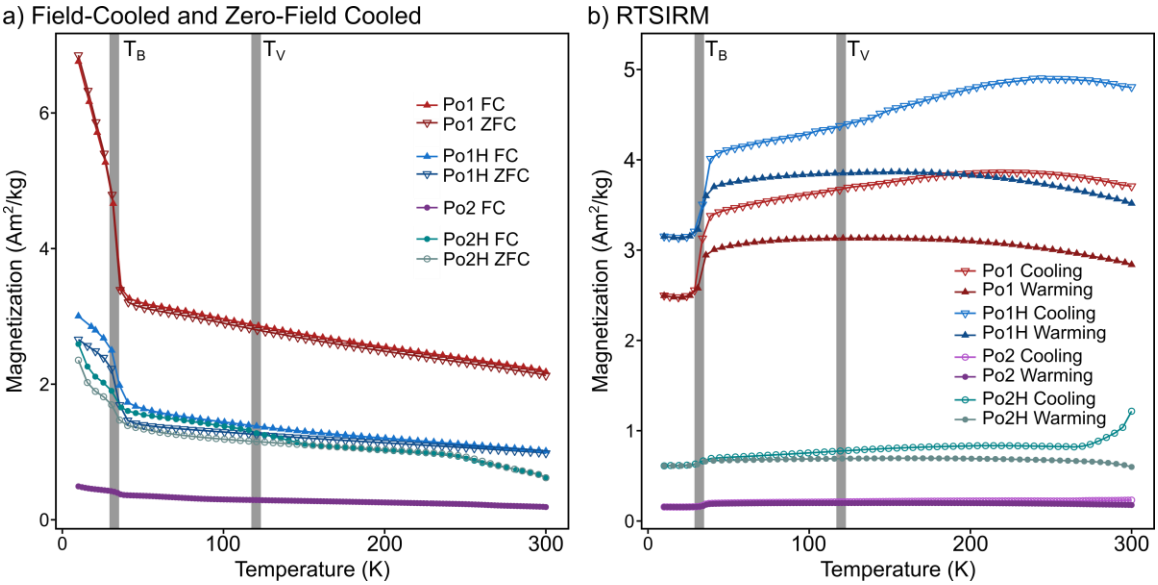

Figure 2-6: Field-cooled (FC) and zero-field-cooled (ZFC) low-temperature saturation isothermal remanent magnetization (LTSIRM) and room-temperature saturation isothermal remanent magnetization (RTSIRM) experiments for Po1 and Po2 before and after the HTXRD experiments. The temperatures of the Besnus transition (TB = 32 K) and Verwey transition (TV = 120 K) are marked by the gray bars.

c. Pyrrhotite Annealing

The heating experiments on Po1 and Po2 were conducted on an hours-long time scale. An outstanding question regarding pyrrhotite phase transitions is the effect of thermal history on the lambda transition temperature and magnitude. Protocols used to produce synthetic pyrrhotite for structural and magnetic studies frequently involve extended (hours to days) heating and annealing steps to increase the extent of vacancy ordering (e.g., Horiuchi & Wada, 1971; Lambert et al., 1980; O'Reilly et al., 2000; Rao & Rao, 1968; Rhodes et al., 2017; Vanitha & Brien, 2008). To investigate whether these protocols are useful for characterizating natural samples, the Po2 sample was annealed using a protocol to optimize monoclinic 4C pyrrhotite synthesis (O'Reilly et al., 2000). First stage annealing involves holding the sample at 500°C for 24 hours and bringing all pyrrhotite phases into the 1C region of the phase diagram (Herbert et al., 2015), thereby randomizing any pre-existing vacancy ordering in the pyrrhotite. Second stage annealing held the sample at 250°C for 50 hours and allowed the pyrrhotite to acquire a lower energy vacancy ordering configuration within the "NC" field of the phase diagram. Mineralogical and magnetic properties following annealing were measured using the same methods as for the starting material. Crystallographic and magnetic changes in pyrrhotite superstructure

were measured after the annealing experiment on Po2 and are reported in Figure 2-7 and Table 2-3.

Based on the differences between Po2 (original massive sulfide) and Po3 (annealed), the major crystallographic changes on annealing were the conversion of 5C Po to 4C and 6C Po, and nucleation and growth of greigite, marcasite, chalcopyrite, and magnetite. While the total amount of pyrrhotite stays largely the same over this annealing period (85.5% Po in Po2, 80.2% Po in Po3), the proportion of each polytype has shifted. Additionally, while the primary structural peaks of pyrrhotite are present, the location and intensity of the low-angle superstructural peaks (Figure 2-7b) and the most intense pyrrhotite peak(s) at ~51° 2θ (Figure 2-7c), which allow different superstructures to be resolved, do not correlate well with published 3C, 4C, 5C, or 6C diffraction patterns. This suggests that a range of irregular NC pyrrhotite forms were produced because of the annealing protocol, and calls into question the precision of compositional estimates derived from Rietveld (1967) analysis. Electron microprobe measurements indicate a <1% change in the average iron and sulfur atomic percentages before and after annealing. The average Fe composition of pyrrhotite grains changed from 48.45±0.14 at% Fe to 48.03±0.36 at% Fe while S changed from 51.53±0.13 at% S to 51.88±0.12 at% S after annealing. Thus, the loss of indexable pyrrhotite superstructures after annealing is not likely to be attributed to bulk compositional change (e.g. sulfur loss during heating), and instead is more likely to be linked to enhanced vacancy disorder created during the annealing process.

Magnetic measurements for the annealed sample are substantially different than those of the unheated sample. After annealing, the Mr/Ms ratio increased to 0.36 and the coercivity decreased slightly from Po2 to 41 mT. Magnetization at the beginning of the RTSIRM experiment decreases by 18% (Figure 2-7d) from Po2 (teal circles) to Po3 (dark blue squares), which indicates that the magnetic mineral assemblage was altered during annealing and is not as capable of retaining remanence. The Besnus transition is absent from the Po3 RTSIRM experiment, which indicates that no 4C Po is present in the annealed sample. Even though there is an apparent increase in the amount of the 4C polytype identified by diffraction pattern indexing of the annealed sample, the lack of a Besnus transition rules out its presence. Instead, we argue that annealing led to a decreased vacancy ordering in the pyrrhotite (relative to the unheated natural sample) and that diffraction pattern indexing is unable to robustly identify the disordered “4C-like” polytypes or other non-integral pyrrhotite polytypes in the annealed sample.

The low temperature magnetic behavior of Po3 provides clues about the magnetic mineralogy after annealing. Upon cooling of the RTSIRM, the sample experiences a slight loss of remanence across the Verwey transition, which indicates the presence of magnetite. Upon continued cooling. the sample retains a slightly greater magnetization at 10K than in the unannealed sample (see Table 2-3, Po3 is greater by 0.002 Am^2kg^{-1}). On warming, the RTSIRM remains lower than the cooling path and is broadly similar to the RTSIRM data for greigite reported by Roberts et al. (2011, see their Fig. 13). Thus, we interpret the

RTSIRM behavior of Po3 as due to the superposition of greigite and magnetite. While remanence behavior is greatly affected by magnetic particle size, Roberts et al. (2011) find this type of "triangular" remanence behavior in all grain sizes of greigite measured, with larger (multi-domain) grains losing proportionally more remanence than smaller (single-domain) ones. From the XRD data for Po3, pyrrhotite dominates this sample, and while we cannot rule out contributions from non-4C pyrrhotite polytypes to the RTSIRM of Po3, the low temperature magnetic data contains no definitive evidence of 4C pyrrhotite.

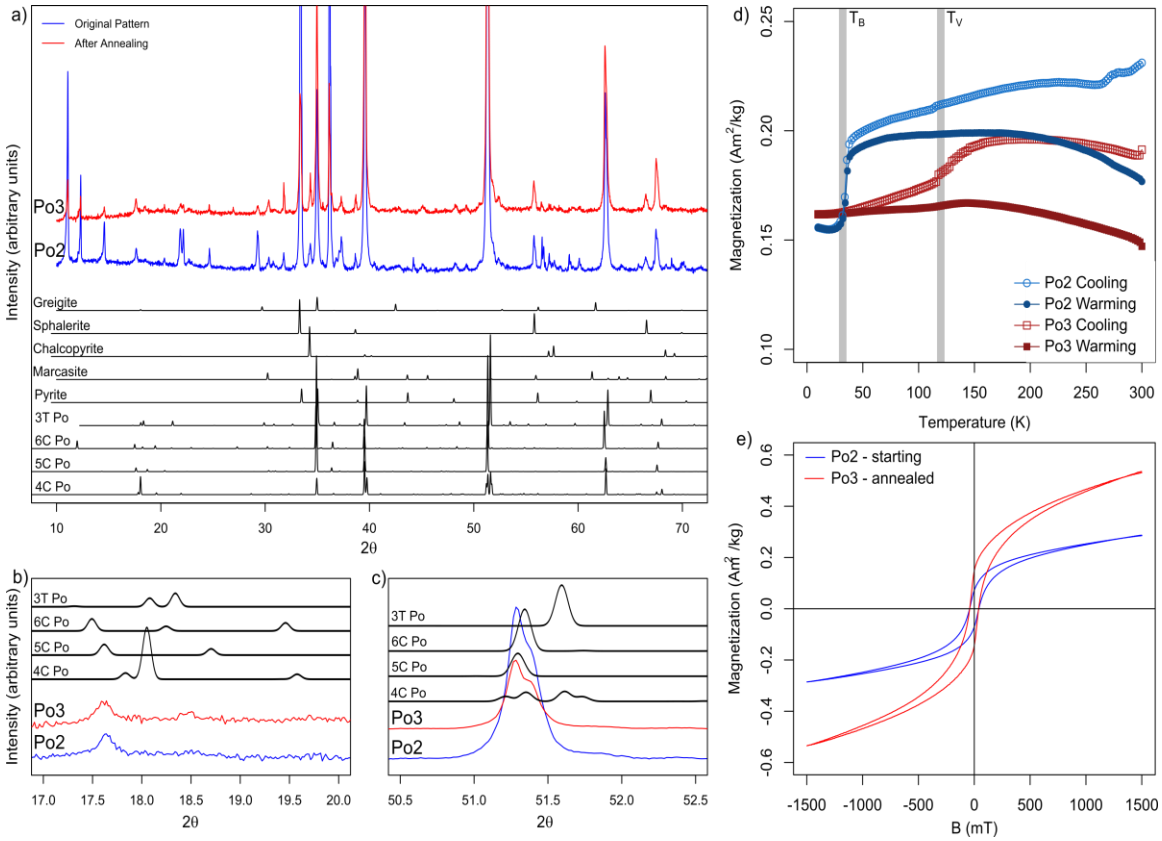

Figure 2-7. Summary of results of annealing experiments for Po3. (a) XRD patterns for the starting material (blue) and annealed material (red) calculated using Co Kα radiation. Diffractograms are shifted along the y-axis to facilitate comparison. Peak patterns are shown for 4C, 5C, and 6C pyrrhotite (Po), along with greigite, sphalerite, chalcopyrite, marcasite, and pyrite below for reference. (a) Whole pattern from 10° to 90° 2θ, and (b) and (c) important regions that help to determine the proportions of different pyrrhotite superstructures. (d) Low-temperature magnetic experiments (RTSIRM) for Po2 and Po3. The Besnus transition (4C Po, 32 K) and the Verwey transition (magnetite, 120 K) are indicated by the solid grey lines. (e) Hysteresis loops for the starting material, Po2, and the annealed material, Po3.

IV. Discussion

The combination of powder XRD data and magnetic measurements collected as functions of temperature provide a clearer perspective on how intergrown pyrrhotite polytypes transform across the λ-transition; more than would otherwise be gained using

only magnetic susceptibility or simple pre- and post-heating XRD patterns. This approach allows the λ-transition to be observed as an irreversible stepwise process, as suggested by Haines et al. (2019), rather than an instantaneous transformation of superstructures. This progressive step-wise change is captured here by changing magnetic behavior and vacancy superstructure peaks in XRD patterns. The λ-transition in both samples is both associated with the transformation of 5C to 4C pyrrhotite and the formation of non-pyrrhotite minerals. The approach used here enables identification of the onset of pyrite and greigite production during heating and cooling, as well as other non-sulfide mineralogical changes.

a. Po1 – transformation of 5C Po to 4C, 3C Po, pyrite, and greigite on heating

Po1, which starts out as a single intergrown crystal of equal amounts of 4C and 5C, alters on heating such that the 5C polytype transforms into 3C, pyrite, marcasite, and greigite. These alteration products formed over different temperature intervals and the process is non-reversible. Magnetically, various changes are observed during heating of Po1. B_C and B_{CR} decrease after heating, while χ, M_S, and the remanence ratio all increase (Figure 5). Post-heating RTSIRM remanence is greater than in the original sample, although the magnitude of the Besnus transition (an indicator only of 4C pyrrhotite) remains relatively unchanged (Table 2-1). Bulk coercivity does not recover to pre-heating levels, which indicates that the newly formed magnetic carrier has lower coercivity than the starting assemblage, and is not likely to be hematite or goethite. A change in magnetic grain size (e.g., from single-domain to multidomain 4C pyrrhotite) could also contribute to these changes in magnetic properties, although this would not explain the increased remanence seen in the RTSIRM measurements of Po1H. Instead, the increase in magnetization and decrease in coercivity may be variably explained by (1) greigite formation, and /or (2) formation of 3C or a non-integral ferrimagnetic pyrrhotite polytype. In addition to finding little magnetite in the diffraction indexing, magnetite is unlikely to have formed given the heating in nitrogen and the lack of clear expression of the Verwey transition (though we acknowledge a subtle inflection in the cooling of the Po1H RTSIRM near 120 K). Instead, greigite formation is consistent with much of the collected magnetic data. Powder diffraction data indicate greigite formation beginning at 200°C. Greigite has a higher *sat*uration magnetization and lower coercivity than 4C pyrrhotite, and no low temperature phase transition (Li et al., 2014; Roberts et al., 2011). Despite evidence that gregite is not thermally stable at these high temperatures (e.g., Krs et al. (1992) find greigite reflections start to decrease in intensity between 250°C and 300°C, and disappear completely before 350°C), under the conditions used in this study, we find greigite reflections appear in Po1 starting at 210°C and persist through heating to 320°C and on cooling. Here, the combination of increasing *sat*uration magnetization and decreasing coercivity in Po1 on heating, combined with the identification of gregite in the XRD patterns, provides multiple lines of support towards greigite formation during heating in this sample. Although the formation of the 3C polytype was identified in the powder

diffraction data, recent studies of this polytype indicate that its coercivity is relatively high, 100-130 mT at room temperature, and that its *sat*uration magnetization is lower than that of 4C pyrrhotite (Horng & Roberts, 2018). Thus, while its presence would contribute to a higher MS, it is not clear that formation of the 3C polytype would explain the coercivity decrease.

Heat capacity measurements on synthetic 5C pyrrhotite have three peaks on heating (Grønvold et al., 1991) with the λ-transition being the smallest. Grønvold et al. (1991) interpreted the two larger peaks (261°C, 318°C) as episodes of vacancy randomization that create additional disorder. Each peak corresponds in temperature to changes in both structure and in χ, M_S, and coercivity in Po1 as it is heated (Figure 2-3Figure 2-4Figure 2-5). Untangling the combined effects of these structural, magnetic, and thermodynamic transitions requires additional study; here we note only the link between changes in integral superstructures and magnetic properties.

Based on the proportions of each magnetic mineral determined using XRD and their respective magnetizations, we calculate a theoretical Ms for Po1H and compare it to the (assumed) pure 4C pyrrhotite Ms of Po1. 4C pyrrhotite has a *sat*uration magnetization of 21 Am^2kg^{-1} (Néel, 1953; Volk et al., 2018), 3C pyrrhotite has a *sat*uration magnetization of $\leq$10 Am^2kg^{-1} (Horng & Roberts, 2018), greigite has a *sat*uration magnetization of 67 Am^2kg^{-1} (Li et al., 2014), and magnetite has a *sat*uration magnetization of 92 Am^2kg^{-1} (A. R. Muxworthy & McClelland, 2000). Linearly combining these *sat*uration magnetizations with respect to the phase quantification generated from the XRD patterns gives a predicted Ms of 26.78 Am^2kg^{-1}; this is larger than the measured Ms of Po1H (15.25 Am^2kg^{-1}). However, the 41.9% increase in magnetization in Po1H compared to Po1 (10.75 Am^2kg^{-1}) is similar to the 27.5% MS increase predicted by the XRD phase identification data. The amount of 4C pyrrhotite decreased slightly on heating, but the magnitude of the Besnus transition stayed largely the same, which suggests that additional 4C pyrrhotite is not responsible for the magnetization increase. Further, more 4C pyrrhotite after heating would need to have a larger grainsize than in the unheated Po1 sample to contribute to a lower coercivity. Given these data, it is likely that much of the remanence change in Po1H is due to greigite formation, whose higher magnetization and lower coercivity would account for these changes. This assumes only a minor contribution from the 3C polytype, which would also result in an increased coercivity. An additional source for this "excess" magnetization could be stacking faults and lattice mismatches between the pyrrhotite polytypes, resulting in locally uncompen*sat*ed magnetic moments (e.g., Jin et al., 2021; Pósfai & Buseck, 1997). Further investigation via TEM and magnetic analyses of the structure of intergrowths and the effect on magnetic properties is necessary to establish the contribution of this phenomenon to overall sample magnetization.

b. Po2 – transformation of 5C Po to 4C Po and ferrimagnetic non-integral Po on heating

The massive sulfide sample Po2 is a complex, poly-mineral "bulk rock" system dominated by the 5C-polytype with accessory 4C and 6C polytypes, sphalerite, pyrite, chalcopyrite, and galena. After heating, some of the pyrrhotite transforms into marcasite and greigite, and diffraction pattern indexing suggests that the distribution of polytypes changes such that there is less 5C and more 3C and 4C pyrrhotite. Portions of this polytype shift are observed in Figure 2d across the 200°C and 225°C heating steps, where the superstructure peaks near 17° to 19° 2θ transition sharply from "5C-like" to a more "4C-like" superstructure.

Magnetically, we observe a variety of changes in Po2 as it is cycled to, above, and below through the λ-transition. Coercivity decreases, while susceptibility, *sat*uration magnetization, and the remanence ratio all increase (Figure 2-5). The pre-and post-heating low temperature measurements for Po2 indicate that RTSIRM is greater in the heated sample, and the Besnus transition magnitude has increased (Table 2-3).

The 5C polytype in Po2 is more resistant to alteration than in Po1. In Po1, most of the 5C polytype was transformed into new phases like 3C pyrrhotite and greigite. Although 5C is more abundant in Po2, only a small fraction was transformed into other minerals after heating through the λ-transition. This is important because it demonstrates why general rules of thumb are so difficult to establish for thermal alteration of pyrrhotite polytypes. The reasons for this difference in 5C behavior may simply be based on the overall chemistry of the mineral assemblage, but could also be related to factors including the length scale of the polytype intergrowths, the particular polytypes that are intergrown, the density of intergrowths, and/or differing thermal histories of the two samples.

Similar to Po1, the change in room temperature IRM intensity between Po2 and Po2H is not reflected by an equivalent change in the Besnus transition magnitude (Table 2-3). Thus, thermal cycling across the λ-transition is not simply producing more 4C pyrrhotite, nor is it exclusively attributable to an increase in magnetic grain size. Instead, the increase in room temperature and low temperature magnetization must be due to either a ferrimagnetic form of pyrrhotite that lacks the Besnus transition (perhaps 3C) or to formation of a separate ferrimagnetic mineral (such as greigite formed during heating).

Despite the complexity of Po2, combined magnetic and mineralogic data collected as a function of temperature provide more information than either would provide alone, and highlight the limitations of applying studies on synthetic, mono-phase pyrrhotites to complex natural samples. In this complex setting, understanding interactions and temperature-driven transitions between polytypes become equally as important as understanding the thermal behavior of individual polytypes in predicting the magnetic and mineralogical changes that occur on heating, and studies that evaluate samples which contain pyrrhotite need to consider this complexity when interpreting the results of their experiments.

c. Po3 – formation of a non-integral, ferrimagnetic pyrrhotite

The annealing process of O'Reilly et al. (2000) on Po2 resulted in a slight increase in M_r/M_s (0.32 to 0.36), a slight decrease in B_c (43 mT to 41 mT) and disappearance of the Besnus transition, which indicates a loss of ordered 4C monoclinic pyrrhotite. There is also a slight decrease in the remanent hysteretic magnetization (M_{rh}) of Po3 as compared to Po2, and the distribution of coercivities is narrower (Figure B-8). These changes are consistent with a model where after annealing, some fraction of the pyrrhotite was transformed into a ferrimagnetic pyrrhotite polytype which lacks the Besnus transition. Incommensurate, non-integer vacancy structures in the pyrrhotite may have been created on annealing. While some of these magnetic property changes could be due to an increase in 4C magnetic grain size, we would still expect to see a Besnus transition were (magnetically ordered) 4C pyrrhotite a significant component of the sample (see e.g., Koulialias et al., 2018, who find a distinct Bensus transition in multidomain 4C pyrrhotite). The primary structural pyrrhotite peaks are present in Po3, but the low-angle peaks needed to distinguish various superstructures do not correlate well with published 3C, 4C, 5C, or 6C patterns, despite their broad compositional and structural similarity to the starting material. This suggests that annealing, like the shorter-term heating experiments that produced Po1H and Po2H, produced a pyrrhotite structure that retains the general NiAs unit cell of pyrrhotite, but lacks the long-range vacancy ordering that results in the low-angle, high d-spacing superstructure peaks. The low temperature magnetic data for Po3 provides no diagnostic evidence of 4C pyrrhotite, and instead are consistent with newly formed greigite, and resemble the low temperature behavior of synthetic greigite (Chang et al., 2008). However, we cannot rule out that another form of ferrimagnetic pyrrhotite could be contributing to the magnetization of Po3, as proposed by Haines et al. (2019).

Annealing at relatively low temperatures and for a relatively short time (geologically speaking) has dramatically altered the vacancy structure and magnetic properties of pyrrhotite in Po3. This outcome is different from that of synthetic pyrrhotites, which are produced with a narrow distribution of iron-sulfur ratios but initially may have a great deal of vacancy disorder. Since the iron-sulfur ratio of synthetic samples is fixed (and the preferred polytype has, in theory, been "selected" by this Fe-S ratio), annealing protocols are likely to improve the overall order of the vacancy superstructure because these integral superstructures can be assumed to represent thermodynamic and magnetic end-members that have been selected by the composition. However, the underlying mechanism of this assumption, and the thermodynamics of pyrrhotite polytype stability, deserve close further study. Natural pyrrhotite samples from massive sulfide deposits or other igneous or metamorphic environments have already experienced prolonged annealing during formation, and the mixture of preexisting superstructures combined with the heterogeneous chemistry of the system causes annealing on laboratory timescales to produce increased amounts of non-equilibrium, metastable pyrrhotite superstructures.

d. Discrepancies between diffraction pattern indexing and observed magnetic behavior

In this study, we observe discrepancies between the pyrrhotite polytype estimates during heating from XRD pattern indexing, hysteresis behavior on heating, and low temperature magnetic observations. For example, diffraction pattern indexing suggests that heating of Po2 increased the abundance of the 4C polytype from 3.9% to 17.3% (a 4.4-fold increase), whereas the magnitude of the Besnus transition increased only by a factor of 1.2 (where ΔM_B = RTSIRM(40K)-RTSIRM(10K) on cooling). Similarly, diffraction pattern indexing for Po2H and Po3 suggest abundances of 2.5% and 1.8% magnetite, respectively. These abundances would normally result in prominent Verwey transitions and high M_s values, neither of which are observed in magnetic measurements. These discrepancies highlight one of the challenges of characterizing pyrrhotite when it occurs with other minerals in rocks and sediments. Diffraction pattern indexing works best when the total number of mineral phases in a sample is small so that multiple peaks that overlap within 0.1° 2θ can be identified and to differentiate peaks with low relative intensities. However, when pyrrhotite occurs at low concentrations with other non-pyrrhotite phases, it becomes more challenging to confidently identify the abundance of different pyrrhotite polytypes. Po2 contains ~80% pyrrhotite, 15% other sulfides, and 5% silicates and approximates what might occur in a magnetic separate. Yet even in this instance, indexing results vary with only minor adjustments to indexing parameters (especially at the higher temperatures in this study), which is indicatve of non-uniqueness of abundance estimates.

While the technique of Arnold (1966) and Graham (1969), which uses the ratio of the peak height at ~51° 2θ to the height of the "shoulder" on the higher 2θ side of the peak, can be used to estimate the amount of monoclinic versus hexagonal pyrrhotite in a sample, it does not provide additional important information about which integral (or non-integral) superstructures may be present. Furthermore, the reference patterns used to index pyrrhotite polytypes are established under room temperature conditions. Measurements collected at elevated temperatures, such as those in Figure 2-2, must also take into account thermal expansion of the various phases. Non-isotropic minerals expand at different rates along different crystallographic axes. Such considerations make indexing routines, such as Rietveld analyses, non-trivial endeavors. Thus, while powder diffraction measurements collected as a function of temperature are important tools that show us when and how diffraction peaks are changing across the λ-transition, it is difficult to use them to calculate quantitative estimates of the mineral change during the transition itself. This remains an important area for future research. However, techniques that can evaluate fine-scale changes in vacancy ordering, like TEM, are defined by the small length-scale of the measurements, and it can be difficult to extrapolate observations made on this small scale to the behavior of a bulk natural sample.

Despite the inherent challenges, we argue that collecting temperature dependent powder diffraction data is still important for untangling pyrrhotite polytype changes and

for the interpretating of magnetic behavior and remanence. By examining progressive changes in the positions and intensities of superstructure peaks at low 2θ angles and those of the more prominent peaks at 35°, 40°, and 51° 2θ, it will be possible to identify changes in the vacancy ordering of pyrrhotite. Even without concrete quantifications or identifications of polytype transformations, observed changes in magnetic behavior with temperature can be linked to observed changes in pyrrhotite polytype. Additionally, this approach also allows users to see when non-pyrrhotite minerals begin to form during this process, which may also contribute to sample magnetization. Most of the temperature-dependent diffraction data collected here were gathered using a conventional X-ray diffractometer at the University of Minnesota and are of sufficient quality to identify most of the important structural changes across the λ-transition. However, we encourage future users to gather temperature-dependent diffraction data using synchrotron facilities because the resolution of these data would allow for less ambiguous identification of changing peak positions and intensities. Synchrotron-based XRD analyses allow both rapid analysies and better resolved peak locations and intensities such that minerals at extremely low (<0.1%) concentration can be analyzed, compared to the ~1-5% detection limit of conventional Co Kα XRD experiments. Figures 1b and 1c demonstrate the superior quality of data collected with a synchrotron compared with those from an X-ray diffractometer. This is particularly evident when examining greigite peaks (most visible in Figure 1a, marked by ♦) that are nearly or completely hidden by the background in the Co Kα, but are distinct in the synchrotron patterns for the same samples.

V. Conclusions

While temperature-driven magnetic transitions in pyrrhotite have been the focus of many rock magnetic studies over the last half century, few incorporate detailed powder diffraction analyses measured at the temperatures at which these transitions occur. This lack of temperature-dependent crystallography has resulted in two important impasses that must be resolved: we cannot yet confidently describe (1) which pyrrhotite superstructures can retain a permanent magnetization (though progress is being made on this front), and (2) how these superstructures respond to temperature cycling over varying timescales.

We demonstrate how coupled powder diffraction and magnetic measurements can provide a clearer understanding of the diversity of mineral transformations that can occur during the λ-transition. The dominance of a particular polytype in the starting pyrrhotite assemblage can change the magnitude of magnetic changes observed after heating as well as the temperatures at which these changes occur. Powder diffraction data sets like those shown in Figure 2 also demonstrate that crystallographic changes associated with the λ-transition occur over a temperature range rather than a discrete one. Powder diffraction data collected at room temperature before and after heating are useful for constraining which polytypes are likely to have altered, but diffraction data collected at a range of temperatures gives a much more comprehensive view of the transition process.

More complex non-magnetic techniques for determining pyrrhotite superstructures, such as single-crystal diffraction, transmission electron microscopy selected area electron diffraction, and neutron scattering hold great potential, but often analyze such small volumes that they do not adequately capture the heterogeneous nature of geologic materials and may not provide a representative view of a bulk sample. In this context, magnetic measurements potentially offer an important counterbalance to the limitations of conventional powder diffraction data. Representative samples are easily analyzed and many forms of magnetic instrumentation are already established to measure magnetic properties as a function of temperature. Magnetic susceptibility is already a standard tool for identifying the λ-transition, and low temperature RT-SIRM experiments are routinely used to detect 4C pyrrhotite. However, on their own, magnetic measurements cannot yet be used to accurately determine the concentration of all pyrrhotite in a sample or its distribution of polytypes. The magnitude of the Besnus transition is often used to identify and determine the quantity of 4C monoclinic pyrrhotite in bulk samples (e.g., Gilder et al., 2011; Rochette et al., 1990; Torii et al., 1996). As the results of Horng & Roberts (2018) demonstrate, there exist additional environmentally stable and geologically relevant ferrimagnetic pyrrhotite polytypes that are distinct from 4C pyrrhotite and do not express the Besnus transition. The 3C polytype identified in marine sediments by Horng and Roberts (2018) is an example of a ferrimagnetic "integral" pyrrhotite that carries a room-temperature remanence. However, the vacancies of non-integral pyrrhotites could also form pyrrhotite capable of holding a room-temperature remanence – weaker than that carried by 4C pyrrhotite, but with unknown thermal and temporal stability. The combination of powder X-Ray diffraction and magnetic property measurements collected with temperature can provide multiple, supporting lines of evidence for phase transformations in natural samples, and can illuminate the mineralogical source of magnetic property changes on heating and cooling.

Being able to properly characterize the total pyrrhotite concentration in a sample, the relative abundance of various polytypes, and to determine which contribute to a sample's magnetism is important for a broad range of research themes, ranging from paleomagnetism to acid mine drainage to solar cell production. We highlight the need for further studies at the intersection of crystallography and mineral magnetism to determine the strength, stability, and behavior of both integral and non-integral pyrrhotite polytypes.

Acknowledgements: The authors acknowledge Javier Garcia Barriocanal, University of Minnesota Characterization Facility, for assisting in conducting the XRD-with-temperature experiments and for providing guidance in indexing the patterns collected. MWRV was supported by NSF-EAR-1620582. KKH was supported by a MnDRIVE Environment grant to JMF and DSJ, funding from the University of Minnesota Department of Earth & Environmental Sciences, a Geological Society of America Student Research Grant, and the Mineralogical Society of America Edward H. Krauss Crystallographic

Research Award. Part of this work was performed at the Institute for Rock Magnetism (IRM) at the University of Minnesota. The IRM is a US National Multi-user Facility supported through the Instrumentation and Facilities program of the National Science Foundation, Earth Sciences Division, and by funding from the University of Minnesota. We thank Dario Bilardello, Maxwell Brown, and Peat Solheid for help with data acquisition, processing, and troubleshooting in the lab. This is IRM publication #2106. XRD data are deposited in the Data Repository for U of M (DRUM) as Hobart et al. (2021). Magnetic data for Po2 are deposited in the Magnetics Information Consortium (MagIC) as Hobart et al. (2022), and magnetic data for all samples are deposited in the Data Repository for U of M (DRUM) as Hobart et al. (2022).

Chapter 3: Sulfur-oxidizing bacteria accelerate pyrrhotite dissolution under near-neutral and mildly acidic conditions

Microorganisms are significant catalysts of sulfide mineral dissolution in acidic systems and play a key role in the formation of acid rock drainage. Decades of fundamental research on the interactions between microorganisms and pyrite (FeS_2) have led to improved management of mine wastes and novel strategies for ore extraction. The Duluth Complex, located in northern Minnesota, hosts the largest undeveloped copper, nickel, and platinum-group element deposit in the world, but much of the previous research on the biogeochemistry of sulfide minerals does not apply to this system as the dominant sulfide mineral in these ores is pyrrhotite ($Fe_{1-x}S$, $0 \leq x \leq 0.125$), and experimental weathering of waste rock and tailings from these deposits remains near-neutral to mildly acidic. Therefore, we evaluated the role of microorganisms on pyrrhotite dissolution under the circumneutral conditions (pH 4.5-7) predicted to occur in Duluth Complex mine waste and tailings. Using microorganisms and microbial communities isolated and enriched from experimentally weathered waste rock and tailings, we find that sulfur-oxidizing *Sulfuriferula* spp. increase the amount of pyrrhotite dissolved, *Sulfuriferula* preferentially attaches to pyrrhotite mineral surfaces over other sulfides, and that different iron oxide precipitates are formed in the presence of microorganisms than form during abiotic dissolution. Microbial communities containing *Sulfuriferula* spp. and other sulfur-oxidizing and heterotrophic bacteria show similar rates of pyrrhotite dissolution to isolate cultures of *Sulfuriferula* spp., suggesting that these microorganisms are uniquely adapted to sulfide mineral weathering environments.

The work presented in this chapter was written for submission to the journal *Geobiology* and has been modified to meet formatting guidelines. Co-author Elizabeth Roepke conducted the attachment experiments described in section III-b, and co-author Daniel Jones conducted the experiments on Duluth Complex waste rock and tailings (Experiment 5, described in section III-a) and conducted the sequencing library preparation for the experiments. Co-authors Daniel Jones, Jake Bailey, and Joshua Feinberg assisted with experimental design, data analysis, and results interpretation.

I. Introduction

Microorganisms serve as important catalysts for sulfide mineral dissolution and oxidation in acidic systems, and play a key role in the formation of acid rock drainage (ARD) (Baker & Banfield, 2003; Edwards et al., 1999; Ňancucheo & Johnson, 2011; Schippers, 2004; Schippers et al., 1996; Schippers & Sand, 1999). Under extremely acidic conditions (below pH 4), iron-oxidizing microorganisms are actively involved in oxidation

of pyrite (FeS_2) and other sulfide minerals by maintaining low pH conditions and regenerating the oxidant iron (III). These microbially-driven reactions can result in highly acidic and metal-rich drainage in both natural and engineered systems (Nordstrom et al., 2015; Schippers et al., 1996; Schippers & Sand, 1999), and decades of research on microbial oxidation of pyrite have improved management of mine waste (Dugan & Apel, 1983; Onysko et al., 1984; Schippers et al., 1998) and led to new strategies for ore processing (Brune & Bayer, 2012; D. Johnson, 2018; Rawlings & Johnson, 2007; Rohwerder & Sand, 2003; Vera et al., 2013). The rate of microbial pyrite oxidation decreases dramatically above pH 4 (Arkesteyn, 1980; Korehi et al., 2014; Nordstrom, 1982; Schippers, 2004; Schippers & Jørgensen, 2002), and until recently, microorganisms were not thought to be important catalysts for sulfide mineral oxidation at more neutral pH (Napieralski et al., 2022; Percak-Dennett et al., 2017). While pyrite is the most extensively studied sulfide mineral system, microorganisms can have important interactions with other sulfide minerals, although the importance of these interactions in an environmental context is not as well-constrained.

The Duluth Complex, located in Northern Minnesota, hosts the largest undeveloped copper, nickel, and platinum-group element deposit in the world (Miller et al., 2002; Severson et al., 2002; Thériault et al., 2000). The primary gangue mineral in the Duluth Complex is the mineral pyrrhotite ($Fe_{1-x}S$, $0 \leq x \leq 0.125$), and so the extensive research on microbial pyrite oxidation does not apply to this system. Rates for pyrrhotite oxidation below pH 4 range from 10 to 100 times higher than pyrite oxidation (Bădică & Chiriță, 2015; Belzile et al., 2004; Chiriță, 2016; Chiriță & Rimstidt, 2014; Cruz et al., 2005; Harries et al., 2013; Janzen et al., 2000). However, the rate of abiotic pyrrhotite dissolution in more neutral systems, and the role microorganisms play in altering that rate, is not well understood. Two studies address pyrrhotite dissolution rates at pH >5, although they describe different effects of pH on dissolution rate and different fundamental rates (Chiriță, 2016; R. V. Nicholson & Scharer, 1993).

Long-running humidity cell and field pile leaching experiments conducted by the Minnesota Department of Natural Resources have constrained the pH of leachate from experimentally-generated ore, waste rock, and tailings. The low overall sulfide mineral content of the ore (only up to 2wt% S), and the acid-neutralizing capacity of the surrounding silicate minerals result in neutral to mildly acidic leachate (pH ~7 to ~4.5, (Lapakko, 1988, 2015; Lapakko & Antonson, 1994)). Further, the microbial communities that populate both the lab and field weathering experiments (Jones, Lapakko, et al., 2017) and naturally-weathered, sulfide-bearing Duluth Complex outcrops (Chapter 4, this thesis) are populated by organisms that are not typically associated with acidic mine waste environments. The primary lithotrophic organisms in these communities, and in similar circumneutral, sulfidic mine wastes, are sulfur- rather than iron-oxidizers, and frequently contain uncultivated taxa (Bailey et al., 2016; L. Chen et al., 2013; Dockrey et al., 2014; Koski et al., 2008; Langman et al., 2017; Mendez et al., 2008; Whaley-Martin et al., 2019).

One of the major genera of sulfur-oxidizing bacteria found in the waste rock and tailings leaching experiments was *Sulfuriferula* (Jones, Lapakko, et al., 2017), and several metabolically-distinct strains were isolated from those experiments (Jones et al., 2017b & Chapter 5, this thesis).

Without experimental data on the role of environmentally relevant microorganisms in modifying pyrrhotite dissolution rate, it is difficult to assess potential microbiological solutions for metal extraction of Duluth Complex ores or consider microbial dynamics in remediation and management of mine waste after closure. Therefore, we conducted laboratory pyrrhotite oxidation experiments using microorganisms isolated from Duluth Complex waste rock and tailings to evaluate the role of microorganisms in pyrrhotite oxidation under near-neutral conditions. Batch reactors at a range of starting pH conditions, from pH 4.5 to 7, allow us to evaluate pH controls on pyrrhotite oxidation, and the use of four metabolically distinct strains of *Sulfuriferula*, a strain of *Thiobacillus*, and an enrichment community allow us to examine the ways in which strains with different sulfur oxidation pathways and other metabolic differences affect pyrrhotite oxidation. In addition to measuring aqueous chemical species to track dissolution, we used the magnetic properties of pyrrhotite and secondary iron oxides as a tool to track mineralogical evolution during pyrrhotite oxidation.

II. Methods

a. Dissolution Experiments:

Laboratory dissolution experiments were conducted with crushed pyrrhotite as a substrate. The pyrrhotite used in these experiments is described in more detail in (Hobart et al., 2021), but briefly, is a mixture of 4C and 6C pyrrhotite with trace sphalerite, chalcopyrite, and galena from Ward's Scientific, crushed and sieved to a grain size of between 75 and 150μm. Some of the pyrrhotite was annealed before use in these experiments (corresponding to sample Po3 in Hobart et al., 2021 and Chapter 2, this thesis), while other experiments used unannealed pyrrhotite (corresponding to sample Po2 in Hobart et al., 2021 and Chapter 2, this thesis), as described below. The annealed pyrrhotite underwent mineralogical changes on annealing, and is a mixture of 4C, 5C, and 6C pyrrhotite. Experiments using the annealed pyrrhotite are indicated with "annealed Po" in the figure body and figure caption; all other dissolution experiments use the unannealed pyrrhotite. Prior to use in the experiments, the pyrrhotite was washed with 1M HCl to remove surface oxidation, washed and sonicated three times in milliQ water, then sonicated in ethanol, air-dried, and loaded into acid-washed serum bottles. The serum bottles and pyrrhotite were then stored for 24 hours in an anaerobic chamber (Coy, Grass Lake MI, USA) with a (N_2/ 5% H_2) headspace, sealed, and sterilized at 121°C for 30 minutes in an anoxic headspace.

The media used in these experiments contained 6mM NH_4Cl, 1.5mM $MgCl_2 \cdot 6H_2O$, 0.3mM $CaCl_2 \cdot 2H_2O$, 0.3mM KH_2PO_4, 0.1mM Na_2HPO_4, trace element solution (Flood et

al., 2015), and 20mM MES buffer (2-(*N*-morpholino)ethanesulfonic acid) or phosphate buffer (30mM KH_2PO_4, 10mM Na_2HPO_4) titrated to the required pH with 4M NaOH or 4M HCl. The isolates used in these experiments included four strains of *Sulfuriferula*, including *S.* sp. strain AH1 (Jones, Roepke, et al., 2017) and two other strains (GW1 and HF6a, Chapter 5, this thesis). Experiments also included a strain of *Thiobacillus* that was isolated from pyrite-containing tailings from a taconite mine (Jones et al. *in prep*). The enrichment inoculum was a homogenized microbial community collected from weathered Duluth Complex rock maintained in the laboratory in mixed culture with solid, crushed pyrrhotite as the growth substrate. At the beginning of each experiment, bottles were inoculated with 0.5mL of turbid isolate culture grown on the media described above with the addition of 40mM $Na_2S_2O_3 \cdot 5H_2O$, or 0.5mL of the enrichment culture containing suspended pyrrhotite particles. Inoculum from thiosulfate media was harvested late in the growth phase to reduce the amount of thiosulfate transferred into each experiment.

Four separate sets of experiments were performed. Experiments 1 and 2 were conducted in 25mL serum bottles containing ~0.2g of pyrrhotite and 10mL media. Experiments 3 and 4 were conducted in 125mL serum bottles containing ~0.5g pyrrhotite and 50mL media. Table 3-1 describes the starting pH, inoculum, and pyrrhotite substrate used in each experiment. Each set of batch reactors was maintained at room temperature for the duration of the experiment on an oscillatory shaker. At each sampling point, some of the liquid media was removed for chemical analysis and an equivalent volume of sterile media was added to maintain a constant volume. 0.5mL of the removed sample was analyzed for pH with a LAQUAtwin pH-22 handheld pH meter (HORIBA, Kyoto, Japan), 1.5mL of the leachate was acidified with 20µL of 6M hydrochloric acid and stored at -4°C for aqueous metal concentrations, and 2mL of the leachate was stored at -20°C for measurement of anion concentrations. Anion concentrations (chloride, fluoride, bromide, nitrate, sulfate) were measured using a Metrohm 930 Compact IC Flex ion chromatograph with a A Supp 5 column, 20µL sample loop, and an eluent carbonate buffer (3.2mM Na_2CO_3 and 1.0mM $NaHCO_3$). Sulfate release was calculated based on the measured concentration of sulfate at each time point, corrected for the amount of leachate that was removed and replaced with sulfate-free media at each sampling interval. Experiments 1 and 2 were additionally measured for bulk magnetic susceptibility (χ) at each sampling interval with a Geofyzika KLY-2 Kappabridge (300 Am^{-1} field at 920 Hz) at the University of Minnesota Institute for Rock Magnetism. Magnetic susceptibility is a measure of the response of a material to a weak applied magnetic field, and for a given ferromagnetic material, scales linearly with the amount of magnetic material in a sample. The magnetic susceptibility of each batch reactor was measured in duplicate at each time point and the measurements were averaged. Each of these measurements was then normalized to the original (time 0) susceptibility of the bottle to represent the percent change in susceptibility from T0 at each time point (add a reference to another study that does this). Each bottle was capped with a 3D-printed HDPE cap to facilitate these measurements that was

sterilized with ethanol; metal or aluminum foil caps would contain trace ferrimagnetic material that would interfere with these measurements. Figure C-1 provides images of these smaller reactors at three time points.

Table 3-1. Overview of experimental parameters for batch experiments.

Exp. #	Po, reactor volume	pH	Abiotic	Abiotic + PFA	Enrichment	Isolate AH1	Isolate GW1	Isolate CT1	Isolate HF6a	PFA-poisoned AH1	E. coli	AH1 + MES (no Po)
1	~0.2g Annealed, 10mL	4.5	x3		x3	x3						
		5.0	x3		x3	x3						
		6.0	x3		x3	x3						
		7.0	x3		x3	x3						
	~0.2g Unannealed, 10mL	6.0	x3		x3	x3						
2	~0.2g Annealed, 10mL	4.5	x4		x3	x3						
		6.0	x5		x3	x3						
	~0.2g Unannealed, 10mL	4.5	x4		x3	x3						
		6.0	x5		x3	x3	x3	x3	x3	x3	x3	
3	~0.5g Unannealed, 50mL	6.0	x4		x3	x3	x3	x3				
4	~0.5g Unannealed, 50mL	6.0	x3	x3	x3	x3						x3
5	DC waste rock, tailings		x3		x3	x3						

At the termination of experiments 1, 3, and 4, pyrrhotite and iron oxide precipitates were collected and aliquots were stored at -80℃ for mineralogical, microbiological, and elemental sulfur concentrations. Experiment 3 and 4 were additionally sampled for solid material at an intermediate timepoint (day 21 for experiment 3 and day 30 for experiment 4). Elemental sulfur was analyzed by a solid-liquid perchloroethylene extraction as described in (McGuire & Hamers, 2000). Extracted elemental sulfur was measured by HPLC using a Sorbax C18 StableBond column (at 30 °C), 40 mM aqueous acetate buffer (pH 5) and ~35% acetonitrile, with a UV-absorbance detector at $\lambda = 254$ nm. Iron oxide precipitate and pyrrhotite mineralogy were examined by low-temperature magnetic properties and visual examination by SEM. Low temperature magnetic properties were measured using a Magnetic Property Measurement System (MPMS; Quantum Design, San Diego, CA, USA) at the University of Minnesota Institute for Rock Magnetism. The measurements consist of (1) low temperature (10 K) cycling of a 2.5 Tesla (T) room temperature *sat*urating isothermal remanent magnetization (RTSIRM) in zero-field, (2) field cooling (FC) in a 2.5 T magnetic field and subsequent warming of the remanence

acquired at 10 K after FC (FC-LTSIRM), and (3) zero-field warming of a 2.5 T SIRM imparted at 10 K (ZFC-LTSIRM), after cooling in zero-field (Kruiver et al., 2001; Adrian R. Muxworthy et al., 2003). All MPMS measurements were conducted using a heating/cooling rate of 5 K/min in 5 K steps, as in (Kathryn Kiku Hobart et al., 2021). SEM images were collected using a JEOL 6500 field-emission gun scanning electron microscope (SEM) equipped with an energy-dispersive spectrometer (EDS) at the University of Minnesota Characterization Facility.

DNA extractions of samples were collected at the termination of experiment 1. DNA extractions were conducted using the PowerSoil or PowerSoilPro DNA isolation kits (Qiagen, Hilden, Germany). To reduce DNA extraction bias, the vortexing step was modified, with aliquots removed after vortexing for 5, 10, and 15 minutes, and then recombined. Libraries were then prepared following the "in house" method of Jones et al. (2017a). Briefly, the V4 region of the 16S rRNA gene was first amplified with primers "515f modified" and "806r modified" (Walters et al. 2015) that were amended with Nextera adaptors to allow barcoding (Jones, Lapakko, et al., 2017). PCR was performed as in (Jones, Lapakko, et al., 2017): 5 min initial denaturation at 94°C, either 25 or 30 cycles of 45 s denaturation at 94°C, 60 s annealing at 50°C, and 90 s elongation at 72°C, and final elongation at 72°C for 10 min. Blank controls were included with all DNA extractions, and no product was visible in the blanks. PCR products were then submitted to the University of Minnesota Genomics Center for barcoding (10 cycles after 1:100 dilution) and sequencing on an Illumina MiSeq (Illumina, San Diego, CA, USA), 250 paired end cycles.

OTU calling was performed as in (Jones et al., 2021). Raw sequences were filtered and trimmed with Sickle (https://github.com/najoshi/sickle) to average quality above 28 (5' trimming only) and ≥ 100 bp; any residual adapters reverse complemented on the 3' end were removed with cutadapt (Martin, 2011); R1 and R2 reads were assembled with PEAR (J. Zhang et al., 2014); and primers removed by trimming the assembled reads with prinseq v.0.20.4 (Schmieder & Edwards, 2011). OTUs were defined at 97% similarity with a modified version of the UPARSE pipeline (USEARCH v.10.0; (Edgar, 2013)), in which the "derep_fulllength" script from VSEARCH v.1.9.5 (Rognes et al., 2016) was used. OTUs were classified with mothur v.1.36.1 (Schloss, 2020) to the Silva database v.132 (64) (Quast et al., 2013) with a confidence score cutoff of 50.

b. Attachment Experiments:

The association of *Sulfuriferula* sp. strain AH1 with different sulfide minerals was evaluated by incubating sulfide chips of Duluth Complex ore. The ore samples were originally collected by the International Nickel Company (INCO) in 1974 as part of an application to mine in the Spruce Road area south of Ely, MN. The material used in these experiments was first shipped to the now-defunct Mineral Resources Research Center at the University of Minnesota and was later stored outdoors for ~10 years at the University Recycling Center where they were collected for this study.

Chips of these sulfide-mineral-bearing Duluth Complex rock were cut to ~3x1x0.5 cm. The side of the chip to be analyzed was polished to 600 grit (~25μm), and the other side was polished with 240 grit. Four rock chips were suspended in 125mL Erlenmeyer flasks with monofilament and then autoclaved. 80mL of sterile media was added to each flask, using the same media recipe as discussed above (except using 10mM Na_2HPO_4 and 30mM KH_2PO_4 as a buffer instead of MES) and inoculated with a 0.2μm filter containing the filtrate of 20mL of a culture of isolate *Sulfuriferula* sp. strain AH1. An image of one of the Erlenmeyer flasks with rock chips is provided as Supplemental Figure S2.

Chips were collected after 4 weeks incubation and the surfaces were stained with DAPI (4',6-diamidino-2-phenylindole) and imaged using an Olympus BX61 compound microscope with a DP72 camera running CellSens Dimensions software (Olympus, Japan). Following microbial attachment experiments, the chips were examined using a TM-1000 tabletop scanning electron microscope (SEM) (Hitachi, Tokyo, Japan) equipped with an energy-dispersive spectrometer (EDS) at the University of Minnesota LacCore.

III. Results & Discussion

a. Microorganisms increase sulfate release from pyrrhotite dissolution over abiotic controls.

Sulfate release for the four sets of experiments are shown in Figure 3-1, and pH change over the duration of the experiments are shown in Figure 3-2. In both Figure 3-1 and Figure 3-2, the data are separated by starting pH of the experiment. In all cases, the batch reactors that were inoculated with microorganisms (either *Sulfuriferula* or *Thiobacillus* isolates or the enrichment community) show increased sulfate release over the abiotic reactors. The difference in sulfate release between the abiotic and microbial reactors is most apparent in the lowest pH experiments (Figure 3-1a, f, g), which show an approximately 20-fold increase in sulfate release in the reactors inoculated with the isolate *Sulfuriferula* strain over the abiotic reactors. The difference in sulfate release between the abiotic and inoculated reactors decreases with increasing pH, although more sulfate was released in the inoculated experiments. Very little sulfate was released from the abiotic reactors, suggesting that only minimal abiotic pyrrhotite dissolution is occurring. However, many of the abiotic reactors were contaminated. In addition to unexpectedly high sulfate release, cells were visible on mineral surfaces in both pH 6 and the pH 7 "abiotic" reactors examined at the termination of experiment 1 (Figure 3-1c, d) by SEM and fluorescent staining, and rRNA gene libraries were generated from abiotic controls (discussed below). Similarly, DNA extractions from solids from the "abiotic" reactors at the termination of Experiment 3 (Figure 3-1e) had positive PCR amplification using primers for 16S rRNA genes, although fluorescent staining at day 21 did not show contamination. In order to avoid contamination, paraformaldehyde-poisoned controls were used in experiment 4, which showed very low sulfate release (Figure 3-1j). Experiments without pyrrhotite

showed no sulfate release (Figure 3-1j), indicating no interactions between AH1 and the ethanesulfonic sulfur in the MES buffer.

The pH of the reactor media varied over the lifetime of the experiments. The experiments in the smaller 25mL serum bottles (Figure 3-2a-d, f-i) show an initial increase in pH of about 0.7 pH units over the first 10 days, followed by a decrease in pH until the end of the experiment. The initial pH increase likely indicates proton consumption during pyrrhotite and ferrous iron oxidation, and the decrease is probably due to ferric iron precipitation that lags behind the initial step in pyrrhotite oxidation. Experiments that were inoculated with either the isolate strain or the enrichment became more acidic. This is consistent with the increase in sulfate release seen in the biological experiments, where increased oxidation of sulfide to sulfate in the biological experiments results in an increase in acidity. The larger-volume reactors (Experiments 3 and 4, Figure 3-1e, j and Figure 3-2e, j) have more stable pH, likely due to an increased media to rock ratio, but the reactors inoculated with both the enrichment and the isolate ultimately become more acidic than the abiotic reactors.

The experiments inoculated with the enrichment community show an increase in sulfate release over the experiments inoculated with the isolate strain in the lower pH experiments (pH 4.5, Figure 3-1a, f, g, and pH 5.0, Figure 3-1b). In the higher pH reactors from experiment 1, the enrichment and isolate-inoculated experiments show roughly the same rate and amount of sulfate release. In the pH 6 reactors from experiment 2, sulfate release from the enrichment reactors track the abiotic reactors closely, suggesting that the enrichment culture did not grow in these reactors. In the larger volume reactors (Figure 3-1e, j), where pH stayed more stable, sulfate release from the enrichment and isolate track closely. In experiment 4, the enrichment reactors show more sulfate release early in the experiment (e.g., at day 16, there has been ~20mmol of sulfate released from the enrichment reactors, while the isolate reactors show ~7mmol sulfate released), but by the termination of the experiment, the isolate and enrichment reactors had released about the same amount of sulfate.

Reactors that used the annealed pyrrhotite as a substrate (Figure 3-1f, h, Figure C-3a) show slightly higher amounts of sulfate released than the reactors that used the unannealed pyrrhotite as a substrate (Figure 3-1g, I, Figure C-3b), although the difference in sulfate release between the two substrates are not as significant as the variation among individual reactors.

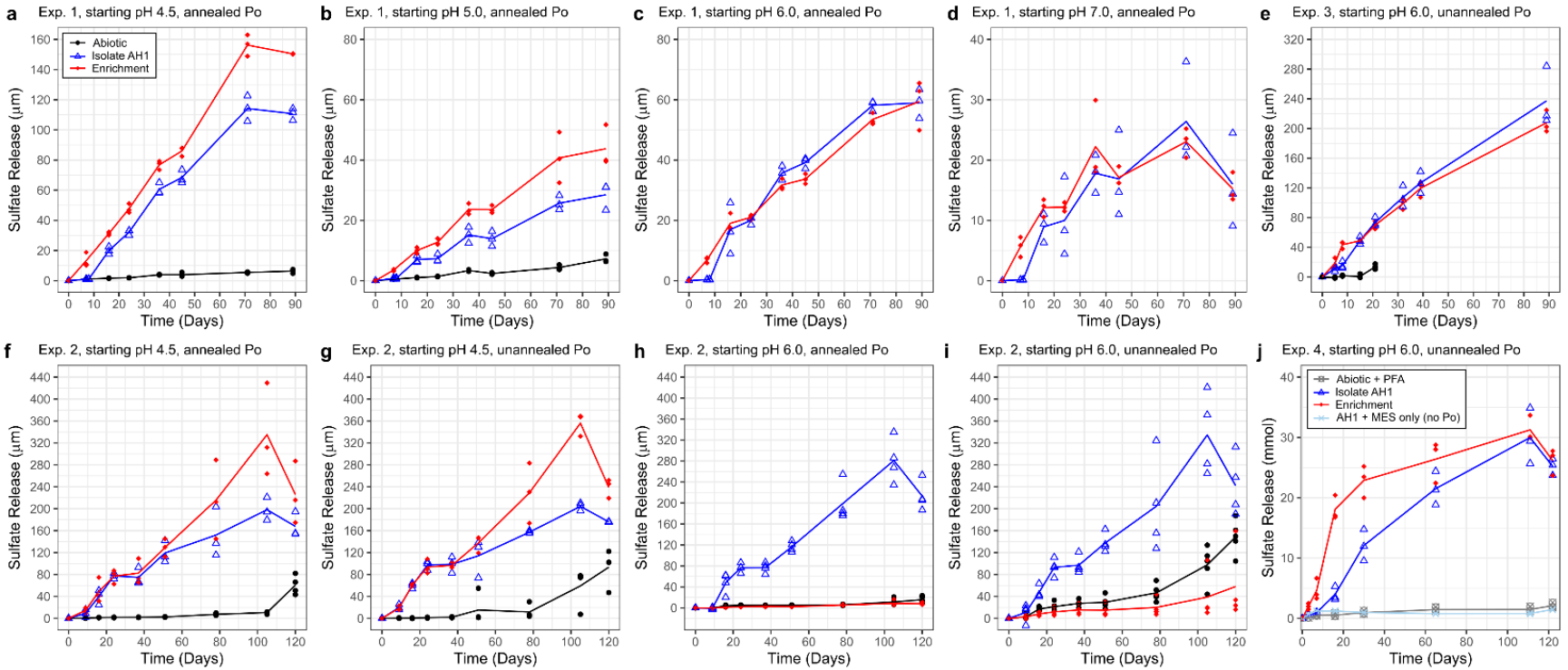

Figure 3-1. Sulfate release for experiment 1 (a-d), experiment 2 (f-i), experiment 3 (e), and experiment 4 (j). Individual measurements for each experiment are plotted as points, and the solid line represents the mean of the set of replicate experiments. Data from abiotic experiments was removed in panels (c) and (d) due to confirmed contamination, and after day 21 in (e) before which cells were not visible on mineral surfaces. All data is reported in Appendix 1.

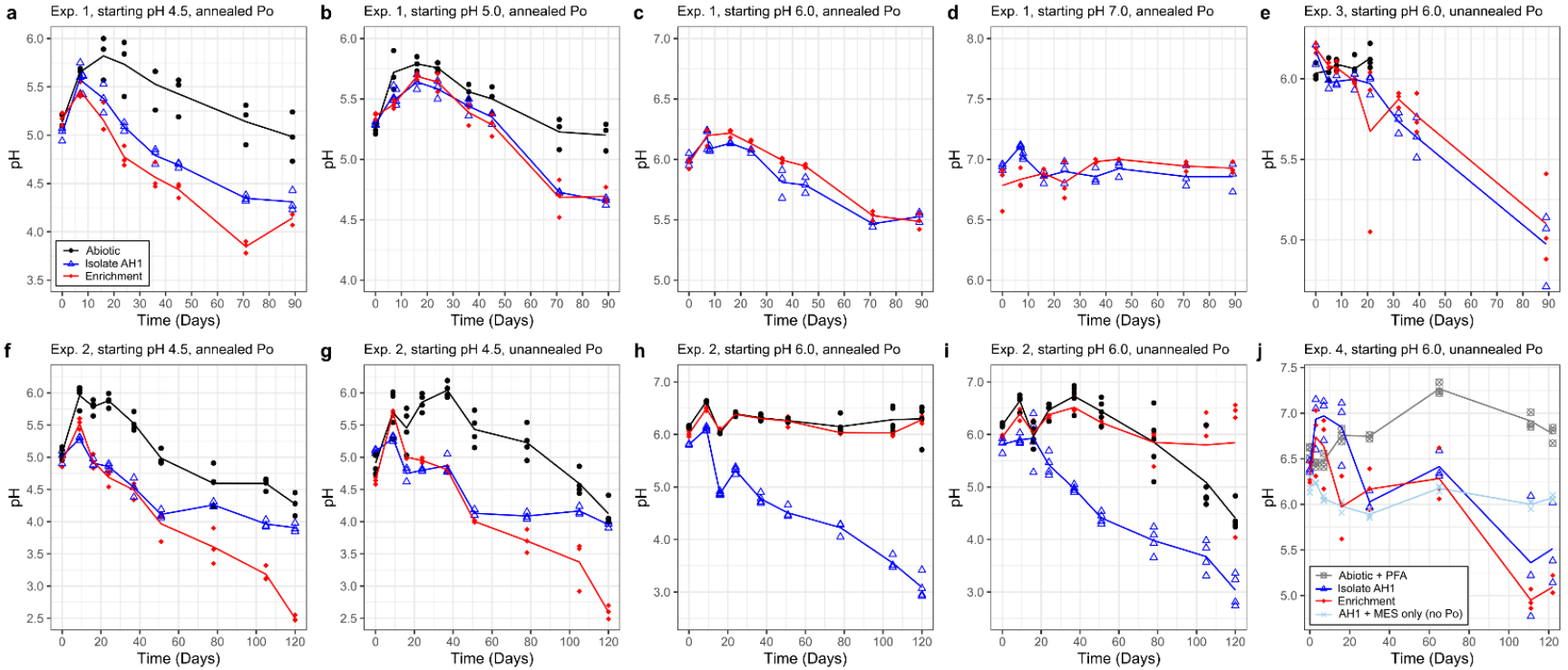

Figure 3-2. pH change over time for experiment 1 (a-d), experiment 2 (f-i), experiment 3 (e), and experiment 4 (j). Individual measurements for each experiment are plotted as points, and the solid line represents the mean of the set of replicate experiments. Data from abiotic experiments was removed in panels (c) and (d) due to confirmed contamination, and after day 21 in (e) before which cells were not visible on mineral surfaces. All data is reported in Appendix 1.

Not all of the reduced sulfur from pyrrhotite would have been oxidized completely to sulfate. Further, there is some evidence that abiotic pyrrhotite oxidation under acidic conditions (pH <4) results in the formation of an increasingly sulfur-enriched layer, that contains unoxidized sulfide from the pyrrhotite and partially oxidized elemental sulfur, as iron is preferentially removed by dissolution and oxidation (Buckley & Woods, 1985). To evaluate differences in the amount of elemental sulfur formed due to pyrrhotite oxidation, elemental sulfur was analyzed from solid material was collected from the reactors at the termination of experiment 1, and at day 21 and the termination of experiment 3. Calculated weight-percent of elemental sulfur in each reactor is presented in Figure 3-3. The pH 4.5 reactors (Figure 3-3a) accumulated the most elemental sulfur over the 89-day lifetime of the first experiment. Within the pH 4.5 set of reactors, the abiotic reactors had the most elemental sulfur by wt.%, while the reactors inoculated with the enrichment culture contained the least elemental sulfur as a percentage of the final mass. More elemental sulfur was produced in the lower-pH reactors (Figure 3-3a, b) than in the higher pH reactors (Figure 3-3c-f). The reactors inoculated with the isolate strain of *Sulfuriferula*, AH1, appear to accumulate more elemental sulfur than the enrichment community, particularly at low pH.

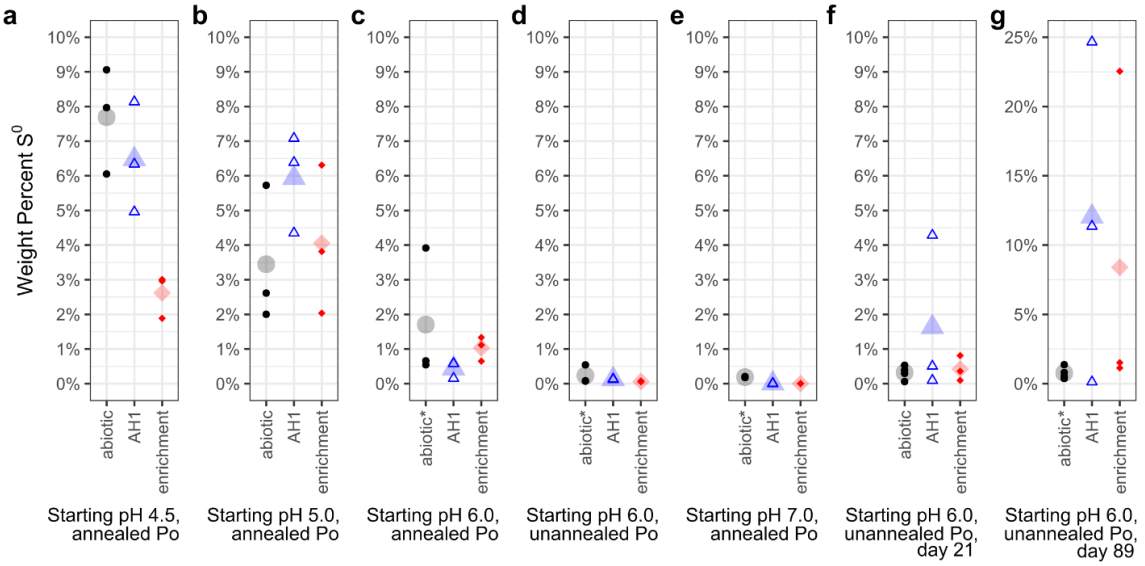

*Figure 3-3. Elemental sulfur measured at the termination of experiment 1 (a-e) and at day 21 (f) and termination (day 89) of experiment 3 (g). Individual measurements for each experiment are plotted as smaller points, and the larger point is the mean of the three replicate experiments. The abiotic reactors in the pH 6 and 7 reactors for experiment 1 (c, d, e) and at the termination of experiment 3 (g) were contaminated and are marked by an *.*

Measurements of bulk magnetic susceptibility were used to track changes in the magnetic mineralogy through time. Bulk magnetic susceptibility is a measure of the amount of magnetic material in a sample, so for a mono-phase magnetic sample (in this case, the pyrrhotite added to the batch reactors), any change in bulk magnetic susceptibility

over the duration of the experiment is expected to be proportional to the amount of magnetic material lost (i.e., pyrrhotite dissolved and converted to nonmagnetic sulfate). Similarly, as iron oxides accumulate in the experiments over time, bulk magnetic susceptibility would be expected to increase proportional to the amount of iron oxides that accumulate but will be affected by the crystallinity and mineralogy of the iron oxides (amorphous Fe-oxides would contribute less to susceptibility than highly crystalline magnetite, for example). Change in bulk susceptibility through time for experiments 1 and 2 is presented in Figure C-4. The pH 4.5 reactors for both experiment 1 and experiment 2 show the clearest trends, where the abiotic reactors slowly increase in susceptibility over the course of the experiment, while the reactors inoculated with the isolate or the enrichment slowly decrease in susceptibility. The unannealed pyrrhotite is less strongly ferrimagnetic, and so the proportional changes in magnetization are greater than in the experiments containing the annealed pyrrhotite. Similar time-resolved studies of magnetic susceptibility have been used in the field to track microbial iron reduction due to the movement of a subsurface hydrocarbon plume (Atekwana et al., 2014; Lund et al., 2017), but this is the first study of which we are aware which uses bulk magnetic susceptibility as an experimental proxy for iron mineral transformations in a laboratory setting.

Experiments on sulfide-mineral-containing, synthesized Duluth Complex waste rock (Figure C-5a) and tailings (Figure C-5b) show similar patterns of sulfate release over time as the experiments on pyrrhotite substrate. In both the waste rock and tailings experiments, the enrichment community shows increased sulfate release over the isolate-inoculated experiments, with the difference being more pronounced in the tailings experiment than in the waste rock.

The presence of sulfur-oxidizing isolate microorganisms, and the presence of an enrichment community, increases sulfate release from pyrrhotite oxidation over abiotic controls at a range of neutral to mildly acidic pH. Although pH varied over the course of the experiments, the difference between the abiotic and microbial reactors cannot be explained by differences in pH alone, because the increased acidity of the microbially-inoculated reactors is a result of the microbial oxidation of the reduced sulfur in the pyrrhotite to sulfate, generating sulfuric acid which lowers pH. The abiotic precipitation of iron oxyhydroxides at these pH conditions would also consume OH^-, contributing to pH decrease.

b. *Sulfuriferula* sp. strain AH1 preferentially attaches to pyrrhotite.

To evaluate the affinity of *Sulfuriferula* spp. to sulfide minerals, polished rock surfaces were incubated in media inoculated with *Sulfuriferula* sp. strain AH1. These experiments were conducted on Duluth Complex ore-bearing rock, which contains a mixture of pyrrhotite, chalcopyrite ($CuFeS_2$), pentlandite ($(Fe,Ni)_9S_8$), and cubanite ($CuFe_2S_3$) in a troctolitic (olivine-Ca plagioclase) matrix. DAPI-stained cells on rock chip surfaces show that *Sulfuriferula* sp. strain AH1 preferentially attaches to sulfide mineral surfaces over the silicate matrix (Figure 3-4a-c) and attaches in much greater numbers to

pyrrhotite over other sulfides (Figure 3-4d-f). The close association of *Sulfuriferula* with pyrrhotite mineral surfaces (Figure 3-4) reinforces its importance in pyrrhotite oxidation and may help explain its abundance in the humidity cell experiments if it is uniquely capable of taking advantage of energy from pyrrhotite oxidation. Humidity cells undergo frequent wet-dry cycles, so surface-attached cells would have a competitive advantage over planktonic cells.

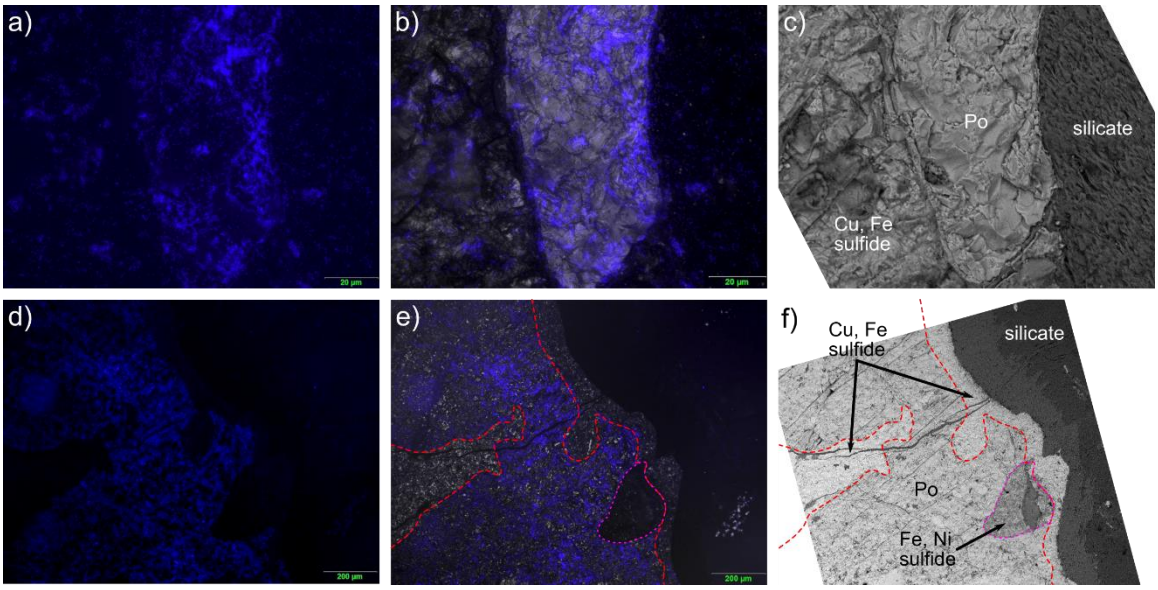

Figure 3-4. Fluorescent microscope images (a, d), merged reflected light and fluorescent images (b, e), and EDS images (c, f) showing the preferential attachment of Sulfuriferula to pyrrhotite grain surfaces.

c. Different strains of *Sulfuriferula* and other sulfur-oxidizing bacteria have different rates of sulfate release.

Metabolically distinct strains of *Sulfuriferula* and a strain of *Thiobacillus* were evaluated to compare sulfate release from pyrrhotite dissolution for each strain at pH 6. The amount of sulfate released during sulfide mineral oxidation in incubations with each strain (Figure 3-5) was compared to (a) autoclaved *Sulfuriferula* sp. strain AH1, PFA-poisoned *Sulfuriferula* sp. strain AH1, and E. coli, or to (b) abiotic reactors and reactors containing an enrichment community. *Sulfuriferula* sp. strain AH1 (Figure 3-5a, blue triangles) displays the highest rate of sulfate release over the other strains of *Sulfuriferula* (str. GW1, pink triangles, str. HF6a, orange triangles) and the *Thiobacillus* strain (str. CT1, yellow squares). All showed greater sulfate release than the reactors containing E. coli (light blue Xs), and PFA-poisoned AH1 (dark green upside-down triangles). In experiment 3, differences among reactors containing isolate strains were less apparent in (Figure 3-5b), although the reactors inoculated with *Sulfuriferula* sp. strain AH1 still had the highest sulfate release. The data in (Figure 3-5b) are from the larger-volume reactors and have less variability in the solution pH (pH decreased to 3 by the end of Experiment 2, while reactors

in Experiment 3 varied in pH from 6.5 – 4.8, Figure C-6a, b). Reactors with strain AH1 accumulated the most elemental sulfur (Figure C-6c) from the larger-volume Experiment 3, with the other isolates and the abiotic reactors all accumulating similar amounts of elemental sulfur. Trends in bulk susceptibility were similar for reactors containing all strains; there is a slight decrease in bulk susceptibility for each of the sets of reactors that generally follows the same pattern as the abiotic reactors and the killed controls (Figure C-7). The exception was the reactor containing *Thiobacillus* sp. strain CT1, which shows a dramatic decrease in bulk susceptibility.

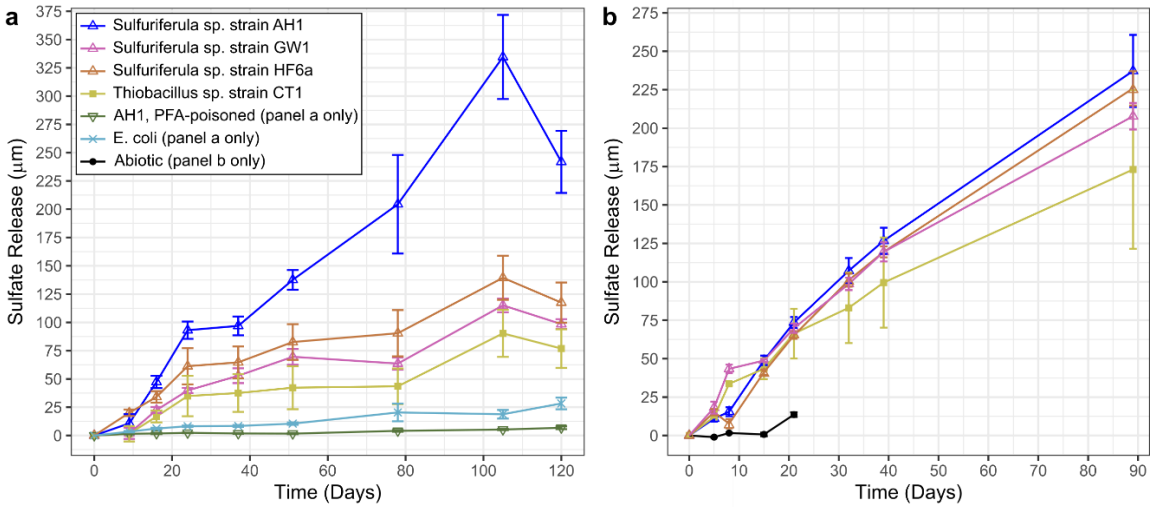

Figure 3-5. (a) Mean sulfate release for multiple strains of Sulfuriferula, a strain of Thiobacillus, E. coli, and a killed control (PFA-killed AH1) from experiment 2. (b) Sulfate release for three strains of Sulfuriferula and a strain of Thiobacillus from experiment 3. In both (a) and (b) the line and point mark the mean for the set of replicate reactors, and the error bars represent the standard deviation between replicate reactors.

Isolate AH1 produces both the most sulfate over time (Figure 3-5) and results in the accumulation of the most elemental sulfur (Figure 3-3, Figure C-6), with the net result of catalyzing the most pyrrhotite oxidation. Other strains of *Sulfuriferula* (GW1, GW19, HF6a) show less sulfate release over time, although the difference between these strains and AH1 is more pronounced in Experiment 2 than Experiment 3. These strains also produce less elemental sulfur over time. This could be due to differences in sulfur oxidation pathway. AH1 possesses genes for an incomplete *sox* pathway, *sqr*, *hdr*, *sir*, and *tth* (Chapter 5, this thesis), while *Thiobacillus* strain CT1, possesses genes for the complete *sox* pathway, *sqr*, *dsr*, *sir*, *tth*, *doxD*, *soeABC*, *aprAB*, and *sat* (Jones et al. *in prep.*). Despite having the most apparently flexible sulfur oxidation pathway, strain CT1 produces the least elemental sulfur of the five isolates used in these experiments, and results in a middling amount of sulfate release. This suggests that additional metabolic capabilities or other genetic qualiies of strain AH1, and *Sulfuriferula* in general, make them more effective sulfur oxidizers in this environment. The genomes of both *Sulfuriferula* strain AH1 and

Thiobacillus strain CT1 contain putative iron oxidation genes (*cyc1* and *cyc2*, cite genome paper and in prep), so their role in neutrophilic iron oxidation in this system will have to be evaluated. One metabolic distinction between strains AH1 and CT1 is that strain AH1 has a complete set of genes for nitrogen fixation (*nifDKH*) while CT1 does not, suggesting that CT1 may become nitrogen-limited over the course of the experiments, which in turn would limit the total amount of pyrrhotite dissolved.

d. Experiments inoculated with enrichment cultures contain Sulfuriferula spp. and other sulfur-oxidizing organisms.

The enrichment communities that developed over the course of experiment 1 are compared to the libraries from the isolate *Sulfuriferula*-inoculated reactors and the abiotic reactors in Figure 3-6. The enrichment communities include *Sulfuriferula* spp., but also include OTUs identified as *Thiomonas* as a dominant member of the community, as well as minor OTUs identified as *Bradyrhizhobium*, *Burkholderia-Caballeronia-Paraburkholderia*, *Caulobacter*, *Chitinophagaceae*, *Mitochondria*, *Mesorhizobium*, *Nitrobacter*, *Pseudoncardia*, *Sinomonas*, and *Terracidiphilus*. *Thiomonas* spp. is the dominant organism in the pH 4.5 experiments, averaging 72.3% of the OTUs identified, while *Sulfuriferula* spp. make up only an average of 17.5% of the community. As pH increases, the relative proportion of *Thiomonas* spp. decreases and the proportion of *Sulfuriferula* spp. increases, with *Sulfuriferula* spp. making up an average of 43.8% of the community in the pH 7.0 libraries and *Thiomonas* spp. making up 17.8%. Similar trends can be seen in the less abundant OTUs. For example *Terracidiphilus* OTU are only present in the pH 4.5 enrichments at >1% abundance, while the OTU classified as *Burkholderia-Caballeronia-Paraburkholderia* only appears in the enrichment reactors with a starting pH of 6.0 or greater, and are more abundant in the pH 7.0 reactors than the pH 6.0 reactors.

By the end of the 121-day incubation, the initially abiotic experiments from pH 6.0 and 7 in Experiment 1 were contaminated with *Sulfuriferula* spp. and minor other OTUs. The libraries created from two of the three pH 5.0 abiotic reactors also showed evidence of contamination once sequenced, although no PCR product was visible from these extractions, indicating that any contamination was at low levels by the end of the incubations. Despite contamination in the abiotic reactors, the reactors inoculated with the isolate *Sulfuriferula* strain are >90% *Sulfuriferula* at the termination of the experiment; the pH 4.5 reactors are 99.7% *Sulfuriferula*, the pH 5.0 reactor is 96.4% *Sulfuriferula*, the pH 6 annealed set of rectors are 96.4% *Sulfuriferula*, the pH 6 unannealed reactors are 95.4% *Sulfuriferula*, and the pH 7 reactors are 93.3% *Sulfuriferula* on average.

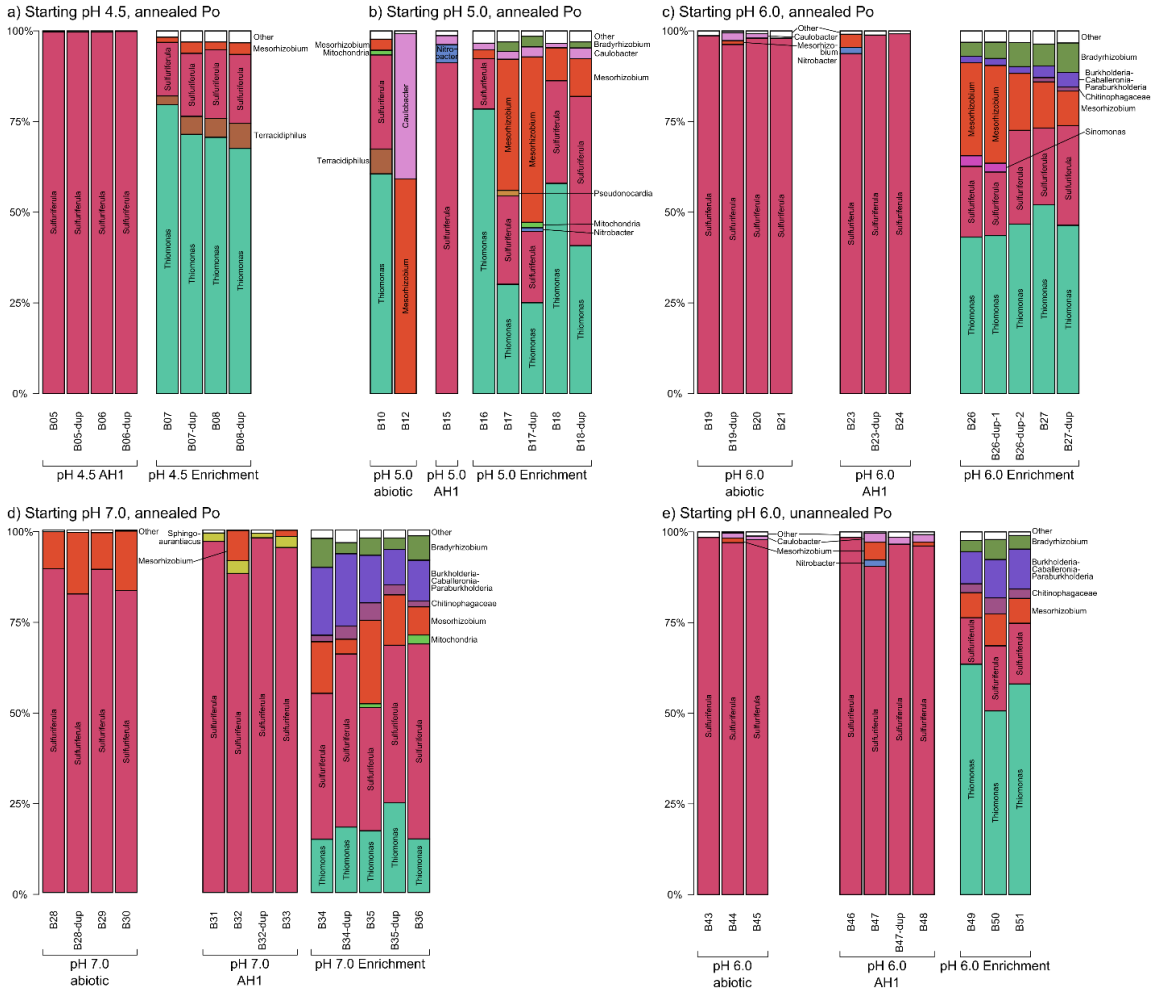

Figure 3-6. Stacked bar charts showing taxonomic assignments of OTUs >1% abundance found in reactors from Experiment 1 at the termination of the experiment. OTUs are labeled and colored by their genus, or by the highest available taxonomic classification for that OTU. Bars labeled "BXX-dup" are replicate PCRs from the same DNA extraction.

Experiments on waste rock and tailings highlight how different substrates affect community composition. The inoculum initially added to the enrichment reactors contained 20% *Sulfuriferula* spp. In the experiments with waste rock as the substrate, which was ~2% sulfide minerals, OTUs identified as *Sulfuriferula* spp. were absent from one replicate, 6.5% of community in the second replicate, and 3.7% of the community in the third replicate, after 8 weeks. Conversely, the percentage of OTUs identified as *Sulfuriferula* spp. increased in the tailings experiments, increasing to between 35% and 41% of the community in the three replicates (Figure C-8). The most abundant OTU in the waste rock, and second-most abundant OTU in the tailings experiments, is identified as members of the family *Leeiaceae* (S. Chen et al., 2021), which made up 8% of the inoculum community. The type strain for this family is *Leeia oryzae*, which is a heterotrophic bacteria capable of nitrate reduction to nitrite (Lim et al., 2007). Taxonomically-similar

OTUs were identified in pyrrhotite incubation experiments of samples collected from naturally-weathered Duluth Complex outcrops (Chapter 4, this thesis).

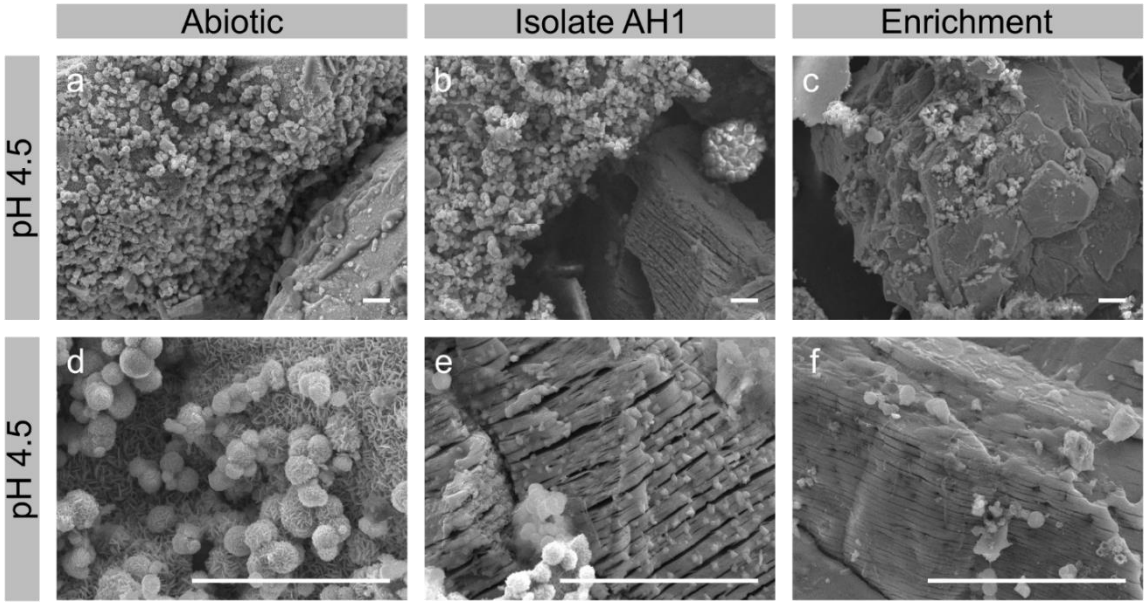

Figure 3-7. Secondary electron images of pyrrhotite grain surfaces collected from pH 4.5 reactors at the termination of Experiment 1. Scale bar in all images is 10μm.

e. The presence of microorganisms affects the pyrrhotite surface and crystallinity of secondary iron oxide minerals.

Pyrrhotite grains and precipitated iron oxides from experiment 1 were examined by SEM imaging, and low-temperature magnetic measurements were used to characterize the pyrrhotite and precipitated iron oxides collected from experiment 3 at day 21. SEM images from experiment 1 are presented in Figure 3-7. There are clear differences between the pyrrhotite grains and iron oxides from the pH 4.5 reactors; pyrrhotite grain surfaces in the abiotic reactors (Figure 3-7 a, d) are coated with a layer of highly crystalline, intersecting iron oxide platelets, while bare pyrrhotite grain surfaces are visible in the isolate (Figure 3-7b, e) and enrichment (Figure 3-7c, f) images. Small, 1-5 μm balls of iron oxide with finer-scale tabular crystals and amorphous blebs of elemental sulfur are adhered to the tabular iron oxide crystals. In the experiments inoculated with *Sulfuriferula* sp. strain AH1, and in the experiments inoculated with the enrichment community, the iron oxides imaged were less crystalline and not as strongly adhered to the pyrrhotite grain surfaces as in the abiotic reactors. Visually, however, the reactor bottles appeared to have similar amounts of iron oxide produced (Figure C-1). The bare pyrrhotite surfaces from the isolate-inoculated reactors have small, equant, tabular crystals adhered to the surface, and the pyrrhotite surface itself shows strong, parallel parting (Figure 3-7e) that is not apparent in the unreacted pyrrhotite (Figure C-9). Grains from the pH 4.5 enrichment experiments are similar to the pyrrhotite from the isolate-inoculated reactors, although the iron oxide

precipitates are less crystalline and the parting of the pyrrhotite grains is less pronounced. These differences in iron oxide mineralogy would account for the different patterns in time-resolved bulk susceptibility seen in these experiments (Figure C-4)

At pH 6, the differences between the pyrrhotite grain surfaces from the isolate and enrichment experiments are not as apparent, but in both cases the bare pyrrhotite surface is visible in the SEM. There is less iron oxide accumulation visible in these reactors, as well (Figure C-1, d-f). The pyrrhotite grain surfaces from both the isolate and the enrichment reactors is pitted (Figure 3-8a, b), which might reflect a crystallographic or structural control on dissolution based on the parallel and angular etch pits visible at high magnification, as well as small, raised, oriented lamellae present in the etch pits (Figure 3-8c, d).

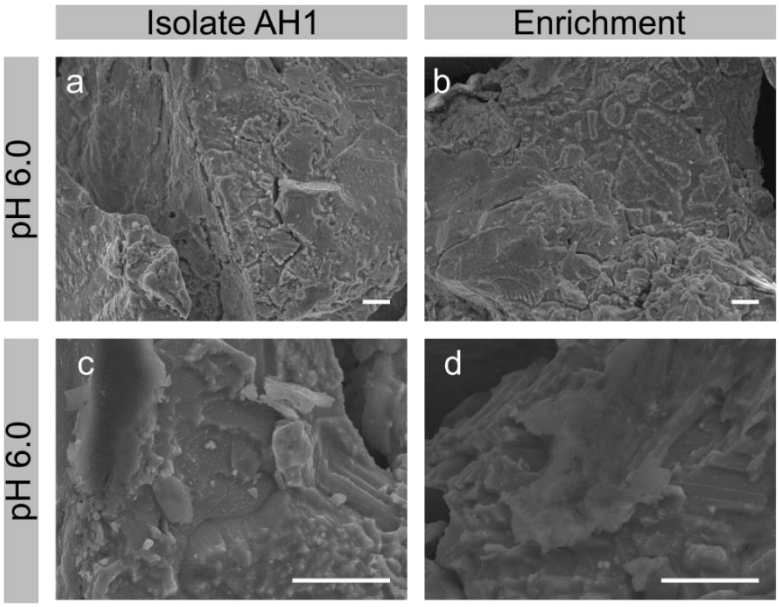

Figure 3-8. Secondary electron images of pyrrhotite grain surfaces collected from pH 6.0 reactors at the termination of experiment 1. Scale bar in all images is 10μm.

Field-cooled and zero-field-cooled low-temperature *sat*uration isothermal remanent magnetization (FC/ZFC LTSIRM) and room-temperature *sat*uration isothermal remanent magnetization (RTSIRM) experiments were performed on solid material from the reactors in Experiment 3. These measurements highlight differences in the magnetic mineralogy between samples and can help identify and quantify magnetic minerals present in the sample. By comparing the low-temperature magnetic properties of unreacted pyrrhotite to the reacted pyrrhotite (plus iron oxides) present in each experiment, information about the identity, crystallinity, and (magnetic) grain size of the reaction products can be determined. The results of the FC-LTSIRM and ZFC-LTSIRM experiments are presented in Figure 3-9a, and the results of the RTSIRM experiments are presented in Figure 3-9b. All of the solid samples in these experiments were collected from

the pH 6.0 Experiment 3 at Day 21. Characteristic low-temperature magnetic transitions – for example the 4C polytype of pyrrhotite shows a distinctive change in magnetization at the 32K Besnus transition.

First, the remanent magnetization of the reacted pyrrhotite (whether abiotic or inoculated with microbes) is in all cases lower than the original pyrrhotite, indicating that some of the remanence-carrying pyrrhotite has been dissolved. Comparing the abiotic reactors (black circles) and the isolate *Sulfuriferula* strain AH1 (blue triangles) to the original, unreacted pyrrhotite (grey line) at the start of the RTSIRM experiment (at 300 K, Figure 3-9b), the remanent magnetization of the solids from the abiotic reactor has decreased by 9%, while the remanent magnetization of the solids from the reactor inoculated with AH1 has decreased by 27%. There is a similar decrease in the magnetization at the start of the field-cooled experiment (at 10 K, Figure 3-9a) when comparing the original, unreacted pyrrhotite to the pyrrhotite from the abiotic and AH1-inoculated reactors, although the difference in magnetization between the two reacted samples is less – the abiotic-reacted pyrrhotite lost 34% of its low-temperature remanence, while the AH1-reacted pyrrhotite lost 39% of its low-temperature remanence. The change in magnetization of the unreacted pyrrhotite is relatively smooth between ~40K and 300K in both the FC-LTSIRM and the RTSIRM and is consistent with pyrrhotite being the dominant magnetic mineral in these experiments. The reacted pyrrhotite from the abiotic reactor shows a similar shape of the FC-LTSIRM curve to the unreacted pyrrhotite, but the overall magnetization is lower. The RTSIRM of the abiotic experiment shows a slow loss of magnetization between 260 K and 100 K, and then a sharp loss of magnetization at the Besnus transition. The AH1-reacted pyrrhotite shows two distinct transitions in both the FC-ZFC and RTSIRM curves, with the sharp Besnus transition and a more broad change in magnetization between 100 K and 200 K. Similarly, the other isolates examined (Figure 3-9c, d) have a different starting magnetization, and loses its magnetization on thermal cycling in different ways, suggesting that the iron mineralogy created in the presence of each isolate is distinct.

The magnitude of the Besnus transition, measured as the loss in magnetization on cooling from 40K to 10K in the RTSIRM (Hobart et al., 2021), can be used to evaluate differences in the amount of 4C pyrrhotite present in the sample. The magnitude of the Besnus transition in the abiotic-reacted pyrrhotite has decreased by 30%, the magnitude of both the AH1 and GW1-reacted pyrrhotite has decreased by 41%, the magnitude of the HF6a-reacted pyrrhotite has decreased by 53%, and the magnitude of the CT1-reacted pyrrhotite has decreased by 58% from the Besnus transition of the unreacted pyrrhotite.

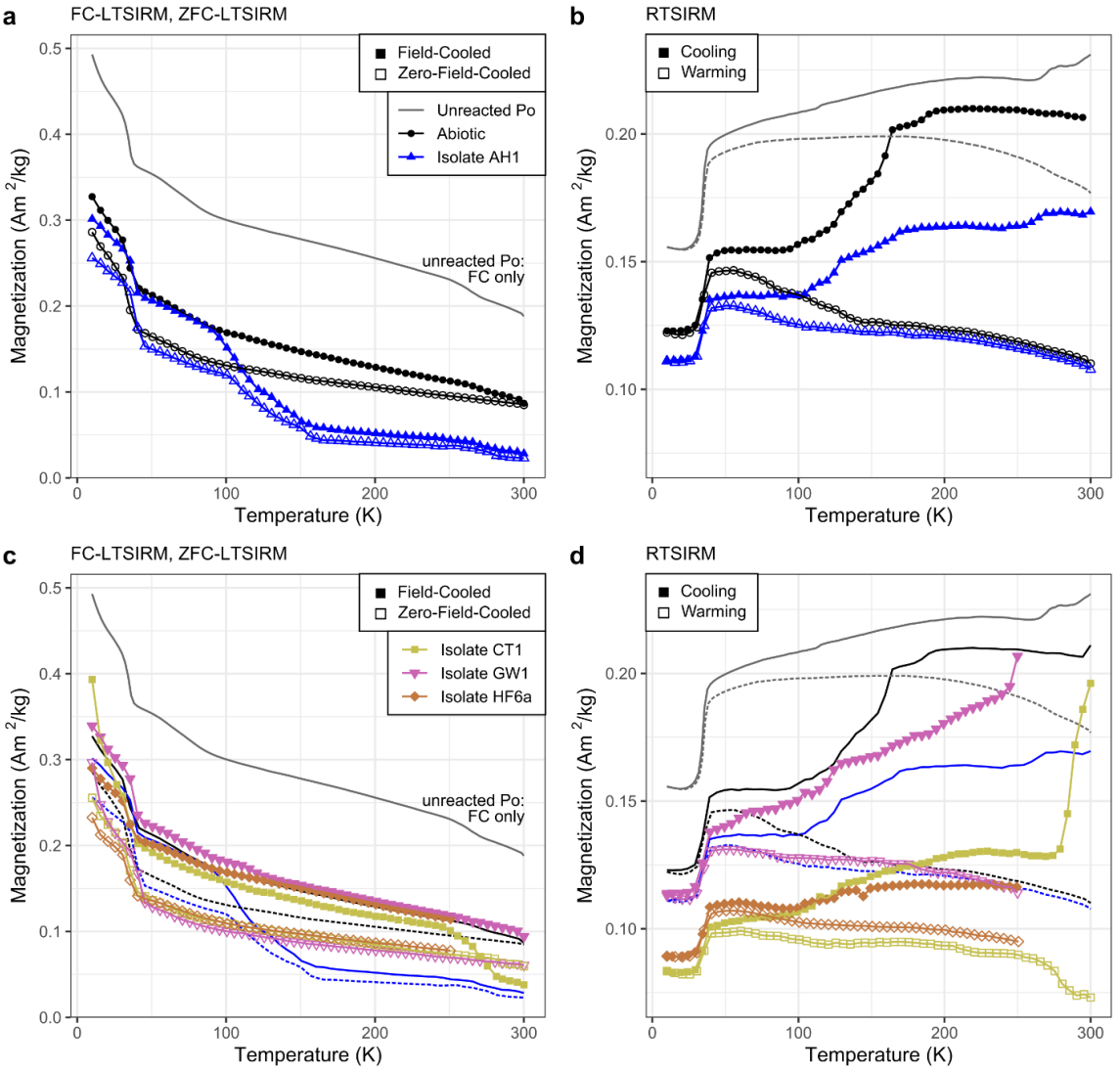

Figure 3-9. (a, c) Field-cooled and zero-field-cooled low-temperature saturation isothermal remanent magnetization and (b, d) room-temperature saturation isothermal remanent magnetization experiments on the solid material from experiment 3 at Day 21, comparing the magnetic properties of the pyrrhotite, plus any magnetic precipitates (e.g., iron oxides) that formed during pyrrhotite oxidation to the low-temperature magnetic properties of the original, unoxidized pyrrhotite.

IV. Implications for microbiological oxidation of pyrrhotite under moderately acidic to circumneutral conditions.

Combining the increased rate of sulfate release in the reactors inoculated with *Sulfuriferula* over abiotic sulfate release (Figure 3-1), the close association of *Sulfuriferula* with pyrrhotite surfaces over other sulfide minerals (Figure 3-4), and the differences in iron oxide precipitate morphology in the inoculated and abiotic reactors (Figure 3-7), allows us to propose a mechanism for the role sulfur-oxidizing bacteria play in increasing pyrrhotite oxidation. When pyrrhotite oxidizes abiotically under near-neutral pH, iron (II) and

inorganic reduced sulfur compounds are released. Under these conditions, the iron (II) is oxidized to iron (III), which has a very low solubility, and so the iron (III) precipitates as an iron oxide or oxyhydroxides. In abiotic reactors, reactive pyrrhotite surfaces become coated with an iron oxide crust that "armors" the pyrrhotite grain from further dissolution. This passivation of reactive pyrrhotite surfaces is described in other abiotic, acidic studies. (Harries et al., 2013) describes an alteration crust of elemental sulfur and iron oxyhydroxides that formed on pyrrhotite surfaces oxidized at pH 2.0 by $FeCl_3$. Similarly, (Chiriță, 2016) describes the formation of an iron-deficient sulfide layer in contact with the pyrrhotite surface, an intermediate layer of elemental sulfur, and an external layer of iron (III) oxyhydroxides such as goethite (α-FeOOH). However, in biotic reactors, sulfur-oxidizing bacteria interrupt the formation and adhesion of this passivation layer. *Sulfuriferula* preferentially adhere to pyrrhotite grains over other sulfides, bringing the surface-attached cells and associated extracellular polymeric substances (EPS) in close proximity to their source of energy. This surface attachment results in increased pyrrhotite dissolution and decreased elemental sulfur formation. Sulfur-oxidizing microorganisms can increase dissolution in two ways – by directly consuming reduced sulfur species from the mineral, preventing or minimizing the accumulation of zero-valent sulfur that forms abiotically, and/or by consuming some of the elemental sulfur that accumulates through abiotic dissolution. The iron oxide precipitates that do form in the inoculated experiments are less crystalline (the crystals are visually smaller and less euhedral, and do not contribute as much to the bulk susceptibility or remanent magnetization) and are not adhered as strongly to the pyrrhotite grain surfaces. This leaves the reactive pyrrhotite surfaces exposed to further (biological or abiotic) oxidation, and results in increased pyrrhotite dissolution in the presence of microorganisms.

Low pH reactors (pH 4.5, 5) inoculated with the enrichment community displayed more sulfate release than the reactors inoculated with the isolate *Sulfuriferula* (Figure 3-1), while at higher pH (pH 6, 7), sulfate release from the enrichment community reactors more closely matches sulfate release from the isolate-inoculated reactors. The enrichment communities were consistently dominated by OTUs identified as *Sulfuriferula* and *Thiomonas*, with minor contributions from other OTUs. One species of *Thiomonas*, *T. cuprina*, has been shown to grow on chalcopyrite ($CuFeS_2$), arsenopyrite (FeAsS), or aqueous H_2S, but not on pyrite, and cannot utilize thiosulfate or tetrathionate (Huber & Stetter, 1990). Another species of *Thiomonas*, *T. delicata*, is also able to oxidize iron (II), and most strains of *Thiomonas* show optimum growth under mixotrophic, mildly acidic conditions (pH 3-6), and show high tolerance for aqueous heavy metals (Kelly et al., 2007). *Thiomonas* OTUs become a larger proportion of the enrichment under lower pH conditions in these experiments; this suggests that this OTU has a lower pH tolerance than *Sulfuriferula*. This is consistent with the environmental distribution of *Thiomonas* OTUs, which were found in the most acidic humidity cell experiments in (Jones, Lapakko, et al., 2017). Further work investigating the genetic capabilities of *Thiomonas* spp. will help

explain the relative distribution of *Sulfuriferula* and *Thiomonas* spp. with pH found in these experiments.

All other OTUs identified in the enrichment communities are primarily related to heterotrophic organisms, some of which are also capable of fixing nitrogen. *Terracidiphilus* OTUs were present only in the pH 4.5 enrichment communities. The type strain for this genus, *T. gabretensis*, was isolated from a montane coniferous forest soil in the Czech Republic, and is a heterotrophic organisms that degrades organic matter, particularly plant-derived biopolymers, grows under mildly acidic conditions (pH 3-6), and is particularly active in forest soils during the winter (García-Fraile et al., 2016). The acidic, coniferous soils in the Czech Republic that *T. gabretensis* was isolated from are similar to the environment present in in Northern Minnesota. In the higher pH enrichments, a large portion of the community is identified as *Mesorhizobium* OTUs. These organisms are typically nitrogen-fixing, heterotrophic bacteria isolated from root nodules of leguminous plants and show optimal growth at near-neutral pH (Kaneko et al., 2000; Martínez-Hidalgo et al., 2015). *Bradyrhizobium* OTUs, which occupy a smaller proportion of the OTUs in the enrichments, have cultured representatives isolated from nitrogen-fixing soybean nodules and fill a similar environmental niche as the *Mesorhizobium* (van Berkum & Fuhrmann, 2000). OTUs identified as the genus *Burkholderia-Caballeronia-Parabulkholderia* are particularly abundant in the highest pH enrichment libraries. Organisms in this genus were originally described under the paraphyletic genus *Burkholderia* (Yabuuchi et al., 1992); the animal and plant pathogens from this group were later separated from the environmental soil and water bacteria into the *Burkholderia* and *Paraburkholderia* (Sawana et al., 2014), with the *Burkholderia* further subdivided into the *Caballeronia* based on the phylogenetic relationships of 21 highly-conserved proteins (Dobritsa & Samadpour, 2016). The environmental members of this larger genus are typically heterotrophic, nitrogen-fixing, soil-associated bacteria, with some species isolated from legume nodules, hydrothermal marine sediments, and weathered rock surfaces (Sawana et al., 2014).

OTUs identified at the family level as *Chitinophagaceae* make up a small proportion (<5%) of the enrichment community. Described species in this family are aerobic or anaerobic heterotrophs, some of which can ferment limited substrates (Kämpfer et al., 2011). *Sinomonas* OTUs are present in >1% abundance in one of the pH 5 enrichments. A similar isolate, *S. soli*, was isolated from a polluted forest soil and is a neutrophilic, aerobic heterotrophic bacteria (Y. Zhou et al., 2012). OTUs identified as members of the ogliotrophic genus *Caulobacter* (Abraham et al., 1999) are most abundant in the pH 5 reactors.

Why are *Sulfuriferula* OTUs less abundant in the enrichment communities, despite their dominance in the isolate-inoculated experiments? *Sulfuriferula* strains typically show optimal growth at neutral or near-neutral pH (pH ~5-7) (Chapter 5, this thesis, and Meyer et al., 2007; Watanabe et al., 2014, 2015, 2016, 2019), and so particularly in the lower pH

reactors, sulfide-mineral-oxidizing *Thiomonas* is closer to its ideal pH growth range. The strains of *Sulfuriferula* used in this study are particularly sensitive to organic acids and are unable to grow exclusively heterotrophically (Chapter 5, this thesis, and Watanabe et al., 2014, 2015, 2016, 2019)), and so especially in the lower pH reactors where these *Sulfuriferula* strains are outside their ideal growth conditions, *Thiomonas* species will have an additional advantage because of their ability to grow mixotrophically. Additionally, heterotrophic organisms play an important role in more acidic ARD environments by acting as "janitors," metabolizing organic acids and other compounds that could be toxic to lithotrophic organisms, and can also generate important metabolites for other organisms (D. Johnson, 2018). In isolation, *Sulfuriferula* strains are able to fix nitrogen, which would be advantageous in the low organic-input humidity cells but not necessarily in the batch reactors, since ammonia is added to the media and the presence of other, heterotrophic nitrogen-fixing organisms like *Mesorhizobium* and *Bradyrhizobium* means that ammonia is more available in the enrichment environment. The interactions between microbial community members ultimately leads to similar or increased rates of pyrrhotite oxidation, particularly in the lower pH experiments, and highlight the importance of studying both isolates and mixed cultures.

Interestingly, similar incubations on pyrrhotite that were inoculated with strain AH1 and algal-containing biomass had no or very little *Sulfuriferula* and were instead dominated by *Thiobacillus* (Chapter 4, this thesis). Likewise, incubations with crushed Duluth Complex waste rock (experiment 5) that were inoculated with strain AH1 and a mixed community had very low proportions of OTUs identified as *Sulfuriferula* by the end of the experiments, while the incubations that contained tailings were dominated by OTUs identified as *Sulfuriferula* spp. (Figure C-8). This suggests that *Sulfuriferula* may not be competitive in organic-rich or sulfide mineral-poor environments, where its' obligate lithoautotrophy and inability to utilize organic carbon (comparative genome paper) puts it at an energetic disadvantage when compared to heterotrophic or mixotrophic organisms like *Thiomonas*, *Leeiaceae* spp., and *Mesorhizobium*.

16S sequencing of the "isolate" and "abiotic" reactors from Experiment 1 reveals consistent contamination, particularly in the higher pH reactors. The isolate-inoculated reactors are consistently >90% *Sulfuriferula*, although the presence of *Mesorhizobium*, *Caulobacter*, and *Sphingoauranticus* OTUs indicate that these are not pure culture reactors. None of these organisms are lithotrophic sulfur-oxidizers (*Sphingoauranticus* are typically motile, polyphosphate-accumulating heterotrophs found in low-organic soils (Kim et al., 2016; Tan et al., 2016)), but their presence could still affect the growth of *Sulfuriferula* strains by metabolizing organic compounds or by producing secondary metabolites.

V. Implications for metal extraction and mine waste management from the Duluth Complex.

We show here that microorganisms accelerate pyrrhotite dissolution over abiotic controls, which has important implications for the management of Duluth Complex mine waste. One compelling possibility is the application of microorganisms like *Sulfuriferula* for ore extraction. Because *Sulfuriferula* spp. show strong spatial affinity for pyrrhotite mineral surfaces and result in higher rates of mineral dissolution than occur abiotically, they could be utilized as part of biomining consortia. Much of the previous research on biomining of sulfide minerals has been focused on the role of iron-oxidizing extreme acidophiles (e.g., (Brierley & Brierley, 2013; Johnson, 2018; Johnson, 2014), and so understanding the interactions between neutrophilic *Sulfuriferula* spp. and a range of sulfide minerals opens up new avenues for biomining at more neutral pH.

These findings also have important ramifications for management and remediation of mine waste from the Duluth Complex. Because *Sulfuriferula* increase the rate of sulfate release from pyrrhotite over that which occurs abiotically, characterizing the microbial communities and environmental conditions that are present in waste rock and tailings piles is essential to more accurately predicting their environmental risk. Pyrrhotite in a tailings pile that is primarily colonized by *Sulfuriferula* spp., for example, especially located in an otherwise nutrient-poor environment, is likely to release more sulfate and acidic effluent than a tailings pile in a more organic-carbon-rich environment. Further, the lack of abundant *Sulfuriferula* in relatively sulfide-poor and organic-carbon-rich experiments (e.g., in the waste rock enrichments presented here or in co-cultures of strain AH1 and algae, (cite env. genome paper)) suggests that the abundance of one of the primary mineral-oxidizing microorganisms in Duluth Complex waste rock could be controlled, and their effects on pyrrhotite oxidation mitigated, by engineering waste rock and tailings environments to be hostile to *Sulfuriferula* spp. growth.

Acknowledgements: The authors would like to acknowledge Dr. Nicholas Seaton for assistance gathering SEM images of pyrrhotite grain surfaces. KKH was supported by a MnDRIVE Environment grant to JMF and DSJ, funding from the University of Minnesota Department of Earth & Environmental Sciences, a Geological Society of America Student Research Grant, and the Mineralogical Society of America Edward H. Krauss Crystallographic Research Award. Part of this work was performed at the Institute for Rock Magnetism (IRM) at the University of Minnesota. The IRM is a US National Multi-user Facility supported through the Instrumentation and Facilities program of the National Science Foundation, Earth Sciences Division, and by funding from the University of Minnesota. We thank Dario Bilardello, Maxwell Brown, and Peat Solheid for help with data acquisition, processing, and troubleshooting in the lab.

Chapter 4: Microbial communities from weathered outcrops of a sulfide-rich ultramafic intrusion, and implications for mine waste management

The Duluth Complex, Northeastern Minnesota, contains sulfide-rich magmatic intrusions that, collectively, represent one of the world's largest known economic deposits of copper, nickel, and platinum group elements (Cu-Ni-PGEs). Previous work showed that microbial communities associated with experimentally-weathered Duluth Complex waste rock and tailings were dominated by uncultivated taxa and other populations not typically associated with mine waste. However, those experiments were designed for kinetic testing and do not necessarily represent the conditions expected for reclaimed mine waste or long-term weathering in the environment. We therefore used 16S rRNA gene methods to characterize the microbial communities present on the surfaces of naturally-weathered and historically disturbed outcrops of Duluth Complex material, as well as a circumneutral seep draining a reclaimed blast pit. Rock surfaces were dominated by diverse uncultured *Ktedonobacteria*, *Acetobacteria*, and *Actinobacteria* while seeps were dominated by diverse *Proteobacteria*, including *Leptothrix* spp. and *Methylovulum* spp. All samples had abundant algae and bacterial phototrophs, including euglenoid algae and cyanobacteria. These communities were distinct from previously-described microbial assemblages from experimentally-weathered Duluth Complex rocks, suggested different energy and nutrient resources in the reclaimed rocks, outcrops, and seeps. Sulfide mineral incubations performed with and without algae showed that photosynthetic microorganisms could have an inhibitory effect on some of the autotrophic populations from the site, resulting in slightly lower sulfate release and differences in the dominant microorganisms. The microbial assemblages from these weathered outcrops show how communities are expected to develop during natural weathering processes, and represent baseline data that could be used to evaluate the effectiveness of future reclamation of tailings and waste rock produced by large scale mining operations.

This work was originally formatted for the journal *Environmental Microbiology* and has been reformatted to fit guidelines for this document. Co-authors Zhaazhaawaanong Greensky and Kimberly Hernandez assisted with field sampling and conducted the bioshrouding incubations described in section II-d. Co-author Daniel Jones prepared the 16s rRNA libraries for analysis.

I. Introduction

Microorganisms are important catalysts for sulfide mineral oxidation and dissolution in natural and engineered settings. Their role in generating acid rock drainage

(ARD) is frequently taken into account when examining the risks of proposed, current, and legacy mining activities (Baker & Banfield, 2003; Edwards et al., 1999; Ňancucheo & Johnson, 2011; Schippers et al., 1996; Schippers & Sand, 1999). Under extremely acidic conditions (pH < 4), iron- and sulfur-oxidizing microorganisms regenerate the oxidant Fe(III) and produce acids that accelerate the oxidation of metal sulfide minerals and intensify the production of acidic and metal-rich waste streams (Nordstrom et al., 2015; Schippers et al., 1996; Schippers & Sand, 1999). Decades of research on the microbiology of acidic, sulfide-mineral-dominated systems and ARD has improved our management of mine waste (Dugan & Apel, 1983; Onysko et al., 1984; Schippers et al., 1998) and led to new strategies for mineral extraction (Brune & Bayer, 2012; D. Johnson, 2018; Rawlings & Johnson, 2007; Rohwerder et al., 2003; Vera et al., 2013).

The Duluth Complex, located in Northern Minnesota, USA, is a layered mafic intrusion that hosts one of the largest undeveloped Cu-Ni-PGE deposits in the world (Miller et al., 2002; Severson et al., 2002; Thériault et al., 2000). The relatively low total sulfide mineral content of these deposits and the buffering capacity of the host silicate minerals means that they are not expected to produce extremely acidic drainage (Lapakko, 1988, 2015; Seal et al., 2015). Field and laboratory weathering experiments on experimentally-generated tailings and waste rock produce moderately acidic leachate (pH 4 to 7), only rarely reaching pH values below pH 4 (Lapakko & Antonson, 2012). Unlike highly acidic systems, the microbial role in sulfide mineral oxidation under mildly acidic to circumneutral conditions is not well understood, and until recently (Napieralski et al., 2022; Percak-Dennett et al., 2017), microorganisms were not thought to significantly accelerate the oxidation of the acid-insoluble sulfide pyrite (FeS_2) above pH 4 (Arkesteyn, 1980; Korehi et al., 2014; Nordstrom, 1982; Schippers, 2004; Schippers & Jørgensen, 2002). The microbial communities found in circumneutral sulfidic mine waste are not as well understood as those found in extremely acidic environments, and are often characterized by the presence of sulfur-oxidizing rather than iron-oxidizing bacteria (L. Chen et al., 2013; Lindsay et al., 2009; Schippers et al., 1996, 1996), and frequently contain uncultivated taxa (L. Chen et al., 2013; Korehi et al., 2014; Mendez et al., 2008). Furthermore, the most abundant primary sulfide mineral in Duluth Complex deposits is pyrrhotite ($Fe_{1-x}S$, where $0 \leq x \leq 0.125$), for which biological oxidation rates have not been established as extensively as for pyrite, especially at high pH.

Recent work showed that long-term laboratory and field-leaching experiments with waste rock and tailings from Duluth Complex materials contained diverse microbial communities that were populated by organisms not typically associated with mine waste (Jones, Lapakko, et al., 2017). These communities included numerous 16S rRNA sequences from groups that are only known from environmental samples. Further, the microbial communities sampled from these experiments were primarily composed of taxa associated with organoheterotrophic or sulfur-oxidizing lifestyles and had a conspicuous

absence of known iron-oxidizing taxa that are typically implicated in sulfide mineral dissolution.

These weathering experiments were performed in a controlled setting that is appropriate for kinetic testing but might not necessarily mimic the conditions encountered in large-scale tailings and waste rock piles or leach pads (Lapakko, 2015; Maest & Nordstrom, 2017). Furthermore, once mine waste is stabilized by planting or reclaimed following mine closure, sulfide mineral-associated microbial communities are subjected to very different redox conditions and nutrient inputs through plant colonization and soil development. Therefore, we characterized microbial communities associated with naturally weathered sulfide-bearing Duluth Complex rocks that are exposed in outcrops in Northern Minnesota, including from a reclaimed former blast pit where rocks were extracted in 1974 and has since been reclaimed. We compare the microbial communities that developed on rock surfaces and in seeps and associated waters in these areas to those described by (Jones, Lapakko, et al., 2017) in field and laboratory weathering experiments. We also observed abundant photosynthetic bacteria and algae at the sites. In light of previous studies that show that organic inputs by algae can limit sulfide mineral oxidation (Bwapwa et al., 2017; Das et al., 2009; Gruzdev et al., 2020; D. B. Johnson, 2014; Rambabu et al., 2020), we compared how algal growth affected sulfide mineral oxidation in laboratory incubations with communities from the site.

II. Results

a. Samples, field observations, and geochemistry.

Weathered rock, sediment, and water samples were collected from four sites in Northern Minnesota. All four sites are located in the South Kawishiwi Intrusion of the Duluth Complex (Severson, 1994). The “INCO Pit” site (samples IB) is a surface outcrop of ore-bearing Duluth Complex material. The International Nickel Company (INCO) removed roughly 10,000 tons of ore-grade material in 1974 as part of an application to mine in this area; the site was reclaimed when the application was withdrawn in 1975. Discharge was then intermittently monitored for water chemistry to evaluate specific risks from this site and understand the weathering of Duluth Complex material more broadly (e.g., Minnesota Environmental Quality Board, 1977). Discharge from the seep immediately below the bulk sample site was sampled and analyzed for specific conductivity, alkalinity, turbidity, color, sulfate concentration, and dissolved cations (Fe, Ca, Mg, K, Na, Ni, Cu, Cd, Pb, Zn, Si) three times in the spring of 1976 and was found to have a pH of 6.8-7.0, with conductivities between 628-711 μS/cm and sulfate concentrations between 250 and 270 mg/L (see Minnesota Environmental Quality Board, 1977, for complete data). Similarly, pH, specific conductivity, alkalinity, and concentration of aqueous metals (Fe, Ni, Cu, Cd, Pb, Zn) was measured in the nearby stream both upstream and downstream of the bulk sample site six times in the spring/summer of 1976. Although pH did not change significantly between the two sample sites (the upstream site

had an average pH of 5.8, while the downstream site had an average pH of 5.7), a statistically significant increase in aqueous copper and nickel concentration was found downstream of the bulk sample site (Minnesota Environmental Quality Board, 1977).

We collected water and sediment from a seep flowing out of the reclaimed material, and water and algal biomass from a stream approximately 10m from the seep. Effluent from the seep was pH 6.42 at the time of sampling. We also collected exposed, weathered rock from the northeast edges of the reclaimed bulk sample site. Samples collected from this area also include naturally-weathered Duluth Complex material approximately a quarter kilometer from the reclaimed test pit, at the "Gravel Pit" (GG) site. Here, glacial till deposits were extracted for gravel as part of road-building operations in the 1940s, exposing the glaciated Duluth Complex surface to weathering. We sampled the exposed, crumbly weathered rock at this site, as well as water and biomass from algae-filled drill holes in exposed (but consolidated) weathered rock. Samples are summarized in Table 1, and concentration of dissolved anions from the three aqueous samples collected at this site are reported in the supplementary information as Table D-1.

We also collected samples of weathered Duluth Complex material from the surfaces of two additional roadside outcrops: the "Hammer Breaker" outcrop of the Duluth Complex along Forest Rte. 429 (HB samples), and from an outcrop of Duluth Complex material off St. Louis Co. Road 623 (DO samples), which was exposed when the road was re-routed to allow for the expansion of the Cliffs Natural Resources Northshore mine. Samples from this site are listed in Table 4-1. See Figure 4-1 for field images of sampling sites, and Figure D- and Figure D-2 in the supplementary information for spatial relationship between sampling sites, geographic locations, and additional field images.

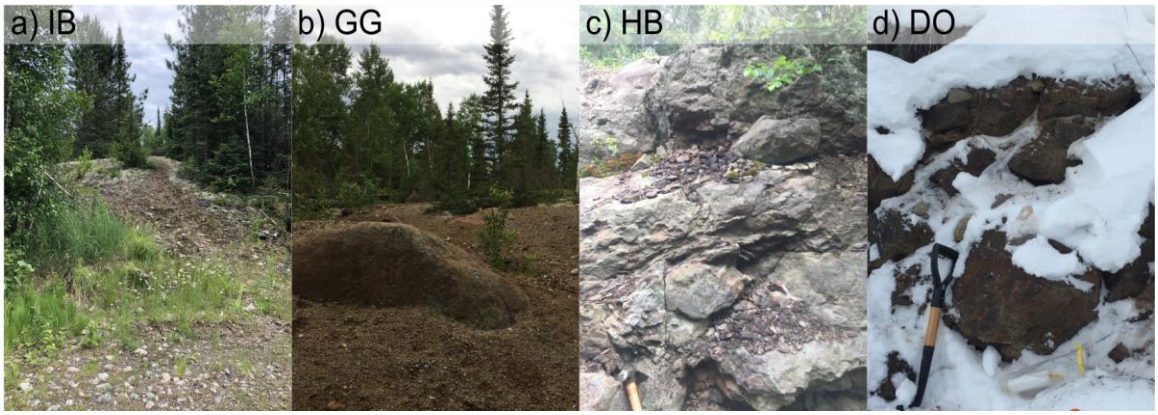

Figure 4-1. Field images for the (a) IB, (b) GG, (c) HB, and (d) DO sampling sites.

Table 4-1. Samples collected for this study.

Name	**Site**	**Description**
IB-2	INCO Pit	Sediment from a pH 6.42 seep
IB-4	INCO Pit	Algal biomass from stream below reclaimed test pit area

IB-5	INCO Pit	Weathered, poorly-consolidated Duluth Complex rock and soil
IB-6	INCO Pit	Weathered, poorly-consolidated Duluth Complex rock and soil
GG-1	Gravel Pit	Weathered, poorly-consolidated Duluth Complex rock
GG-2	Gravel Pit	Water and algal biomass from inside a drill hole in weathered (but consolidated) Duluth Complex rock
HB-1	Hammer Breaker	Weathered Duluth Complex rock and sediment
HB-2	Hammer Breaker	Weathered Duluth Complex rock and sediment
DO-1	Duluth Outcrop	Weathered Duluth Complex rock and sediment
DO-2	Duluth Outcrop	Weathered Duluth Complex rock and sediment
DO-3	Duluth Outcrop	Weathered Duluth Complex rock and sediment
DO-4	Duluth Outcrop	Weathered Duluth Complex rock and sediment

b. 16S rRNA gene libraries from field samples.

We generated 20 rRNA gene amplicon libraries from 12 samples of weathered, sulfide-bearing Duluth Complex material collected from four sites (Table 4-1). The libraries had between 18,504 and 158,184 sequences per sample, with an average library size of 52,703 sequences (standard deviation 37,929). Replicate libraries produced with 25 and 30 PCR cycles for the first amplification step were similar (Figure D-3), so we only report results from the 25-cycle libraries.

Several operational taxonomic units (OTUs) were abundant across libraries, with chloroplasts representing many of the most abundant OTUs. To evaluate how the presence of algae and other eukaryotes affected sample clustering and to more closely investigate the non-photosynthetic microbial community, hierarchical agglomerative cluster analysis was performed with and without OTUs identified as chloroplasts, mitochondria, Eukaryotes, and an abundant Gammaproteobacteria that represents a protist symbiont (OTU 2, discussed below) (Figure 4-2, Figure D-4).

Without chloroplasts and other eukaryote-affiliated OTUs (Figure 4-2), all weathered rock samples clustered together. The seep sediment and green seep mat samples from the INCO reclaimed pit site (IB-2 and IB-4) cluster separately from the weathered rock libraries (Figure 4-2). Similarly, GG2, the library generated from the algal biomass collected from the drill hole at the glaciated DC outcrop (Figure 4-1b), clusters separately from other libraries, and is more similar to the seep sediment and green seep mat libraries than the weathered rock libraries. The seep sediment and algal biomass samples from both the IB and GG sites contain unique non-chloroplast OTUs in addition to small numbers of the OTUs that are most abundant in the weathered rock samples. When chloroplasts, mitochondria, and Eukaryotes are included (Figure D-4), the weathered rock samples continue to cluster separately from the seep sediment and algal mat samples, indicating that

these samples are separated by distinct groups of both photosynthetic and non-photosynthetic taxa.

IB-2 and IB-4 share two abundant OTUs (OTU 95, chloroplast, and OTU 102, *Leptothrix* spp.) that separate these samples from the weathered rock samples taken from the same site (IB-5 and IB-6, Figure 4-2). Similarly, GG-2, the library generated from the algal biomass collected from the drill hole at glaciated DC outcrop (Figure 4-1b), clusters separately from weathered rock collected at the same site (GG-1). GG-2 is dominated by an OTU (OTU 5) that is most closely related (99.2% similarity) to a chloroplast from *Euglena granulata* (strain UTEX 2345, Kosmala *et al.*, 2009), and an OTU (OTU 2) initially classified only as a Gammaproteobacterium. By placing OTU 2 into an ARB (Ludwig et al., 2004) database (SILVA version 138.1, (Quast et al., 2013) showed that this OTU is a member of an "*incertae sedis*" group in the *Gammaproteobacteria* and clusters in a sister clade to *candidatus* Ovatusbacter (Dirren & Posch, 2016). A similar environmental sequence, as determined by a BLASTN search of the NCBI database ("Database resources of the National Center for Biotechnology Information," 2016), is associated with the euglenoid algae *Trachelomonas scabra*. This suggests OTU 2 is a proteobacterial symbiont of the euglenoid algae in the green mat. Similar gammaproteobacterial symbionts of *Trachelomonas scabra* have been associated with euglenid biofilms in ARD environments (Jones et al., 2015). Because the abundance of OTU 2 matches the abundance of the euglenoid algae in this sample (OTU 5), and given its likely role as a symbiont of that algae, we have grouped OTU 2 with the chloroplast, mitochondria, and Eukaryote OTUs.

All other IB, GG, and HB libraries were generated from weathered rock samples, and cluster together (Figure 4-2, Figure D-5). In addition to the most abundant chloroplast OTUs in this cluster (OTUs 3, 9, and 52), these samples contained abundant uncultured representatives of the family *Ktedonobacteraceae* (OTUs 6, 38, 49, 88, and 105), genus *Acidiphilum* (OTU 44), and uncultured representatives of the *Solirubrobacteraceae*, (OTU 178), *Beijerinckiaceae* (OTU 60), and *Verrucomicrobia* ("*candidatus Udaeobacter*", OTU 57) (Fig. 2).

The libraries generated from weathered rock samples DO-3 and DO-4 cluster separately from the IB, GG, and HB samples (Figure 4-2). These libraries contain abundant OTUs that are only minor components of the IB and HB libraries (<1%). Two of the most abundant OTUs in this group (OTU 13 and 70) are most closely related to mitochondrial rRNA genes of the ascomycetous fungi *Leotiomycetes* (92% similar to *Leotiomycetes* sp. A910, Muggia *et al.*, 2016) and *Chaetothyriales* (86% similar to *Chaethothyriales* sp. KhNk32 str. CBS 129052, Vasse *et al.*, 2017). Other abundant OTUs in these samples are classified as uncultured Acetobacteraceae (OTUs 26, 63, and 6325), Acidobacteria (*Bryocella*, OTU 104, and *Granulicella*, OTU 156), Actinobacteria (*Jartrophihabitans*, OTU 174, *Amnibacterium*, OTU 71, and *Curtobacterium*, OTU 7059), *Endobacter* (OTU 83), and *Sulfuriferula* (OTU 111). DO-1 and DO-2 cluster more closely with the IB and

HB weathered rock samples than DO-3 and DO-4 (Figure 4-2), and share a mixture of the OTUs abundant in both clusters.

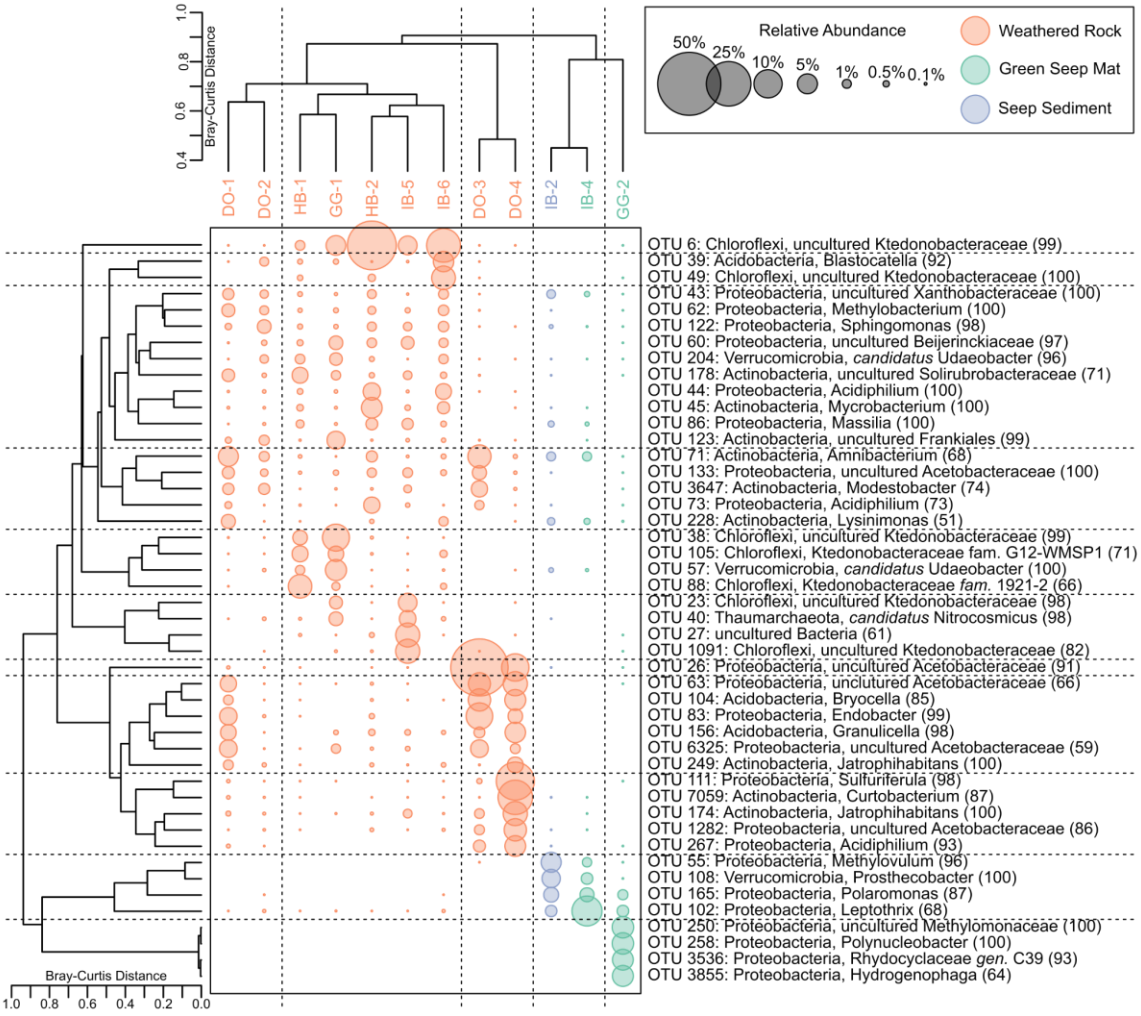

Figure 4-2. Hierarchical agglomerative cluster analysis of libraries collected for this study, with OTUs identified as chloroplasts, mitochondria, and eukaryotes removed. Sizes of the points scales with the relative abundance of the OTUs. The Q-mode cluster analysis was calculated with all OTUs, while the R-mode cluster analysis only included OTUs abundant in at least one sample at 5% or greater abundance. The taxonomic affiliation of each OTU includes its phylum- and genus-level classification, with confidence scores provided in parentheses. OTUs that are unclassified at the genus level are identified with the highest available taxonomic classification. An equivalent analysis including all OTUs is presented in Figure S4.

c. Comparison to laboratory and field leaching experiments.

We compared the microbial communities sampled here to similar rRNA gene libraries from weathering experiments described by Jones et al. (2017). These authors examined the microbial communities present in Duluth Complex waste rock and tailings

from long-running laboratory and field leaching experiments (Lapakko, 2015; Lapakko & Antonson, 1994): amplicon libraries were generated from samples of laboratory humidity cell experiments ("Lab" samples) and a field weathering pile of simulated waste rock from pyrrhotite-containing Duluth Complex ("Field DC") and pyrite-containing Ely Greenstone ("Field GS") sources. For this comparison, we refer to the libraries from naturally weathered rock, seep sediment, and algal biomass for the present study as "outcrop" libraries to clearly separate them from libraries from the laboratory and field leaching experiments from the earlier work (Jones, Lapakko, et al., 2017).

In non-metric multidimensional scaling (NMS) analyses, libraries from outcrop samples (this study) separate from laboratory and field experiments (Jones, Lapakko, et al., 2017) along the first ordination axis (Figure 3). Outcrop libraries are more similar to those from field experiments, with libraries from laboratory experiments plotting to the extreme of the first axis (Figure 4-3a). Some outcrop libraries overlapped with libraries from weathered Ely Greenstone. When laboratory experiments were excluded (Figure 4-3b), libraries from the Duluth Complex field leaching experiment still separate from the outcrop samples along the first ordination axis, but outcrop libraries also separate along both ordination axes, with libraries from the green seep mat (teal dotted circle) and seep sediment (blue solid circle) overlapping with the libraries generated from the Ely Greenstone field weathering experiments (purple open circles). Like in the hierarchical agglomerative cluster analysis (Figure 4-2), libraries from samples DO-3 and DO-4 (points enclosed by the black dashed line) cluster separately from the other outcrop samples as well as the laboratory and field experiments. Removal of OTUs classified as chloroplasts, as well as all chloroplast, mitochondria, and other eukaryote OTUs did not affect the overall structure of this NMS analysis (Figure D-5).

Many OTUs co-occur in both the field weathering experiments and naturally-weathered outcrop samples. However, their abundances differ substantially. The OTUs that make up the most abundant communities in the naturally-weathered outcrop samples are present only at low abundances in the field weathering experiments. Accordingly, the OTUs that are most abundant in the field weathering experiments are present only at low abundances in the outcrop samples (Figure D-6).

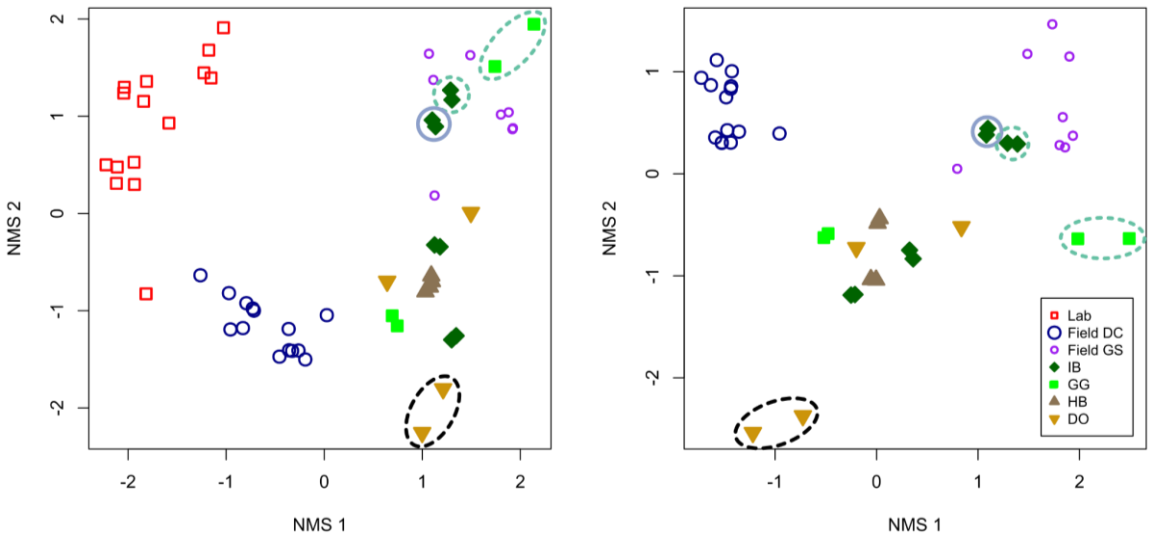

Figure 4-3. (a) NMS ordinations of rRNA amplicon libraries from naturally-weathered Duluth Complex outcrops (libraries IB, GG, HB, and DO, this study), laboratory humidity cells and reactors, and experimental field rock piles, with OTUs identified as chloroplasts, mitochondria, and eukaryotes removed. Libraries from laboratory experiments ("lab," red open squares), and experimental field rock piles ("Field DC," Duluth Complex material, dark blue larger circles, and "Field GS," Ely Greenstone material, purple smaller circles) are from (Jones, Lapakko, et al., 2017). (b) NMS ordinations of rRNA amplicon libraries from the experimental field rock piles and naturally weathered outcrops only. Stress for (a) is 7.5, stress for (b) is 5.8. Sky blue solid circled points indicate seep sediment samples, teal green dotted circled points indicate water and algal biomass samples. All other IB, GG, HB, and DO samples were collected from weathered rock. The black dashed circle indicates DO samples that are separated from the other weathered rock samples in the hierarchical agglomerative cluster analysis (Figure 4-2).

d. Laboratory incubations.

Laboratory incubations were used to evaluate the effect of algae on sulfide mineral weathering. Crushed pyrrhotite (sample Po2, Hobart *et al.*, 2021) was incubated for 19 days with either an isolate or a mixed microbial community, with and without an algal inoculum. The isolate used in these experiments is *Sulfuriferula* sp. strain AH1 (Jones, Roepke, et al., 2017), an autotrophic sulfur-oxidizing proteobacterium isolated from humidity cell experiments described in (Jones, Lapakko, et al., 2017). The enrichment was a microbial community from weathered Duluth Complex rock samples IB-5 and GG-1, and mixed with a microbial community from lab and field experiments HF15-6, DT, and DCW15 (Jones, Lapakko, et al., 2017). The algae inoculum was a mixture of material from samples IB-4, GG-2, and algae from a sulfate-reducing bioreactor (Anderson, 2018). The following treatments were performed, each in triplicate: (1) isolate only, (2) environmental inoculum only, (3) isolate plus algae, (4) environmental inoculum plus algae, and (5) algae alone. Samples with algae were incubated in the light on a diel cycle, and samples without were covered. At the termination of the experiment, 16S rRNA gene amplicon libraries

were generated from the solids in order to evaluate which organisms were enriched, and how the presence of algae affected the community composition.

The enrichment experiments were dominated by OTUs classified in the *Leeiaciae* family, with smaller amounts of *Sulfuriferula* spp. and *Thiomonas* spp., as well as OTUs classified as *Oxalicibacterium* spp. (Figure 4-4a). At the end of the experiment, all experiments inoculated with the algal biomass were dominated by OTUs classified as *Thiobacillus* (68-90%; Figure 4-4a), regardless of whether they started with the isolate, enrichment, or algal inoculum alone. OTUs identified as *Nitrospira*, *Nitrosomonas*, and *Sediminibacterium* were also abundant in these experiments. The algae inoculum was not a pure culture of algae strains but also included lithotrophic organisms, of which *Thiobacillus* was initially a minor component (0.04%) and was evidently enriched in the incubations (Figure 4-4a).

Sulfate release was observed in all experiments, with slightly more sulfate release in the experiments without algae. By the end of the experiment, 18% less sulfate was released from environmental enrichments with algae than without, and 33% less sulfate was released from incubations with isolate AH1 with algae than without. In each incubation, pH dropped slightly over the course of the experiment, with those inoculated with algae measuring approximately 0.3 pH units lower than the incubations without algae at the termination. Only small concentrations of aqueous iron (II) were measured over the course of the experiment (Figure D-7), with the AH1 + algae incubation showing the most variability in measured Fe^{2+} concentration.

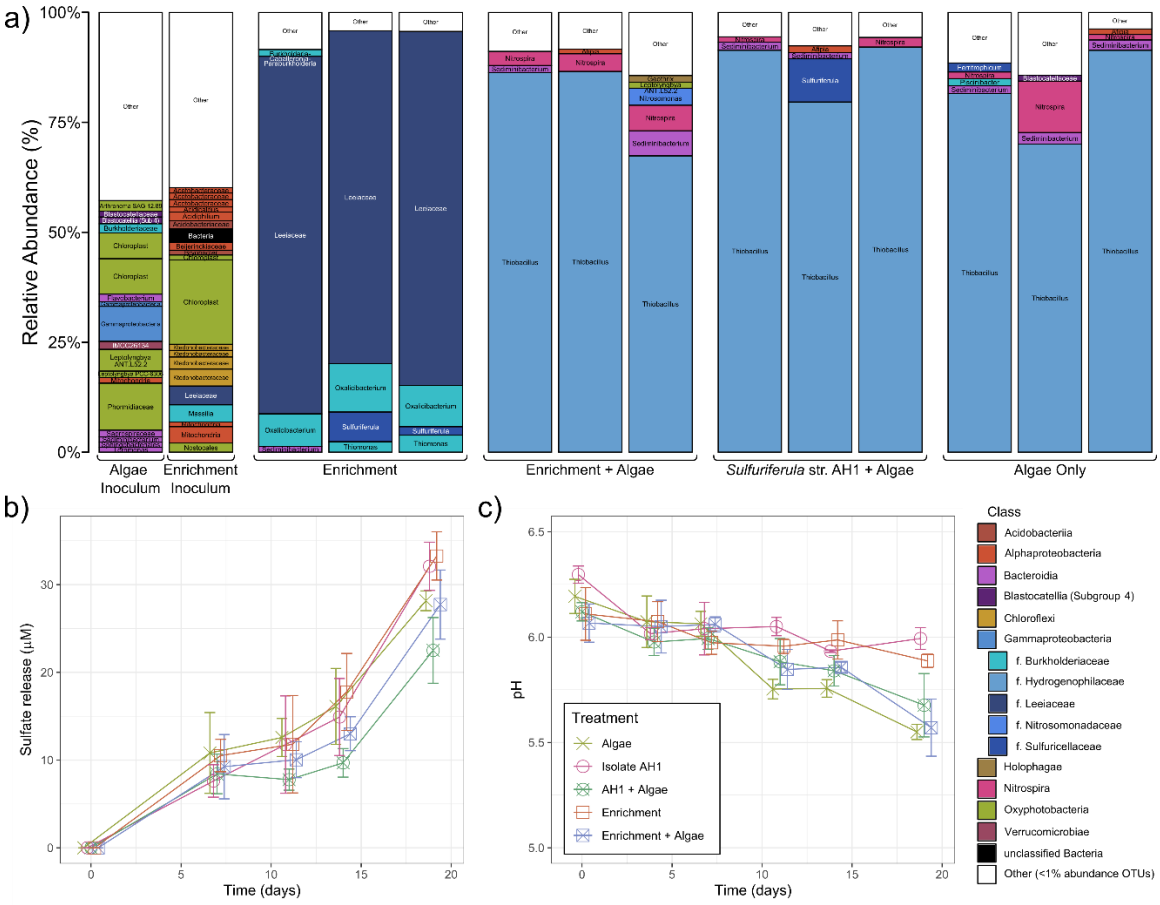

Figure 4-4. (a) Stacked bar chart showing taxonomic assignments of OTUs >1% relative abundance for the incubation experiments. "Other" represents those OTUs <1% abundance in each sample. Bars are colored by OTU taxonomic identification at the class level, with the exception of the Gammaproteobacteria, *which are colored at the family level in varying shades of blue. Each bar is labeled with the OTU taxonomic classification at the genus level, or, at the highest available taxonomic classification. (b) Average sulfate release and (c) pH over the 19-day lifetime of the incubation experiments. Error bars represent standard deviations in sulfate concentrations or pH measured for the three treatment replicates. The x-axis position was shifted slightly in these plots to allow visualization of overlapping points.*

III. Discussion

a. Weathered rock-associated microbial communities.

The microbial communities present on naturally-weathered outcrops of Duluth Complex material contain a diverse population of photosynthesizers, organotrophs, and lithotrophs. The libraries from naturally-weathered Duluth Complex material, even those collected from samples of seemingly bare weathered rock, contain substantial photosynthetic populations, with 6 OTUs representing chloroplasts present in the top 30 most abundant OTUs. The DO samples, which were collected in early January, contain

fewer OTUs classified as chloroplasts compared to the IB and HB samples that were collected in late June.

The seep sediment and green algal mats contained distinct OTUs from the weathered rock samples from the same site. These libraries contain OTUs classified as the microaerophilic iron oxidizers *Leptothrix* and *Gallionella*, indicating that iron oxidation is a possible source of metabolic energy in the circumneutral seep environment. This is consistent with the reddish color of the seep sediment, which is distinct from the surrounding sediment and indicative of the presence of iron oxides.

The microbial community from water-filled drill holes in consolidated DC rock at the gravel extraction site (sample GG-2) were distinct from the other samples, dominated by OTUs representing euglenoid algal chloroplasts and associated symbiotic organisms. Euglenoid algae can be tolerant of high aqueous concentrations of metals and low pH, and are frequently found in AMD and other contaminated water systems (Brake et al., 2001; Casiot et al., 2004; Das et al., 2009; Freitas et al., 2011; Jones et al., 2015; Valente & Gomes, 2007). Their dominance in this sample, and their absence in other samples, is consistent with higher metal content of waters that are in direct contact with the sulfide-rich rocks at site GG as compared to the more diverse photosynthetic communities found in the other samples.

The microbial communities from the naturally-weathered outcrops and associated seeps are distinct from the communities that developed in laboratory and field weathering experiments described in earlier work (Jones, Lapakko, et al., 2017). The outcrop samples were most similar to experimentally-weathered Ely Greenstone (Figure 4-3). The most abundant sulfide in the Ely Greenstone is pyrite, while the sulfide mineral assemblage in the Duluth Complex is dominated by pyrrhotite and other acid soluble sulfides. However, the experimentally-weathered Duluth Complex field experiment had an average leachate pH of 4.7, while the pH of the Ely Greenstone field rock pile ranged from 7.2-7.3 (Jones, Lapakko, et al., 2017), closer to the pH 6.42 water measured in the effluent from the seep at the INCO site. This suggests that pH rather than the specific sulfide mineral assemblage is probably more important for determining microbial community composition in this setting. Further, we suspect that the distance between humidity cell experiments and the field piles and outcrop samples in multivariate statistical analyses ("Lab" in Figure 4-3) is due to differences in organic material input and the corresponding effect on nitrogen and carbon cycling. The "Lab" humidity cell experiments were performed (by design) in an indoor environment with no or little low organic input, while both the field experiments and the naturally-weathered outcrops were from outdoor environments that would have a much higher level of organic input. The humidity cell experiments are designed to evaluate acid generation potential and mimic the weathering that would occur in the well-drained surface of a waste rock or tailings pile (Lapakko, 1988, 2015; Lapakko & Antonson, 2012), rather than weathering of reclaimed mine waste or weathering in a natural forested setting.

Members of the class *Ktedonobacter* are abundant in both the experimental weathering field experiments (Field DC and Field GS) and in the naturally-weathered outcrop samples. Three OTUs (23, 38, and 1091) are abundant in both the field and outcrop libraries (Figure S4). Numerous other *Ktedonobacter* OTUs are present in either the naturally-weathered outcrop samples or the experimental weathering field experiments, but these three OTUs are similar across all samples. OTU 1091 is most closely related (99.2% similarity) to an uncultured bacterium identified as part of a population of organisms that are early colonizers of volcanic rock deposits in Hawaii (Gomez-Alvarez et al., 2007), OTU 23 is most closely related (97.2% similarity) to a bacteria from an Antarctic soil (NCBI accession FR749799), and OTU 38 is most closely related (97.6% similarity) to an organism whose 16S rRNA gene was found in a chromium(IV) contaminated soil in China (NCBI accession KT016028). Ktedonobacteria appear to be ubiquitous in terrestrial environments, especially in organic-poor environments and during the early stages of soil formation (Delmont et al., 2015). The type strain for the genus *Ktedonobacter*, *Kt. racemifer* (SOSP1-21T), is an aerobic, filamentous, Gram-positive heterotroph isolated from the soil of a black locust wood in northern Italy (Chang et al., 2011). Organisms classified as *Ktedonobacter* have been identified in metagenome-assembled genomes in northern California grasslands (Butterfield et al., 2016), in Antarctic desert soils (Mezzasoma et al., 2022; Ortiz et al., 2021), and in hydrothermal sediments at an active deep-sea black smoker in the South Atlantic Ocean (Zhou et al., 2020). Related organisms in the same class have been isolated from a soil-like granular mass (Tengu-no-mugimeshi) collected from an alpine area in Gunma Prefecture, Japan (Wang et al., 2019), an ant nest collected in Honduras, soil from a pine wood in Spain, and soil "collected under a bush" in Corsica, France (Cavaletti et al., 2006). (Yabe et al., 2021) describes the metabolic capabilities of seven *Ktedonobacter* isolates, all of which are mesophiles, heterotrophic, and form aerial mycelia, with an optimal growth pH of 5-7. Other members of this class, genus *Thermogemmatispora*, have been isolated from geothermally heated environments, and can oxidize carbon monoxide in addition to a diversity of carbon sources (King & King, 2014; Yabe et al., 2011). In the weathered rock environment sampled here, the Ktedonobacteria OTUs likely occupy a similar niche as part of the heterotrophic microbial community that forms early in the process of soil formation.

There were two OTUs identified as *Sulfuriferula* sp., a sulfur-oxidizing proteobacterium in the family Sulfuricellaceae that was abundant in weathered Duluth Complex rock from humidity cells and field experiments (Jones, Lapakko, et al., 2017). A *Sulfuriferula* strain isolated from the humidity cell experiments is an obligate autotroph that oxidizes inorganic sulfur compounds (Jones, Roepke, et al., 2017). The *Sulfuriferula* OTU that is most abundant in libraries from the field experiments ("Field DC", Figure D-6) (OTU 8) makes up only a small fraction (less than 0.1%) of the OTUs found in the naturally-weathered "outcrop" libraries, while the *Sulfuriferula* OTU that is most abundant in libraries from the naturally-weathered outcrops (OTU 111) is only a minor component

of the Field DC libraries (<1%) (Figure D-6). The genus *Sulfuriferula* contains multiple species that have different growth requirements, including both obligate autotrophs and mixotrophs, some of which can grow both aerobically and anaerobically (Jones, Roepke, et al., 2017; Kojima et al., 2020; Watanabe et al., 2015, 2016b). Because of the diversity of metabolic capabilities in this genus, it would not be surprising if certain *Sulfuriferula* spp. have an advantage in the natural weathering environment, while different *Sulfuriferula* spp. have with an advantage in the lower organic input humidity cell experiments.

b. Impact of algae on microbial communities and sulfide weathering.

Photosynthetic organisms such as algae have been explored as a tool for mitigating microbial breakdown of reactive sulfide minerals in a process broadly known as "bioshrouding" (Bwapwa et al., 2017; Johnson, 2014; Johnson et al., 2008; Rawlings & Johnson, 2007). Sulfide mineral oxidation by iron and sulfur-oxidizing bacteria can be mitigated by growing algae on the surface of reactive sulfide-rich tailings, which excrete organic compounds that are toxic to acidophilic autotrophs and also form an organic surface layer that limits oxygen penetration (Johnson et al., 2008; Johnson, 2014). Furthermore, the addition of algae and other photosynthetic organisms can have additional benefits for mitigating the impacts of acidic rock drainage: algae can accumulate and adsorb heavy metals, increase the alkalinity of the system, and can produce organic acids such as lactic and acetic acid that mitigate the growth of acid-tolerant lithotrophs while providing food for heterotrophs (Peppas et al., 2000; Rambabu et al., 2020). However, these bioshrouding experiments have been performed on highly acidic materials, where mineral-oxidizing autotrophs are especially sensitive to the presence of organic acids that act as decouplers (Baker-Austin & Dopson, 2007). Here, we saw that incubation experiments with pyrrhotite at circumneutral pH did have less sulfate release (and presumably less sulfide mineral dissolution) when a diverse algal culture was added to the experiments. However, the effects were relatively minor, as substantial sulfate release still occurred in the unamended incubations.

One of the major effects of algal growth on the lithotrophic microbial community was the absence of *Sulfuriferula* OTUs and the dominance of *Thiobacillus* OTUs in the algae-amended incubations. The initial enrichment inoculum, a mixture of field samples from this study and laboratory enrichments from the (Jones, Lapakko, et al., 2017) samples, lacked OTUs identified as *Thiobacillus*, while the algae inoculum was 0.04% *Thiobacillus*. Conditions in the algae-amended incubations are evidently more favorable to *Thiobacillus*, perhaps because *Sulfuriferula* is especially sensitive to organic compounds. Although the differences between sulfate release in each incubation were small, there was less sulfate released in the incubation inoculated with the *Sulfuriferula* strain AH1 and algae than in the experiment inoculated with *Sulfuriferula* alone, suggesting that the presence of algae and the algae-associated lithotrophs was able to outcompete the *Sulfuriferula* strain and result in less sulfide mineral dissolution. Future work will explore whether algal growth

can be applied to limit sulfide mineral oxidation in mildly acidic or circumneutral waste like that anticipated from mining activities in the Duluth Complex.

c. Implications for weathering of Duluth Complex and other mixed sulfide ores.

This study shows that the microbial communities that develop on naturally weathered Duluth Complex surfaces and in reclaimed mine waste are distinct from "active" mine waste communities (Figure 4-3). Microbial communities are sensitive indicators of environmental conditions, and so evaluating microbial community composition can be used to compare how preexisting microbial communities change with varying levels of human disturbance. In this case, the natural microbial communities that are present before mining occurs (i.e., on naturally-weathered outcrops) could be used as a baseline to evaluate the successful reclamation of mine sites by the "return" of these communities or similar community structures. In this study, the clear distinction between the experimental and outcrop microbial communities highlights the difference between the natural microbial communities and those that thrive in a disturbed environment. Conversely, the similarities between the microbial communities at the IB, GG, HB, and DO sites (Figure 4-3a) suggests that environmental conditions at the disturbed IB and GG sites have converged with the more natural conditions at the HB and DO sites, and may be one indication of the effectiveness of the reclamation process at IB. However, more extensive sampling would be needed to fully characterize the existing microbial communities associated with the diverse ecosystems that have developed on natural and disturbed Duluth Complex material.

IV. Materials and Methods

a. Field Samples.

Field sampling was performed on 6 January 2016 (DO samples) and 28 June 2018 (IB, GG, and HB samples). Weathered rock and sediment samples were collected using sterile spatulas into sterile Whirl-Pac sample bags and sterile 50mL centrifuge tubes. For all sites, samples for DNA extraction were immediately frozen on dry ice after collection, and subsequently stored at -80℃ until analysis. Samples for cell counts and imaging were preserved in 3% paraformaldehyde (PFA) in 1x phosphate-buffered saline (PBS), incubated for 24 hours, and PFA was then removed by gently washing once with 1x PBS. These samples were subsequently stored at -4℃ in a 1:1 solution of 1x PBS and 100% ethanol. Samples for water chemistry measurements were filtered through an 0.2μm polyethersulfone (PES) filter, and either acidified with ~0.5mL 4M HCl and frozen or immediately frozen. Water samples for measurement of sulfide concentration were filtered into 15mL tubes containing pre-weighed ~4mL aliquots of (molarity) zinc acetate. No sulfide was detectable using the Cline assay using Hach reagents (Cline, 1969) (#2244500, Hach, Loveland, CO, USA).

b. DNA extraction and amplicon library preparation.

Total DNA from field samples and laboratory experiments was extracted using the PowerSoil DNA isolation kit (Qiagen, Hilden, Germany). To reduce DNA extraction bias, the vortexing step was modified, with aliquots removed after vortexing for 5, 10, and 15 minutes, and then recombined. Libraries were then prepared following the "in house" method of Jones et al. (2017a). Briefly, the V4 region of the 16S rRNA gene was first amplified with primers "515f modified" and "806r modified" (Walters et al. 2015) that were amended with Nextera adaptors to allow barcoding (Jones, Lapakko, et al., 2017). PCR was performed as in (Jones, Lapakko, et al., 2017): 5 min initial denaturation at 94°C, either 25 or 30 cycles of 45 s denaturation at 94°C, 60 s annealing at 50°C, and 90 s elongation at 72°C, and final elongation at 72°C for 10 min. Blank controls were included with all DNA extractions, and no product was visible in the blanks. PCR products were then submitted to the University of Minnesota Genomics Center for barcoding (10 cycles after 1:100 dilution) and sequencing on an Illumina MiSeq (Illumina, San Diego, CA, USA), 250 paired end cycles.

c. Bioinformatic analyses.

OTU calling was performed as in (Jones et al., 2021). Raw sequences were filtered and trimmed with Sickle (https://github.com/najoshi/sickle) to average quality above 28 (5' trimming only) and ≥ 100 bp; any residual adapters reverse complemented on the 3' end were removed with cutadapt (Martin, 2011); R1 and R2 reads were assembled with PEAR (J. Zhang et al., 2014); and primers removed by trimming the assembled reads with prinseq v.0.20.4 (Schmieder & Edwards, 2011). OTUs were defined at 97% similarity with a modified version of the UPARSE pipeline (USEARCH v.10.0; (Edgar, 2013)), in which the "derep_fulllength" script from VSEARCH v.1.9.5 (Rognes et al., 2016) was used. OTUs were classified with mothur v.1.36.1 (Schloss, 2020) to the Silva database v.132 (64) (Quast et al., 2013) with a confidence score cutoff of 50.

Libraries were organized into a matrix of samples versus OTUs. Raw counts (i.e., the number of sequences of each OTU per sample) were first converted to proportional values to account for uneven library sizes by dividing by the total number of sequences in each library. OTUs that occurred at less than 0.01% were then removed from the dataset.

Prior to statistical analyses, the data were transformed using an arcsine square root transformation (Jones, Lapakko, et al., 2017). The use of transformed data lowered the stress in subsequent NMS and clustering analyses. NMS ordinations were performed using 3 dimensions, with rotation to principal components, using the metaMDS() function in Vegan package v2.5-7 (Dixon, 2003) in R v4.1.0 (R Core Team, 2021) in RStudio (RStudio Team, 2021). Hierarchical agglomerative cluster analyses were performed with Bray-Curtis dissimilarity and unweighted pair-group method using arithmetic averages (UPGMA) clustering (cite). Q-mode cluster analyses (clustering of samples) were calculated using all OTUS in the transformed dataset, while R-mode cluster analysis (clustering of OTUs) only included the top 30 most abundant OTUs. The table of OTU

occurrence across samples used for statistical analyses is included as Data Set S1. Plots were created using ggplot2 (Wickham, 2016).

d. Laboratory Experiments.

Laboratory weathering experiments and tests of "bioshrouding" by algal growth were conducted with crushed pyrrhotite as a substrate. Pyrrhotite used in these experiments was a mixture of 4C and 6C pyrrhotite with trace sphalerite, chalcopyrite, and galena from Ward's Scientific, crushed to a grain size of between 75 and 150μm. See (Kathryn Kiku Hobart et al., 2021) for a more complete description; this is sample Po2.

Five experimental treatments were conducted in triplicate in 50mL glass serum bottles: enrichment, enrichment + algae, isolate, isolate + algae, and algae only. 50mL of sterile growth media was added to each bottle, containing: 6mM NH_4Cl, 3mM KH_2PO_4, 1mM Na_2HPO_4, 1.5mM $MgCl_2{\cdot}6H_2O$, 0.3mM $CaCl_2{\cdot}2H_2O$, trace element solution (Flood et al., 2015), and 20mM MES buffer titrated to pH 6.0 with 4M NaOH. The isolate organism used in these experiments is *Sulfuriferula* sp. strain AH1 (Jones, Roepke, et al., 2017), an autotrophic sulfur-oxidizing β-proteobacteria isolated from humidity cell experiments described in (Jones, Lapakko, et al., 2017). The enrichment inoculum was a homogenized microbial community collected from weathered Duluth Complex rock and previous incubation experiments, maintained in the laboratory in mixed culture with solid, crushed pyrrhotite as the growth substrate. The microbial communities identified through 16S rRNA libraries at the termination of the 19-day experiment are presented in Figure 4a, and sulfate release (as a proxy for sulfide mineral dissolution) is reported in Figure 4b. Experiments were placed on an orbital oscillating shaker exposed to a grow light on a 12 hour diel cycle. Those without the algae inoculum were covered to keep them in continuous darkness.

Experiments were sampled every four to five days. At each sampling point, 6mL of leachate removed for chemical analysis and then replaced with 6mL of sterile growth media to maintain constant volume. 0.5mL of the leachate was analyzed for pH using a LAQUAtwin pH-22 handheld pH meter (HORIBA, Kyoto, Japan); 1.5mL of the leachate was acidified with 20μm of 4M hydrochloric acid and stored at -4℃ for ferrous iron analysis; 2mL of the leachate was stored at -20℃ for measurement of anion concentrations. Ferrous iron concentration was measured using the ferrozine assay (Stookey, 1970) using the method described in (Viollier et al., 2000). Anion concentrations (chloride, fluoride, bromide, nitrate, sulfate) were measured using a Metrohm 930 Compact IC Flex ion chromatograph with a A Supp 5 column, 20μL sample loop, and an eluent carbonate buffer (3.2mM Na_2CO_3 and 1.0mM $NaHCO_3$). Sulfate release was calculated based on the measured concentration of sulfate at each time point and subsequently correcting for the amount of leachate replaced with sulfate-free media at each sampling interval.

Acknowledgements: The authors acknowledge Dean M. Peterson for field sampling assistance and insightful advice, and *Sat*oshi Ishi for algae culturing advice and algae

samples for use in the incubation experiments. Access to the IB and GG sampling sites was provided by the USFS and Twin Metals. KKH was supported by a MnDRIVE Environment grant to JMF and DSJ, funding from the University of Minnesota Department of Earth & Environmental Sciences, and a Geological Society of America Student Research Grant. ZG and KH were supported by a NSF Reserch Experience for Undergraduates on Sustainable Land and Water Resources coordinated by Diana Dalbotten.

Chapter 5: Metabolically Diverse *Sulfuriferula* spp. from Sulfide Mineral Weathering Environments in Northern Minnesota

Microorganisms are important catalysts for oxidation of inorganic sulfur compounds, and there are a diversity of metabolic pathways available to sulfur-oxidizing microorganisms that interact with inorganic sulfur compounds in different ways. Here we report the metabolic capabilities of four strains of *Sulfuriferula* spp. isolated from experimentally weathered Duluth Complex waste rock and tailings. These strains are all neutrophilic, lithoautotrophic sulfur-oxidizers, but each strain showed unique growth behaviors and possesses genes for different sets of sulfur- and nitrogen-cycling enzymes. Differences in observed growth behavior, including differences in environmental distribution (Chapter 4, this thesis) and pyrrhotite oxidation capabilities (Chapter 3, this thesis) are evaluated through the lens of these strains' metabolic capabilities. Strain AH1 shows the highest cell densities when grown on thiosulfate and the highest rates of pyrrhotite dissolution, but has the most fewest genes that code for sulfur-oxidizing enzymes, suggesting that it is uniquely adapted to its sulfide mineral weathering environment.

Co-authors Gabriel Walker, An-An Hua, and Daniel Jones isolated the strains described in this chapter, and Daniel Jones prepared the genome sequences for analysis.

I. Introduction

The oxidation of reduced inorganic sulfur compounds is a crucial step in the global sulfur cycle. Sources of reduced sulfur include metal sulfide minerals that are present in sedimentary, igneous, and metamorphic rocks, dissolved and gaseous hydrogen sulfide species that are common in anoxic environments, and compounds with intermediate valences that include short-lived compounds like thiosulfate ($S_2O_3^{2-}$) and tetrathionate ($S_4O_6^{2-}$) and more stable species like elemental sulfur. Sulfur compounds are a dynamic source of energy for modern microorganisms that drive the oxidation of these compounds in diverse environmental conditions (Baker & Banfield, 2003; Hamilton et al., 2017; Hamilton et al., 2014; Holmer & Storkholm, 2001; Macalady et al., 2007; Sharrar et al., 2017), and have done so throughout Earth's history (Bontognali et al., 2012; Fike et al., 2015). Many of these inorganic-sulfur-oxidizing bacteria and archaea are primary producers that fix carbon and nitrogen and are abundant in environments with a range of pH conditions (from pH ~1 to ~10) and temperatures (from ~10 to ~90°C) (Muyzer et al., 2013). Terrestrial environments are particularly diverse settings for sulfur cycling because sulfur sources can be heterogeneously distributed in the environment. Steep gradients in environmental conditions like pH, temperature, and redox potential provide many distinct

niches for different sulfur cycling organisms to thrive (Aronson et al., 2022; Capone & Kiene, 1988; Diao et al., 2017; Holmer & Storkholm, 2001; Klatt et al., 2020).

Sulfuriferula are a recently described genus of sulfur-oxidizing bacteria. The first *Sulfuriferula* strains were isolated from a uranium mine using galena (PbS) as the sole electron donor, and was originally named '*Thiobacillus plumbophilus*' (Drobner et al., 1991). The genus *Sulfuriferula* was formally described in 2015 within the novel family *Sulfuricellaceae*, which included members reclassified from the polyphyletic family *Thiobacillus* (Watanabe et al., 2015). Members of the genus *Sulfuriferula* can grow autotrophically on inorganic sulfur compounds, and some can grow organoheterotrophically on organic substrates (Watanabe et al., 2015). Formally described members of the genus *Sulfuriferula* include *S. multivorans*, which was isolated from a freshwater lake in Hokkaido, Japan (Watanabe et al., 2015); *S. thiophila*, which was isolated from a storage tank at a public hot spring bath in Yamanashi Prefecture, Japan (Watanabe et al., 2016a); *S. nivalis*, isolated from snow collected at the shore of a pond in Daisetsuzan National Park, Japan (Kojima et al., 2020); and *S. plumbiphila*, the original "*Thiobacillus* plumbophilus" isolate that was formally described and later renamed (Drobner et al., 1991; Watanabe et al., 2015). All species have been reported to grow aerobically on thiosulfate, tetrathionate, and elemental sulfur, while only *S. multivorans* can grow heterotrophically and anaerobically with nitrate as an electron acceptor (Kojima et al., 2020; Watanabe et al., 2016a) and *S. plumbiphila* can also grow autotrophically on H_2 and PbS (Drobner et al., 1991). *Sulfuriferula* are now known from diverse sulfur-rich terrestrial environments, and relatives of *Sulfuriferula* in metagenomic and 16S rRNA gene datasets have been found in metal- and sulfide- rich mine tailings and drainage (Gruzdev et al., 2020; Jones, Lapakko, et al., 2017; Kadnikov et al., 2019; Laroche et al., 2018; Liu, Yao, Lu, et al., 2019; Liu, Yao, Wang, et al., 2019; Liu et al., 2019; Pakostova et al., 2020; Sun et al., 2020), sewer and groundwater environments (Li et al., 2017; Liang et al., 2020; Novikov et al., 2020), hot springs and volcanic deposits (Arce-Rodríguez et al., 2019; Lathifah et al., 2019; Lopez Bedogni et al., 2019), seawater-influenced sulfide caves (D'Angeli et al., 2019), and low-temperature lake bottom sediments (Shen et al., 2021; Zakharyuk et al., 2019).

Here we describe new strains of *Sulfuriferula* that were isolated from weathered rocks from the sulfide mineral-bearing Duluth Complex in Northern Minnesota. The Duluth Complex contains copper, nickel, and platinum group element (Cu-Ni-PGE) deposits that may represent the world's largest undeveloped economic Cu-Ni-PGE resource (Miller et al., 2002). The most abundant sulfide mineral in these rocks is pyrrhotite ($Fe_{1-x}S$, $0 < x < 0.125$), followed by chalcopyrite ($CuFeS_2$), cubanite ($CuFe_2S_3$), and pentlandite ($(Fe, Ni)_9S_8$), with smaller amounts of other Cu, Ni, and PGE-bearing sulfide minerals (Severson et al., 2002)**.** Sulfur- and iron-oxidizing microorganisms are known to accelerate the dissolution of sulfide minerals under highly acidic conditions (Nordstrom et al., 2015). However, in contrast to many other well-studied ore and mine-waste

environments where extreme acidity is generated, the relatively low sulfide mineral content (usually <1% total sulfur) and high buffering capacity of the surrounding silicate minerals means that leachate from Duluth Complex waste rock and tailings is only moderately acidic and rarely reaches pH values of less than 4 (Lapakko, 2015; Lapakko & Antonson, 1994). The role of microorganisms in this mildly acidic environment is not as well-constrained as in extremely acidic systems.

Based on rRNA gene and transcript sequencing, *Sulfuriferula* spp. were some of the most abundant and active organisms in experimentally weathered Duluth Complex rocks and tailings (Jones, Lapakko, et al., 2017), and were also found (although at lower abundances) in naturally-weathered Duluth Complex outcrops (Chapter 4, this thesis), suggesting that they are important members of the rock weathering community. Characterizing the metabolic potential of these populations is vital to understanding the biogeochemistry of proposed mines and developing biological solutions to managing mine waste and water from proposed mines throughout their lifecycle; however, we currently know little about these rock-associated *Sulfuriferula* spp. To learn more about these important organisms and the role they play in the biogeochemistry of Duluth Complex mine waste and water, we isolated and characterized four strains of *Sulfuriferula* from experimentally weathered Duluth Complex materials. We describe the genomic and physiological properties of the strains and what this means for their surprisingly diverse roles in the waste rock community.

II. Results

a. Isolation and identification of Sulfuriferula.

Strains of *Sulfuriferula* were isolated from weathering experiments on mine tailings and crushed rock from copper-nickel deposits in the Duluth Complex, northeastern Minnesota. The tailings and crushed rock had been experimentally weathered for more than 12 years using a humidity cell apparatus and in a field weathering pile (Lapakko, 2015; Lapakko & Antonson, 1994). Sixteen isolates were obtained, and four phylogenetically distinct strains, referred to as AH1, GW1, GW6, and HF6a, were selected for further study. Strains AH1, GW1, and HF6a were enriched and isolated on solid thiosulfate media that contained 6 mM ammonium, while GW6 was enriched and isolated on media with urea as the sole provided N source.

Phylogenetic analysis of 16S rRNA gene sequences from these isolates confirm that all cluster with described *Sulfuriferula* species (Figure 5-1). Strains GW1 and HF6a are most closely related to *S. multivorans* (Watanabe et al., 2015), strain GW6 is most closely related to *S. plumbiphila* (Drobner et al., 1991; Watanabe et al., 2015), and strain AH1 is located in its own clade within the *Sulfuriferula* but is most closely related to *S. thiophila* and *S. nivalis* (Kojima et al., 2020; Watanabe et al., 2016b).

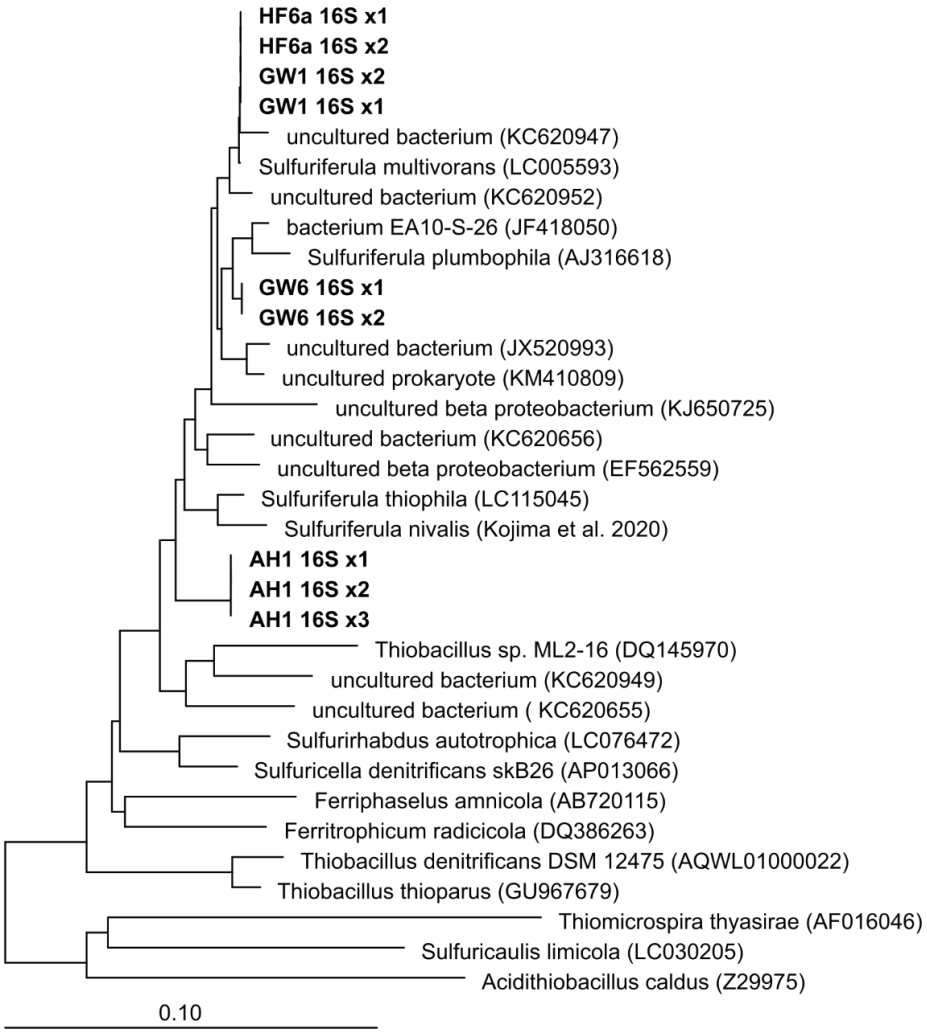

Figure 5-1. Neighbor-joining phylogenetic tree of 16S rRNA gene sequences, showing the relationship of the four Sulfuriferula isolates to other members of family Sulfuricellaceae. Names in bold font are sequences from this study, and the numbers after each name (x1, x2) indicate rRNA gene copies from multiple rrn operons in the genome.

b. Growth characteristics.

All four *Sulfuriferula* isolates grew on autotrophic media with thiosulfate as the only available electron donor. No growth was detected on tetrathionate, sulfite, or elemental sulfur. All strains grew on pyrrhotite ($Fe_{1-x}S$, $0 \leq x \leq 0.125$) as the sole electron donor (Chapter 3, this thesis). When grown on thiosulfate, strain AH1 accumulates sulfate and H^+ ions in the growth media, consistent with complete thiosulfate oxidation to sulfate (Figure 5-2).

While growth in strains AH1 and GW1 was enhanced by the addition of 1% w/v yeast extract to the media, no growth was observed on LB broth or 1:10 diluted LB broth. No increase in growth was observed when 5mM glucose, acetate, or succinate was added to the thiosulfate media, suggesting that these strains are obligate autotrophs (Figure E-1).

Growth rate decreased in media buffered with organic buffers rather than phosphate. Growth occurred in MES- and HEPES- but not citrate-buffered media.

Figure 5-3 shows the effect of pH on the growth of all strains, in media buffered with MES. No growth was observed below pH 4 or above 8, and the maximum growth rate occurred between 6 and 7. Strain HF6a had the lowest pH optima and growth range.

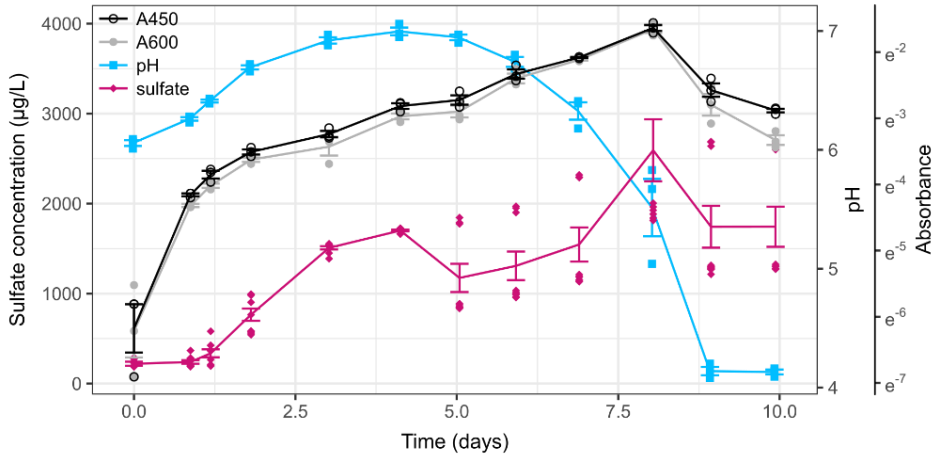

Figure 5-2. pH, aqueous sulfate concentration, and absorbance at 450nm (A450) and 600nm (A600) for Sulfuriferula sp. strain AH1 grown on thiosulfate in pH 6.0 growth media.

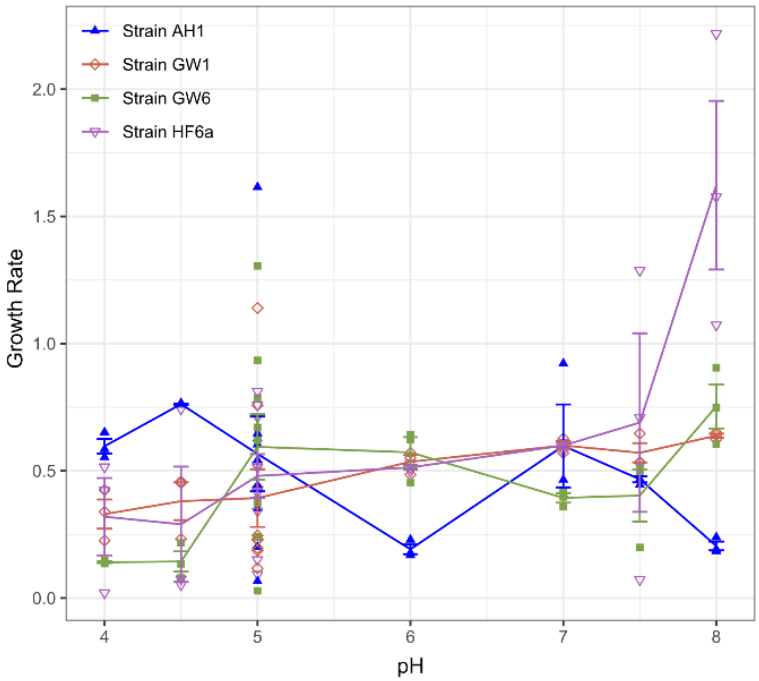

Figure 5-3. Effect of pH on growth rate (calculated as culture doubling times from the log-phase of OD_{600} absorbance) of Sulfuriferula spp. The solid line is the mean of replicates for each pH and strain, and the error bars represent the standard deviation of replicates around the mean.

Whole genome sequencing and assembly. The genomes of the four isolates were each assembled into a single large chromosome, between 2.92 and 3.33 Mb. One 39.1 Kb plasmid was recovered for strain AH1, and two plasmids, 23.8 and 39.5 Kb, were recovered from strain GW6. Table 5-1 contains an overview of the properties of the assembled genomes, which range from 55-58.7 % G+C content and 97-98% protein-coding genes. GW1, GW6, and HF6a each have two *rrn* operons, and AH1 encodes three. A summary of genes associated with sulfur, nitrogen, carbon, and iron metabolisms and genes associated with biofilm formation are presented in Figure 5-4.

c. Carbon metabolism.

All four strains of *Sulfuriferula* encode complete Calvin cycles for CO_2 fixation. *S*train AH1 has 2 copies of RuBisCo form I and 1 copy of RuBisCo form II, strain GW1 has 2 copies of RuBisCo form I, strain GW6 has 3 copies of RuBisCo form I, and strain HF6a has one copy each of RuBisCo form I and form II. All four strains have a full complement of carboxysome and carbonic anhydrase-coding genes (Figure 5-4). All four strains possess complete glycolysis pathways and incomplete TCA cycles. However, the lack of growth or increased growth with the inclusion of organic carbon compounds to the media suggests that these are primarily autotrophic organisms.

Table 5-1. Summary of assembled genomes.

		AH1	**GW1**	**GW6**	**HF6a**
DNA	Total # Bases	2,916,145	3,363,341	3,329,881	3,261,505
	G+C %	54.99%	57.10% (1,920,508)	58.71% (1,954,947)	57.07% (1,861,310)
	# Contigs	1 circular contig	1 circular contig	1 circular contig	1 circular contig
	Plasmids	1 plasmid, 39,138 bp		2 plasmids, 23,830 bp & 39,480 bp	
GENES	Total # Genes	2972	3369	3559	3319
	Protein-coding genes	2906 (97.78%)	3301 (97.98%)	3450 (96.94%)	3252 (97.98%)
	rRNAs	9 (0.30%)	6 (0.18%)	6 (0.17%)	6 (0.18%)
	tRNAs	47 (1.58%)	50 (1.48%)	51 (1.43%)	48 (1.45%)
	Protein-coding genes w/ functional prediction	2360 (79.41%)	2634 (78.18%)	2712 (76.20%)	2553 (76.92%)
	Assigned to COGs	2042 (68.71%)	2705 (80.29%)	2786 (78.28%)	2624 (80.81%)
	Assigned to KEGG Orthology (KO)	1659 (55.82%)	1810 (53.73%)	1835 (51.56%)	1722 (51.88%)

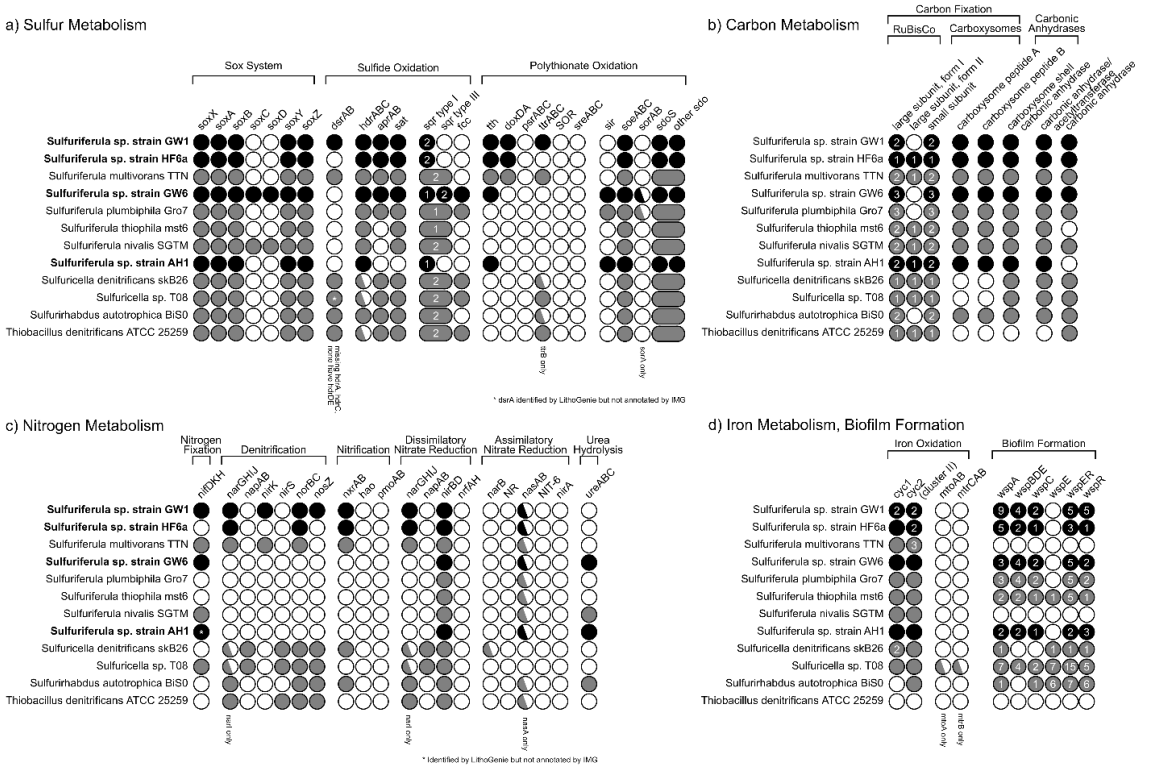

Figure 5-4. Metabolic overview of (a) sulfur, (b) carbon, (c) nitrogen, and (d) iron metabolism and biofilm formation. Filled circles indicate the presence of the gene as annotated by IMG and confirmed by hidden Markov models. A half-filled circle indicates an incomplete pathway, or the absence of one or more subunits. The number inside the filled circle indicates the number of copies of the gene found in the genome.

d. Nitrogen metabolism.

The four strains have diverse capabilities for nitrogen acquisition and dissimilatory nitrogen metabolism (Figure 5-4c). Strains AH1, GW1, and GW6 encode genes for a molybdenum-dependent nitrogenase typically associated with nitrogen fixation. Strains GW1 and HF6a possess the denitrification genes narGHIJ and norBC, indicating that these strains can reduce nitrate and nitrous oxide, respectively, as a source of energy. Strain GW1 additionally possesses nirK and nosZ, providing this strain with a complete set of genes necessary for denitrification. All four strains possess nirBD genes for dissimilatory nitrate reduction to ammonia. Strains GW1 and HF6a also possess the nxrAB genes, indicating the potential for nitrite oxidation. No strains possess complete assimilatory nitrate reduction pathway genes, although all strains possess the nasA gene. Additionally, the genomes of strains AH1 and GW6 contain the urea hydrolysis genes ureABC, indicating an ability to utilize urea as a source of ammonia.

e. Sulfur oxidation pathways.

The four strains encode diverse pathways for the complete oxidation of reduced inorganic sulfur compouonds (Figure 5-4a). All four strains of sulfide have the ability to utilize sulfide as an electron donor. All four strains of *Sulfuriferula* encode sulfide:quinone oxidoreductase (sqr) homologues. SQR are found in all domains of life as a tool for sulfide oxidation and detoxification. Six structural types of SQR are known; microorganisms encoding at least one representative enzyme from each of type I, III, IV, V, and VI can use sulfide as an electron donor. Type II has not been directly linked to metabolic oxidation of sulfide and may be used for detoxification (Lencina et al., 2013; Marcia et al., 2010). All four *Sulfuriferula* strains have genes identified as type I sqr, with strains GW1 and HF6a having two copies. Strain GW6 also possesses two copies of the sqr type III, as well as *fcc*, which encodes flavocytochrome-c sulfide dehydrogenase, a structurally-related protein that can also be utilized for sulfide oxidation (Tikhonova et al., 2021).

Strains AH1, GW1 and HF6a possess partial *sox* systems, with genes coding for *soxAX*, *soxYZ*, and *soxB* but not the *soxCD* enzyme complex, while strain GW6 possesses a complete sox system including *soxCD*. In the complete pathway, SoxYZ complexes with thiosulfate to form a SoxY-cysteine S-thiosulfate derivative, which move to sequential reactions with SoxAX and SoxB that oxidize one of the sulfur atoms in the thiosulfate to sulfate, with two electrons transferred to the electron transport chain. *SoxCD* then oxidizes the remaining sulfane sulfur of the residual SoxY-cysteine-S to sulfate, which is hydrolyzed by SoxB, ultimately generating sulfate and transferring six electrons to the electron transport chain (Friedrich et al., 2001). The sox pathway is able to catalyze oxidation of reduced sulfur species besides thiosulfate, including sulfide, elemental sulfur, sulfite, and tetrathionate (Appia-Ayme et al., 2001; Lahiri et al., 2006; Mukhopadhyaya et al., 2000; Wodara et al., 1997), and this ability seems to be facilitated by the modular nature of the reactions (Sauvé et al., 2007). While *SoxCD* is not essential for completely thiosulfate or sulfide oxidation, partial sox systems lacking *SoxCD* are thought to produce elemental sulfur or polysulfides (Friedrich et al., 2005). In some organisms with a partial *sox* system, that sulfur is then completely oxidized by the *DSR* system (Beller et al., 2006; Dahl et al., 2013). Only strain GW1 contains genes encoding *DsrAB* (dissimilatory (bi)sulfate reductase), however, indicating that the other strains either produce S(0) as a final product or use another process to completely oxidize the S(0).

All four strains possess *hdrABC*, which encodes heterodisulfide reductase that is linked to the oxidation of zero-valent sulfur in some bacteria (Boughanemi et al., 2016). All four strains also possess genes coding for sulfur dioxygenases (*sdo*). *Sdo* oxidizes the sulfate sulfur in glutathione persulfide (GSSH) to sulfite (Liu et al., 2014). Homologous genes are found in mitochondria, where mutations on this gene are implicated in a rare herediataroy human disease (Tiranti et al., 2006, p. 1). Widely distributed through the Proteobacteria, *sdo* genes are used both in sulfide detoxification and in primary metabolism. The isolate *Sulfuriferula* strains examined in this study have two types of *sdo*

sequences: one set are most similar to the mitochondrial sulfide detoxification ETHE1 genes, while the other set are most similar to the *sdoS* genes found in acidophillic bacteria like *Acidithiobacillus* (Figure 5-5). Strains AH1, GW1, and HF6a have one copy of each of the two types of *sdo*, while strain GW6 has one copy homologous with ETHE1 and two distinct copies of genes within the *sdoS* group. The strains did not encode other known genes involved in S(0) oxidation like SOR (Kletzin, 1989).

All four strains also possess genes for tth (tetrathionate hydrolase), which catalyzes the oxidation of tetrathionate to thiosulfate, elemental sulfur, and sulfate (Kanao et al., 2018) and *soeABC* (sulfite dehydrogenase (quinone)), which allows the transfer of electrons to the quinone pool by the oxidation of sulfite to sulfate (Boughanemi et al., 2020). Strain GW1 additionally possesses genes for *doxDA* (thiosulfate dehydrogenase), which catalyzes the oxidation of thiosulfate to tetrathionate (Müller et al., 2004) and *ttrABC* (tetrathionate reductase), which catalyzes the oxidation of tetrathionate to thiosulfate (Hensel et al., 1999). Strains AH1 and GW6 possess sir genes which code for ferrodoxin:sulfite reductase, catalyzing the assimilatory reduction of sulfite to sulfide (Gisselmann et al., 1993), and GW6 possesses *sorA*, which codes for the A subunit of sulfide dehydrogenase (cytochrome) (Kappler et al., 2000). Strains GW1, GW6 and HF6a possess genes coding for *sat*, sulfate adenylyltransferase, and *aprAB*, adenylylsulfate reductase. Both of these proteins typically catalyze the reduction of sulfate (Carlson et al., 2021; Lampreia et al., 1990) although similarly to *dsrAB* the function can run in reverse, oxidizing intermediate organosulfur compounds to sulfate (Kappler & Dahl, 2001; Yamamoto & Takai, 2011).

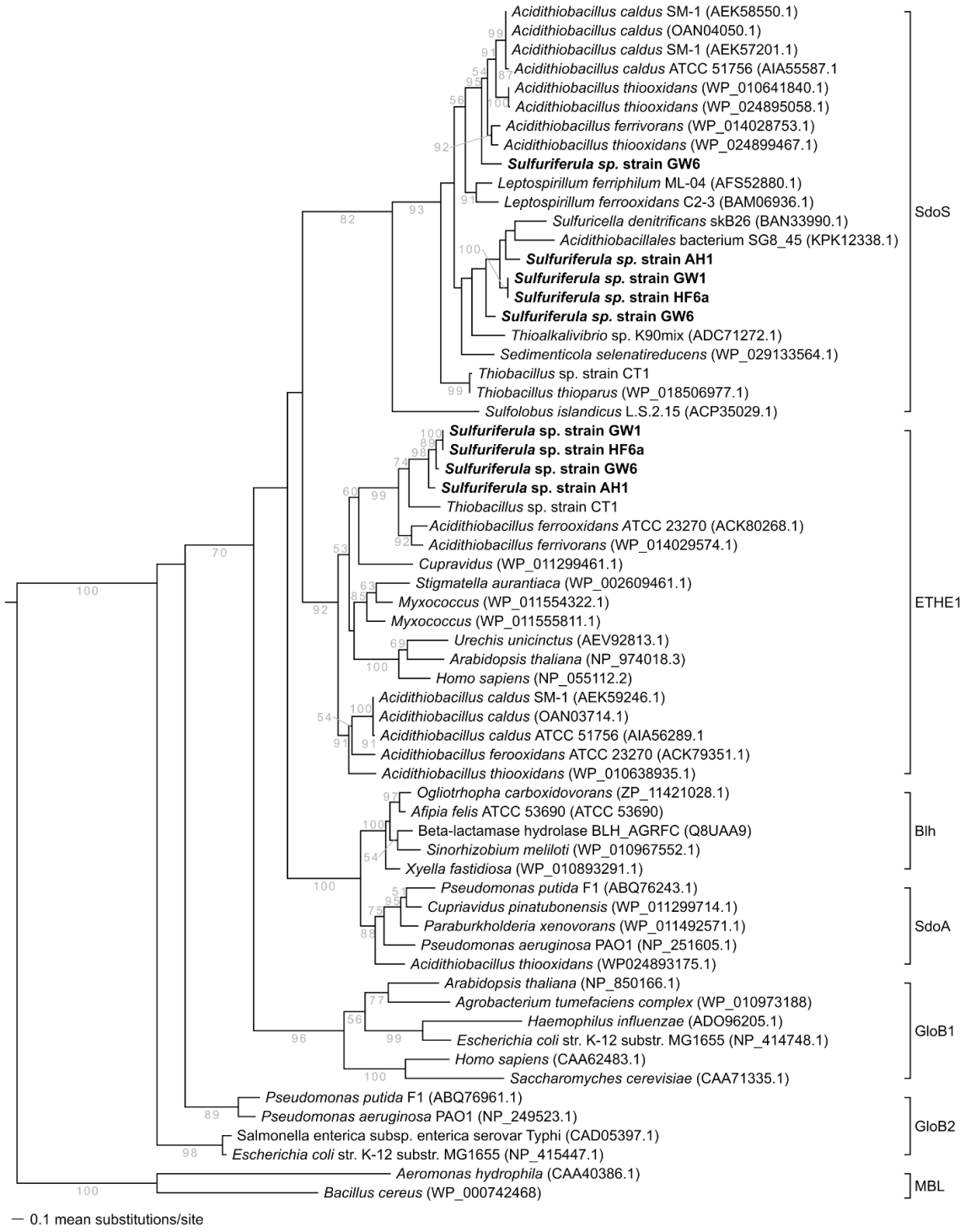

Figure 5-5. Maximum likelihood analysis of full-length sdo *genes from isolate organisms, with the genes from the isolates in this study highlighted in bold. The clade of metallo-beta-lactamase (*MBL*) sequences was used as the outgroup after (Liu et al., 2014).*

f. Other energy and nutrient metabolisms.

All four strains of *Sulfuriferula* described here contain genes identified by hidden Markov models as iron-oxidizing cytochromes *Cyc1* and *Cyc2* (Figure 5-4d). *Cyc1* is a c-type cytochrome likely located in the periplasm implicated in iron oxidation in extreme acidophiles (Appia-Ayme et al., 2001; Bonnefoy & Holmes, 2012; Peng et al., 2022), while *Cyc2* is a candidate iron oxidase found in both neutrophilic and acidophilic iron oxidizers (Barco et al., 2015; Castelle et al., 2008). *Cyc2* is further divided into three phylogenetically distinct clusters: cluster 1, which has not been experimentally verified but is found in most well-established neutrophilic iron oxidizing organisms; cluster 2, found in *Acidithiobacillus ferrooxidans, Ferrovum* spp., *Thiomonas* spp. and other acidophiles, and cluster 3, found in marine iron-oxidizing bacteria and acidophilic *Leptospirillum* spp. (McAllister et al., 2020). Because similar c-type cytochromes could be implicated in intracellular electron transport without directly catalyzing metabolic iron oxidation, these putative iron oxidation genes identified here will have to be verified by additional culturing experiments to evaluate whether any of the strains of *Sulfuriferula* investigated here are able to oxidize iron.

All four strains of *Sulfuriferula* contain genes identified as belonging to the *wsp* system, implicated in biofilm formation (Arkadiy-Garber, 2019) (Figure 5-4d). In *Pseudomonas aeruginosa*, the *wsp* system senses surface contact and activates genes that promote biofilm formation and regulation (Armbruster et al., 2019; Hickman et al., 2005). Homologs of the *wsp* system are found in the *Beta-* and *Gammaproteobacteria* (Kessler et al., 2021). The four strains are missing *wspE* (Fig. 4d), although studies in *P. aeruginosa* found that mutations on this gene did not affect biofilm formation or morphology (Hickman et al., 2005) although a recent study implicated mutations on *wspE* to the formation of "wrinkly" type biofilms in *Burkholderia* spp. that result in more severe human disease (Cooper et al., 2014).

III. Discussion

a. Metabolic and genomic diversity of *Sulfuriferula*.

Sulfuriferula strains, both those isolated and described here and in earlier work, show remarkable diversity in their metabolic capabilities. The four strains of *Sulfuriferula* investigated in this study each have distinct sulfur oxidation pathways and nitrogen metabolisms that could facilitate differences in growth behavior. Two of the strains described here, GW1 and HF6a, have the capacity to partially reduce nitrate, with GW1 having a complete set of denitrification genes. Strain GW1 also has genes for iron oxidation (*cyc1*, *cyc2*), suggesting that this strain could grow under both the aerobic conditions tested as well as anaerobic or microoxic conditions.

The highest concentration of cells on thiosulfate, measured by optical density, are seen in strain AH1, which has the fewest genes identified here as important for sulfur oxidation. A schematic overview of the pathway of sulfur through the cell in each strain is

shown in Figure 5. In strain AH1, thiosulfate is oxidized to a mixture of sulfate and elemental sulfur by the incomplete sox pathway. Elemental sulfur is thought to accumulate in organisms that lack both *soxCD* and *dsr*, which oxidizes elemental sulfur to sulfate (Dahl et al., 1993, 2005). In strain AH1, however, produced elemental sulfur could be oxidized to sulfite (SO_3^-) by *sdo* or hdr.

Conversely, strain GW6, which is the only strain with the complete sox pathway but otherwise possesses an identical set of sulfur-oxidation genes to AH1, consistently shows the lowest OD (and therefore the least growth) at all pH conditions tested, suggesting that under these conditions there are other factors at play affecting growth rate. The addition of organic carbon sources to the growth media (yeast extract, glucose, acetate, succinate) did not increase the growth rate or maximum optical density of strain GW6, so its lower growth rate when compared to other strains is not likely linked to heterotrophic requirements. Strain GW6 does differ from strain AH1 in that it lacks a form II RuBisCo – since form II is higher efficiency (although lower specificity) than type I (Berg, 2011), the growth rate differences between strains AH1 and GW6 could be a result of differences in efficiency of the carbon fixation pathways.

Strains GW1 and HF6a share many metabolic similarities with their closest-related isolate, *S. multivorans* (Watanabe et al., 2015), including the presence of *dsrAB* genes (in GW1) and genes for thiosulfate oxidation and reduction (tth, *doxDA*). They also share a number of genes encoding nitrogen cycling, including both denitrification and nitrogen fixation abilities. Interestingly, *S. multivorans* lacks the *wsp* genes that are present in all the strains of *Sulfuriferula* described here, suggesting that biofilm formation is not an important part of its metabolic capabilities. *S. multivorans* was initially enriched by anaerobic thiosulfate oxidation linked to nitrate reduction (Watanabe et al., 2015), and so the similarities of the metabolic capabilities of *S. multivorans* and strains GW1 and HF6a suggest that they may also have the ability to grow anaerobically.

Strain GW6 is most closely related to *S. plumbiphila*, which was isolated on galena (PbS) and was initially found to grow strictly aerobically on H_2S and H_2, but not on iron(II), elemental sulfur, thiosulfate, tetrathionate, or other metal sulfides. However, recent work has described growth of *S. plumbiphila* on tetrathionate, thiosulfate, and elemental sulfur (Kojima et al., 2020). Strain GW6 and *S. plumbiphila* both lack most of the genes affiliated with nitrogen cycling, although GW6 possesses genes encoding for a Mo-dependent nitrogenase complex. Strain GW6 is the only isolate described here that possesses the complete *Sox* system; the only other isolate with genes homologous to *soxCD* is *S. nivalis* (Kojima et al., 2020).

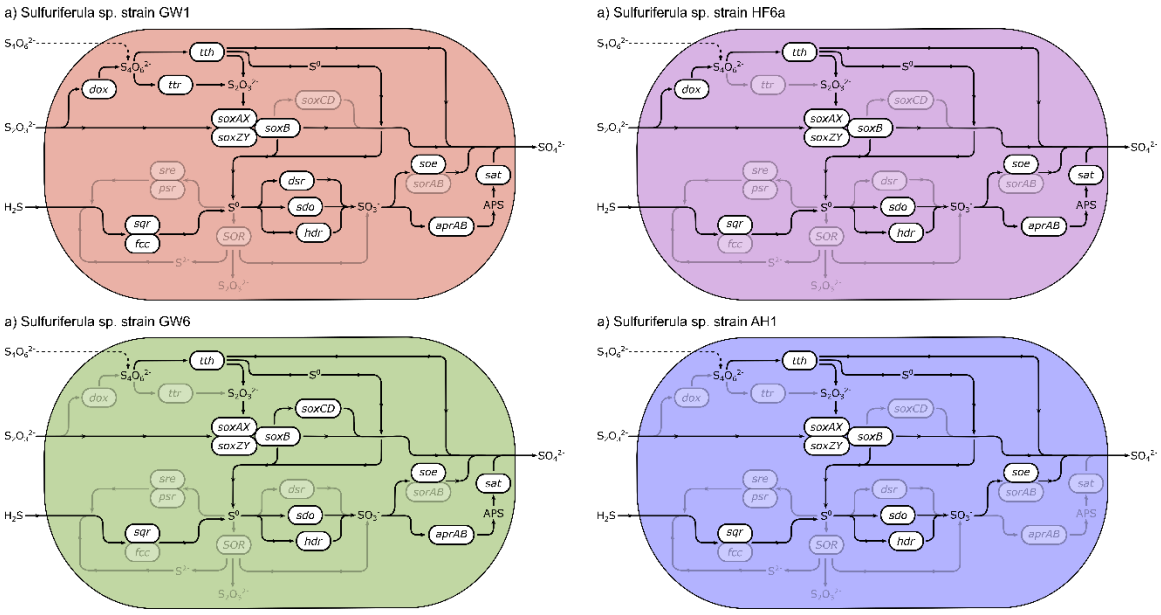

Figure 5-6. Summary of sulfur oxidation pathways in the four Sulfuriferula strains highlighting differences in metabolic capabilities. Enzymes are as follows: tth, tetrathionate hydrolase (Kanao et al., 2018); dox, thiosulfate oxidoreductase, tetrathionate-forming (Müller et al., 2004); ttr, tetrathionate reductase (Hensel et al., 1999), sox, multicomponent sulfur oxidation pathway (Friedrich et al., 2001); sre, sulfur reductase (Laska et al., 2003); psr, polysulfide reductase (Dietrich & Klimmek, 2002); sqr, sulfide:quinone oxidureductase (Marcia et al., 2010); fcc, flavocytochrome c sulfide dehydrogenase (Kusai & Yamanaka, 1973); SOR, sulfur oxygenase reductase (Kletzin, 1989); dsr, dissimilatory sulfite reductase (Pott & Dahl, 1998); sdo, sulfur dioxygenase (H. Liu et al., 2014); hdr, heterodisulfide reductase (Boughanemi et al., 2020); soe, sulfite dehydrogenase (Dahl et al., 2013); sorAB, sulfite dehydrogenase (Lyric & Suzuki, 1970); aprAB, adenylylsulfate reductase (Fritz et al., 2002), sat, dissimilatory sulfate adenylyltransferase (Laue & Nelson, 1994).

b. Implications for the biogeochemistry of Duluth Complex mine waste.

The metabolic diversity of *Sulfuriferula* strains could impact their fitness for, and distribution in, different weathering environments. Previous work found that the *Sulfuriferula* OTUs found in humidity cell experiments on Duluth Complex ore tailings were distinct (<97% 16S sequence similarity) from *Sulfuriferula* OTUs found in sediment from naturally weathered outcrops of ore-bearing Duluth Complex rock (cite env. genome paper). The diversity of sulfur oxidation and nitrogen fixation capabilities in *Sulfuriferula* spp. could result in different strains being more abundant in different environments.

Humidity cell experiments, for example, are typically conducted indoors and have negligible inputs of organic carbon or nitrogen, so *Sulfuriferula* strains with the capability to fix nitrogen (e.g., strains AH1, GW1, GW6) will have a competitive advantage over strains that cannot (e.g., strain HF6a). Conversely, in a natural weathering environment, where organic carbon and nitrogen species will be available from plants or soil bacteria, the ability to metabolize oxidized or reduced nitrogen species (like strain GW1, which possesses a complete denitrification pathway) could provide an advantage. Similarly, other

strains of *Sulfuriferula* or other organisms which are able to utilize organic carbon as part of their metabolism will have an energetic advantage over the obligate chemoautotrophic strains studied here. Although the pH of leachate from experimentally-generated Duluth Complex mine waste remains near-neutral (Lapakko, 2015; Lapakko & Antonson, 1994), the ability to oxidize iron, particularly if conditions in a waste rock pile or tailings basin became microoxic, could provide an additional source of metabolic energy to these strains.

Strain AH1 displays the most rapid thiosulfate oxidation rates and has also been show to oxidize sulfide minerals (specifically pyrrhotite, $Fe_{1-x}S$, $0 \leq x \leq 0.125$) much more rapidly than other strains (see e.g., Chapter 3, this thesis). This strain appears to have the simplest sulfur oxidation pathway and has the smallest genome out of the four strains examined. This suggests that *Sulfuriferula* sp, strain AH1 is highly specialized for nutrient-poor sulfide mineral weathering environments, and indicate that strain AH1 may have applicability in biomining and mine remediation. *Sulfuriferula* spp. are sensitive to organic acids, and do not appear to be able to utilize organic carbon, and so this suggests that their proliferation in a tailings pile or similar environment could be controlled by the application or removal of organic carbon compounds. If the desired goal is to *prevent* sulfide mineral oxidation, adding organic compounds to the tailings pile will result in the chemoautotrophic *Sulfuriferula* spp. being outcompeted by heterotrophic organisms (see e.g., the incubation experiments presented in Chapter 4, this thesis). Conversely, if the goal is to accelerate sulfide mineral dissolution, *Sulfuriferula* spp. can be enriched by maintaining an organic-carbon-poor environment.

Despite being isolated from the same site and under similar conditions, the four strains of *Sulfuriferula* described here are phylogenetically distinct, show different growth behavior, and each possess different sets of core metabolic genes. The metabolic diversity found in described here highlights the metabolic heterogeneity that can be found in taxonomically similar microorganisms and emphasizes the need for detailed consideration of the genetic potential of individual organisms within a larger microbial community.

IV. Methods

a. Isolation and identification of *Sulfuriferula* strains.

Isolates AH1, GW1, and HF6a were isolated on solid thiosulfate media containing 40mM $NaS_2O_3 \cdot 5H_2O$, 30mM KH_2PO_4, 10mM Na_2HPO_4, 6mM $(NH_4)_2SO_4$, 1.5mM $MgSO_4 \cdot 7H_2O$, 0.3mM $CaCl_2 \cdot 2H_2O$, trace element solution (Flood et al., 2015), and 1.5% agar. Isolate GW6 was isolated similarly, but with urea provided as the sole N source.

b. Growth conditions.

Growth of *Sulfuriferula* strains was assessed on liquid thiosulfate media, either phosphate-buffered (containing 40mM $NaS_2O_3 \cdot 5H_2O$, 30mM KH_2PO_4, 10mM Na_2HPO_4, 6mM $(NH_4)_2SO_4$, 1.5mM $MgSO_4 \cdot 7H_2O$, 0.3mM $CaCl_2 \cdot 2H_2O$, trace element solution (Flood et al., 2015)) or MES-buffered (20mM MES buffer, 6mM $(NH_4)_2SO_4$, 1.5mM

$MgSO_4 \cdot 7H_2O$, 0.3mM $CaCl_2 \cdot 2H_2O$, 0.3mM KH_2PO_4, 0.3 1mM Na_2HPO_4, trace element solution (Flood et al., 2015)) to the appropriate pH. Growth was assessed by measuring optical density (OD) at 600nm and 450nm. Potential utilization of different carbon sources was tested by growing the isolates on LB broth, 1:10 LB broth, or the phosphate-buffered thiosulfate media with added 1% yeast extract, 5mM glucose, 5mM acetate, or 5mM succinate. Growth curve experiments were conducted in clear borosilicate test tubes. pH was measured using a LAQUAtwin pH-22 handheld pH meter (HORIBA, Kyoto, Japan) and sulfate was measured in duplicate by barium sulfate ($BaSO_4$) precipitation and absorbance at 450nm.

c. Genome sequencing, assembly, and annotation.

Cells of the strains investigated in this manuscript were collected from batch cultures onto 0.2μm-pore filters and genomic DNA (gDNA) was isolated from the filters using the PowerSoil DNA isolation kit (Qiagen). For strain AH1, SMRTbell libraries were prepared with 20μg of high molecular weight DNA, and sequenced on a Pacific Biosciences (PacBio) RSII platform. For other strains, SMRTbell libraries were prepared with 2-3 ug of high molecular weight DNA was prepared with a 10 Kb insert size at the University of Minnesota Genomics Center (UMGC), and pooled and sequenced on a PacBio Sequel platform. Assembly of AH1 was described in Jones et al. (2017), and the other genomes were assembled using HGAP version 6 with default parameters.

Sequences were uploaded to IMG/MER (I.-M. A. Chen et al., 2021) and annotated using the JGI Integrated Microbial Genomes (IMG) Pipeline (Markowitz et al., 2009). Presence and function of genes involved in carbon and nitrogen metabolic pathways were determined using KEGG Ortholog annotation (Kanehisa et al., 2016). Genes involved in sulfur metabolism, iron metabolism, and biofilm formation were initially determined using KEGG Orthology and were confirmed using hidden Markov models (HMM) with HMMer v. 3 (L. S. Johnson et al., 2010). HMMs for genes in the *SoxB*, *SoxC*, and *SoxD*, as well as *Sqr*/*Fcc* pathways were constructed by aligning a database of sequences using TCOFFEE's Expresso aligner (Notredame et al., 2000) and using HMMER to create the model out of the aligned sequences. Databases for *soxB* were generated using sequence compilations from (Edwardson & Hollibaugh, 2017; Meyer et al., 2007), databases for sqr were generated from (Trinity L. Hamilton et al., 2014; Marcia et al., 2010), and databases for *sdo* were generated from (H. Liu et al., 2014; Wu et al., 2017). The isolate genomes were then converted from DNA to proteins using Prodigal v. 2.6.3 (Hyatt et al., 2010) and screened for matches using hmmsearch with an E-value cutoff of 10^{-7}. All other HMMs used were part of the MagicCave package (Arkadiy I. Garber et al., 2020; Arkaidy I. Garber et al., 2020).

d. Phylogenetic analysis.

For phylogenetic analysis of 16S rRNA genes, sequences were aligned in ARB (Ludwig et al., 2004) using the Silva database v. 132 (Quast et al., 2013). Sequences were filtered so that all *Sulfuriferula* sequences were the same length and positions with more than 50% gaps removed (final alignment 1449 positions). Neighbor joining analyses were

performed with the ARB-implementation of phylip (Felsenstein, 1981) with Jukes-Cantor-corrected distance. *Sdo* phylogenies were created with maximum likelihood analysis using RAxML v.8.0.24 (Stamatakis, 2006) with the LG model of amino acid substitution (Le and Gascuel 2008) with observed amino acid frequencies and the fraction of invariant sites and the shape parameter (α) value estimated from the data.

Works Cited

Abraham, W.-R., Strömpl, C., Meyer, H., Lindholst, S., Moore, E. R. B., Christ, R., et al. (1999). Phylogeny and polyphasic taxonomy of Caulobacter species. Proposal of Maricaulis gen. nov. with Maricaulis maris (Poindexter) comb. nov. as the type species, and emended description of the genera Brevundimonas and Caulobacter. *International Journal of Systematic and Evolutionary Microbiology*, *49*(3), 1053–1073. https://doi.org/10.1099/00207713-49-3-1053

Adams, D. C., & Keller, G. R. (1994). Possible extension of the Midcontinent Rift in west Texas and eastern New Mexico. *Canadian Journal of Earth Sciences*, *31*(4), 709–720. https://doi.org/10.1139/e94-063

Allen, D. J., Hinze, W. J., Dickas, A. B., & Mudrey, M. G. (1997). Integrated geophysical modeling of the North American Midcontinent Rift System: New interpretations for western Lake Superior, northwestern Wisconsin, and eastern Minnesota. In R. W. Ojakangas, A. B. Dickas, & J. C. Green, *Middle Proterozoic to Cambrian rifting, central North America*. Geological Society of America. https://doi.org/10.1130/0-8137-2312-4.47

Anderson, E. (2018). *Identification of Microorganisms for the Bioremediation of Nitrate and Manganese in Minnesota Water* (M.S.). University of Minnesota, United States -- Minnesota. Retrieved from https://www.proquest.com/docview/2315502466/abstract/C7EC3C4A766B4FD5PQ/1

Andrews, M. S., & Ripley, E. M. (1989). Mass transfer and sulfur fixation in the contact aureole of the Duluth Complex, Dunka Road Cu-Ni deposit, Minnesota. *The Canadian Mineralogist*, *27*(2), 293–310.

Appia-Ayme, C., Little, P. J., Matsumoto, Y., Leech, A. P., & Berks, B. C. (2001). Cytochrome Complex Essential for Photosynthetic Oxidation of both Thiosulfate and Sulfide in *Rhodovulum sulfidophilum*. *Journal of Bacteriology*, *183*(20), 6107–6118. https://doi.org/10.1128/JB.183.20.6107-6118.2001

Arce-Rodríguez, A., Puente-Sánchez, F., Avendaño, R., Martínez-Cruz, M., de Moor, J. M., Pieper, D. H., & Chavarría, M. (2019). Thermoplasmatales and sulfur-oxidizing bacteria dominate the microbial community at the surface water of a CO2-rich hydrothermal spring located in Tenorio Volcano National Park, Costa Rica. *Extremophiles*, *23*(2), 177–187. https://doi.org/10.1007/s00792-018-01072-6

Arkadiy-Garber. (2019, December 16). *Wsp*Genie. Python. Retrieved from https://github.com/Arkadiy-Garber/*Wsp*Genie (Original work published February 17, 2019)

Arkesteyn, G. J. M. W. (1980). Pyrite oxidation in acid sulphate soils: The role of miroorganisms. *Plant and Soil*, *54*(1), 119–134. https://doi.org/10.1007/BF02182004

Armbruster, C. R., Lee, C. K., Parker-Gilham, J., de Anda, J., Xia, A., Zhao, K., et al. (2019). Heterogeneity in surface sensing suggests a division of labor in Pseudomonas aeruginosa populations. *Elife*, *8*.

Arnold, R. G. (1962). Equilibrium relations between pyrrhotite and pyrite from 325 degrees to 743 degrees C. *Economic Geology*, *57*(1), 72–90. https://doi.org/10.2113/gsecongeo.57.1.72

Arnold, R. G. (1966). Mixtures of hexagonal and monoclinic pyrrhotite and the measurement of the metal content of pyrrhotite by X-ray diffraction. *American Mineralogist: Journal of Earth and Planetary Materials*, *51*(7), 1221–1227.

Arnold, R. G. (1967). Range in composition and structure of 82 natural terrestrial pyrrhotites. *The Canadian Mineralogist*, *9*(1), 31–50.

Aronson, H. S., Monteverde, D. R., Barnes, B. D., Johnson, B. R., Zawaski, M. J., Speth, D. R., et al. (2022). Sulfur cycling at natural hydrocarbon and sulfur seeps in Santa Paula Creek, CA. *Geobiology*, *20*(5), 707–725. https://doi.org/10.1111/gbi.12512

Atekwana, E. A., Mewafy, F. M., Abdel Aal, G., Werkema Jr., D. D., Revil, A., & Slater, L. D. (2014). High-resolution magnetic susceptibility measurements for investigating magnetic mineral formation during microbial mediated iron reduction. *Journal of Geophysical Research: Biogeosciences*, *119*(1), 80–94. https://doi.org/10.1002/2013JG002414

Aubourg, C., & Pozzi, J.-P. (2010). Toward a new <250°C pyrrhotite–magnetite geothermometer for claystones. *Earth and Planetary Science Letters*, *294*(1), 47–57. https://doi.org/10.1016/j.epsl.2010.02.045

Bădică, C. E., & Chiriță, P. (2015). An electrochemical study of the oxidative dissolution of iron monosulfide (FeS) in air-equilibrated solutions. *Electrochimica Acta*, *178*, 786–796. https://doi.org/10.1016/j.electacta.2015.08.093

Bailey, B. L., Blowes, D. W., Smith, L., & Sego, D. C. (2016). The Diavik Waste Rock Project: Geochemical and microbiological characterization of low sulfide content large-scale waste rock test piles. *Applied Geochemistry*, *65*, 54–72. https://doi.org/10.1016/j.apgeochem.2015.10.010

Baker, B. J., & Banfield, J. F. (2003). Microbial communities in acid mine drainage. *FEMS Microbiology Ecology*, *44*(2), 139–152. https://doi.org/10.1016/S0168-6496(03)00028-X

Baker-Austin, C., & Dopson, M. (2007). Life in acid: pH homeostasis in acidophiles. *Trends in Microbiology*, *15*(4), 165–171. https://doi.org/10.1016/j.tim.2007.02.005

Baranov, N. V., Ibrahim, P. N. G., Selezneva, N. V., Kazantsev, V. A., Volegov, A. S., & Shishkin, D. A. (2014). Crystal structure, phase transitions and magnetic properties of pyrrhotite-type compounds Fe7−xTixS8. *Physica B: Condensed Matter*, *449*, 229–235. https://doi.org/10.1016/j.physb.2014.05.040

Barco, R. A., Emerson, D., Sylvan, J. B., Orcutt, B. N., Jacobson Meyers, M. E., Ramírez, G. A., et al. (2015). New Insight into Microbial Iron Oxidation as Revealed by the Proteomic Profile of an Obligate Iron-Oxidizing Chemolithoautotroph. *Applied and Environmental Microbiology*, *81*(17), 5927–5937. https://doi.org/10.1128/AEM.01374-15

Beller, H. R., Chain, P. S. G., Letain, T. E., Chakicherla, A., Larimer, F. W., Richardson, P. M., et al. (2006). The Genome Sequence of the Obligately Chemolithoautotrophic, Facultatively Anaerobic Bacterium *Thiobacillus* denitrificans. *Journal of Bacteriology*, *188*(4), 1473–1488. https://doi.org/10.1128/JB.188.4.1473-1488.2006

Belzile, N., Chen, Y. W., Cai, M. F., & Li, Y. (2004). A review on pyrrhotite oxidation. *Journal of Geochemical Exploration*, *84*(2), 65–76. https://doi.org/10.1016/j.gexplo.2004.03.003

Benko, Z., Mogessie, A., Molnar, F., Severson, M. J., Hauck, S. A., & Rai, S. (2015). Partial Melting Processes and Cu-Ni-PGE Mineralization in the Footwall of the South Kawishiwi Intrusion at the Spruce Road Deposit, Duluth Complex, Minnesota. *Economic Geology*, *110*(5), 1269–1293. https://doi.org/10.2113/econgeo.110.5.1269

Bennett, C. E. G., & Graham, J. (1981). New observations on natural pyrrhotites: magnetic transition in hexagonal pyrrhotite. *American Mineralogist*, *66*(11–12), 1254–1257.

Berg, I. A. (2011). Ecological Aspects of the Distribution of Different Autotrophic CO2 Fixation Pathways. *Applied and Environmental Microbiology*, *77*(6), 1925–1936. https://doi.org/10.1128/AEM.02473-10

van Berkum, P., & Fuhrmann, J. J. (2000). Evolutionary relationships among the soybean bradyrhizobia reconstructed from 16S rRNA gene and internally transcribed spacer region sequence divergence. *International Journal of Systematic and Evolutionary Microbiology*, *50*(6), 2165–2172. https://doi.org/10.1099/00207713-50-6-2165

Bertaut, E. F. (1953). Contribution à l'étude des structures lacunaires: la pyrrhotine. *Acta Crystallographica*, *6*(6), 557–561. https://doi.org/10.1107/S0365110X53001502

Besnus, M. J., & Meyer, A. J. (1964). Nouvelles données expérimentales sur le magnétisme de la pyrrhotine naturelle. *Proceedings of the International Conference on Magnetism*, *20*, 507–511.

Bin, M., & Pauthenet, R. (1963). Magnetic Anisotropy in Pyrrhotite. *Journal of Applied Physics*, *34*(4), 1161–1162. https://doi.org/10.1063/1.1729413

Bonnefoy, V., & Holmes, D. S. (2012). Genomic insights into microbial iron oxidation and iron uptake strategies in extremely acidic environments: Iron oxidation and iron homeostasis in acidophiles. *Environmental Microbiology*, *14*(7), 1597–1611. https://doi.org/10.1111/j.1462-2920.2011.02626.x

Bonnichsen, B. (1974). *Information Circular 10. Copper and Nickel Resources in the Duluth Complex, Northeastern Minnesota* (Map). Minnesota Geological Survey. Retrieved from http://conservancy.umn.edu/handle/11299/59299

Bontognali, T. R. R., Sessions, A. L., Allwood, A. C., Fischer, W. W., Grotzinger, J. P., Summons, R. E., & Eiler, J. M. (2012). Sulfur isotopes of organic matter preserved in 3.45-billion-year-old stromatolites reveal microbial metabolism. *Proceedings of the National Academy of Sciences*, *109*(38), 15146–15151. https://doi.org/10.1073/pnas.1207491109

Bornhorst, T. J., & Mathur, R. (2017). Copper isotope constraints on the genesis of the Keweenaw Peninsula native copper district, Michigan, USA. *Minerals*, *7*(10), 185.
Boughanemi, S., Lyonnet, J., Infossi, P., Bauzan, M., Kosta, A., Lignon, S., et al. (2016). Microbial oxidative sulfur metabolism: biochemical evidence of the membrane-bound heterodisulfide reductase-like complex of the bacterium Aquifex aeolicus. *FEMS Microbiology Letters*, *363*(15), fnw156. https://doi.org/10.1093/femsle/fnw156
Boughanemi, S., Infossi, P., Giudici-Orticoni, M.-T., Schoepp-Cothenet, B., & Guiral, M. (2020). Sulfite oxidation by the quinone-reducing molybdenum sulfite dehydrogenase *SoeABC* from the bacterium Aquifex aeolicus. *Biochimica et Biophysica Acta (BBA) - Bioenergetics*, *1861*(11), 148279. https://doi.org/10.1016/j.bbabio.2020.148279
Bragg, W. H. (1915). The Structure of Magnetite and the Spinels. *Nature*, *95*(2386), 561–561. https://doi.org/10.1038/095561a0
Brake, S. S., Dannelly, H. K., Connors, K. A., & Hasiotis, S. T. (2001). Influence of water chemistry on the distribution of an acidophilic protozoan in an acid mine drainage system at the abandoned Green Valley coal mine, Indiana, USA. *Applied Geochemistry*, *16*(14), 1641–1652. https://doi.org/10.1016/S0883-2927(01)00033-6
Brierley, C. L., & Brierley, J. A. (2013). Progress in bioleaching: part B: applications of microbial processes by the minerals industries. *Applied Microbiology and Biotechnology*, *97*(17), 7543–7552. https://doi.org/10.1007/s00253-013-5095-3
Bright, R. M., Amato, J. M., Denyszyn, S. W., & Ernst, R. E. (2014). U-Pb geochronology of 1.1 Ga diabase in the southwestern United States: Testing models for the origin of a post-Grenville large igneous province. *Lithosphere*, *6*(3), 135–156. https://doi.org/10.1130/L335.1
Brune, K., & Bayer, T. (2012). Engineering microbial consortia to enhance biomining and bioremediation. *Frontiers in Microbiology*, *3*. Retrieved from https://www.frontiersin.org/article/10.3389/fmicb.2012.00203
Buckley, A. N., & Woods, R. (1985). X-ray photoelectron spectroscopy of oxidized pyrrhotite surfaces. *Applications of Surface Science*, *22–23*, 280–287. https://doi.org/10.1016/0378-5963(85)90061-3
Buerger, M. J. (1931). The crystal structure of marcasite. *American Mineralogist*, *16*(9), 361–395.
Bugajski, J., & Gamsjäger, H. (1982). The kinetics of the dissolution of monoclinic pyrrhotite in aqueous acidic solutions. *Monatshefte Fur Chemie Chemical Monthly*, *113*(10), 1087–1092. https://doi.org/10.1007/BF00808622
Butterfield, C. N., Li, Z., Andeer, P. F., Spaulding, S., Thomas, B. C., Singh, A., et al. (2016). Proteogenomic analyses indicate bacterial methylotrophy and archaeal heterotrophy are prevalent below the grass root zone. *PeerJ*, *4*, e2687. https://doi.org/10.7717/peerj.2687
Bwapwa, J. K., Jaiyeola, A. T., & Chetty, R. (2017). Bioremediation of acid mine drainage using algae strains: A review. *South African Journal of Chemical Engineering*, *24*, 62–70. https://doi.org/10.1016/j.sajce.2017.06.005
Cannon, W. F. (1992). The Midcontinent Rift in the Lake Superior region with emphasis on its geodynamic evolution. *Tectonophysics*, *213*(1–2), 41–48. https://doi.org/10.1016/0040-1951(92)90250-A
Cannon, W. F., Peterman, Z. E., & Sims, P. K. (1993). Crustal-scale thrusting and origin of the Montreal River monocline-A 35-km-thick cross section of the midcontinent rift in northern Michigan and Wisconsin. *Tectonics*, *12*(3), 728–744. https://doi.org/10.1029/93TC00204
Capone, D. G., & Kiene, R. P. (1988). Comparison of microbial dynamics in marine and freshwater sediments: Contrasts in anaerobic carbon catabolism1. *Limnology and Oceanography*, *33*(4part2), 725–749. https://doi.org/10.4319/lo.1988.33.4part2.0725
Carlson, H. K., Youngblut, M. D., Redford, S. A., Williamson, A. J., & Coates, J. D. (2021). Sulfate adenylyl transferase kinetics and mechanisms of metabolic inhibitors of microbial sulfate respiration. *ISME Communications*, *1*(1), 1–4. https://doi.org/10.1038/s43705-021-00069-1
Casiot, C., Bruneel, O., Personné, J.-C., Leblanc, M., & Elbaz-Poulichet, F. (2004). Arsenic oxidation and bioaccumulation by the acidophilic protozoan, Euglena mutabilis, in acid mine drainage (Carnoulès, France). *Science of The Total Environment*, *320*(2), 259–267. https://doi.org/10.1016/j.scitotenv.2003.08.004
Castelle, C., Guiral, M., Malarte, G., Ledgham, F., Leroy, G., Brugna, M., & Giudici-Orticoni, M.-T. (2008). A New Iron-oxidizing/O2-reducing Supercomplex Spanning Both Inner and Outer

Membranes, Isolated from the Extreme Acidophile Acidi*Thiobacillus* ferrooxidans*. *Journal of Biological Chemistry*, *283*(38), 25803–25811. https://doi.org/10.1074/jbc.M802496200
Cavaletti, L., Monciardini, P., Bamonte, R., Schumann, P., Rohde, M., Sosio, M., & Donadio, S. (2006). New Lineage of Filamentous, Spore-Forming, Gram-Positive Bacteria from Soil. *Applied and Environmental Microbiology*, *72*(6), 4360–4369. https://doi.org/10.1128/AEM.00132-06
Chandra, A. P., & Gerson, A. R. (2010). The mechanisms of pyrite oxidation and leaching: A fundamental perspective. *Surface Science Reports*, *65*(9), 293–315. https://doi.org/10.1016/j.surfrep.2010.08.003
Chang, L., Roberts, A. P., Tang, Y., Rainford, B. D., Muxworthy, A. R., & Chen, Q. (2008). Fundamental magnetic parameters from pure synthetic greigite (Fe3S4). *Journal of Geophysical Research: Solid Earth*, *113*(B6). https://doi.org/10.1029/2007JB005502
Chang, Y., Land, M., Hauser, L., Chertkov, O., Glavina Del Rio, T., Nolan, M., et al. (2011). Non-contiguous finished genome sequence and contextual data of the filamentous soil bacterium Ktedonobacter racemifer type strain (SOSP1-21T). *Standards in Genomic Sciences*, *5*(1), 97–111. https://doi.org/10.4056/sigs.2114901
Charilaou, M., Kind, J., Koulialias, D., Weidler, P. G., Mensing, C., Löffler, J. F., & Gehring, A. U. (2015). Magneto-electronic coupling in modulated defect-structures of natural Fe $_{1-x}$ S. *Journal of Applied Physics*, *118*(8), 083903. https://doi.org/10.1063/1.4929634
Chen, I.-M. A., Chu, K., Palaniappan, K., Ratner, A., Huang, J., Huntemann, M., et al. (2021). The IMG/M data management and analysis system v.6.0: new tools and advanced capabilities. *Nucleic Acids Research*, *49*(D1), D751–D763. https://doi.org/10.1093/nar/gkaa939
Chen, L., Li, J., Chen, Y., Huang, L., Hua, Z., Hu, M., & Shu, W. (2013). Shifts in microbial community composition and function in the acidification of a lead/zinc mine tailings. *Environmental Microbiology*, *15*(9), 2431–2444. https://doi.org/10.1111/1462-2920.12114
Chen, S., Rudra, B., & Gupta, R. S. (2021). Phylogenomics and molecular signatures support division of the order Neisseriales into emended families Neisseriaceae and Chromobacteriaceae and three new families Aquaspirillaceae fam. nov., Chitinibacteraceae fam. nov., and Leeiaceae fam. nov. *Systematic and Applied Microbiology*, *44*(6), 126251. https://doi.org/10.1016/j.syapm.2021.126251
Chen, Y.-H., Chen, Y.-H., Hsu, W.-D., Chang, Y.-C., Sheu, H.-S., Lee, J.-J., & Lin, S.-K. (2019). Using the high-temperature phase transition of iron sulfide minerals as an indicator of fault slip temperature. *Scientific Reports*, *9*(1), 7950. https://doi.org/10.1038/s41598-019-44319-8
Chiriță, P. (2016). Aqueous Oxidation of Iron Monosulfide (FeS) by Molecular Oxygen. *Mineral Processing and Extractive Metallurgy Review*, *37*(5), 305–310. https://doi.org/10.1080/08827508.2016.1218866
Chiriță, P., & Rimstidt, J. D. (2014). Pyrrhotite dissolution in acidic media. *Applied Geochemistry*, *41*, 1–10. https://doi.org/10.1016/j.apgeochem.2013.11.013
Cline, J. D. (1969). Spectrophotometric determination of hydrogen sulfide in natural waters 1. *Limnology and Oceanography*, *14*(3), 454–458.
Cooper, V. S., Staples, R. K., Traverse, C. C., & Ellis, C. N. (2014). Parallel evolution of small colony variants in Burkholderia cenocepacia biofilms. *Genomics*, *104*(6, Part A), 447–452. https://doi.org/10.1016/j.ygeno.2014.09.007
Cruz, R., González, I., & Monroy, M. (2005). Electrochemical characterization of pyrrhotite reactivity under simulated weathering conditions. *Applied Geochemistry*, *20*(1), 109–121. https://doi.org/10.1016/j.apgeochem.2004.07.007
Dahl, C., Kredich, N. M., Deutzmann, R., & Trlfper, H. G. Y. 1993. (1993). Dissimilatory sulphite reductase from Archaeoglobus fulgidus: physico-chemical properties of the enzyme and cloning, sequencing and analysis of the reductase genes. *Microbiology*, *139*(8), 1817–1828. https://doi.org/10.1099/00221287-139-8-1817
Dahl, C., Prange, A., & Steudel, R. (2005). Metabolism of Natural Polymeric Sulfur Compounds. In *Biopolymers Online*. John Wiley & Sons, Ltd. https://doi.org/10.1002/3527600035.bpol9002
Dahl, C., Franz, B., Hensen, D., Kesselheim, A., & Zigann, R. (2013). Sulfite oxidation in the purple sulfur bacterium Allochromatium vinosum: identification of *SoeABC* as a major player and relevance of SoxYZ in the process. *Microbiology*, *159*(Pt_12), 2626–2638. https://doi.org/10.1099/mic.0.071019-0

D'Angeli, I. M., Ghezzi, D., Leuko, S., Firrincieli, A., Parise, M., Fiorucci, A., et al. (2019). Geomicrobiology of a seawater-influenced active sulfuric acid cave. *PLOS ONE*, *14*(8), e0220706. https://doi.org/10.1371/journal.pone.0220706

Daniels, P. A., Jr. (1982). 7C: Upper Precambrian sedimentary rocks: Oronto Group, Michigan- Wisconsin. In R. J. Wold & W. J. Hinze (Eds.), *Geology and Tectonics of the Lake Superior Basin* (Vol. 156, p. 0). Geological Society of America. https://doi.org/10.1130/MEM156-p107

Das, B. K., Roy, A., Koschorreck, M., Mandal, S. M., Wendt-Potthoff, K., & Bhattacharya, J. (2009). Occurrence and role of algae and fungi in acid mine drainage environment with special reference to metals and sulfate immobilization. *Water Research*, *43*(4), 883–894. https://doi.org/10.1016/j.watres.2008.11.046

Database resources of the National Center for Biotechnology Information. (2016). *Nucleic Acids Research*, *44*(Database issue), D7–D19. https://doi.org/10.1093/nar/gkv1290

De Villiers, J., & Liles, D. C. (2010). The crystal-structure and vacancy distribution in 6C pyrrhotite. *American Mineralogist*, *95*(1), 148–152. https://doi.org/10.2138/am.2010.3266

De Villiers, J., Liles, D. C., & Becker, M. (2009). The crystal structure of a naturally occurring 5C pyrrhotite from sudbury, its chemistry, and vacancy distribution. *American Mineralogist*, *94*(10), 1405–1410. https://doi.org/10.2138/am.2009.3081

Dekkers, M. J. (1990). Magnetic monitoring of pyrrhotite alteration during thermal demagnetization. *Geophysical Research Letters*, *17*(6), 779–782. https://doi.org/10.1029/GL017i006p00779

Dekkers, Mark J. (1988). Magnetic properties of natural pyrrhotite Part I: Behaviour of initial susceptibility and *sat*uration-magnetization-related rock-magnetic parameters in a grain-size dependent framework. *Physics of the Earth and Planetary Interiors*, *52*(3–4), 376–393. https://doi.org/10.1016/0031-9201(88)90129-X

Dekkers, M.J. (1989). Magnetic properties of natural pyrrhotite. II. High- and low-temperature behaviour of Jrs and TRM as function of grain size. *Physics of the Earth and Planetary Interiors*, *57*(3–4), 266–283. https://doi.org/10.1016/0031-9201(89)90116-7

Delmont, T. O., Eren, A. M., Maccario, L., Prestat, E., Esen, Ö. C., Pelletier, E., et al. (2015). Reconstructing rare soil microbial genomes using in situ enrichments and metagenomics. *Frontiers in Microbiology*, *6*. Retrieved from https://www.frontiersin.org/articles/10.3389/fmicb.2015.00358

Diao, M., Sinnige, R., Kalbitz, K., Huisman, J., & Muyzer, G. (2017). Succession of Bacterial Communities in a Seasonally Stratified Lake with an Anoxic and Sulfidic Hypolimnion. *Frontiers in Microbiology*, *8*. Retrieved from https://www.frontiersin.org/articles/10.3389/fmicb.2017.02511

Dietrich, W., & Klimmek, O. (2002). The function of methyl-menaquinone-6 and polysulfide reductase membrane anchor (PsrC) in polysulfide respiration of Wolinella succinogenes. *European Journal of Biochemistry*, *269*(4), 1086–1095. https://doi.org/10.1046/j.0014-2956.2001.02662.x

Dirren, S., & Posch, T. (2016). Promiscuous and specific bacterial symbiont acquisition in the amoeboid genus Nuclearia (Opisthokonta). *FEMS Microbiology Ecology*, *92*(8), fiw105. https://doi.org/10.1093/femsec/fiw105

Dixon, P. (2003). VEGAN, A Package of R Functions for Community Ecology. *Journal of Vegetation Science*, *14*(6), 927–930.

Dobritsa, A. P., & Samadpour, M. (2016). Transfer of eleven species of the genus Burkholderia to the genus Paraburkholderia and proposal of Caballeronia gen. nov. to accommodate twelve species of the genera Burkholderia and Paraburkholderia. *International Journal of Systematic and Evolutionary Microbiology*, *66*(8), 2836–2846. https://doi.org/10.1099/ijsem.0.001065

Dockrey, J. W., Lindsay, M. B. J., Mayer, K. U., Beckie, R. D., Norlund, K. L. I., Warren, L. A., & Southam, G. (2014). Acidic Microenvironments in Waste Rock Characterized by Neutral Drainage: Bacteria–Mineral Interactions at Sulfide Surfaces. *Minerals*, *4*(1), 170–190. https://doi.org/10.3390/min4010170

Dorogina, G. A., Gulyaeva, R. I., Selivanov, E. N., & Balakirev, V. F. (2015). Thermal and thermomagnetic properties of pyrrhotites. *Russian Journal of Inorganic Chemistry*, *60*(3), 301–306. https://doi.org/10.1134/S003602361503002X

Drahovzal, J. A., Harris, D. C., Wickstrom, L. H., Walker, D., Baranoski, M. T., Keith, B., & Furer, L. C. (1992). *The East Continent Rift Basin: A New Discovery*. Kentucky Geological Survey, University of Kentucky, Lexington.

Drobner, E., Huber, H., Rachel, R., & Stetter, K. O. (1991). *Thiobacillus* plumbophilus spee. nov., a novel galena and hydrogen oxidizer, 5.

Dufréchou, G., & Harris, L. B. (2013). Tectonic models for the origin of regional transverse structures in the Grenville Province of SW Quebec interpreted from regional gravity. *Journal of Geodynamics*, *64*, 15–39. https://doi.org/10.1016/j.jog.2012.12.001

Dugan, P. R., & Apel, W. A. (1983). Bacteria and Acidic Drainage from Coal Refuse: Inhibition by Sodium Lauryl Sulfate and Sodium Benzoate. *Applied and Environmental Microbiology*, *46*(1), 279–282. https://doi.org/10.1128/aem.46.1.279-282.1983

Dunlop, D. J., & Özdemir, Ö. (2001). *Rock Magnetism: Fundamentals and Frontiers*. Cambridge University Press.

Eckstrand, O. R., & Hulbert, L. J. (2007). Magmatic nickel-copper-platinum group element deposits. In W. D. Goodfellow (Ed.), *Mineral Deposits of Canada: A Synthesis of Major Deposit Types, District Metallogeny, the Evolution of Geological Provinces, and Exploration Methods* (pp. 205–222). Geological Association of Canada, Mineral Deposits Division.

Edgar, R. C. (2013). UPARSE: highly accurate OTU sequences from microbial amplicon reads. *Nature Methods*, *10*(10), 996–998. https://doi.org/10.1038/nmeth.2604

Edwards, K. J., Goebel, B. M., Rodgers, T. M., Schrenk, M. O., Gihring, T. M., Cardona, M. M., et al. (1999). Geomicrobiology of Pyrite (FeS2) Dissolution: Case Study at Iron Mountain, California. *Geomicrobiology Journal*, *16*(2), 155–179. https://doi.org/10.1080/014904599270668

Edwards, K. J., Bond, P. L., Druschel, G. K., McGuire, M. M., Hamers, R. J., & Banfield, J. F. (2000). Geochemical and biological aspects of sulfide mineral dissolution: lessons from Iron Mountain, California. *Chemical Geology*, *169*(3–4), 383–397. https://doi.org/10.1016/S0009-2541(00)00216-3

Edwardson, C. F., & Hollibaugh, J. T. (2017). Metatranscriptomic analysis of prokaryotic communities active in sulfur and arsenic cycling in Mono Lake, California, USA. *ISME Journal*, *11*(10), 2195–2208. https://doi.org/10.1038/ismej.2017.80

Elliot, A. D. (2010). Structure of pyrrhotite 5C (Fe9S10). *Acta Crystallographica Section B: Structural Science*, *66*(3), 271–279. https://doi.org/10.1107/S0108768110011845

Evans, H. T. (1970). Lunar troilite: crystallography. *Science (New York, N.Y.)*, *167*(3918), 621–623. https://doi.org/10.1126/science.167.3918.621

Feinberg, J. M., Solheid, P. A., Swanson-Hysell, N. L., Jackson, M. J., & Bowles, J. A. (2015). Full vector low-temperature magnetic measurements of geologic materials. *Geochemistry, Geophysics, Geosystems*, *16*(1), 301–314. https://doi.org/10.1002/2014GC005591

Fike, D. A., Bradley, A. S., & Rose, C. V. (2015). Rethinking the Ancient Sulfur Cycle. *Annual Review of Earth and Planetary Sciences*, *43*(1), 593–622. https://doi.org/10.1146/annurev-earth-060313-054802

Fleet, M. E. (1971). The crystal structure of a pyrrhotite (Fe7S8). *Acta Crystallographica Section B Structural Crystallography and Crystal Chemistry*, *27*(10), 1864–1867. https://doi.org/10.1107/S0567740871004990

Fleet, M. E., & Macrae, N. (1969). Two-phase hexagonal pyrrhotites. *The Canadian Mineralogist*. Retrieved from http://canmin.geoscienceworld.org/content/9/5/699.short

Flood, B. E., Jones, D. S., & Bailey, J. V. (2015). Sedimenticola thiotaurini sp. nov., a sulfur-oxidizing bacterium isolated from salt marsh sediments, and emended descriptions of the genus Sedimenticola and Sedimenticola selenatireducens. *International Journal of Systematic and Evolutionary Microbiology*, *65*(Pt_8), 2522–2530. https://doi.org/10.1099/ijs.0.000295

Franklin, J. M., McIlwaine, W. H., Poulsen, K. H., & Wanless, R. K. (1980). Stratigraphy and depositional setting of the Sibley Group, Thunder Bay district, Ontario, Canada. *Canadian Journal of Earth Sciences*, *17*(5), 633–651. https://doi.org/10.1139/e80-060

Freitas, A. P. P., Schneider, I. A. H., & Schwartzbold, A. (2011). Biosorption of heavy metals by algal communities in water streams affected by the acid mine drainage in the coal-mining region of Santa Catarina state, Brazil. *Minerals Engineering*, *24*(11), 1215–1218. https://doi.org/10.1016/j.mineng.2011.04.013

Friedrich, C. G., Rother, D., Bardischewsky, F., Quentmeier, A., & Fischer, J. (2001). Oxidation of Reduced Inorganic Sulfur Compounds by Bacteria: Emergence of a Common Mechanism?

Applied and Environmental Microbiology, *67*(7), 2873–2882. https://doi.org/10.1128/AEM.67.7.2873-2882.2001

Friedrich, C. G., Bardischewsky, F., Rother, D., Quentmeier, A., & Fischer, J. (2005). Prokaryotic sulfur oxidation. *Current Opinion in Microbiology*, *8*(3), 253–259. https://doi.org/10.1016/j.mib.2005.04.005

Fritz, G., Roth, A., Schiffer, A., Buchert, T., Bourenkov, G., Bartunik, H. D., et al. (2002). Structure of adenylylsulfate reductase from the hyperthermophilic Archaeoglobus fulgidus at 1.6-A resolution. *Proceedings of the National Academy of Sciences*, *99*(4), 1836–1841. https://doi.org/10.1073/pnas.042664399

Fu, R. R., Volk, M. W. R., Bilardello, D., Libourel, G., Lesur, G., & Ben Dor, O. (2021). The Fine-Scale Magnetic History of the Allende Meteorite: Implications for the Structure of the SolarNebula. In *Lunar and Planetary Science Conference* (p. 2727).

Gál, B., Molnár, F., & Peterson, D. M. (2011). Cu-Ni-PGE Mineralization in the South Filson Creek Area, South Kawishiwi Intrusion, Duluth Complex: Mineralization Styles and Magmatic and Hydrothermal Processes. *Economic Geology*, *106*(3), 481–509. https://doi.org/10.2113/econgeo.106.3.481

Garber, Arkadiy I., Nealson, K. H., Okamoto, A., McAllister, S. M., Chan, C. S., Barco, R. A., & Merino, N. (2020). FeGenie: A Comprehensive Tool for the Identification of Iron Genes and Iron Gene Neighborhoods in Genome and Metagenome Assemblies. *Frontiers in Microbiology*, *11*. Retrieved from https://www.frontiersin.org/articles/10.3389/fmicb.2020.00037

Garber, Arkaidy I., Merino, N., Pavia, M. J., & McAllister, S. M. (2020). MagicLamp: toolkit for annotation of 'omics datasets using curated HMM sets. Retrieved from https://github.com/Arkadiy-Garber/MagicLamp

García-Fraile, P., Benada, O., Cajthaml, T., Baldrian, P., & Lladó, S. (2016). Terracidiphilus gabretensis gen. nov., sp. nov., an Abundant and Active Forest Soil Acidobacterium Important in Organic Matter Transformation. *Applied and Environmental Microbiology*, *82*(2), 560–569. https://doi.org/10.1128/AEM.03353-15

Gilder, S. A., Egli, R., Hochleitner, R., Roud, S. C., Volk, M. W. R., Goff, M. L., & Wit, M. de. (2011). Anatomy of a pressure-induced, ferromagnetic-to-paramagnetic transition in pyrrhotite: Implications for the formation pressure of diamonds. *Journal of Geophysical Research: Solid Earth*, *116*(B10). https://doi.org/10.1029/2011JB008292

Gisselmann, G., Klausmeier, P., & Schwenn, J. D. (1993). The ferredoxin:sulphite reductase gene from Synechococcus PCC7942. *Biochimica et Biophysica Acta (BBA) - Bioenergetics*, *1144*(1), 102–106. https://doi.org/10.1016/0005-2728(93)90037-G

Gomez-Alvarez, V., King, G. M., & Nüsslein, K. (2007). Comparative bacterial diversity in recent Hawaiian volcanic deposits of different ages. *FEMS Microbiology Ecology*, *60*(1), 60–73. https://doi.org/10.1111/j.1574-6941.2006.00253.x

Graham, A. R. (1969). Quantitative determination of hexagonal and monoclinic pyrrhotites by X-ray diffraction. *The Canadian Mineralogist*, *10*(1), 4–24.

Green, J. C. (1983). Geologic and geochemical evidence for the nature and development of the middle proterozoic (keweenawan) midcontinent Rift of north america. *Tectonophysics*, *94*(1), 413–437. https://doi.org/10.1016/0040-1951(83)90027-6

Green, J. C. (1989). Physical volcanology of mid-Proterozoic plateau lavas: The Keweenawan North Shore Volcanic Group, Minnesota. *GSA Bulletin*, *101*(4), 486–500. https://doi.org/10.1130/0016-7606(1989)101<0486:PVOMPP>2.3.CO;2

Grønvold, F., & Haraldsen, H. (1952). On the Phase relation of Synthetic and Natural Pyrrhotites(Fe1-xS). *Acta Chemica Scandinavica*.

Grønvold, F., Stølen, S., Labban, A. K., & Westrum, E. F. (1991). Thermodynamics of iron sulfides I. Heat capacity and thermodynamic properties of Fe9S10 at temperatures from 5 K to 740 K. *The Journal of Chemical Thermodynamics*, *23*(3), 261–272. https://doi.org/10.1016/S0021-9614(05)80184-3

Gruzdev, E. V., Beletsky, A. V., Kadnikov, V. V., Mardanov, A. V., Ivanov, M. V., Karnachuk, O. V., & Ravin, N. V. (2020). Diversity of Eukaryotic Microorganisms in the Drainage Waters of a Coal Open-Cast Mine. *Microbiology*, *89*(5), 641–646. https://doi.org/10.1134/S0026261720050100

Haines, C., Dutton, S. E., Volk, M. W. R., & Carpenter, M. A. (2020). Magnetoelastic properties and behaviour of 4C pyrrhotite, Fe7S8, through the Besnus transition. *Journal of Physics: Condensed Matter*. https://doi.org/10.1088/1361-648X/ab8fd3

Haines, C. R. S., Howard, C. J., Harrison, R. J., & Carpenter, M. A. (2019). Group-theoretical analysis of structural instability, vacancy ordering and magnetic transitions in the system troilite (FeS)–pyrrhotite (Fe $_{1-x}$ S). *Acta Crystallographica Section B Structural Science, Crystal Engineering and Materials*, *75*(6), 1208–1224. https://doi.org/10.1107/S2052520619014197

Haines, C. R. S., Lampronti, G. I., Klooster, W. T., Coles, S. J., Dutton, S. E., & Carpenter, M. A. (2020). Morin-type transition in 5C pyrrhotite. *American Mineralogist*, *105*(9), 1404–1411. https://doi.org/10.2138/am-2020-7266

Hamilton, I. C., & Woods, R. (1981). An investigation of surface oxidation of pyrite and pyrrhotite by linear potential sweep voltammetry. *Journal of Electroanalytical Chemistry and Interfacial Electrochemistry*, *118*, 327–343. https://doi.org/10.1016/S0022-0728(81)80551-7

Hamilton, T. L., Welander, P. V., Albrecht, H. L., Fulton, J. M., Schaperdoth, I., Bird, L. R., et al. (2017). Microbial communities and organic biomarkers in a Proterozoic-analog sinkhole. *Geobiology*, *15*(6), 784–797. https://doi.org/10.1111/gbi.12252

Hamilton, Trinity L., Jones, D. S., Schaperdoth, I., & Macalady, J. L. (2014). Metagenomic insights into S(0) precipitation in a terrestrial subsurface lithoautotrophic ecosystem. *Frontiers in Microbiology*, *5*(DEC), 1–16. https://doi.org/10.3389/fmicb.2014.00756

Haraldsen, H. (1937). Magnetochemische Untersuchungen. XXIV. Eine thermomagnetische Untersuchung der Umwandlungen im Troilit-Pyrrhotin-Gebiet des Eisen-Schwefel-Systems. *Zeitschrift für anorganische und allgemeine Chemie*, *231*(1–2), 78–96. https://doi.org/10.1002/zaac.19372310110

Harries, D. (2012). *Structure and Reactivity of Terrestrial and Extraterrestrial Pyrrhotite*. University of Bayreuth. Retrieved from https://epub.uni-bayreuth.de/238/

Harries, D., Pollok, K., & Langenhorst, F. (2011). Translation interface modulation in NC-pyrrhotites: Direct imaging by TEM and a model toward understanding partially disordered structural states. *American Mineralogist*, *96*(5–6), 716–731. https://doi.org/10.2138/am.2011.3644

Harries, D., Pollok, K., & Langenhorst, F. (2013). Oxidative dissolution of 4C- and NC-pyrrhotite: Intrinsic reactivity differences, pH dependence, and the effect of anisotropy. *Geochimica et Cosmochimica Acta*, *102*, 23–44. https://doi.org/10.1016/j.gca.2012.10.021

Hauck, S. A., Severson, M. J., Zanko, L. M., Barnes, S. J., Morton, P., Alminas, H. V., et al. (1997). An overview of the geology and oxide, sulfide, and platinum-group element mineralization along the western and northern contacts of the Duluth Complex. In R. W. Ojakangas, A. B. Dickas, & J. C. Green (Eds.), *Middle Proterozoic to Cambrian rifting, central North America* (Vol. 312, p. 0). Geological Society of America. https://doi.org/10.1130/0-8137-2312-4.137

Heaman, L. M., & Machado, N. (1992). Timing and origin of midcontinent rift alkaline magmatism, North America: evidence from the Coldwell Complex. *Contributions to Mineralogy and Petrology*, *110*(2), 289–303. https://doi.org/10.1007/BF00310744

Hensel, M., Hinsley, A. P., Nikolaus, T., Sawers, G., & Berks, B. C. (1999). The genetic basis of tetrathionate respiration in Salmonella typhimurium. *Molecular Microbiology*, *32*(2), 275–287. https://doi.org/10.1046/j.1365-2958.1999.01345.x

Herbert, F. W., Krishnamoorthy, A., Yildiz, B., & Van Vliet, K. J. (2015). Diffusion-limited kinetics of the antiferromagnetic to ferrimagnetic lambda-transition in Fe1-xS. *Applied Physics Letters*, *106*(9). https://doi.org/10.1063/1.4913201

Hickman, J. W., Tifrea, D. F., & Harwood, C. S. (2005). A chemosensory system that regulates biofilm formation through modulation of cyclic diguanylate levels. *Proceedings of the National Academy of Sciences*, *102*(40), 14422–14427. https://doi.org/10.1073/pnas.0507170102

Hinze, W. J., & Chandler, V. W. (2020). Reviewing the configuration and extent of the Midcontinent rift system. *Precambrian Research*, *342*, 105688. https://doi.org/10.1016/j.precamres.2020.105688

Hobart, Kathryn K., Feinberg, J. M., Jones, D. S., & Volk, M. W. R. (2021). X-Ray Diffraction Data with Temperature for Two Mixed Polytype Pyrrhotite Samples [Data set]. Retrieved from http://conservancy.umn.edu/handle/11299/222247

Hobart, Kathryn Kiku, Feinberg, J. M., Volk, M. W. R., & Jones, D. S. (2021). The importance of temperature-dependent diffraction data in understanding magnetic changes across the pyrrhotite λ-transition. *Earth and Space Science Open Archive*. https://doi.org/10.1002/essoar.10507692.1

Hoffmann, V., Stanjek, H., & Murad, E. (1993). Mineralogical, magnetic and mössbauer data of symthite (Fe9S11). *Studia Geophysica et Geodaetica*, *37*(4), 366–381. https://doi.org/10.1007/BF01613583

Holmer, M., & Storkholm, P. (2001). Sulphate reduction and sulphur cycling in lake sediments: a review. *Freshwater Biology*, *46*(4), 431–451. https://doi.org/10.1046/j.1365-2427.2001.00687.x

Horiuchi, S., & Wada, H. (1971). Two-dimensional superstructure of hydrothermally synthesized pyrrhotite. *Acta Crystallographica*, *B27*, 504–505.

Horng, C.-S. (2018). Unusual Magnetic Properties of Sedimentary Pyrrhotite in Methane Seepage Sediments: Comparison With Metamorphic Pyrrhotite and Sedimentary Greigite. *Journal of Geophysical Research: Solid Earth*, *123*(6), 4601–4617. https://doi.org/10.1002/2017JB015262

Horng, C.-S., & Roberts, A. P. (2018). The low-temperature Besnus magnetic transition: Signals due to monoclinic and hexagonal pyrrhotite. *Geochemistry, Geophysics, Geosystems*, *19*(9), 3364–3375.

Horng, C.-S., Huh, C.-A., Chen, K.-H., Lin, C.-H., Shea, K.-S., & Hsiung, K.-H. (2012). Pyrrhotite as a tracer for denudation of the Taiwan orogen. *Geochemistry, Geophysics, Geosystems*, *13*(8). https://doi.org/10.1029/2012GC004195

Horng, C.-S., Roberts, A. P., Chen, Y.-H., Shea, K.-S., Chen, K.-H., Lin, C.-H., et al. (2020). Magnetic Properties of Sedimentary Smythite (Fe9S11). *Journal of Geophysical Research: Solid Earth*, *125*(6), e2019JB018812. https://doi.org/10.1029/2019JB018812

Horwood, J. L., Townsend, M. G., & Webster, A. H. (1976). Magnetic susceptibility of single-crystal Fe1−xS. *Journal of Solid State Chemistry*, *17*(1–2), 35–42. https://doi.org/10.1016/0022-4596(76)90198-5

Huber, H., & Stetter, K. O. (1990). *Thiobacillus cuprinus* sp. nov., a Novel Facultatively Organotrophic Metal-Mobilizing Bacterium. *Applied and Environmental Microbiology*, *56*(2), 315–322. https://doi.org/10.1128/aem.56.2.315-322.1990

Hutchinson, D. R., White, R. S., Cannon, W. F., & Schulz, K. J. (1990). Keweenaw hot spot: Geophysical evidence for a 1.1 Ga mantle plume beneath the Midcontinent Rift System. *Journal of Geophysical Research*, *95*(B7), 10869. https://doi.org/10.1029/JB095iB07p10869

Hyatt, D., Chen, G.-L., LoCascio, P. F., Land, M. L., Larimer, F. W., & Hauser, L. J. (2010). Prodigal: prokaryotic gene recognition and translation initiation site identification. *BMC Bioinformatics*, *11*(1), 119. https://doi.org/10.1186/1471-2105-11-119

Janzen, M. P., Nicholson, R. V., & Scharer, J. M. (2000). Pyrrhotite reaction kinetics: reaction rates for oxidation by oxygen, ferric iron, and for nonoxidative dissolution. *Geochimica et Cosmochimica Acta*, *64*(9), 1511–1522. https://doi.org/10.1016/S0016-7037(99)00421-4

Jin, L., Koulialias, D., Schnedler, M., Gehring, A. U., Pósfai, M., Ebert, P., et al. (2021). Atomic-Scale Characterization of Commensurate and Incommensurate Vacancy Superstructures in Natural Pyrrhotites. *American Mineralogist*, *106*(1), 82–96. https://doi.org/10.2138/am-2020-7479CCBY

Johnson, D. (2018). The Evolution, Current Status, and Future Prospects of Using Biotechnologies in the Mineral Extraction and Metal Recovery Sectors. *Minerals*, *8*(8), 343. https://doi.org/10.3390/min8080343

Johnson, D. B. (2014). Recent Developments in Microbiological Approaches for Securing Mine Wastes and for Recovering Metals from Mine Waters. *Minerals*, *4*(2), 279–292. https://doi.org/10.3390/min4020279

Johnson, D. B., Yajie, L., & Okibe, N. (2008). "Bioshrouding"—a novel approach for securing reactive mineral tailings. *Biotechnology Letters*, *30*(3), 445–449. https://doi.org/10.1007/s10529-007-9574-4

Johnson, L. S., Eddy, S. R., & Portugaly, E. (2010). Hidden Markov model speed heuristic and iterative HMM search procedure. *BMC Bioinformatics*, *11*(1), 431. https://doi.org/10.1186/1471-2105-11-431

Jones, D. S., Kohl, C., Grettenberger, C., Larson, L. N., Burgos, W. D., & Macalady, J. L. (2015). Geochemical Niches of Iron-Oxidizing Acidophiles in Acidic Coal Mine Drainage. *Applied and Environmental Microbiology*, *81*(4), 1242–1250. https://doi.org/10.1128/AEM.02919-14

Jones, D. S., Roepke, E. W., Hua, A. A., Flood, B. E., & Bailey, J. V. (2017). Complete genome sequence of *Sulfuriferula* sp. strain AH1, a sulfur- oxidizing autotroph isolated from weathered mine tailings

from the Duluth Complex in Minnesota. *Genome Announcements*, *5*(32), 17–18. https://doi.org/10.1128/genomeA.00673-17

Jones, D. S., Lapakko, K. A., Wenz, Z. J., Olson, M. C., Roepke, E. W., Sadowsky, M. J., et al. (2017). Novel microbial assemblages dominate weathered sulfide bearing rock from copper-nickel deposits in the Duluth Complex, Minnesota, USA. *Applied and Environmental Microbiology*, *83*(16), 1–15. https://doi.org/10.1128/AEM.00909-17

Jones, D. S., Monnier, G., Cooper, A., Baković, M., Pajović, G., Borovinić, N., & Tostevin, G. (2021). Applying high-throughput rRNA gene sequencing to assess microbial contamination of a 40-year old exposed archaeological profile. *Journal of Archaeological Science*, *126*, 105308. https://doi.org/10.1016/j.jas.2020.105308

Kadnikov, V. V., Gruzdev, E. V., Ivasenko, D. A., Beletsky, A. V., Mardanov, A. V., Danilova, E. V., et al. (2019). Selection of a Microbial Community in the Course of Formation of Acid Mine Drainage. *Microbiology*, *88*(3), 292–299. https://doi.org/10.1134/S0026261719030056

Kämpfer, P., Lodders, N., & Falsen, E. (2011). Hydrotalea flava gen. nov., sp. nov., a new member of the phylum Bacteroidetes and allocation of the genera Chitinophaga, Sediminibacterium, Lacibacter, Flavihumibacter, Flavisolibacter, Niabella, Niastella, Segetibacter, Parasegetibacter, Terrimonas, Ferruginibacter, Filimonas and Hydrotalea to the family Chitinophagaceae fam. nov. *International Journal of Systematic and Evolutionary Microbiology*, *61*(3), 518–523. https://doi.org/10.1099/ijs.0.023002-0

Kanao, T., Onishi, M., Kajitani, Y., Hashimoto, Y., Toge, T., Kikukawa, H., & Kamimura, K. (2018). Characterization of tetrathionate hydrolase from the marine acidophilic sulfur-oxidizing bacterium, Acidi*Thiobacillus* thiooxidans strain SH. *Bioscience, Biotechnology, and Biochemistry*, *82*(1), 152–160. https://doi.org/10.1080/09168451.2017.1415128

Kanehisa, M., *Sat*o, Y., Kawashima, M., Furumichi, M., & Tanabe, M. (2016). KEGG as a reference resource for gene and protein annotation. *Nucleic Acids Research*, *44*(D1), D457-462. https://doi.org/10.1093/nar/gkv1070

Kaneko, T., Nakamura, Y., *Sat*o, S., Asamizu, E., Kato, T., Sasamoto, S., et al. (2000). Complete Genome Structure of the Nitrogen-fixing Symbiotic Bacterium Mesorhizobium loti. *DNA Research*, *7*(6), 331–338. https://doi.org/10.1093/dnares/7.6.331

Kappler, U., & Dahl, C. (2001). Enzymology and molecular biology of prokaryotic sulfite oxidation. *FEMS Microbiology Letters*, *203*(1), 1–9. https://doi.org/10.1111/j.1574-6968.2001.tb10813.x

Kappler, U., Bennett, B., Rethmeier, J., Schwarz, G., Deutzmann, R., McEwan, A. G., & Dahl, C. (2000). Sulfite:Cytochrome *c* Oxidoreductase from *Thiobacillus novellus*: PURIFICATION, CHARACTERIZATION, AND MOLECULAR BIOLOGY OF A HETERODIMERIC MEMBER OF THE SULFITE OXIDASE FAMILY. *Journal of Biological Chemistry*, *275*(18), 13202–13212. https://doi.org/10.1074/jbc.275.18.13202

Kargi, H., & Barnes, C. G. (1995). A Grenville-age layered intrusion in the subsurface of west Texas: petrology, petrography, and possible tectonic setting. *Canadian Journal of Earth Sciences*, *32*(12), 2159–2166. https://doi.org/10.1139/e95-168

Keller-Besrest, F., Collin, G., & Comès, R. (1983). Structure and planar faults in the defective NiAs-type compound 3c Fe7S8. *Acta Crystallographica Section B: Structural Science*, *39*(3), 296–303. https://doi.org/10.1107/S0108768183002438

Kelly, D. P., Uchino, Y., Huber, H., Amils, R., & Wood, A. P. (2007). Reassessment of the phylogenetic relationships of *Thiomonas* cuprina. *International Journal of Systematic and Evolutionary Microbiology*, *57*(11), 2720–2724. https://doi.org/10.1099/ijs.0.65537-0

Kessler, C., Mhatre, E., Cooper, V., & Kim, W. (2021). Evolutionary Divergence of the *Wsp* Signal Transduction Systems in Beta- and Gammaproteobacteria. *Applied and Environmental Microbiology*, *87*(22), e01306-21. https://doi.org/10.1128/AEM.01306-21

Kim, M., Kang, O., Zhang, Y., Ren, L., Chang, X., Jiang, F., et al. (2016). Sphingoaurantiacus polygranulatus gen. nov., sp. nov., isolated from high-Arctic tundra soil, and emended descriptions of the genera Sandarakinorhabdus, Polymorphobacter and Rhizorhabdus and the species Sandarakinorhabdus limnophila, Rhizorhabdus argentea and Sphingomonas wittichii. *International Journal of Systematic and Evolutionary Microbiology*, *66*(1), 91–100. https://doi.org/10.1099/ijsem.0.000677

King, C. E., & King, G. M. (2014). Description of Thermogemmatispora carboxidivorans sp. nov., a carbon-monoxide-oxidizing member of the class Ktedonobacteria isolated from a geothermally heated biofilm, and analysis of carbon monoxide oxidation by members of the class Ktedonobacteria. *International Journal of Systematic and Evolutionary Microbiology*, *64*(Pt_4), 1244–1251. https://doi.org/10.1099/ijs.0.059675-0

Kissin, S. A., & Scott, S. D. (1982). Phase relations involving pyrrhotite below 350 degrees C. *Economic Geology*, *77*(7), 1739–1754. https://doi.org/10.2113/gsecongeo.77.7.1739

Klatt, J. M., Gomez-Saez, G. V., Meyer, S., Ristova, P. P., Yilmaz, P., Granitsiotis, M. S., et al. (2020). Vers*at*ile cyanobacteria control the timing and extent of sulfide production in a Proterozoic analog microbial mat. *The ISME Journal*, *14*(12), 3024–3037. https://doi.org/10.1038/s41396-020-0734-z

Kletzin, A. (1989). Coupled enzymatic production of sulfite, thiosulfate, and hydrogen sulfide from sulfur: purification and properties of a sulfur oxygenase reductase from the facultatively anaerobic archaebacterium Desulfurolobus ambivalens. *Journal of Bacteriology*, *171*(3), 1638–1643. https://doi.org/10.1128/JB.171.3.1638-1643.1989

Knight, K. S., Marshall, W. G., & Zochowski, S. W. (2011). THE LOW-TEMPERATURE AND HIGH-PRESSURE THERMOELASTIC AND STRUCTURAL PROPERTIES OF CHALCOPYRITE, CuFeS2. *The Canadian Mineralogist*, *49*(4), 1015–1034. https://doi.org/10.3749/canmin.49.4.1015

Kojima, H., Mochizuki, J., & Fukui, M. (2020). *Sulfuriferula* nivalis sp. nov., a sulfur oxidizer isolated from snow and emended description of *Sulfuriferula* plumbiphila. *International Journal of Systematic and Evolutionary Microbiology*, *70*(5), 3273–3277. https://doi.org/10.1099/ijsem.0.004166

Kontny, A., De Wall, H., Sharp, T. G., & Posfai, M. (2000). Mineralogy and magnetic behavior of pyrrhotite from a 260°C section at the KTB drilling site, Germany. *American Mineralogist*, *85*(10), 1416–1427. https://doi.org/10.2138/am-2000-1010

Korehi, H., Blöthe, M., & Schippers, A. (2014). Microbial diversity at the moderate acidic stage in three different sulfidic mine tailings dumps generating acid mine drainage. *Research in Microbiology*, *165*(9), 713–718. https://doi.org/10.1016/j.resmic.2014.08.007

Koski, R. A., Munk, L., Foster, A. L., Shanks, W. C., & Stillings, L. L. (2008). Sulfide oxidation and distribution of metals near abandoned copper mines in coastal environments, Prince William Sound, Alaska, USA. *Applied Geochemistry*, *23*(2), 227–254. https://doi.org/10.1016/j.apgeochem.2007.10.007

Kosmala, S., Karnkowska-Ishikawa, A., Milanowski, R., Kwiatowski, J., & Zakryś, B. (2009). PHYLOGENY AND SYSTEMATICS OF EUGLENA (EUGLENACEAE) SPECIES WITH AXIAL, STELLATE CHLOROPLASTS BASED ON MORPHOLOGICAL AND MOLECULAR DATA-NEW TAXA, EMENDED DIAGNOSES, AND EPITYPIFICATIONS(1). *Journal of Phycology*, *45*(2), 464–481. https://doi.org/10.1111/j.1529-8817.2009.00653.x

Koto, K., Morimoto, N., & Gyobu, a. (1975). The superstructure of the intermediate pyrrhotite. I. Partially disordered distribution of metal vacancy in the 6C type, Fe11S12. *Acta Crystallographica Section B Structural Crystallography and Crystal Chemistry*, *31*, 2759–2764. https://doi.org/10.1107/S0567740875008849

Koulialias, D., Kind, J., Charilaou, M., Weidler, P. G., Löffler, J. F., & Gehring, A. U. (2016). Variable defect structures cause the magnetic low-temperature transition in natural monoclinic pyrrhotite. *Geophysical Journal International*, *204*(2), 961–967. https://doi.org/10.1093/gji/ggv498

Koulialias, D., Schäublin, R., Kurtuldu, G., Weidler, P. G., Löffler, J. F., & Gehring, A. U. (2018). On the Magnetism Behind the Besnus Transition in Monoclinic Pyrrhotite. *Journal of Geophysical Research: Solid Earth*. https://doi.org/10.1029/2018JB015548

Koulialias, D., Charilaou, M., Schäublin, R., Mensing, C., Weidler, P. G., Löffler, J. F., & Gehring, A. U. (2018). Ordered defects in Fe1− x S generate additional magnetic anisotropy symmetries. *Journal of Applied Physics*, *123*(3), 033902.

Koulialias, D., Canévet, E., Charilaou, M., Weidler, P. G., Löffler, J. F., & Gehring, A. U. (2018). The relation between local structural distortion and the low-temperature magnetic anomaly in Fe_7S_8. *Journal of Physics: Condensed Matter*, *30*(42), 425803. https://doi.org/10.1088/1361-648X/aadf54

Koulialias, D., Weidler, P. G., Charilaou, M., Löffler, J. F., & Gehring, A. U. (2019). Cation diffusion patterns across the magneto-structural transition in Fe7S8. *Physical Chemistry Chemical Physics*, *21*(24), 13040–13046. https://doi.org/10.1039/c9cp01387c

Koulialias, D., Schawe, J. E., Löffler, J. F., & Gehring, A. U. (2021). Structural relaxation in layered, non-stoichiometric Fe 7 S 8. *Physical Chemistry Chemical Physics*, *23*(2), 1165–1171.

Krs, M., Novák, F., Krsová, M., Pruner, P., Kouklíková, L., & Jansa, J. (1992). Magnetic properties and metastability of greigite-smythite mineralization in brown-coal basins of the Krušné hory Piedmont, Bohemia. *Physics of the Earth and Planetary Interiors*, *70*(3), 273–287. https://doi.org/10.1016/0031-9201(92)90194-Z

Krs, Miroslav, Novák, F., Krsová, M., Pruner, P., & Jansa, J. (1993). Magnetic properties, self-reversal remanence and thermal alteration products of smythite. *Studia Geophysica et Geodaetica*, *37*(4), 382–400. https://doi.org/10.1007/BF01613584

Kruiver, P. P., Dekkers, M. J., & Heslop, D. (2001). Quantification of magnetic coercivity components by the analysis of acquisition curves of isothermal remanent magnetisation. *Earth and Planetary Science Letters*, *189*(3), 269–276. https://doi.org/10.1016/S0012-821X(01)00367-3

Kusai, K., & Yamanaka, T. (1973). The oxidation mechanisms of thiosulphate and sulphide in Chlorobium thiosulphatophilum: roles of cytochrome c-551 and cytochrome c-553. *Biochimica Et Biophysica Acta*, *325*(2), 304–314. https://doi.org/10.1016/0005-2728(73)90106-0

Lahiri, C., Mandal, S., Ghosh, W., Dam, B., & Roy, P. (2006). A Novel Gene Cluster soxSRT Is Essential for the Chemolithotrophic Oxidation of Thiosulfate and Tetrathionate by Pseudaminobacter salicylatoxidans KCT001. *Current Microbiology*, *52*(4), 267–273. https://doi.org/10.1007/s00284-005-0176-x

Lambert, J. M., Simkovich, G., & Walker, P. L. (1980). Production of pyrrhotites by pyrite reduction. *Fuel*, *59*(10), 687–690.

Lampreia, J., Moura, I., Teixeira, M., PECK Jr, H. D., Legall, J., Huynh, B. H., & Moura, J. J. G. (1990). The active centers of adenylylsulfate reductase from Desulfovibrio gigas. *European Journal of Biochemistry*, *188*(3), 653–664. https://doi.org/10.1111/j.1432-1033.1990.tb15447.x

Langman, J. B., Veeramani, H., Blowes, D. W., Bailey, B., Wilson, D., Smith, L., et al. (2017). Waste Rock Biogeochemistry in a Permafrost Environment: Examination of a Cover Design for a Low-Sulfide, Granitic Waste Rock. *Geomicrobiology Journal*, *34*(8), 656–669. https://doi.org/10.1080/01490451.2016.1238978

Lapakko, K. A. (1988). *Prediction of Acid Mine Drainage From Duluth Complex Mining Wastes in Northeastern Minnesota*. *Journal American Society of Mining and Reclamation* (Vol. 1988, pp. 180–190). Minneosta Department of Natural Resources. https://doi.org/10.21000/JASMR88010180

Lapakko, K. A. (2015). Preoperational assessment of solute release from waste rock at proposed mining operations. *Applied Geochemistry*, *57*, 106–124. https://doi.org/10.1016/j.apgeochem.2015.01.010

Lapakko, K. A., & Antonson, D. A. (1994). Oxidation of Sulfide Minerals Present in Duluth Complex Rock. *Environmental Geochemistry of Sulfide Oxidation*, 593–607.

Lapakko, K. A., & Antonson, D. A. (2012). *Duluth Complex Rock Dissolution and Mitigation Techniques: A summary of 35 years of DNR research* (p. 51). Minnesota Department of Natural Resources.

Laroche, E., Casiot, C., Fernandez-Rojo, L., Desoeuvre, A., Tardy, V., Bruneel, O., et al. (2018). Dynamics of Bacterial Communities Mediating the Treatment of an As-Rich Acid Mine Drainage in a Field Pilot. *Frontiers in Microbiology*, *9*, 3169. https://doi.org/10.3389/fmicb.2018.03169

Laska, S., Lottspeich, F., & Kletzin, A. (2003). Membrane-bound hydrogenase and sulfur reductase of the hyperthermophilic and acidophilic archaeon Acidianus ambivalens. *Microbiology*, *149*(9), 2357–2371. https://doi.org/10.1099/mic.0.26455-0

Lathifah, A. N., Guo, Y., Sakagami, N., Suda, W., Higuchi, M., Nishizawa, T., et al. (2019). Comparative Characterization of Bacterial Communities in Moss-Covered and Unvegetated Volcanic Deposits of Mount Merapi, Indonesia. *Microbes and Environments*, *34*(3), 268–277. https://doi.org/10.1264/jsme2.ME19041

Laue, B. E., & Nelson, D. C. (1994). Characterization of the gene encoding the autotrophic ATP sulfurylase from the bacterial endosymbiont of the hydrothermal vent tubeworm Riftia pachyptila. *Journal of Bacteriology*, *176*(12), 3723–3729. https://doi.org/10.1128/jb.176.12.3723-3729.1994

Lee, I., & Ripley, E. M. (1995). Genesis of Cu-Ni sulfide mineralization in the South Kawishiwi Intrusion, Spruce Road area, Duluth Complex, Minnesota. *The Canadian Mineralogist*, *33*(4), 723–743.

Lencina, A. M., Ding, Z., Schurig-Briccio, L. A., & Gennis, R. B. (2013). Characterization of the Type III sulfide:quinone oxidoreductase from Caldivirga maquilingensis and its membrane binding. *Biochimica et Biophysica Acta (BBA) - Bioenergetics*, *1827*(3), 266–275. https://doi.org/10.1016/j.bbabio.2012.10.010

Levinson, L. M., & Treves, D. (1968). Mössbauer study of the magnetic structure of Fe7S8. *Journal of Physics and Chemistry of Solids*, *29*(12), 2227–2231. https://doi.org/10.1016/0022-3697(68)90019-X

Li, F., & Franzen, H. F. (1996). Ordering, incommensuration, and phase transitions in pyrrhotite. II. A high-temperature x-ray powder diffraction and thermomagnetic study. *J. Solid State Chem.*, *126*(1), 108–120. https://doi.org/10.1006/jssc.1996.0318

Li, G., Zhang, B., Yu, F., Novakova, A. A., Krivenkov, M. S., Kiseleva, T. Y., et al. (2014). High-Purity Fe3S4 Greigite Microcrystals for Magnetic and Electrochemical Performance. *Chemistry of Materials*, *26*(20), 5821–5829. https://doi.org/10.1021/cm501493m

Li, X., Kappler, U., Jiang, G., & Bond, P. L. (2017). The Ecology of Acidophilic Microorganisms in the Corroding Concrete Sewer Environment. *Frontiers in Microbiology*, *8*, 683. https://doi.org/10.3389/fmicb.2017.00683

Liang, Y., Wei, D., Hu, J., Zhang, J., Liu, Z., Li, A., & Li, R. (2020). Glypho*sat*e and nutrients removal from simulated agricultural runoff in a pilot pyrrhotite constructed wetland. *Water Research*, *168*, 115154. https://doi.org/10.1016/j.watres.2019.115154

Lim, J.-M., Jeon, C. O., Lee, G. S., Park, D.-J., Kang, U.-G., Park, C.-Y., & Kim, C.-J. (2007). Leeia oryzae gen. nov., sp. nov., isolated from a rice field in Korea. *International Journal of Systematic and Evolutionary Microbiology*, *57*(6), 1204–1208. https://doi.org/10.1099/ijs.0.64582-0

Lindsay, M. B. J., Condon, P. D., Jambor, J. L., Lear, K. G., Blowes, D. W., & Ptacek, C. J. (2009). Mineralogical, geochemical, and microbial investigation of a sulfide-rich tailings deposit characterized by neutral drainage. *Applied Geochemistry*, *24*(12), 2212–2221. https://doi.org/10.1016/j.apgeochem.2009.09.012

Liu, H., Xin, Y., & Xun, L. (2014). Distribution, Diversity, and Activities of Sulfur Dioxygenases in Heterotrophic Bacteria. *Applied and Environmental Microbiology*, *80*(5), 1799–1806. https://doi.org/10.1128/AEM.03281-13

Liu, Jian-li, Yao, J., Wang, F., Min, N., Gu, J., Li, Z., et al. (2019). Bacterial diversity in typical abandoned multi-contaminated nonferrous metal(loid) tailings during natural attenuation. *Environmental Pollution*, *247*, 98–107. https://doi.org/10.1016/j.envpol.2018.12.045

Liu, Jian-li, Yao, J., Lu, C., Li, H., Li, Z., Duran, R., et al. (2019). Microbial activity and biodiversity responding to contamination of metal(loid) in heterogeneous nonferrous mining and smelting areas. *Chemosphere*, *226*, 659–667. https://doi.org/10.1016/j.chemosphere.2019.03.051

Liu, Juan, Yin, M., Zhang, W., Tsang, D. C. W., Wei, X., Zhou, Y., et al. (2019). Response of microbial communities and interactions to thallium in contaminated sediments near a pyrite mining area. *Environmental Pollution*, *248*, 916–928. https://doi.org/10.1016/j.envpol.2019.02.089

Liu, L., Mavrogenes, J., Holden, P., & Ireland, T. (2020). Quadruple sulfur isotopic fractionation during pyrite desulfidation to pyrrhotite. *Geochimica et Cosmochimica Acta*, *273*, 354–366. https://doi.org/10.1016/j.gca.2020.01.024

Lopez Bedogni, G., Massello, F. L., Giaveno, A., Donati, E. R., & Urbieta, M. S. (2019). A Deeper Look into the Biodiversity of the Extremely Acidic Copahue volcano-Río Agrio System in Neuquén, Argentina. *Microorganisms*, *8*(1), 58. https://doi.org/10.3390/microorganisms8010058

Ludwig, W., Strunk, O., Westram, R., Richter, L., Meier, H., Yadhukumar, et al. (2004). ARB: a software environment for sequence data. *Nucleic Acids Research*, *32*(4), 1363–1371. https://doi.org/10.1093/nar/gkh293

Lund, A. L., Slater, L. D., Atekwana, E. A., Ntarlagiannis, D., Cozzarelli, I., & Bekins, B. A. (2017). Evidence of Coupled Carbon and Iron Cycling at a Hydrocarbon-Contaminated Site from Time Lapse Magnetic Susceptibility. *Environmental Science & Technology*, *51*(19), 11244–11249. https://doi.org/10.1021/acs.est.7b02155

Lyric, R. M., & Suzuki, I. (1970). Enzymes involved in the metabolism of thiosulfate by *Thiobacillus thioparus* . II. Properties of adenosine-5′-phosphosulfate reductase. *Canadian Journal of Biochemistry*, *48*(3), 344–354. https://doi.org/10.1139/o70-057

Macalady, J. L., Jones, D. S., & Lyon, E. H. (2007). Extremely acidic, pendulous cave wall biofilms from the Frasassi cave system, Italy. *Environmental Microbiology*, *9*(6), 1402–1414. https://doi.org/10.1111/j.1462-2920.2007.01256.x

Maest, A. S., & Nordstrom, D. K. (2017). A geochemical examination of humidity cell tests. *Applied Geochemistry*, *81*, 109–131. https://doi.org/10.1016/j.apgeochem.2017.03.016

Mainwaring, P. R., & Naldrett, A. J. (1977). Country-rock assimilation and the genesis of Cu-Ni sulfides in the Water Hen Intrusion, Duluth Complex, Minnesota. *Economic Geology*, *72*(7), 1269–1284.

Marcia, M., Ermler, U., Peng, G., & Michel, H. (2010). A new structure-based classification of sulfide:quinone oxidoreductases. *Proteins: Structure, Function, and Bioinformatics*, *78*(5), 1073–1083. https://doi.org/10.1002/prot.22665

Markowitz, V. M., Mavromatis, K., Ivanova, N. N., Chen, I.-M. A., Chu, K., & Kyrpides, N. C. (2009). IMG ER: a system for microbial genome annotation expert review and curation. *Bioinformatics*, *25*(17), 2271–2278. https://doi.org/10.1093/bioinformatics/btp393

Martin, M. (2011). Cutadapt removes adapter sequences from high-throughput sequencing reads. *EMBnet.Journal*, *17*(1), 10–12. https://doi.org/10.14806/ej.17.1.200

Martínez-Hidalgo, P., Ramírez-Bahena, M. H., Flores-Félix, J. D., Rivas, R., Igual, J. M., Mateos, P. F., et al. (2015). Revision of the taxonomic status of type strains of Mesorhizobium loti and reclassification of strain USDA 3471T as the type strain of Mesorhizobium erdmanii sp. nov. and ATCC 33669T as the type strain of Mesorhizobium jarvisii sp. nov. *International Journal of Systematic and Evolutionary Microbiology*, *65*(Pt_6), 1703–1708. https://doi.org/10.1099/ijs.0.000164

Marusak, L. A., & Mulay, L. N. (1980). Polytypism in the cation-deficient iron sulfide, Fe 9 S 10, and the magnetokinetics of the diffusion process at temperatures about the antiferro-to ferrimagnetic (λ) phase transition. *Physical Review B*, *21*(1), 238.

McAllister, S. M., Polson, S. W., Butterfield, D. A., Glazer, B. T., Sylvan, J. B., & Chan, C. S. (2020). Validating the *Cyc2* Neutrophilic Iron Oxidation Pathway Using Meta-omics of Zetaproteobacteria Iron Mats at Marine Hydrothermal Vents. *MSystems*, *5*(1), e00553-19. https://doi.org/10.1128/mSystems.00553-19

McGuire, M. M., & Hamers, R. J. (2000). Extraction and Quantitative Analysis of Elemental Sulfur from Sulfide Mineral Surfaces by High-Performance Liquid Chromatography. *Environmental Science & Technology*, *34*(21), 4651–4655. https://doi.org/10.1021/es0011663

Mendez, M. O., Neilson, J. W., & Maier, R. M. (2008). Characterization of a Bacterial Community in an Abandoned Semiarid Lead-Zinc Mine Tailing Site. *Applied and Environmental Microbiology*, *74*(12), 3899–3907. https://doi.org/10.1128/AEM.02883-07

Merk, G. P., & Jirsa, M. A. (1982). 7B: Provenance and tectonic significance of the Keweenaw an interflow sedimentary rocks. In *Geological Society of America Memoirs* (Vol. 156, pp. 97–105). Geological Society of America. https://doi.org/10.1130/MEM156-p97

Meruane, G., & Vargas, T. (2003). Bacterial oxidation of ferrous iron by Acidi*Thiobacillus* ferrooxidans in the pH range 2.5–7.0. *Hydrometallurgy*, *71*(1), 149–158. https://doi.org/10.1016/S0304-386X(03)00151-8

Meyer, B., Imhoff, J. F., & Kuever, J. (2007). Molecular analysis of the distribution and phylogeny of the soxB gene among sulfur-oxidizing bacteria - Evolution of the Sox sulfur oxidation enzyme system. *Environmental Microbiology*, *9*(12), 2957–2977. https://doi.org/10.1111/j.1462-2920.2007.01407.x

Mezzasoma, A., Coleine, C., Sannino, C., & Selbmann, L. (2022). Endolithic Bacterial Diversity in Lichen-Dominated Communities Is Shaped by Sun Exposure in McMurdo Dry Valleys, Antarctica. *Microbial Ecology*, *83*(2), 328–339. https://doi.org/10.1007/s00248-021-01769-w

Middleton, M. F. (1989). A model for the formation of intracratonic sag basins. *Geophysical Journal International*, *99*(3), 665–676. https://doi.org/10.1111/j.1365-246X.1989.tb02049.x

Miller, J. D. (2011). Layered intrusions of the Duluth Complex. In *Archean to Anthropocene: Field Guides to the Geology of the Mid-Continent of North America* (pp. 171–201). Geological Society of America. https://doi.org/10.1130/2011.0024(09)

Miller, J. D., Jr., Green, J. C., Severson, M. J., Chandler, V. W., Hauck, S. A., Peterson, D. M., & Wahl, T. E. (2002). *Geology and mineral potential of the Duluth Complex and related rocks of northeastern Minnesota* (Report of Investigations No. RI-58) (p. 218). Minnesota Geological Survey. Retrieved from https://conservancy.umn.edu/handle/11299/58804

Minnesota Environmental Quality Board. (1977). *Preliminary Report: Spruce Road Bulk Sample Site Monitoring Results* (p. 81). Minnesota Environmental Quality Board. Retrieved from https://mnpals-lrl.primo.exlibrisgroup.com/discovery/openurl?institution=01MNPALS_LRL&vid=01MNPALS_LRL:LRL&rft.oclcnum=07048664

Moecher, D. P., Bowersox, J. R., & Hickman, J. B. (2018). Zircon U-Pb Geochronology of Two Basement Cores (Kentucky, USA): Implications for Late Mesoproterozoic Sedimentation and Tectonics in the Eastern Midcontinent. *The Journal of Geology*, *126*(1), 25–39. https://doi.org/10.1086/694825

Morgan, B., & Lahav, O. (2007). The effect of pH on the kinetics of spontaneous Fe(II) oxidation by O2 in aqueous solution--basic principles and a simple heuristic description. *Chemosphere*, *68*(11), 2080–2084. https://doi.org/10.1016/j.chemosphere.2007.02.015

Morimoto, N., Nakazawa, H., Nishigucmi, K., & Tokonami, M. (1970). Pyrrhotites: Stoichiometric Compounds with Composition Fen—1Sn (n≥ 8). *Science*, *168*(3934), 964–966.

Morimoto, N., Gyobu, A., Tsukuma, K., & Koto, K. (1975). Superstructure and nonstoichiometry of intermediate pyrrhotite. *American Mineralogist: Journal of Earth and Planetary Materials*, *60*(3–4), 240–248.

Moses, C. O., & Herman, J. S. (1991). Pyrite oxidation at circumneutral pH. *Geochimica et Cosmochimica Acta*, *55*, 471–482.

Moses, C. O., Kirk Nordstrom, D., Herman, J. S., & Mills, A. L. (1987). Aqueous pyrite oxidation by dissolved oxygen and by ferric iron. *Geochimica et Cosmochimica Acta*, *51*(6), 1561–1571. https://doi.org/10.1016/0016-7037(87)90337-1

Muggia, L., Fleischhacker, A., Kopun, T., & Grube, M. (2016). Extremotolerant fungi from alpine rock lichens and their phylogenetic relationships. *Fungal Diversity*, *76*, 119–142. https://doi.org/10.1007/s13225-015-0343-8

Mukhopadhyaya, P. N., Deb, C., Lahiri, C., & Roy, P. (2000). A soxA Gene, Encoding a Diheme Cytochrome c, and a sox Locus, Essential for Sulfur Oxidation in a New Sulfur Lithotrophic Bacterium. *Journal of Bacteriology*, *182*(15), 4278–4287. https://doi.org/10.1128/JB.182.15.4278-4287.2000

Müller, F. H., Bandeiras, T. M., Urich, T., Teixeira, M., Gomes, C. M., & Kletzin, A. (2004). Coupling of the pathway of sulphur oxidation to dioxygen reduction: characterization of a novel membrane-bound thiosulphate:quinone oxidoreductase: Thiosulphate oxidoreductase from Acidianus ambivalens. *Molecular Microbiology*, *53*(4), 1147–1160. https://doi.org/10.1111/j.1365-2958.2004.04193.x

Muttoni, G. (1995). "Wasp-waisted" hysteresis loops from a pyrrhotite and magnetite-bearing remagnetized Triassic limestone. *Geophysical Research Letters*, *22*(23), 3167–3170. https://doi.org/10.1029/95GL03073

Muxworthy, A. R., & McClelland, E. (2000). Review of the low-temperature magnetic properties of magnetite from a rock magnetic perspective. *Geophysical Journal International*, *140*(1), 101–114. https://doi.org/10.1046/j.1365-246x.2000.00999.x

Muxworthy, Adrian R., Dunlop, D. J., & Özdemir, Ö. (2003). Low-temperature cycling of isothermal and anhysteretic remanence: microcoercivity and magnetic memory. *Earth and Planetary Science Letters*, *205*(3), 173–184. https://doi.org/10.1016/S0012-821X(02)01039-7

Muyzer, G., Kuenen, J. G., & Robertson, L. A. (2013). Colorless Sulfur Bacteria. In E. Rosenberg, E. F. DeLong, F. Thompson, S. Lory, & E. Stackebrandt (Eds.), *The Prokaryotes: Prokaryotic Physiology and Biochemistry* (pp. 555–588). Springer Berlin Heidelberg.

Mycroft, J. R., Nesbitt, H. W., & Pratt, A. R. (1995). X-ray photoelectron and Auger electron spectroscopy of air-oxidized pyrrhotite: Distribution of oxidized species with depth. *Geochimica et Cosmochimica Acta*, *59*(4), 721–733. https://doi.org/10.1016/0016-7037(94)00352-M

Nakano, A., Tokonami, M., & Morimoto, N. (1979). Refinement of 3 *C* pyrrhotite, Fe_7S_8. *Acta Crystallographica Section B Structural Crystallography and Crystal Chemistry*, *35*(3), 722–724. https://doi.org/10.1107/S0567740879004532

Nakazawa, H., & Morimoto, N. (1971). Phase relations and superstructures of pyrrhotite, Fe1− xS. *Materials Research Bulletin*, *6*(5), 345–357. https://doi.org/10.1016/0025-5408(71)90168-1

Ňancucheo, I., & Johnson, D. B. (2011). Significance of Microbial Communities and Interactions in Safeguarding Reactive Mine Tailings by Ecological Engineering. *Applied and Environmental Microbiology*, *77*(23), 8201–8208. https://doi.org/10.1128/AEM.06155-11

Napieralski, S. A., Fang, Y., Marcon, V., Forsythe, B., Brantley, S. L., Xu, H., & Roden, E. E. (2022). Microbial chemolithotrophic oxidation of pyrite in a subsurface shale weathering environment: Geologic considerations and potential mechanisms. *Geobiology*, *20*(2), 271–291. https://doi.org/10.1111/gbi.12474

Néel, L. (1953). Some new results on antiferromagnetism and ferromagnetism. *Reviews of Modern Physics*, *25*(1), 58–63. https://doi.org/10.1103/RevModPhys.25.58

Nicholson, R. V., & Scharer, J. M. (1993). Laboratory Studies of Pyrrhotite Oxidation Kinetics. In *Environmental Geochemistry of Sulfide Oxidation* (Vol. 550, pp. 14–30). American Chemical Society. https://doi.org/10.1021/bk-1994-0550.ch002

Nicholson, S. W., Schulz, K. J., Shirey, S. B., & Green, J. C. (1997). Rift-wide correlation of 1.1 Ga Midcontinent rift system basalts: implications for multiple mantle sources during rift development. *Canadian Journal of Earth Sciences*, *34*(4), 504–520. https://doi.org/10.1139/e17-041

Nordstrom, D. K. (1982). Aqueous Pyrite Oxidation and the Consequent Formation of Secondary Iron Minerals. In J. A. Kittrick, D. S. Fanning, & L. R. Hossner (Eds.), *SSSA Special Publications* (pp. 37–56). Madison, WI, USA: Soil Science Society of America. https://doi.org/10.2136/sssaspecpub10.c3

Nordstrom, D. K., Blowes, D. W., & Ptacek, C. J. (2015). Hydrogeochemistry and microbiology of mine drainage: An update. *Applied Geochemistry*, *57*, 3–16. https://doi.org/10.1016/j.apgeochem.2015.02.008

Notredame, C., Higgins, D. G., & Heringa, J. (2000). T-coffee: a novel method for fast and accurate multiple sequence alignment 1 1Edited by J. Thornton. *Journal of Molecular Biology*, *302*(1), 205–217. https://doi.org/10.1006/jmbi.2000.4042

Novikov, A. P., Safonov, A. V., Babich, T. L., Boldyrev, K. A., Kryuchkov, D. V., Lavrinovich, E. A., et al. (2020). Biotransformation of Neptunium in Model Groundwaters. *Geochemistry International*, *58*(2), 182–188. https://doi.org/10.1134/S0016702920020081

Onysko, S. J., Kleinmann, R. L. P., & Erickson, P. M. (1984). Ferrous Iron Oxidation by *Thiobacillus ferrooxidans* : Inhibition with Benzoic Acid, Sorbic Acid, and Sodium Lauryl Sulfate. *Applied and Environmental Microbiology*, *48*(1), 229–231. https://doi.org/10.1128/aem.48.1.229-231.1984

O'Reilly, W., Hoffmann, V., Chouker, A. C., Soffel, H. C., & Menyeh, A. (2000). Magnetic properties of synthetic analogues of pyrrhotite ore in the grain size range 1-24 μm. *Geophysical Journal International*, *142*(3), 669–683.

Orlova, T. A., Stupnikov, V. M., & Krestan, A. L. (1988). Mechanism of oxidative dissolution of sulfides. *JOURNAL OF APPLIED CHEMISTRY OF THE USSR*, *61*(10), 1989–1993.

Ortiz, M., Leung, P. M., Shelley, G., Jirapanjawat, T., Nauer, P. A., Van Goethem, M. W., et al. (2021). Multiple energy sources and metabolic strategies sustain microbial diversity in Antarctic desert soils. *Proceedings of the National Academy of Sciences*, *118*(45), e2025322118. https://doi.org/10.1073/pnas.2025322118

Pakostova, E., Schmall, A. J., Holland, S. P., White, H., Ptacek, C. J., & Blowes, D. W. (2020). Performance of a geosynthetic clay-liner cover system at a Cu/Zn mine tailings impoundment: microbiological characterization. *Applied and Environmental Microbiology*. https://doi.org/10.1128/AEM.02846-19

Peng, Z., Liu, Z., Jiang, Y., Dong, Y., & Shi, L. (2022). In vivo interactions between *Cyc2* and Rus as well as Rus and *Cyc1* of Acidi*Thiobacillus* ferrooxidans during extracellular oxidization of ferrous iron. *International Biodeterioration & Biodegradation*, *173*, 105453. https://doi.org/10.1016/j.ibiod.2022.105453

Peppas, A., Komnitsas, K., & Halikia, I. (2000). Use of organic covers for acid mine drainage control. *Minerals Engineering*, *13*(5), 563–574. https://doi.org/10.1016/S0892-6875(00)00036-4

Percak-Dennett, E., He, S., Converse, B., Konishi, H., Xu, H., Corcoran, A., et al. (2017). Microbial acceleration of aerobic pyrite oxidation at circumneutral pH. *Geobiology*, *15*(5), 690–703. https://doi.org/10.1111/gbi.12241

Pósfai, M., & Buseck, P. R. (1997). Modular structures in sulphides: sphalerite/wurtzite-, pyrite/marcasite-, and pyrrhotite-type minerals. https://doi.org/10.1180/EMU-notes.1.7

Pósfai, M., Sharp, T. G., & Kontny, A. (2000). Pyrrhotite varieties from the 9.1 km deep borehole of the KTB project. *American Mineralogist*, *85*(10), 1406–1415. https://doi.org/10.2138/am-2000-1009

Pott, A. S., & Dahl, C. (1998). Sirohaem sulfite reductase and other proteins encoded by genes at the *dsr* locus of Chromatium vinosum are involved in the oxidation of intracellular sulfur. *Microbiology (Reading, England)*, *144 (Pt 7)*, 1881–1894. https://doi.org/10.1099/00221287-144-7-1881

Powell, A. V., Vaqueiro, P., Knight, K. S., Chapon, L. C., & Sánchez, R. D. (2004). Structure and magnetism in synthetic pyrrhotite Fe7S 8: A powder neutron-diffraction study. *Physical Review B - Condensed Matter and Materials Physics*, *70*(1), 1–12. https://doi.org/10.1103/PhysRevB.70.014415

Pratt, A. R., Muir, I. J., & Nesbitt, H. W. (1994). X-ray photoelectron and Auger electron spectroscopic studies of pyrrhotite and mechanism of air oxidation. *Geochimica et Cosmochimica Acta*, *58*(2), 827–841. https://doi.org/10.1016/0016-7037(94)90508-8

Pratt, A. R., Nesbitt, H. W., & Mycroft, J. R. (1996). The increased reactivity of pyrrhotite and magnetite phases in sulphide mine tailings. *Journal of Geochemical Exploration*, *56*(1), 1–11. https://doi.org/10.1016/0375-6742(96)00008-8

Putz, H., Brandenburg, K., & GBR. (2020). Match! - Phase Analysis using Powder Diffraction (Version 3.11). Crystal Impact! Retrieved from https://www.crystalimpact.de/match

Quast, C., Pruesse, E., Yilmaz, P., Gerken, J., Schweer, T., Yarza, P., et al. (2013). The SILVA ribosomal RNA gene database project: improved data processing and web-based tools. *Nucleic Acids Research*, *41*(D1), D590–D596. https://doi.org/10.1093/nar/gks1219

Queffurus, M., & Barnes, S.-J. (2014). SELENIUM AND SULFUR CONCENTRATIONS IN COUNTRY ROCKS FROM THE DULUTH COMPLEX, MINNESOTA, USA: IMPLICATIONS FOR FORMATION OF THE Cu-Ni-PGE SULFIDES*. *Economic Geology*, *109*(3), 785–794. https://doi.org/10.2113/econgeo.109.3.785

R Core Team. (2021). R: A language and environment for statistical computing. (Version 4.1.0). ienna, Austria: R Foundation for Statistical Computing. Retrieved from https://www.R-project.org/

Rambabu, K., Banat, F., Pham, Q. M., Ho, S.-H., Ren, N.-Q., & Show, P. L. (2020). Biological remediation of acid mine drainage: Review of past trends and current outlook. *Environmental Science and Ecotechnology*, *2*, 100024. https://doi.org/10.1016/j.ese.2020.100024

Ramsdell, L. S. (1925). The crystal structure of some metallic sulfides*. *American Mineralogist*, *10*(9), 281–304.

Rao, N. K., & Rao, G. V. U. (1968). Ore microscopic study of copper ore from Kolihan, Rajasthan, India. *Economic Geology*, *63*(3).

Rawlings, D. E., & Johnson, D. B. (2007). The microbiology of biomining: development and optimization of mineral-oxidizing microbial consortia. *Microbiology*, *153*(2), 315–324. https://doi.org/10.1099/mic.0.2006/001206-0

Rhodes, J. M., Jones, C. A., Thal, L. B., & Macdonald, J. E. (2017). Phase-Controlled Colloidal Syntheses of Iron Sulfide Nanocrystals via Sulfur Precursor Reactivity and Direct Pyrite Precipitation. *Chemistry of Materials*, acs.chemmater.7b03550. https://doi.org/10.1021/acs.chemmater.7b03550

Rietveld, H. M. (1969). A profile refinement method for nuclear and magnetic structures. *Journal of Applied Crystallography*, *2*(2), 65–71. https://doi.org/10.1107/S0021889869006558

Ripley, E. M., Taib, N. I., Li, C., & Moore, C. H. (2007). Chemical and mineralogical heterogeneity in the basal zone of the Partridge River Intrusion: implications for the origin of Cu–Ni sulfide mineralization in the Duluth Complex, midcontinent rift system. *Contributions to Mineralogy and Petrology*, *154*(1), 35–54. https://doi.org/10.1007/s00410-006-0178-0

Roberts, A. P., Chang, L., Rowan, C. J., Horng, C.-S., & Florindo, F. (2011). Magnetic properties of sedimentary greigite (Fe3S4): An update. *Reviews of Geophysics*, *49*(1). https://doi.org/10.1029/2010RG000336

Rochette, P. (1987). Metamorphic control of the magnetic mineralogy of black shales in the Swiss Alps: toward the use of "magnetic isograds." *Earth and Planetary Science Letters*, *84*(4), 446–456. https://doi.org/10.1016/0012-821X(87)90009-4

Rochette, P., Fillion, G., Mattéi, J.-L., & Dekkers, M. J. (1990). Magnetic transition at 30–34 Kelvin in pyrrhotite: insight into a widespread occurrence of this mineral in rocks. *Earth and Planetary Science Letters*, *98*(3–4), 319–328.

Rochette, P., Lorand, J.-P., Fillion, G., & Sautter, V. (2001). Pyrrhotite and the remanent magnetization of SNC meteorites: a changing perspective on Martian magnetism. *Earth and Planetary Science Letters*, *190*(1), 1–12. https://doi.org/10.1016/S0012-821X(01)00373-9

Rodríguez-Carvajal, J. (1993). Recent advances in magnetic structure determination by neutron powder diffraction. *Physica B: Condensed Matter*, *192*(1), 55–69. https://doi.org/10.1016/0921-4526(93)90108-I

Rognes, T., Flouri, T., Nichols, B., Quince, C., & Mahé, F. (2016). VSEARCH: a vers*at*ile open source tool for metagenomics. *PeerJ*, *4*, e2584. https://doi.org/10.7717/peerj.2584

Rohwerder, T., & Sand, W. (2003). The sulfane sulfur of persulfides is the actual substrate of the sulfur-oxidizing enzymes from Acidi*Thiobacillus* and Acidiphilium spp. *Microbiology*, *149*(7), 1699–1709. https://doi.org/10.1099/mic.0.26212-0

Rohwerder, T., Gehrke, T., Kinzler, K., & Sand, W. (2003). Bioleaching review part A: Progress in bioleaching: fundamentals and mechanisms of bacterial metal sulfide oxidation. *Applied Microbiology and Biotechnology*, *63*(3), 239–248. https://doi.org/10.1007/s00253-003-1448-7

RStudio Team. (2021). RStudio: Integrated Development Environment for R (Version 1.4.1717). Boston, MA: RStudio, PBC. Retrieved from http://www.rstudio.com/

Sand, W., Gerke, T., Hallmann, R., & Schippers, A. (1995). Sulfur chemistry, biofilm, and the (in)direct attack mechanism — a critical evaluation of bacterial leaching. *Applied Microbiology and Biotechnology*, *43*(6), 961–966. https://doi.org/10.1007/BF00166909

Sauvé, V., Bruno, S., Berks, B. C., & Hemmings, A. M. (2007). The SoxYZ Complex Carries Sulfur Cycle Intermediates on a Peptide Swinging Arm *. *Journal of Biological Chemistry*, *282*(32), 23194–23204. https://doi.org/10.1074/jbc.M701602200

Sawana, A., Adeolu, M., & Gupta, R. S. (2014). Molecular signatures and phylogenomic analysis of the genus Burkholderia: proposal for division of this genus into the emended genus Burkholderia containing pathogenic organisms and a new genus Paraburkholderia gen. nov. harboring environmental species. *Frontiers in Genetics*, *5*. https://doi.org/10.3389/fgene.2014.00429

Schippers, A. (2004). Biogeochemistry of metal sulfide oxidation in mining environments, sediments, and soils. In J. P. Amend, K. J. Edwards, & T. W. Lyons, *Sulfur Biogeochemistry - Past and Present*. Geological Society of America. https://doi.org/10.1130/0-8137-2379-5.49

Schippers, A., & Jørgensen, B. B. (2002). Biogeochemistry of pyrite and iron sulfide oxidation in marine sediments. *Geochimica et Cosmochimica Acta*, *66*(1), 85–92. https://doi.org/10.1016/S0016-7037(01)00745-1

Schippers, A., & Sand, W. (1999). Bacterial leaching of metal sulfides proceeds by two indirect mechanisms via thiosulfate or via polysulfides and sulfur. *Applied and Environmental Microbiology*, *65*(1), 319–321.

Schippers, A., Von Rège, H., & Sand, W. (1996). Impact of microbial diversity and sulfur chemistry on safeguarding sulfudic mine waste. *Minerals Engineering*, *9*(10), 1069–1079. https://doi.org/10.1016/0892-6875(96)00099-4

Schippers, A., Jozsa, P.-G., & Sand, W. (1998). Evaluation of the efficiency of measures for sulphidic mine waste mitigation. *Applied Microbiology and Biotechnology*, *49*(6), 698–701. https://doi.org/10.1007/s002530051234

Schloss, P. D. (2020). Reintroducing mothur: 10 Years Later. *Applied and Environmental Microbiology*, *86*(2), e02343-19. https://doi.org/10.1128/AEM.02343-19

Schmieder, R., & Edwards, R. (2011). Quality control and preprocessing of metagenomic datasets. *Bioinformatics (Oxford, England)*, *27*(6), 863–864. https://doi.org/10.1093/bioinformatics/btr026

Schwarz, E. J. (1968). Magnetic Phases in Natural Pyrrhotite Fe0.89S and Fe0.91S. *Journal of Geomagnetism and Geoelectricity*, *20*(2), 67–74. https://doi.org/10.5636/jgg.20.67

Schwarz, E. J. (1975). *Magnetic properties of pyrrhotite and their use in applied geology and geophysics* (No. 74–59) (pp. 74–59). https://doi.org/10.4095/102563

Schwarz, E. J., & Vaughan, D. J. (1972). Magnetic Phase Relations of Pyrrhotite. *Journal of Geomagnetism and Geoelectricity*, *24*, 441–458. https://doi.org/10.1017/CBO9781107415324.004

Seal, R., Lapakko, K. A., Piatak, N., & Woodruff, L. (2015). Reaction modeling of drainage quality in the Duluth Complex, northern Minnesota, USA. In *10th International Conference on Acid Rock Drainage & IMWA Annual Conference*.

Severson, M. J. (1994). *Igneous Stratigraphy of the South Kawishiwi Intrusion, Duluth Complex, Northeastern Minnesota* (Technical Report). University of Minnesota Duluth. Retrieved from http://conservancy.umn.edu/handle/11299/188520

Severson, M. J., Patelke, R. L., Hauck, S. A., & Zanko, L. M. (1996). *The Babbitt Copper-Nickel Deposit: Part C: Igneous Geology, Footwall Lithologies, and Cross-Sections* (Technical Report). University of Minnesota Duluth. Retrieved from http://conservancy.umn.edu/handle/11299/188526

Severson, M. J., Miller, J. D., Peterson, D. M., Green, J. C., Hauck, S. A., Chandler, V. W., & Wahl, T. E. (2002). Mineral potential of the Duluth Complex and related intrusions. *Minnesota Geological Survey, Report of Investigations*, *58*, 164–200.

Sharrar, A. M., Flood, B. E., Bailey, J. V., Jones, D. S., Biddanda, B. A., Ruberg, S. A., et al. (2017). Novel Large Sulfur Bacteria in the Metagenomes of Groundwater-Fed Chemosynthetic Microbial Mats in the Lake Huron Basin. *Frontiers in Microbiology*, *8*. Retrieved from https://www.frontiersin.org/articles/10.3389/fmicb.2017.00791

Shen, L., Huang, T., Chen, Y., Chu, Z., & Xie, Z. (2021). *Diverse Biotransformation of Sulfur in Antarctic Lake Sediments* (preprint). In Review. https://doi.org/10.21203/rs.3.rs-230087/v1

Silverman, M. P. (1967). Mechanism of Bacterial Pyrite Oxidation, *94*(4), 1046–1051.

Skinner, B. J. (1961). Unit-cell edges of natural and synthetic sphalerites*. *American Mineralogist*, *46*(11–12), 1399–1411.

Skinner, B. J., Erd, R. C., & Grimaldi, F. S. (1964). Greigite, the thio-spinel of iron; a new mineral. *American Mineralogist*, *49*(5–6), 543–555.

Stein, C. A., Stein, S., Elling, R., Keller, G. R., & Kley, J. (2018). Is the "Grenville Front" in the central United States really the Midcontinent Rift? *GSA Today*, 4–10. https://doi.org/10.1130/G*SAT*G357A.1

Stookey, L. L. (1970). Ferrozine---a new spectrophotometric reagent for iron. *Analytical Chemistry*, *42*(7), 779–781. https://doi.org/10.1021/ac60289a016

Sun, X., Kong, T., Häggblom, M. M., Kolton, M., Li, F., Dong, Y., et al. (2020). Chemolithoautotropic Diazotrophy Dominates the Nitrogen Fixation Process in Mine Tailings. *Environmental Science & Technology*, *54*(10), 6082–6093. https://doi.org/10.1021/acs.est.9b07835

Swanson-Hysell, N. L., Ramezani, J., Fairchild, L. M., & Rose, I. R. (2019). Failed rifting and fast drifting: Midcontinent Rift development, Laurentia's rapid motion and the driver of Grenvillian orogenesis. *GSA Bulletin*, *131*(5–6), 913–940. https://doi.org/10.1130/B31944.1

Symons, D. T. A., & Kawasaki, K. (2019). Paleomagnetism of the native copper mineralization, Keweenaw Peninsula, Michigan. *Canadian Journal of Earth Sciences*, *56*(9), 932–947. https://doi.org/10.1139/cjes-2017-0251

Tan, Y., Wang, Y., Wang, D., Wang, G., & Zheng, S. 2016. (2016). Sphingoaurantiacus capsulatus sp. nov., isolated from mountain soil, and emended description of the genus Sphingoaurantiacus. *International Journal of Systematic and Evolutionary Microbiology*, *66*(12), 4930–4935. https://doi.org/10.1099/ijsem.0.001447

Taylor, L. A. (1971). Oxidation of Pyrrhotites and the Formation of Anomalous Pyrrhotite. In *Year book - Carnegie Institution of Washington* (Vol. 70, pp. 286–290). Washington, D.C. : Carnegie Institution of Washington. Retrieved from http://archive.org/details/yearbookcarne70197071carn

Thériault, R. D., Barnes, S.-J., & Severson, M. J. (1997). The influence of country-rock assimilation and silicate to sulfide ratios (R factor) on the genesis of the Dunka Road Cu – Ni – platinum-group element deposit, Duluth Complex, Minnesota. *Canadian Journal of Earth Sciences*, *34*(4), 375–389. https://doi.org/10.1139/e17-033

Thériault, R. D., Barnes, S.-J., & Severson, M. J. (2000). Origin of Cu-Ni-PGE Sulfide Mineralization in the Partridge River Intrusion, Duluth Complex, Minnesota. *Economic Geology*, *95*(5), 929–943. https://doi.org/10.2113/gsecongeo.95.5.929

Tikhonova, T. V., Lilina, A. V., Osipov, E. M., Shipkov, N. S., Dergousova, N. I., Kulikova, O. G., & Popov, V. O. (2021). Catalytic Properties of Flavocytochrome c Sulfide Dehydrogenase from

Haloalkaliphilic Bacterium Thioalkalivibrio paradoxus. *Biochemistry. Biokhimiia*, *86*(3), 361–369. https://doi.org/10.1134/S0006297921030111
Tiranti, V., Briem, E., Lamantea, E., Mineri, R., Papaleo, E., Gioia, L. D., et al. (2006). ETHE1 mutations are specific to ethylmalonic encephalopathy. *Journal of Medical Genetics*, *43*(4), 340. https://doi.org/10.1136/jmg.2005.036210
Torii, M., Fukuma, K., Horng, C.-S., & Lee, T.-Q. (1996). Magnetic discrimination of pyrrhotite- and greigite-bearing sediment samples. *Geophysical Research Letters*, *23*(14), 1813–1816. https://doi.org/10.1029/96GL01626
Toulmin, P., & Barton, P. B. (1964). A thermodynamic study of pyrite and pyrrhotite. *Geochimica et Cosmochimica Acta*, *28*(5), 641–671. https://doi.org/10.1016/0016-7037(64)90083-3
Townsend, M. G., Webster, A. H., Horwood, J. L., & Roux-Buisson, H. (1979). Ferrimagnetic transition in Fe0.9S: Magnetic, thermodynamic and kinetic aspects. *Journal of Physics and Chemistry of Solids*, *40*(3), 183–189. https://doi.org/10.1016/0022-3697(79)90013-1
Tyson, R. M., & Chang, L. L. (1984). The petrology and sulfide mineralization of the Partridge River troctolite, Duluth Complex, Minnesota. *The Canadian Mineralogist*, *22*(1), 23–38.
Valente, T., & Gomes, C. (2007). The role of two acidophilic algae as ecological indicators of acid mine drainage sites. *Journal of Iberian Geology*, *2007*, *33*.
Vandenberghe, R. E., de Grave, E., de Bakker, P. M. A., Krs, M., & Hus, J. J. (1992). Mössbauer effect study of natural greigite. *Hyperfine Interactions*, *68*(1), 319–322. https://doi.org/10.1007/BF02396500
Vanitha, P. V., & Brien, P. O. (2008). Phase Control in the Synthesis of Magnetic Iron Sulfide Nanocrystals From a Cubane-Type Fe - S Cluster. *J. Am. Chem. Soc.*, *130*(51), 17256–17257. https://doi.org/10.1021/ja8078187
Vasse, M., Voglmayr, H., Mayer, V., Gueidan, C., Nepel, M., Moreno, L., et al. (2017). A phylogenetic perspective on the association between ants (Hymenoptera: Formicidae) and black yeasts (Ascomycota: Chaetothyriales). *Proceedings. Biological Sciences*, *284*(1850), 20162519. https://doi.org/10.1098/rspb.2016.2519
Vaughan, D. J., Schwarz, E. J., & Owens., D. R. (1971). Pyrrhotites from the Strathcona Mine, Sudbury, Canada; A thermomagnetic and mineralogical study. *Economic Geology*, *66*(8), 1131–1144.
Vera, M., Schippers, A., & Sand, W. (2013). Progress in bioleaching: fundamentals and mechanisms of bacterial metal sulfide oxidation—part A. *Applied Microbiology and Biotechnology*, *97*(17), 7529–7541. https://doi.org/10.1007/s00253-013-4954-2
Viollier, E., Inglett, P. W., Hunter, K., Roychoudhury, A. N., & Van Cappellen, P. (2000). The ferrozine method revisited: Fe(II)/Fe(III) determination in natural waters. *Applied Geochemistry*, *15*(6), 785–790. https://doi.org/10.1016/S0883-2927(99)00097-9
Volk, M. W. R., Gilder, S. A., & Feinberg, J. M. (2016). Low temperature magnetic properties of monoclinic pyrrhotite with particular relevance to the Besnus transition. *Geophysical Journal International*, 1783–1795. https://doi.org/10.1093/gji/ggw376
Volk, M. W. R., McCalla, E., Voight, B., Manno, M., Leighton, C., & Feinberg, J. M. (2018). Changes in physical properties of 4C pyrrhotite, Fe7S8, across the 32K Besnus transition. *American Mineralogist, In Press*. https://doi.org/doi.10.2138/am-2018-6514
Wang, C., Zheng, Y., Sakai, Y., Toyoda, A., Minakuchi, Y., Abe, K., et al. (2019). Tengunoibacter tsumagoiensis gen. nov., sp. nov., Dictyobacter kobayashii sp. nov., Dictyobacter alpinus sp. nov., and description of Dictyobacteraceae fam. nov. within the order Ktedonobacterales isolated from Tengu-no-mugimeshi, a soil-like granular mass of micro-organisms, and emended descriptions of the genera Ktedonobacter and Dictyobacter. *International Journal of Systematic and Evolutionary Microbiology*, *69*(7), 1910–1918. https://doi.org/10.1099/ijsem.0.003396
Wang, H., & Salveson, I. (2005). A review on the mineral chemistry of the non-stoichiometric iron sulphide, Fe1− x S ($0 \leq x \leq 0.125$): polymorphs, phase relations and transitions, electronic and magnetic structures. *Phase Transitions*, *78*(7–8), 547–567. https://doi.org/10.1080/01411590500185542
Watanabe, T., Kojima, H., & Fukui, M. (2014). Complete genomes of freshwater sulfur oxidizers Sulfuricella denitrificans skB26 and Sulfuritalea hydrogenivorans sk43H: Genetic insights into the sulfur oxidation pathway of betaproteobacteria. *Systematic and Applied Microbiology*, *37*(6), 387–395. https://doi.org/10.1016/j.syapm.2014.05.010

Watanabe, T., Kojima, H., & Fukui, M. (2015). *Sulfuriferula* multivorans gen. nov., sp. nov., isolated from a freshwater lake, reclassification of '*Thiobacillus* plumbophilus' as *Sulfuriferula* plumbophilus sp. nov., and description of Sulfuricellaceae fam. nov. and Sulfuricellales ord. nov. *International Journal of Systematic and Evolutionary Microbiology*, *65*(Pt_5), 1504–1508. https://doi.org/10.1099/ijs.0.000129

Watanabe, T., Kojima, H., & Fukui, M. (2016a). Identity of major sulfur-cycle prokaryotes in freshwater lake ecosystems revealed by a comprehensive phylogenetic study of the dissimilatory adenylylsulfate reductase. *Scientific Reports*, *6*(1), 36262. https://doi.org/10.1038/srep36262

Watanabe, T., Kojima, H., & Fukui, M. (2016b). *Sulfuriferula* thiophila sp. nov., a chemolithoautotrophic sulfur-oxidizing bacterium, and correction of the name *Sulfuriferula* plumbophilus Watanabe, Kojima and Fukui 2015 to *Sulfuriferula* plumbiphila corrig. *International Journal of Systematic and Evolutionary Microbiology*, *66*(5), 2041–2045. https://doi.org/10.1099/ijsem.0.000988

Watanabe, T., Kojima, H., Umezawa, K., Hori, C., Takasuka, T. E., Kato, Y., & Fukui, M. (2019). Genomes of Neutrophilic Sulfur-Oxidizing Chemolithoautotrophs Representing 9 Proteobacterial Species From 8 Genera. *Frontiers in Microbiology*, *10*, 316. https://doi.org/10.3389/fmicb.2019.00316

Watson, D. E., Larson, E. E., Herndon, J. M., & Rowe, M. W. (1975). Thermomagnetic analysis of meteorites, 2. C2 chondrites. *Earth and Planetary Science Letters*, *27*(1), 101–107. https://doi.org/10.1016/0012-821X(75)90167-3

Weaver, R., Roberts, A. P., & Barker, A. J. (2002). A late diagenetic (syn-folding) magnetization carried by pyrrhotite: implications for paleomagnetic studies from magnetic iron sulphide-bearing sediments. *Earth and Planetary Science Letters*, *200*(3–4), 371–386. https://doi.org/10.1016/S0012-821X(02)00652-0

Whaley-Martin, K., Jessen, G. L., Nelson, T. C., Mori, J. F., Apte, S., Jarolimek, C., & Warren, L. A. (2019). The Potential Role of Halo*Thiobacillus* spp. in Sulfur Oxidation and Acid Generation in Circum-Neutral Mine Tailings Reservoirs. *Frontiers in Microbiology*, *10*, 297. https://doi.org/10.3389/fmicb.2019.00297

White, W. S. (1960). The Keweenawan lavas of Lake Superior, an example of flood basalts. *American Journal of Science (1880)*, *258-A*, 367–374.

Wickham, H. (2016). *ggplot2: Elegant Graphics for Data Analysis*. Springer-Verlag New York. Retrieved from https://ggplot2.tidyverse.org

Williams, C. D., Ripley, E. M., & Li, C. (2010). Variations in Os isotope ratios of pyrrhotite as a result of water–rock and magma–rock interaction: Constraints from Virginia Formation–Duluth Complex contact zones. *Geochimica et Cosmochimica Acta*, *74*(16), 4772–4792. https://doi.org/10.1016/j.gca.2010.05.030

Wodara, C., Bardischewsky, F., & Friedrich, C. G. (1997). Cloning and characterization of sulfite dehydrogenase, two c-type cytochromes, and a flavoprotein of Paracoccus denitrificans GB17: essential role of sulfite dehydrogenase in lithotrophic sulfur oxidation. *Journal of Bacteriology*, *179*(16), 5014–5023. https://doi.org/10.1128/jb.179.16.5014-5023.1997

Wolfers, P., Fillion, G., Ouladdiaf, B., Ballou, R., & Rochette, P. (2011). The Pyrrhotite 32 K Magnetic Transition. *Solid State Phenomena*, *170*, 174–179. https://doi.org/10.4028/www.scientific.net/SSP.170.174

Woodruff, L. G., Schulz, K. J., Nicholson, S. W., & Dicken, C. L. (2020). Mineral deposits of the Mesoproterozoic Midcontinent Rift system in the Lake Superior region – A space and time classification. *Ore Geology Reviews*, *126*, 103716. https://doi.org/10.1016/j.oregeorev.2020.103716

Wu, W., Pang, X., Lin, J., Liu, X., Wang, R., Lin, J., & Chen, L. (2017). Discovery of a new subgroup of sulfur dioxygenases and characterization of sulfur dioxygenases in the sulfur metabolic network of Acidi*Thiobacillus* caldus. *PLOS ONE*, *12*(9), e0183668. https://doi.org/10.1371/journal.pone.0183668

Yabe, S., Aiba, Y., Sakai, Y., Hazaka, M., & Yokota, A. (2011). Thermogemmatispora onikobensis gen. nov., sp. nov. and Thermogemmatispora foliorum sp. nov., isolated from fallen leaves on geothermal soils, and description of Thermogemmatisporaceae fam. nov. and Thermogemmatisporales ord. nov. within the class Ktedonobacteria. *International Journal of Systematic and Evolutionary Microbiology*, *61*(4), 903–910. https://doi.org/10.1099/ijs.0.024877-0

Yabe, S., Zheng, Y., Wang, C., Sakai, Y., Abe, K., Yokota, A., et al. (2021). Reticulibacter mediterranei gen. nov., sp. nov., within the new family Reticulibacteraceae fam. nov., and Ktedonospora formicarum gen. nov., sp. nov., Ktedonobacter robiniae sp. nov., Dictyobacter formicarum sp. nov. and Dictyobacter arantiisoli sp. nov., belonging to the class Ktedonobacteria. *International Journal of Systematic and Evolutionary Microbiology*, *71*(7). https://doi.org/10.1099/ijsem.0.004883

Yabuuchi, E., Kosako, Y., Oyaizu, H., Yano, I., Hotta, H., Hashimoto, Y., et al. (1992). Proposal of *Burkholderia* gen. nov. and Transfer of Seven Species of the Genus *Pseudomonas* Homology Group II to the New Genus, with the Type Species *Burkholderia cepacia* (Palleroni and Holmes 1981) comb. nov. *Microbiology and Immunology*, *36*(12), 1251–1275. https://doi.org/10.1111/j.1348-0421.1992.tb02129.x

Yamamoto, M., & Takai, K. (2011). Sulfur Metabolisms in Epsilon- and Gamma-Proteobacteria in Deep-Sea Hydrothermal Fields. *Frontiers in Microbiology*, *2*. Retrieved from https://www.frontiersin.org/articles/10.3389/fmicb.2011.00192

Yang, T., Dekkers, M. J., & Chen, J. (2018). Thermal Alteration of Pyrite to Pyrrhotite During Earthquakes: New Evidence of Seismic Slip in the Rock Record. *Journal of Geophysical Research: Solid Earth*, *123*(2), 1116–1131. https://doi.org/10.1002/2017JB014973

Zakharyuk, A. G., Ryzhmanova, Ya. V., Avtukh, A. N., & Shcherbakova, V. A. (2019). Iron-Reducing Microbial Communities of the Lake Baikal Low-Temperature Bottom Sediments. *Microbiology*, *88*(2), 156–163. https://doi.org/10.1134/S0026261719020139

Zanko, L. M., Severson, M. J., & Ripley, E. M. (1994). *Geology and Mineralization of the Serpentine Copper-Nickel Deposit* (Technical Report). University of Minnesota Duluth. Retrieved from http://conservancy.umn.edu/handle/11299/188521

Zhang, J., Kobert, K., Flouri, T., & Stamatakis, A. (2014). PEAR: a fast and accurate Illumina Paired-End reAd mergeR. *Bioinformatics (Oxford, England)*, *30*(5), 614–620. https://doi.org/10.1093/bioinformatics/btt593

Zhang, K., Zheng, H., Wang, J., & Wang, R. (2008). Transmission electron microscopy on iron monosulfide varieties from the Suizhou meteorite. *Physics and Chemistry of Minerals*, *35*(8), 425–432. https://doi.org/10.1007/s00269-008-0237-3

Zhou, Y., Chen, X., Zhang, Y., Wang, W., & Xu, J. (2012). Description of Sinomonas soli sp. nov., reclassification of Arthrobacter echigonensis and Arthrobacter albidus (Ding et al. 2009) as Sinomonas echigonensis comb. nov. and Sinomonas albida comb. nov., respectively, and emended description of the genus Sinomonas. *International Journal of Systematic and Evolutionary Microbiology*, *62*(Pt_4), 764–769. https://doi.org/10.1099/ijs.0.030361-0

Zhou, Z., Liu, Y., Xu, W., Pan, J., Luo, Z.-H., & Li, M. (2020). Genome- and Community-Level Interaction Insights into Carbon Utilization and Element Cycling Functions of Hydrothermarchaeota in Hydrothermal Sediment. *MSystems*, *5*(1), e00795-19. https://doi.org/10.1128/mSystems.00795-19

Zientek, M. L. (2012). *Magmatic ore deposits in layered intrusions—Descriptive model for reef-type PGE and contact-type Cu-Ni-PGE deposits* (Open-File Report) (p. 48). U.S. Geological Survey.

Appendix A: Glossary of Terms

I. Magnetics:

Ferromagnetism – A material is a ferromagnet if all atomic magnetic dipoles within the crystal structure of the material are aligned in the same direction, resulting in a net (external) spontaneous magnetic moment.

Ferrimagnetism – Similar to a ferromagnet, but with two populations of magnetic dipoles whose directions are opposed. The moments of these populations are unequal in magnitude, resulting in a net external magnetic moment.

Antiferromagnetism - Similar to a ferrimagnet, but the two populations of magnetic dipoles are symmetrically opposed, resulting in no net external magnetic moment.

Paramagnetism – Paramagnetic materials have unpaired electron spins, which align with an applied external magnetic field, reinforcing it. This results in a linear response to an applied magnetic field.

Diamagnetism – diamagnetic materials have no unpaired electron spins, so an applied magnetic field induces an internal magnetic field in the material that opposes the applied field. This results in a negative linear response to an applied magnetic field.

Magnetic Susceptibility – Magnetic susceptibility (χ) is a measure of the response of a material to an applied magnetic field. Diamagnets have $\chi < 0$, while paramagnets have $\chi > 0$.

Magnetic hysteresis – Ferromagnetic (and ferrimagnetic) materials can retain a recording (remanent magnetization) of an applied magnetic field that persists when the field is turned off. An applied opposing magnetic field will progressively erase remanent magnetization and re-magnetize the material in the new field direction.

Remanent Magnetization – Magnetic recording of an applied magnetic field. The persistence of this magnetic recording is dependent on material, grain size,

*Sat*uration – *Sat*uration is the maximum induced magnetic moment that can be obtained in a magnetic field, and is a material-specific property. For example, 4C pyrrhotite has a *sat*uration magnetization of 21 Am^2/kg, while magnetite has a *sat*uration magnetization of 90 Am^2/kg.

Coercivity – Essentially a measure of recording strength, this is a function of both material and (magnetic) grain size.

Domain state – Some of the properties of a magnetic material depends on grain size. Magnetic domains are subdivisions within a magnetic grain that reduce surface charge in large grain sizes

Curie temperature – All magnetic materials have a Curie temperature (or Neél temperature, for antiferromagnets) where thermal entropy overpowers magnetic ordering, resulting in a loss in ferromagnetic properties above this temperature. 4C pyrrhotite has a Neél temperature of 320℃, while magnetite has a Curie temperature of 580℃.

II. Biology

OTU – Operational taxonomic unit, which mathematically defines taxa based on genetic sequence differences. Typically defined at 97% similarity, where genetic sequences

16S rRNA – Refers to the small subunit rRNA molecules of bacterial and archaeal ribosomes, which are responsible for translating genetic code (mRNA) to functional cell components (proteins, enzymes, etc.). Because ribosomes are essential for cellular functions, the underlying genes are highly conserved (they have low mutation rates) and so they can be useful markers for tracking evolutionary relationships between microorganisms.

Hmm (hidden Markov model) – a statistical Markov model, used in bioinformatics to evaluate the similarity of an unknown genetic sequence to homologous genetic sequences that code for known proteins

Genes:

rrn – gene that codes for the 16S rRNA molecule

Carbon cycling:

cbbL, rbpL – gene that codes for RuBisCO (ribulose biphosphate carboxylase), essential for carbon fixation as part of the Calvin cycle.

Carboxysome – gene coding for carbonic anhydrase enzymes, which fix CO_2 by the hydration of carbon dioxide

Sulfur Cycling:

Sox system (*soxXABCDYZ*) – genes coding for the thiosulfate-oxidizing multienzyme system, which can catalyze thiosulfate, sulfite, elemental sulfur, and sulfide oxidation either completely to sulfate (for a complete sox pathway) or to elemental sulfur (for an incomplete sox pathway which lacks *soxCD*)

dsrAB – genes coding for dissimilatory sulfite reductase, which was originally described as a sulfur reduction gene but is used by some organisms to oxidize elemental sulfur to sulfite

hdrABC – genes coding for heterodisulfide reductase, which catalyzes the oxidation of elemental sulfur to sulfite

aprAB – genes coding for dissimilatory adenylyl-sulfate reductase, which catalyzes the oxidation of sulfite to adenosine 5'-phosphosulfate (APS)

sat – gene coding for dissimilatory sulfate adenylyltransferase, which oxidizes APS to sulfate or catalyzes the reverse reaction

sqr – gene coding for sulfide:quinone oxidoreductase, which catalyzes the oxidation of sulfide to elemental sulfur

fcc – gene coding for flavocytochrome c sulfide dehydrogenase, which catalyzes the oxidation of hydrogen sulfide to elemental sulfur

tth – sometimes tetH, gene coding for tetrathionate hydrolase which catalyzes the oxidation of tetrathionate to elemental sulfur, thiosulfate, and sulfate

doxDA – genes coding for thiosulfate:quinone oxidoreductase which reduces tetrathionate to thiosulfate

psrABC – genes that code for polysulfide reductase, which catalyzes the reduction of elemental sulfur to sulfide

ttrABC – gene coding for tetrathionate reductase, which catalyzes reversible transformations between tetrathionate and thiosulfate

SOR – genes coding for sulfur oxygenase reductase, which disproportionates elemental sulfur into sulfide, sulfite, and thiosulfate

sreABC – gene coding for sulfur reductase, a molyboprotein that catalyzes the reduction of elemental sulfur to sulfide

sir – gene coding for dissimilatory sulfite reductase, which catalyzes the reduction of sulfite to sulfide

soeABC – gene coding for sulfite dehydrogenase (quinone), which catalyzes the oxidation of sulfite to sulfate

*sor*AB – gene coding for sulfide dehydrogenase, which catalyzes the oxidation of sulfite to sulfate

sdo – gene coding for persulfide dioxygenase, which catalyzes the oxidation of elemental sulfur to sulfite

Appendix B: Supplemental Information for Chapter 2

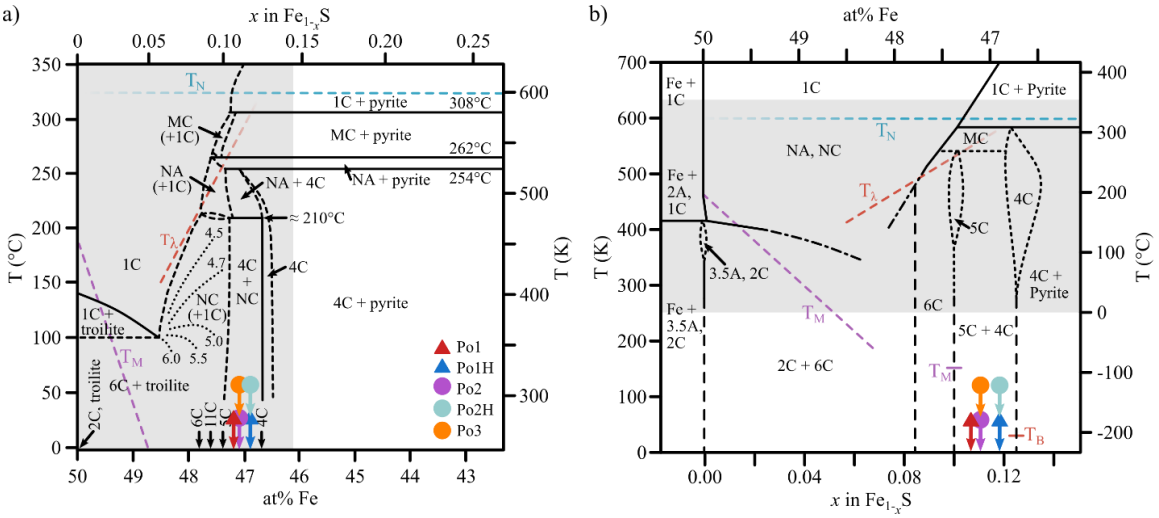

Figure B-1. Phase diagrams for equilibrium phase relationships within the Fe-S system after (a) Harries (2012) and (b) Haines et al. (2019), with the pre- and post-heating mineralogical compositions of the pyrrhotite used in this study marked on the X axis. In both (a) and (b), the high-temperature λ-transition is marked by the red dashed line (T_λ) (Grønvold and Haraldsen, 1952), the Neél temperature (T_N) is marked by the blue dashed line (Dekkers, 1989), and the temperature-composition dependent FeS spin-flop (Morin-type, T_M) transition (Horwood et al., 1976) in purple. NC pyrrhotites are those polytypes with variable and non-integral c axis superstructural repeats. NA and MC pyrrhotites are high-temperature superstructures, and 1C pyrrhotite has completely disordered vacancies but retains the overall NiAs-type unit cell. In (a), tentative phase boundaries are indicated by dashed lines, and values of N for the NC polytypes indicated by the dotted lines, after Nakazawa and Morimoto (1970). In (b), which describes a broader temperature but more restricted Fe-S range, the dashed lines represent the "ideal" superstructure-composition pairs for the 6C, 5C, and 4C polytypes extended to the origin, with observed occurrence of these polytypes off the ideal stoichiometry marked by the dotted lines. The dot-dash lines indicate the poorly-constrained phase transition behavior at elevated temperature between the integral, non-integral, and high-temperature structures. (b) also includes and the ~32 K Besnus transition (T_B) in 4C pyrrhotite (Volk et al., 2019) and the Morin transition in 5C pyrrhotite (Haines et al., 2020). In each phase diagram, the temperature and Fe-S ratio space described in the opposite diagram is marked by the grey shaded region.

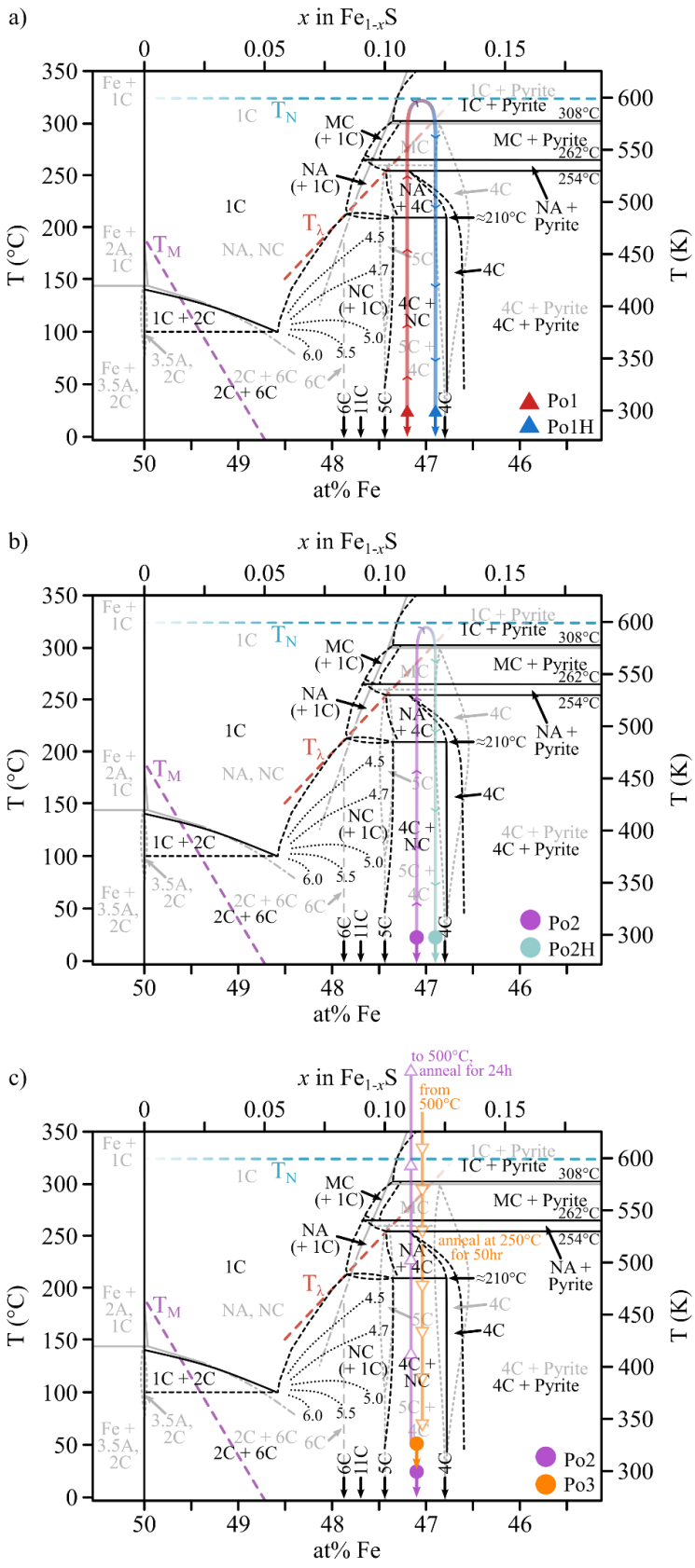

Figure B-2. Heating and cooling paths for (a) Po1-Po1H during HTXRD, (b) Po2-Po2H during HTXRD, and (c) Po2-Po3 during annealing. The phase diagrams from Figure S1 are superimposed, with the Haines et al. (2019) phase diagram in grey and the Harries (2012) phase diagram in black. As in Figure S1, the high-temperature λ-transition is marked by the red dashed line (T_λ) (Grønvold and Haraldsen, 1952), the Neél temperature (T_N) is marked by the blue dashed line (Dekkers, 1989), and the temperature-composition dependent FeS spin-flop (Morin-type, T_M) transition (Horwood et al., 1976) in purple. NC pyrrhotites are those polytypes with variable and non-integral c axis superstructural repeats. NA and MC pyrrhotites are high-temperature superstructures, and 1C pyrrhotite has completely disordered vacancies but retains the overall NiAs-type unit cell.

Table B-1. Ratio of sulfur to iron before and after heating experiments.

	Po1	**Po1H**	**Po2**	**Po2H**	**Po3**
4C Po	47.3%	46.60%	4.70%	17.30%	11.40%
5C Po	43.0%	3.80%	68.30%	44.10%	55.00%
6C Po			8.60%	5.40%	10.50%
3C Po	4.1%	16.10%	3.90%	4.50%	3.30%
Sphalerite			9.80%	10.40%	5.70%
Pyrite	3.0%	25.80%	3.00%	3.50%	3.70%
Marcasite				3.90%	2.60%
Chalcopyrite			1.40%	2.70%	2.60%
Galena			0.30%	1.10%	0.60%
Magnetite	2.5%	7.70%		2.50%	1.80%
Greigite				4.60%	2.70%
Iron	7.57	5.22	7.79	7.30	7.387
Sulfur	8.47	5.91	8.74	7.30	8.29
Ratio (Fe/S)	0.894	0.883	0.891	0.884	0.892
at% Fe	47.19	46.89	47.12	46.92	47.13

To calculate the mass-balance of sulfur and iron before and after heating and annealing, and evaluate the possibility of sulfur loss during the experiments, the "number" of iron and sulfur atoms for each mineral and their respective percentage contributions to the sample as a whole (as determined by the Rietveldt refinement of XRD patterns) were calculated using the following assumptions:

Mineral	**Formula**	**Fe atoms**	**S atoms**
4C Po	Fe_7S_8	7	8
5C Po	Fe_9S_{10}	9	10
6C Po	$Fe_{11}S_{12}$	11	12
3C Po	Fe_7S_8	7	8
Sphalerite	(Zn,Fe)S	0.5*	1
Pyrite	FeS_2	1	2
Marcasite	FeS_2	1	2
Chalcopyrite	$CuFeS_2$	1**	2
Galena	PbS	1	1
Magnetite	Fe_3O_4	3	0
Greigite	Fe_3S_4	3	4

* assuming 50:50::Zn:Fe

** assuming 50:50::Cu:Fe

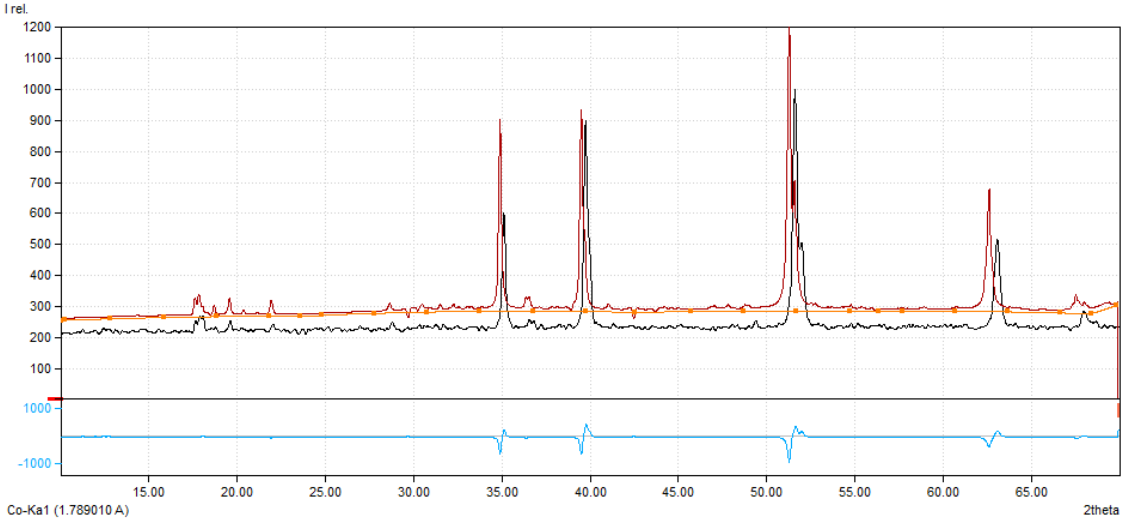

Figure B-3. pXRD pattern for Po1 (black, Co Kα), Rietveldt refinement (red), and difference curve between the collected pattern and refinement (blue). Po1 is indexed as 52.6% 4C Po and 46.9% 5C Po, with a Bragg R-factor of 84.8 and a X^2 of 2.3.

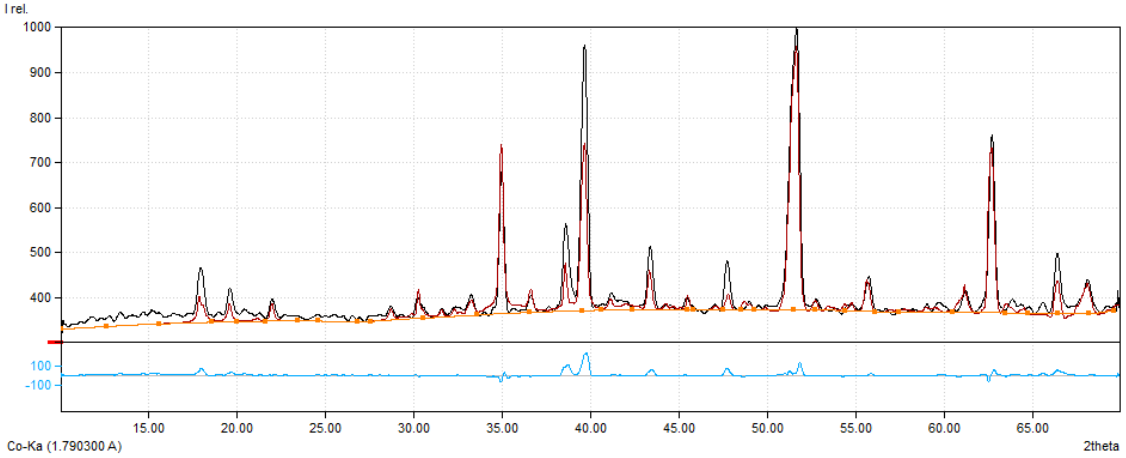

Figure B-4. pXRD pattern for Po1H (black), Rietveldt refinement (red), and difference curve between the collected pattern and refinement (blue). Po1H is indexed as 59.6% 4C Po, 12.1% 3C Po, 9.6% greigite, 8.0% marcasite, 5.5% 5C Po, 2.9% pyrite, and 2.4% magnetite, with a Bragg R-factor of 85.4 and a X^2 of 2.3.

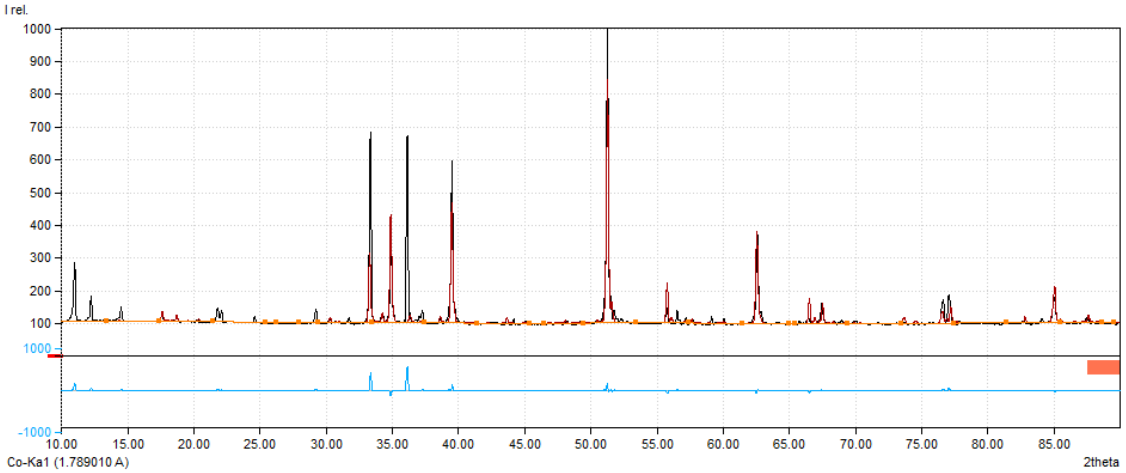

Figure B-5. pXRD pattern for Po2 (black), Rietveldt refinement (red), and difference curve between the collected pattern and refinement (blue). Po2 is indexed as 68.3% 5C Po, 9.8% sphalerite, 8.6% 6C Po, 4.7% 4C Po, 3.9% 3C Po, 3% pyrite, 1.4% chalcopyrite, and 0.3% galena, with a Bragg R-factor of 46.6 and a X^2 of 88.1.

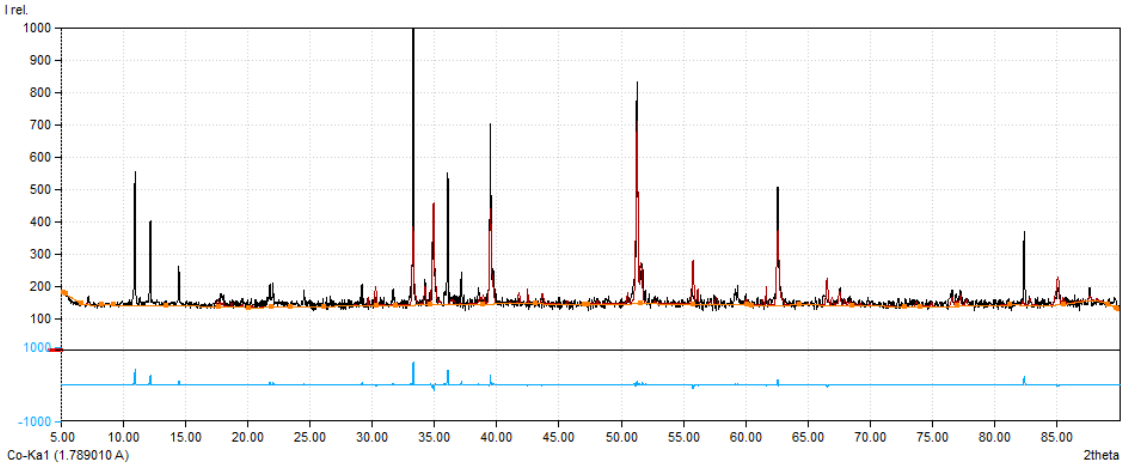

Figure B-6. pXRD pattern for Po2H (black), Rietveldt refinement (red), and difference curve between the collected pattern and refinement (blue). Po2H is indexed as 44.1% 5C Po, 17.3% 4C Po, 10.4% sphalerite, 5.4% 6C Po, 4.6% greigite, 4.5% 3C Po, 3.9% marcasite, 3.5% pyrite, 2.7% chalcopyrite, 2.5% magnetite, and 1.1% galena, with a Bragg R-factor of 87.6 and a X^2 of 6.1.

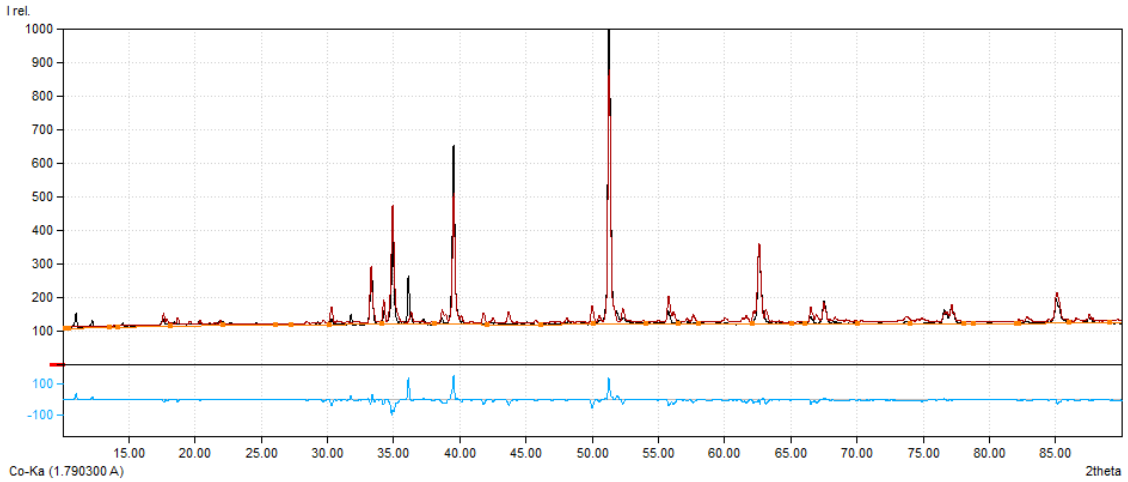

Figure B-7. pXRD pattern for Po3 (black), Rietveldt refinement (red), and difference curve between the collected pattern and refinement (blue). Po3 is indexed as 55.0% 5C Po, 11.4% 4C Po, 10.5% 6C Po, 5.7% sphalerite, 3.7% pyrite, 3.3% 3C Po, 2.7% greigite, 2.6% chalcopyrite, 2.6% marcasite, 1.8% magnetite, and 0.6% galena, with a Bragg R-factor of 57.9 and a X^2 of 51.4.

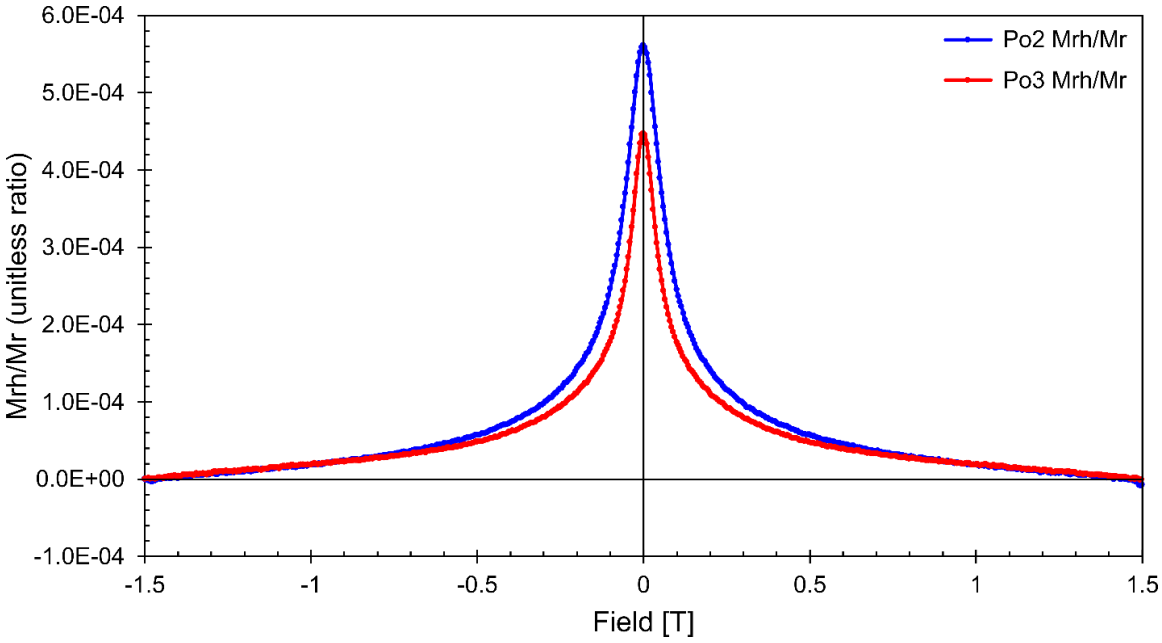

Figure B-8. Plot of remanent hysteretic magnetization (M_{rh}), calculated as half of the difference of the upper and lower hysteresis branches, divided by M_r (saturation remanent magnetization) for Po2 (blue) and Po3 (annealed, red)

Table B-2. Refinement results and phase quantification (in percent) for Po1 on heating from 25°C to 320°C. Abbreviations: Po, pyrrhotite; Py, pyrite; Mrc, marcasite; Grg, greigite; Mag, magnetite; unID, unidentified peak area; R, Bragg R-factor.

	4C Po	5C Po	3C Po	*Total Po*	Py	Mrc	Grg	Mag	*unID*	Sum	R	X^2
25°C	52.60	46.90	0.00	*99.50*	0.10	0.10	0.10	0.10	*3.50*	99.90	84.8	2.3
50°C	49.10	49.80	0.50	*99.40*	0.10	0.00	0.30	0.00	*1.90*	99.80	41.7	0.8
100°C	39.10	47.70	8.30	*95.10*	3.10	0.00	0.00	1.80	*3.20*	100.00	47.8	1.8
150°C	43.00	27.00	26.10	*96.10*	0.30	1.00	1.50	1.10	*1.90*	100.00	76.2	1.7
200°C	40.20	35.70	19.20	*95.10*	2.30	0.10	0.10	2.70	*3.00*	100.30	81.2	3.4
210°C	38.90	26.80	25.00	*90.70*	1.30	2.50	4.00	1.60	*2.80*	100.10	53.1	3.7
220°C	40.80	31.10	24.30	*96.20*	0.10	1.50	1.30	0.90	*1.80*	100.00	87.3	1.4
230°C	27.60	37.90	21.10	*86.60*	0.90	4.30	5.60	2.60	*2.90*	100.00	64.5	5.3
240°C	23.80	40.90	24.10	*88.80*	0.20	3.40	4.80	2.80	*2.10*	100.00	74.1	5.3
250°C	52.60	12.40	28.10	*93.10*	0.60	1.00	4.40	0.90	*1.80*	100.00	49.7	1.6
260°C	66.40	8.30	20.50	*95.20*	0.30	1.40	2.90	0.10	*1.50*	99.90	48.3	2.2
270°C	57.60	9.80	23.70	*91.10*	0.70	2.60	4.80	0.70	*1.90*	99.90	51.3	2.8
280°C	42.00	15.70	29.20	*86.90*	2.60	6.80	2.90	0.80	*1.40*	100.00	82.3	1.5
290°C	53.50	8.60	25.20	*87.30*	2.20	5.30	3.10	2.00	*3.00*	99.90	61.5	2.8
300°C	22.30	28.20	35.10	*85.60*	1.60	6.50	3.00	3.40	*4.20*	100.10	81.2	7.7
310°C	29.60	43.60	17.10	*90.30*	0.80	4.10	2.30	2.40	*3.20*	99.90	55.1	5.7
320°C	34.10	21.20	29.70	*85.00*	0.90	6.80	3.80	3.40	*4.30*	99.90	82.6	6.9

Table B-3. Refinement results and phase quantification (in percent) for Po1 on cooling from 320°C to 25°C. Abbreviations: Po, pyrrhotite; Py, pyrite; Mrc, marcasite; Grg, greigite; Mag, magnetite; unID, unidentified peak area; R, Bragg R-factor.

	4C Po	5C Po	3C Po	*Total Po*	Py	Mrc	Grg	Mag	*unID*	Sum	R	X^2
320°C	34.10	21.20	29.70	*85.00*	0.90	6.80	3.80	3.40	4.30	99.90	82.6	6.9
300°C	42.00	14.40	27.00	*83.40*	1.90	8.80	4.10	1.70	2.40	99.90	55.3	4.9
250°C	49.10	11.50	22.80	*83.40*	2.10	8.30	4.40	1.80	2.40	100.00	91.1	3.4
200°C	58.40	7.50	15.70	*81.60*	2.00	7.20	6.50	2.50	2.70	99.80	91.1	5.9
150°C	69.40	3.10	8.70	*81.20*	1.00	6.20	9.50	2.00	1.50	99.90	73.1	3.3
100°C	67.40	1.30	10.20	*78.90*	2.10	6.80	9.80	2.40	1.70	100.00	70.1	3.8
50°C	63.30	1.90	13.10	*78.30*	2.50	7.00	10.00	2.10	3.50	99.90	76.1	3.2
25°C	59.60	5.50	12.10	*77.20*	2.90	8.00	9.60	2.40	3.40	100.10	85.4	2.3

Appendix C: Supplemental Information for Chapter 3

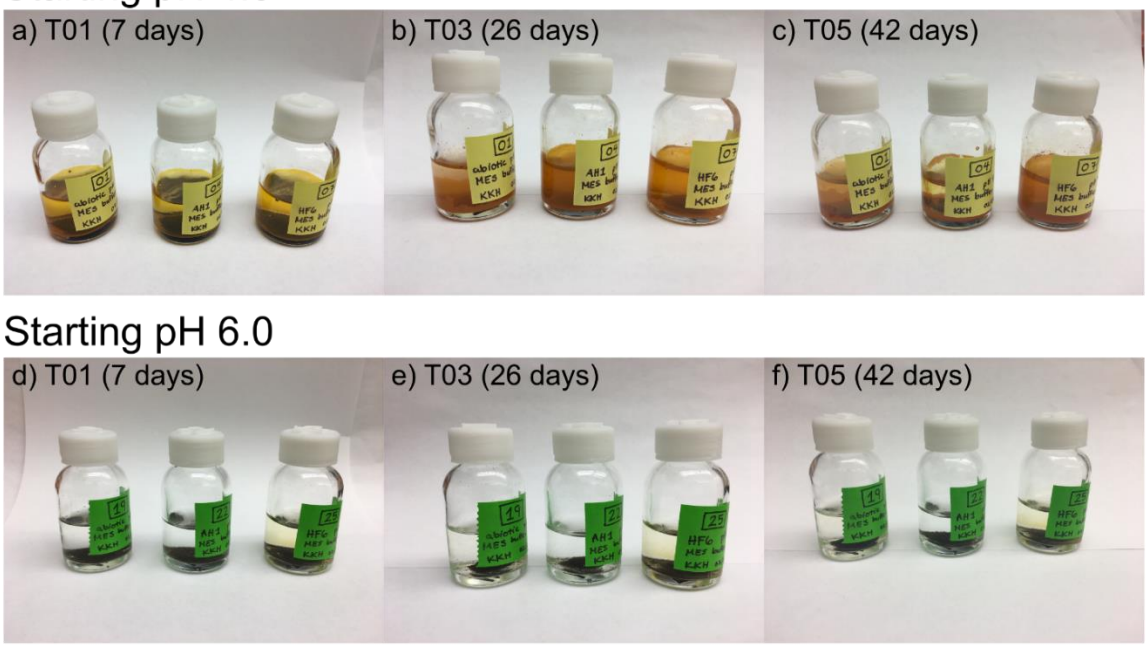

Figure C-1. Selected batch reactor images from Experiment 1 at days 7 (a, d), 26 (b, e), and 42 (c, f) comparing the abiotic (left), isolate-inoculated (middle), and enrichment-inoculated (right) reactors for the starting pH 4.5 (a-c) and starting pH 6.0 (d-f) sets.

Figure C-2. Chips of ore-bearing Duluth Complex rock suspended in leaching media, and a close-up image of rock chip surfaces showing a mixture of sulfide minerals and silicate matrix.

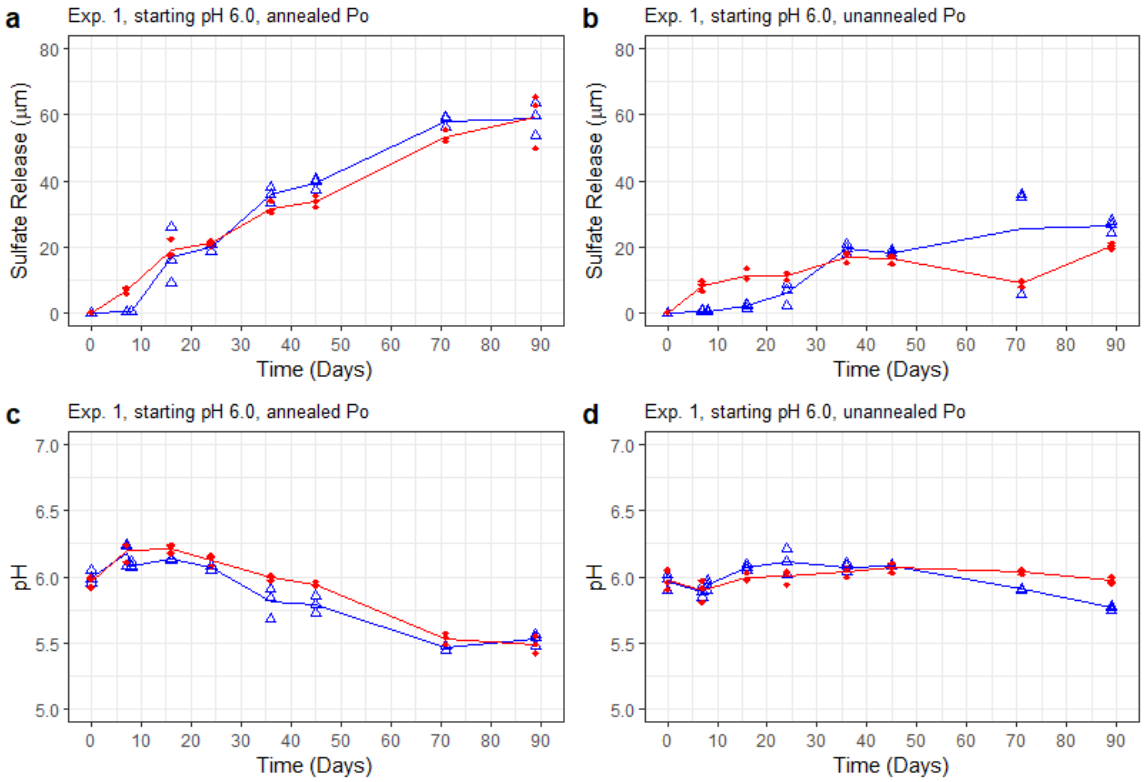

Figure C-3. Sulfate release (a, b) and pH (c, d) from Experiment 1 comparing sulfate release and pH change in reactors containing annealed (a, c) versus unannealed (b, d) pyrrhotite.

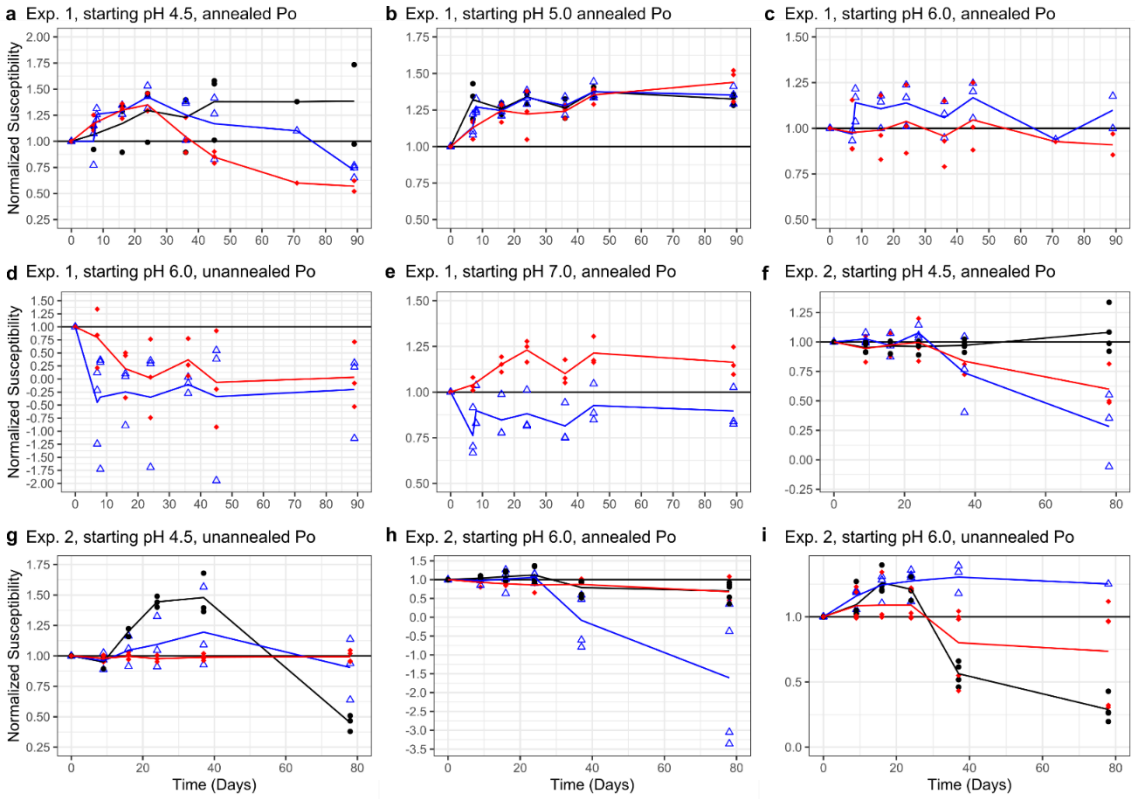

Figure C-4. Normalized bulk magnetic susceptibility for experiments 1 (a-e) and 2 (f-i). Points represent individual measures of susceptibility, while the solid line is the mean for that set of experiments.

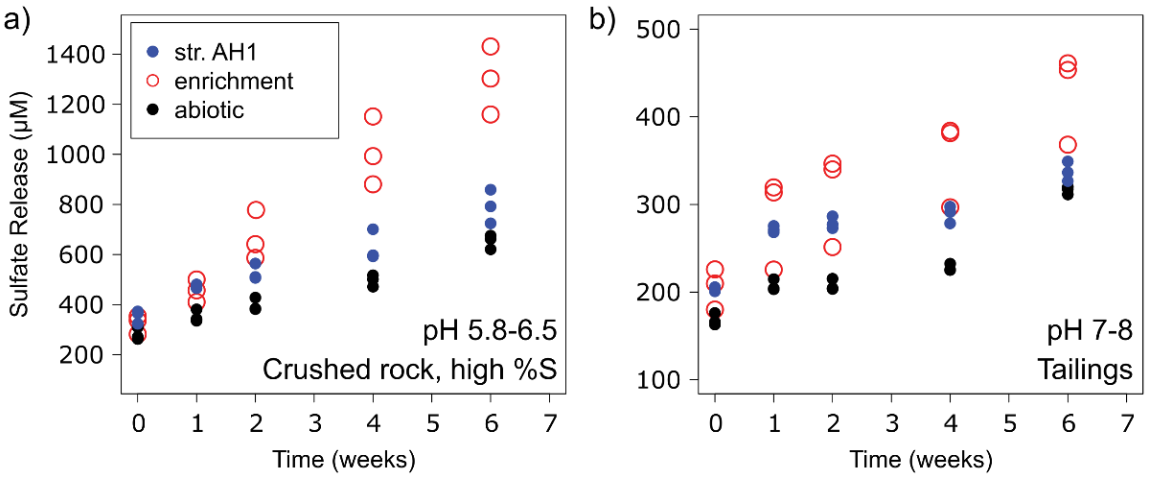

Figure C-5. Sulfate release from experimentally generated Duluth Complex waste rock (a) and tailings (b) abiotically, inoculated with strain AH1, or inoculated with an enrichment.

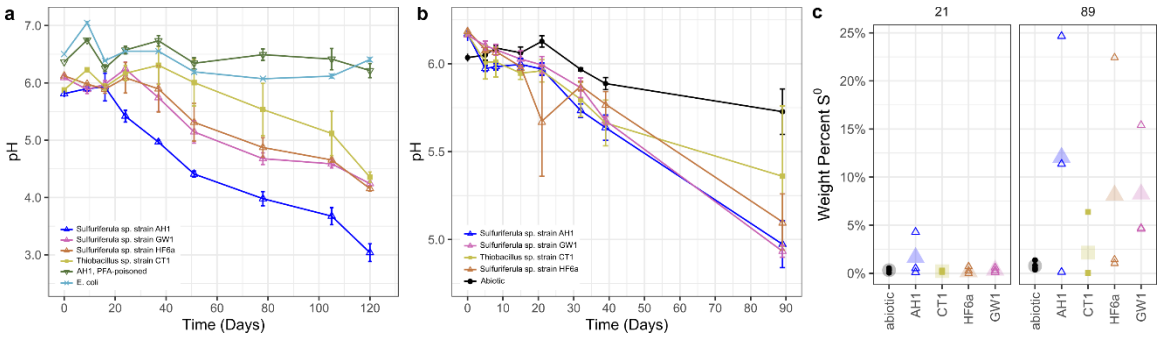

Figure C-6. (a, b) Change in pH over the lifetime of the two experiments with different strains of Sulfuriferula and Thiobacillus, and (c) weight percent elemental sulfur extracted from solids from experiment 3 and day 21 and the termination of the experiment (day 89)

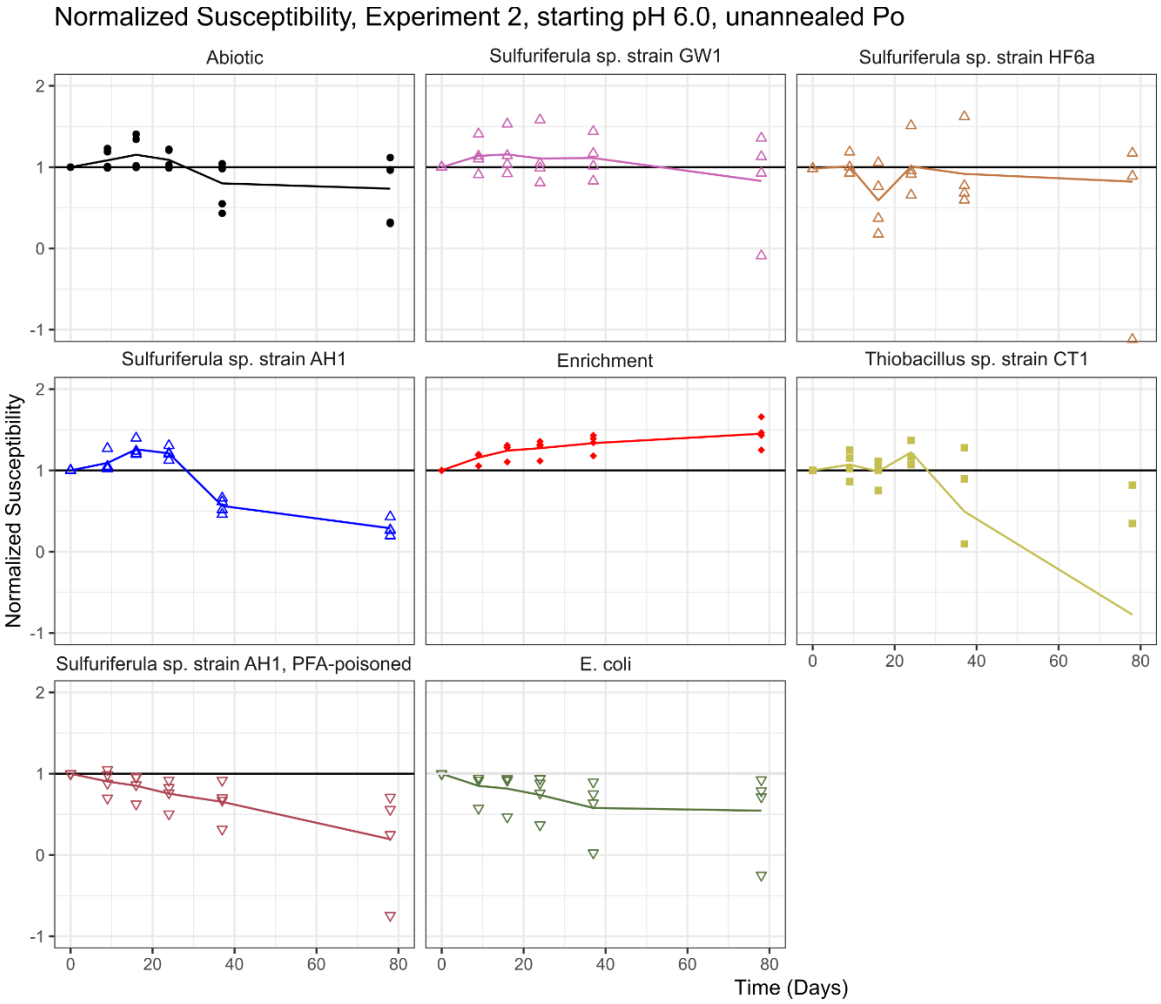

Figure C-7. Normalized bulk magnetic susceptibility for experiment 2, showing changes in magnetic mineralogy for different strains of Sulfuriferula, Thiobacillus, and controls.

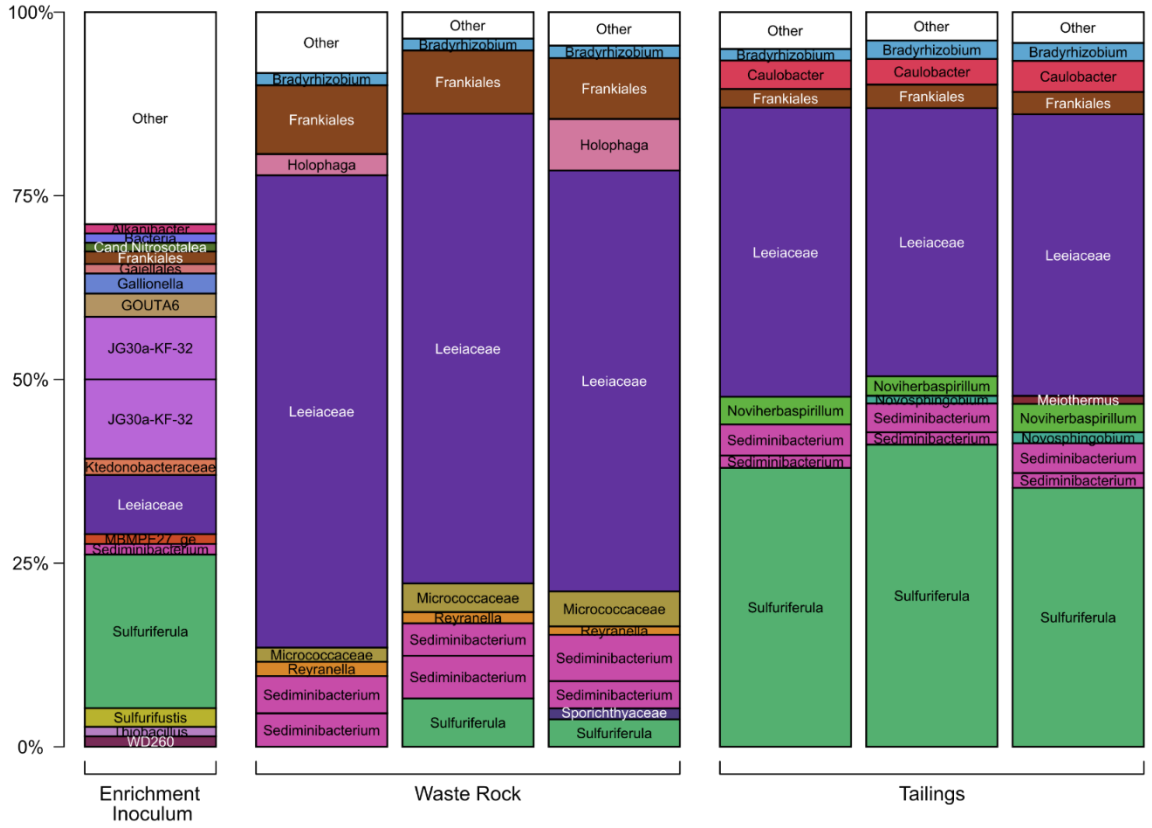

Figure C-8. OTU abundances for the initial enrichment inoculum and enrichment reactors at 8 weeks for experiments on synthesized Duluth Complex waste rock and tailings.

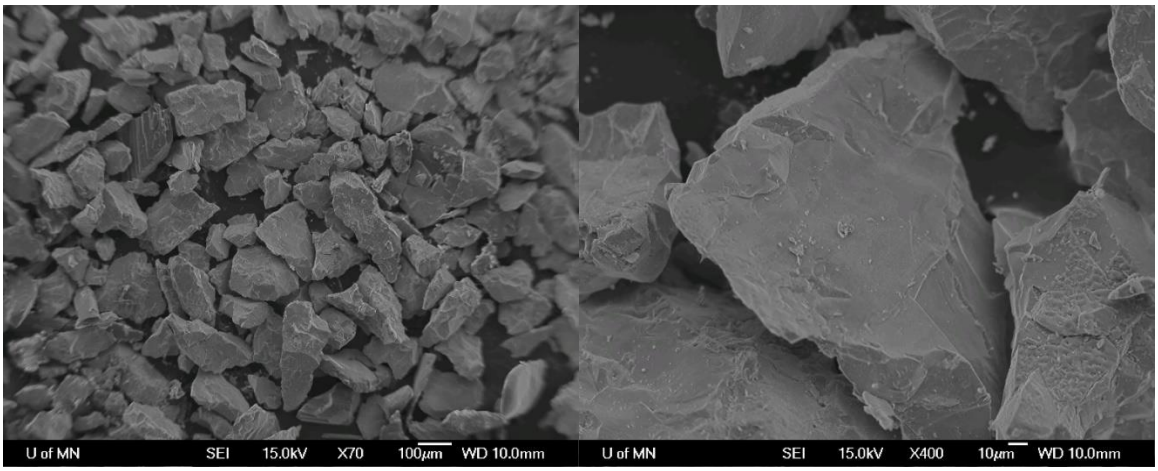

Figure C-9. SEM images of unreacted pyrrhotite surfaces.

Appendix D: Supplemental Information for Chapter 4

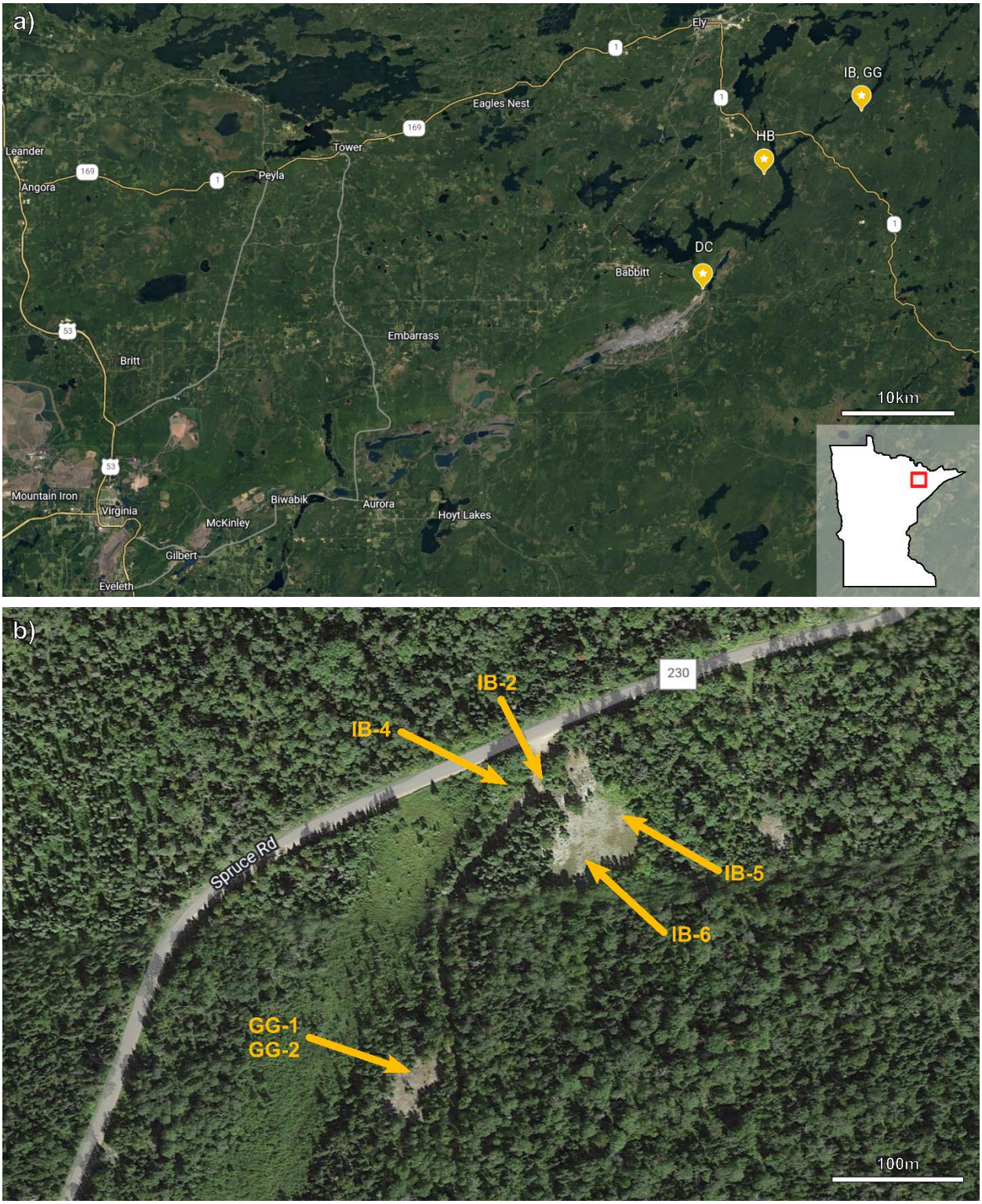

Figure D-1. (a) Map of sampling site locations. (b) Sampling locations at the IB/GG site. Map data from Google Earth; imagery from LANDSAT/Copernicus (NOAA).

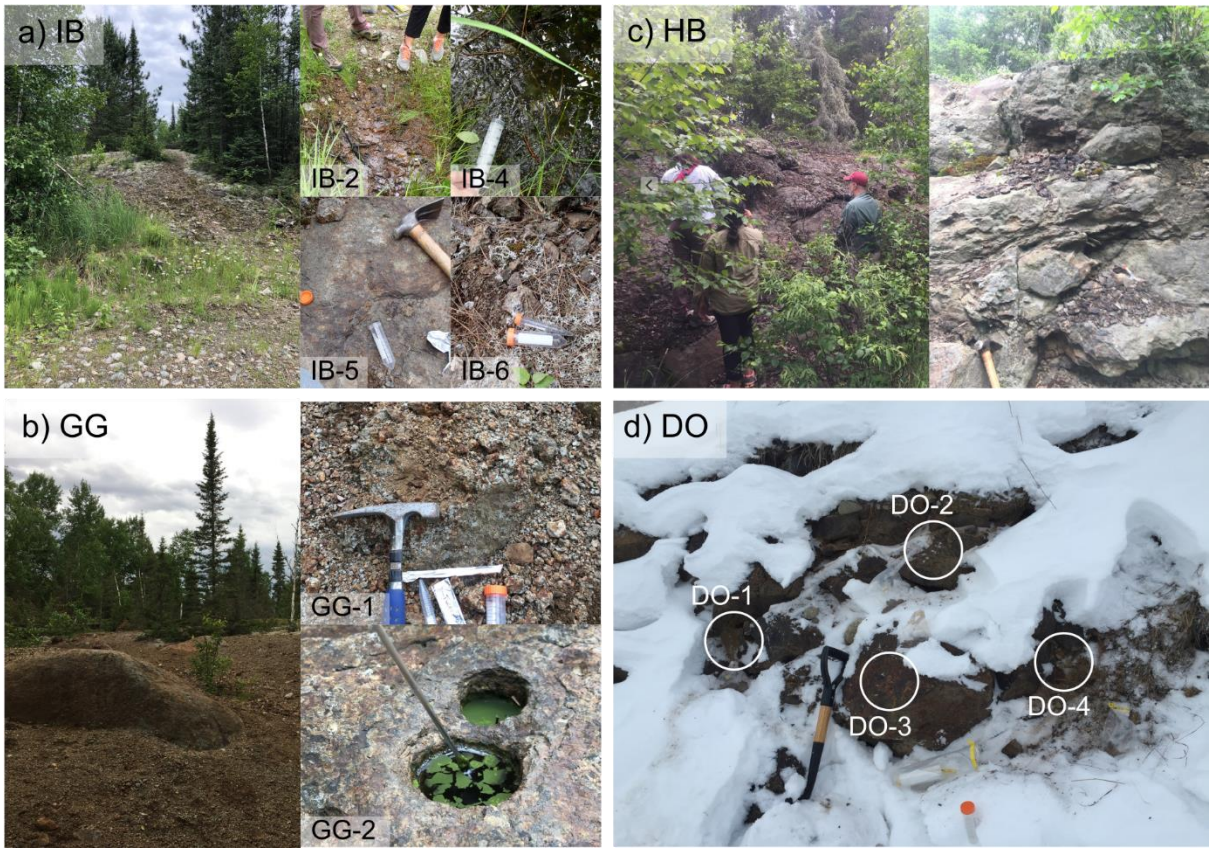

Figure D-2. Sample site images for (a) IB, (b) GG, (c) HB, and (d) DO sites.

Table D-1. Concentration of dissolved anions measured by IC for aqueous samples collected at the IB and GG sampling sites. bd = below detection limit. No detectable phosphate, bromide, or nitrite.

	Sample Type	Fluoride (μM)	Chloride (μM)	Nitrate (μM)	Sulfate (μM)
IB-2	Effluent from seep	52.4	729.4	65.3	477.3
IB-4	Water from stream below seep	31.0	304.4	bd	581.6
GG-2	Water from drill hole in consolidated DC rock	31.0	305.9	bd	360.0

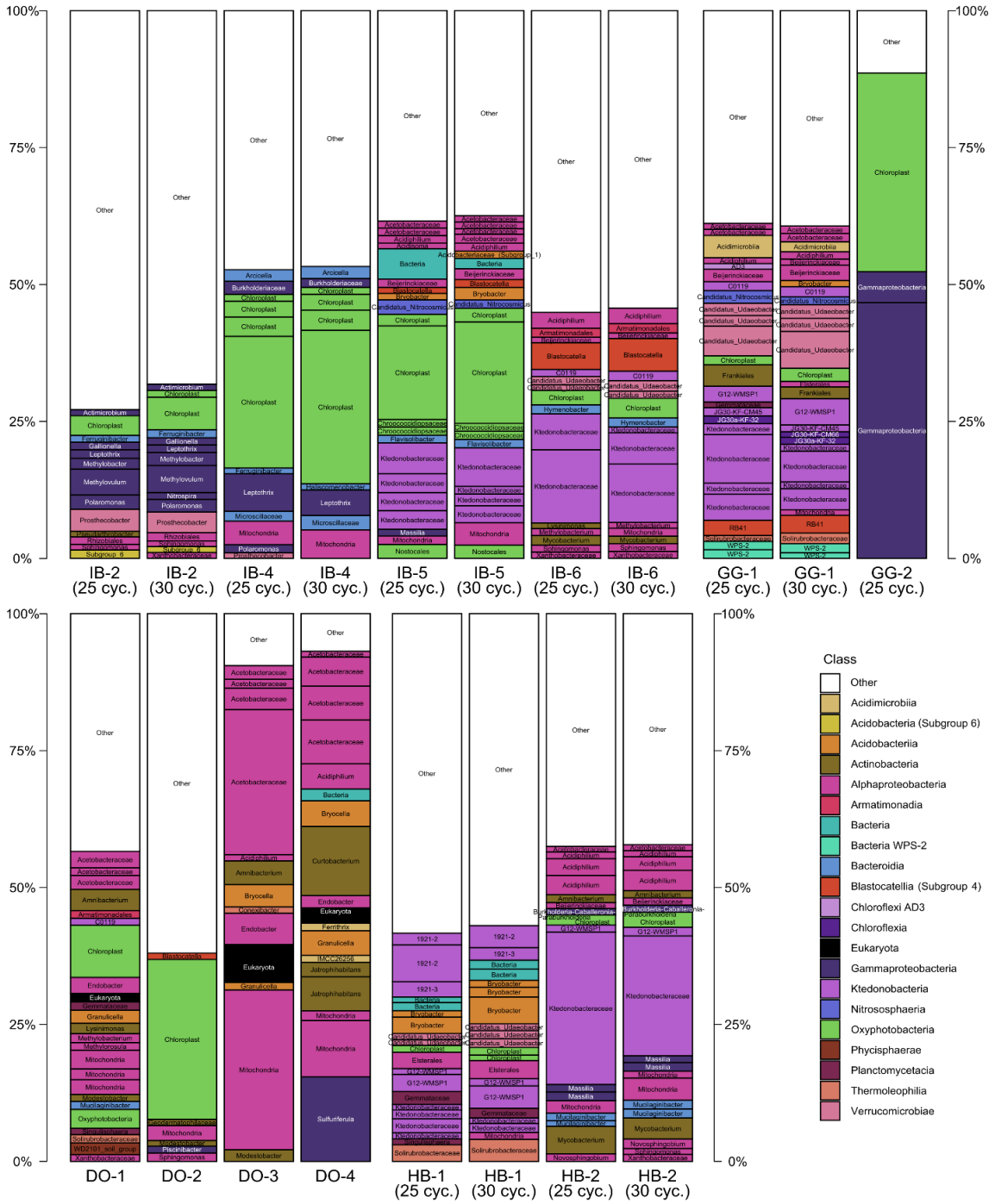

Figure D-3. OTU abundances >1% for the IB, GG, DO, and HB amplicon libraries. OTUs are identified at the genus level, or, at the highest available taxonomic level. OTUs are colored by their classification at the class (or highest available) level. Columns labeled "25 cyc." are the libraries generated from the sample after 25 PCR cycles, and columns labeled "30 cyc." are the libraries generated from the sample after 30 PCR cycles.

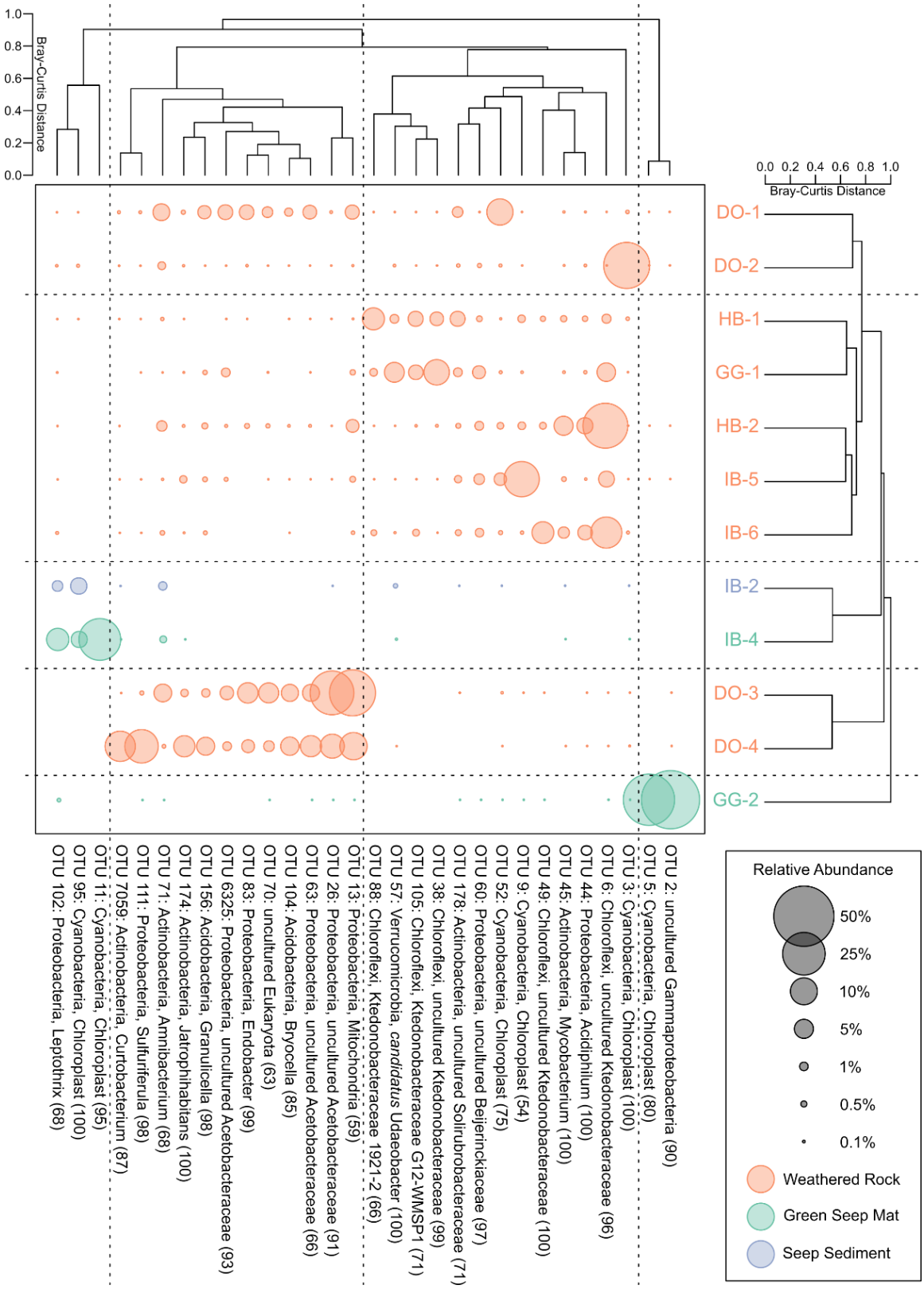

Figure D-4. Hierarchical agglomerative cluster analysis of libraries collected for this study. Size of the points scales with the relative abundance of the OTUs. The Q-mode cluster

analysis was calculated with all OTUs, while the R mode cluster analysis only included the top 30 most abundant OTUs. The taxonomic affiliation of each OTU includes its phylum- and genus-level classification, with confidence scores provided in parentheses. OTUs that are unclassified at the genus level are identified with the highest available taxonomic classification.

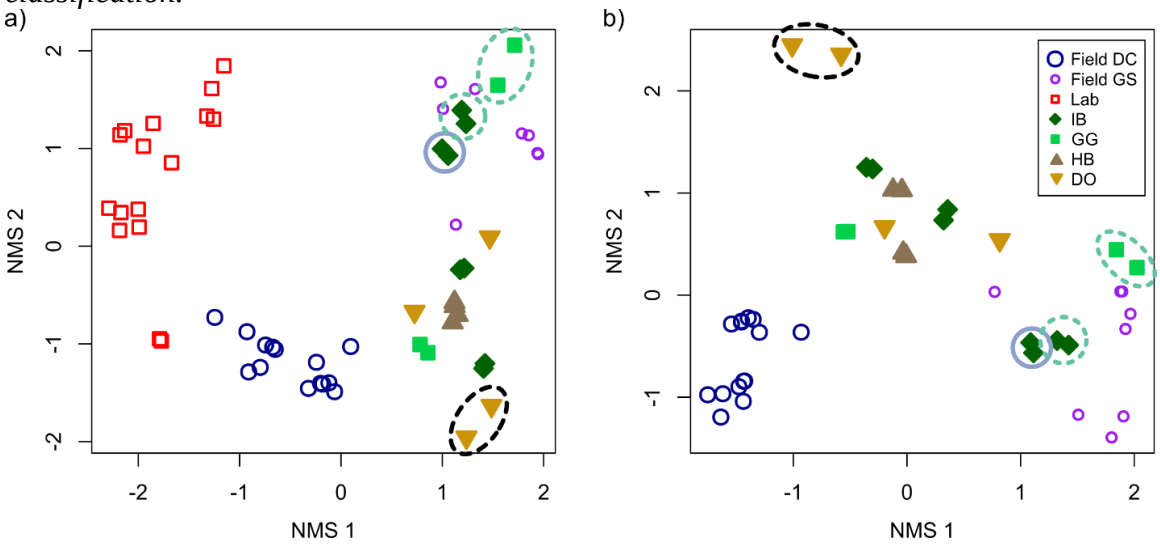

Figure D-5. (a) NMS ordinations of rRNA amplicon libraries from naturally-weathered Duluth Complex outcrops (libraries IB, GG, HB, and DO, this study), laboratory humidity cells ("Lab", red open circles), and experimental field rock piles. This analysis includes the chloroplast, mitochondria, and Eukaryote OTUs removed in Fig. 3. The experimental field rock piles include field leaching experiments with Duluth Complex material ("Field DC," dark blue larger circles) and Ely Greenstone ("Field GS," purple smaller circles). The "Lab" and "Field" leaching experiments are from Jones et al. (2017a). (b) NMS ordinations of rRNA amplicon libraries from the experimental field rock piles and naturally weathered outcrops only, with all OTUs classified as chloroplasts removed. Stress for (a) is 7.464, stress for (b) is 5.806. Sky blue solid circled points indicate seep sediment samples, teal green dotted circled points indicate water and algal biomass samples. All other IB, GG, HB, and DO samples were collected from weathered rock surfaces. The black dashed circle indicates DO samples that are separated from the other weathered rock samples in the hierarchical agglomerative cluster analysis (Figure 2).

Figure D-6. Hierarchical agglomerative clustering analysis of "field" samples from Jones et al. (2017a) with "outcrop" samples from this study. The Q-mode cluster analysis was calculated with all OTUs, while the R-mode cluster analysis only included OTUs appearing

at >10% in any one sample. The taxonomic affiliation of each OTU includes its phylum- and genus-level classification, with confidence scores provided in parentheses. OTUs that are unclassified at the genus level are identified with the highest available taxonomic classification. Outcrop samples (this study) collected from weathered rock are in orange, samples of water and green seep biomass are in teal green, and samples of seep sediments are in sky blue. Samples from experimental field piles of Duluth Complex material (Field DC) are in dark blue, and samples from field piles of Ely Greenstone material (Field EG) are in purple.

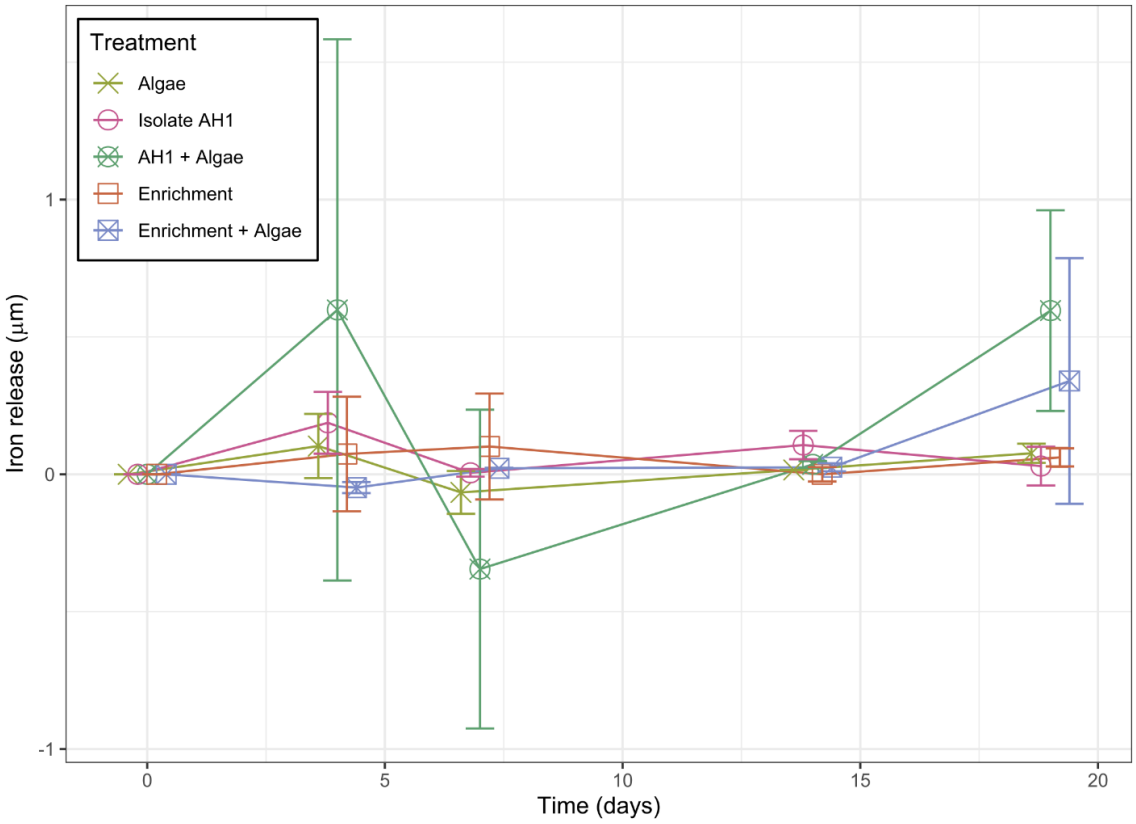

Figure D-7. Average aqueous iron (II) release over the 19-day lifetime of the incubation experiments. Iron (II) concentration was measured colorimetrically by the ferrozine assay.

Appendix E: Supplemental Information for Chapter 5

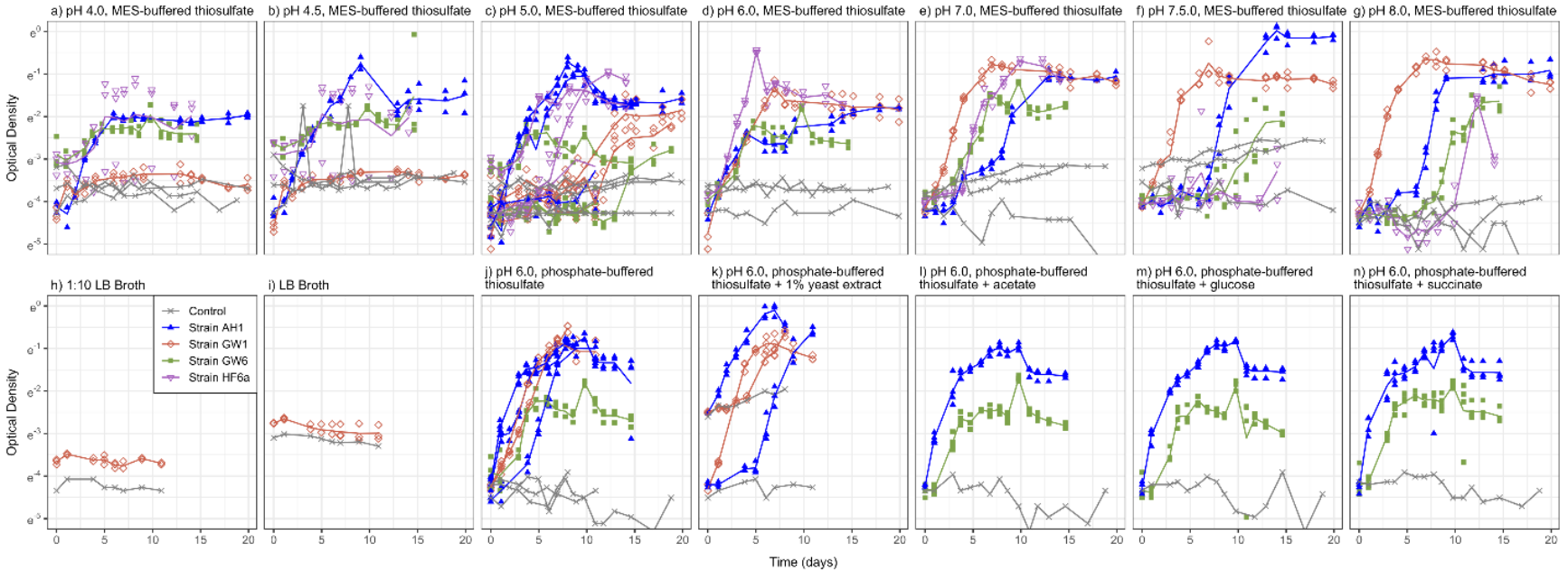

Figure E-1. Growth curve data tracking optical density by absorbance at 600nm for different strains of Sulfuriferula under different pH conditions and on different potential organic substrates.